1-1-2012

IR-UV Spectroscopic Studies of OH and CN Radical Complexes

Bridget Anne O'Donnell
University of Pennsylvania, odonnela@sas.upenn.edu

IR-UV Spectroscopic Studies of OH and CN Radical Complexes

Abstract
Infrared action spectroscopy is used to identify the OH-$HONO_2$ complex, an intermediate proposed to be important in the reaction of OH with $HONO_2$. Two features are observed in the OH stretching region: a rotationally structured band corresponding to the OH radical stretch and a broadened feature assigned to the OH stretch of $HONO_2$. Assignments are based on vibrational frequencies, analysis of rotational structure, and comparison with *ab initio* calculations. Nascent OH product state distributions give a binding energy of ≤5.3 kcal mol^{-1}.

Infrared action spectroscopy is also used to examine the H_2O-HO complex, a primary interaction in the hydration of OH. A rotationally structured band is assigned to the OH radical stretch of H_2O-HO. The stability of the complex, ≤5.14 kcal mol^{-1}, is derived from the nascent OH product state distribution. The assignment is supported by *ab initio* predictions of the spectral shift and dissociation energy. A second feature to lower frequency is attributed to a hot band from an H_2O bending state based on theoretical modeling.

IR-UV double resonance spectroscopy is used to characterize hindered rotor states in the ground electronic state of CN-Ne and CN-Ar. Infrared spectra exhibit perturbations due to Coriolis coupling: a deperturbation analysis gives rotational constants and coupling strengths. The energetic ordering and spacings of the hindered rotor states provide a probe of the anisotropic intermolecular potential, which is compared with *ab initio* calculations. The CN monomer is nearly free rotor-like within both complexes. A similar approach yields the infrared spectrum of H_2-CN, which exhibits rotational structure consistent with *ortho*-H_2-CN in a linear C≡N-H-H configuration.

Lastly, laser-induced fluorescence and IR-UV fluorescence depletion studies are used to characterize the lowest intermolecular levels of CN-Ar correlating with CN $B\ ^2\Sigma^+$ + Ar. Fluorescence depletion spectra confirm that specific features originate from a common ground state. The observed energy level pattern and intensity profile reflect the change in configuration from a weakly anisotropic potential about linear N≡C-Ar in the ground state to linear C≡N-Ar in the excited electronic state.

Degree Type
Dissertation

Degree Name
Doctor of Philosophy (PhD)

Graduate Group
Chemistry

First Advisor
Marsha I. Lester

Keywords
cyano radical, hydrogen bond, hydroxyl radical, infrared spectroscopy, rare gas

Subject Categories
Chemistry

IR-UV SPECTROSCOPIC STUDIES OF OH AND CN RADICAL COMPLEXES

Bridget A. O'Donnell

A DISSERTATION

in

Chemistry

Presented to the Faculties of the University of Pennsylvania

in

Partial Fulfillment of the Requirements for the

Degree of Doctor of Philosophy

2012

Supervisor of Dissertation

_____

Marsha I. Lester

Edmund J. Kahn Distinguished Professor

Graduate Group Chairperson

_____

Gary A. Molander, Hirschmann-Makineni Professor of Chemistry

Dissertation Committee

Michael R. Topp, Professor of Chemistry

Jeffery G. Saven, Associate Professor of Chemistry

Feng Gai, Professor of Chemistry

Dedication

To my parents,

for their unending support.

Acknowledgements

I owe many thanks to those who have supported and encouraged me throughout my graduate career at Penn. First of all, my advisor Marsha Lester, who has been a wonderful mentor and advisor. I would also like to thank my dissertation committee, Prof. Michael Topp, Prof. Feng Gai, and Prof. Jeffrey Saven, for helpful discussions and guidance.

I would also like to thank members of the Lester research group, past and present, who have helped me along the way. Thanks especially to Joseph Beames, who I have worked closely with over the past two years and is more talented than he would care to admit. Thanks also to current graduate students Julia Lehman and Fang Liu. I wish both of you the best of luck at Penn. I would also like to thank past members Eunice Li, Ian Konen, Craig Murray, Logan Dempsey, and Erika Derro, for being patient with me as I began my research and adjusted to the steep learning curve.

Last, but certainly not least, I would like to thank my family. To my parents, who have been incredibly supportive of me throughout my academic career and, without whom, I could not have made it to where I am. To my siblings Janey, Ryan, Erin, and Casey, thank you for keeping me sane throughout this process. And finally, to my husband Rob, who has been incredibly patient, I can't thank you enough for sticking by me through everything.

Abstract

IR-UV SPECTROSCOPIC STUDIES OF OH AND CN RADICAL COMPLEXES

Bridget A. O'Donnell

Marsha I. Lester

Infrared action spectroscopy is used to identify the OH-$HONO_2$ complex, an intermediate proposed to be important in the reaction of OH with $HONO_2$. Two features are observed in the OH stretching region: a rotationally structured band corresponding to the OH radical stretch and a broadened feature assigned to the OH stretch of $HONO_2$. Assignments are based on vibrational frequencies, analysis of rotational structure, and comparison with *ab initio* calculations. Nascent OH product state distributions give a binding energy of $\leq$5.3 kcal mol^{-1}.

Infrared action spectroscopy is also used to examine the H_2O-HO complex, a primary interaction in the hydration of OH. A rotationally structured band is assigned to the OH radical stretch of H_2O-HO. The stability of the complex, $\leq$5.14 kcal mol^{-1}, is derived from the nascent OH product state distribution. The assignment is supported by *ab initio* predictions of the spectral shift and dissociation energy. A second feature to lower frequency is attributed to a hot band from an H_2O bending state based on theoretical modeling.

IR-UV double resonance spectroscopy is used to characterize hindered rotor states in the ground electronic state of CN-Ne and CN-Ar. Infrared spectra exhibit

perturbations due to Coriolis coupling: a deperturbation analysis gives rotational constants and coupling strengths. The energetic ordering and spacings of the hindered rotor states provide a probe of the anisotropic intermolecular potential, which is compared with *ab initio* calculations. The CN monomer is nearly free rotor-like within both complexes. A similar approach yields the infrared spectrum of H_2-CN, which exhibits rotational structure consistent with *ortho*-H_2-CN in a linear C≡N–H-H configuration.

Lastly, laser-induced fluorescence and IR-UV fluorescence depletion studies are used to characterize the lowest intermolecular levels of CN-Ar correlating with CN $B\,^2\Sigma^+$ + Ar. Fluorescence depletion spectra confirm that specific features originate from a common ground state. The observed energy level pattern and intensity profile reflect the change in configuration from a weakly anisotropic potential about linear N≡C–Ar in the ground state to linear C≡N–Ar in the excited electronic state.

Table of Contents

List of Tables

Chapter 2.

Chapter 3.

Chapter 4

List of Figures

Appendix 3

Appendix 4

Chapter 1:

Introduction

Atmospheric chemistry has been a subject of scientific interest for over three centuries beginning with determination of the major constituents which make up Earth's atmosphere. Over the past century, the subject of study has shifted away from the major components of the atmosphere to trace species, which, although small in concentration, play a major role in the chemistry of Earth's atmosphere. In addition, the ever-evolving nature of the atmosphere over time results in significant changes of basic chemical processes. For example, one of the most important trace species whose concentration has changed significantly over time is ozone (O_3), which in the stratosphere acts as a protective screen blocking ultraviolet photons from reaching Earth's surface, but whose rising concentration in the troposphere is harmful to both plants and humans. Particularly in recent years, with ever-increasing concern over pollution and climate change, atmospheric chemistry remains an active field of research.[1,2]

The chemistry of the atmosphere is driven by a wide variety of trace species, but the hydroxyl radical (OH) ranks as one of the most significant. It is widely termed the "detergent" of Earth's atmosphere because of its high reactivity towards a large variety of destructive species in the atmosphere, most notably carbon monoxide (CO) and methane (CH_4). The hydroxyl radical (OH) is formed primarily through the photolysis of ozone by ultraviolet (UV) photons ($\lambda<340$ nm) to form O (^{1}D), which then reacts with water in the atmosphere to produce two OH radicals.

$$O_3 + h\nu \rightarrow O\,(^1D) + O_2$$

$$O\,(^1D) + H_2O \rightarrow 2OH$$

$$O\,(^1D) + M \rightarrow O\,(^3P)$$

The formation of OH competes with deactivation of the excited oxygen atom to form ground state O (^{3}P) via collisional relaxation (*M*). In addition to this primary production pathway, OH may also be formed in polluted areas through photolysis of nitrous acid (HONO) and hydrogen peroxide (H_2O_2) where high concentrations of these species are present.

$$HONO + h\nu\ (\lambda<400\ nm) \rightarrow OH + NO$$

$$HOOH + h\nu\ (\lambda<370\ nm) \rightarrow 2OH$$

There are many varied pathways for OH production aside from the primary one listed above, and the amount of OH in any given scenario varies greatly depending upon the time of day and geographical region being studied. In addition, because the formation pathways are mostly photolytic in nature, OH is a major oxidant during daylight hours.[1,2]

The OH radical is also a key component in the tropospheric HO_x cycle, which is the production pathway responsible for ozone formation and hydrocarbon oxidation.

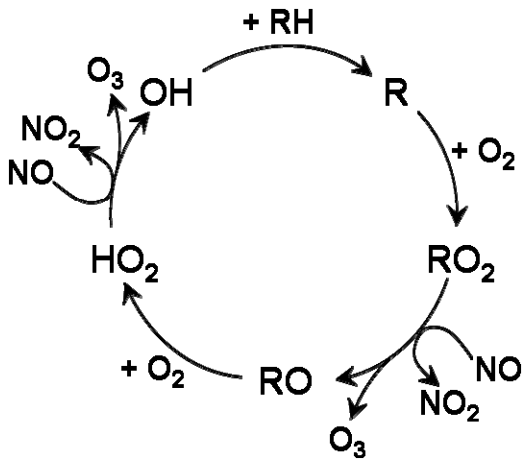

OH reacts with a hydrocarbon (RH) to form an alkyl radical, R, which then reacts with oxygen to form an alkylperoxy radical, RO_2. RO_2 subsequently reacts with NO to form an alkoxy radical, RO, and, in the process, creates ozone and NO_2. RO then reacts with

O_2 to form the hydroperoxyl radical, HO_2, which combines with NO to reform OH and produces another ozone molecule and NO_2. The net result of the tropospheric HO_x cycle is the oxidation of a single hydrocarbon molecule and formation of two ozone molecules. It is important to note that OH is reformed in the process, leading to no net loss.[1,2]

Nitric acid ($HONO_2$) is another important trace species in the atmosphere; it acts as a relatively stable sink for NO_2 and is one of the most abundant acids in Earth's atmosphere. The formation of nitric acid ($HONO_2$) in the gas phase includes several pathways as shown below

$$NO_2 + OH + M \rightarrow HONO_2 + M$$

$$N_2O_5 + H_2O \rightarrow 2HONO_2$$

$$NO_3 + RH \rightarrow HONO_2 + R$$

In the first reaction, formation of nitric acid serves as a reservoir for NO_2, which reacts readily with OH to form $HONO_2$. Again, because OH sources are primarily photolytic, the formation of $HONO_2$ in this case is a daytime reaction. The second reaction is the dominant formation pathway of nitric acid in the Northern Hemisphere arising from hydrolysis of dinitrogen pentoxide, N_2O_5, to form two $HONO_2$ molecules. The reaction is known to be catalyzed by surfaces and the reaction occurs rapidly at aqueous interfaces on many surfaces to form $HONO_2$ (*l*). The last mechanism is reaction of the nitrate radical (NO_3) with an organic species (i.e. aldeydes, alkanes) to form $HONO_2$ and a carbon containing radical, R.[1,2]

The primary removal pathway of nitric acid in the troposphere is through wet or dry deposition, as $HONO_2$ is "sticky" and readily adsorbs, particularly to aqueous

surfaces. However, in the upper troposphere and stratosphere, where there is no rain, $HONO_2$ is removed by solar photolysis and reaction with OH.

$$HONO_2 + h\nu\ (\lambda<350\ nm) \rightarrow OH + NO_2$$

$$\rightarrow O + HONO$$

$$OH + HONO_2 \rightarrow H_2O + NO_3$$

The quantum yield (ϕ) for formation of OH and NO_2 in the first reaction is unity down to 222 nm, while ϕ for production of O and HONO at 193 nm is 0.8. The reaction of nitric acid with OH results in conversion of $HONO_2$ into reactive NO_x species as the unstable NO_3 radical rapidly decomposes to form NO and NO_2.[1,2] The reaction of OH with nitric acid has been the subject of many experimental[3-8] and theoretical studies[4,9,10] aimed at understanding the reaction mechanism.

Kinetic studies of the reaction of OH and $HONO_2$ have revealed several unusual characteristics including a negative temperature dependence, pressure dependence, and a strong isotope effect with deuterium substitution in $HONO_2$.[3-8] The observed kinetics have been modeled using the scheme pictured below. The reaction begins through formation of an energized pre-reactive intermediate, $OH\text{-}HONO_2^*$, which may be stabilized via collisions, redissociate to form OH and $HONO_2$, or react to form products, H_2O and NO_3. The collisionally stabilized complex, $OH\text{-}HONO_2$, may also lead to reaction.

$$\begin{array}{ccccc} OH + HONO_2 & \rightleftarrows & OH-HONO_2^* & \rightarrow & H_2O + NO_3 \\ & & \updownarrow [M] & & \\ & & OH-HONO_2 & \rightarrow & H_2O + NO_3 \end{array}$$

The negative temperature dependence and pressure dependence are attributed to the enhanced stabilization and formation of the reaction intermediate while the greatly decreased reaction rate with deuterium substitution is attributed to lowered tunneling efficiency with increasing mass. It should be noted that deuterium substitution in the hydroxyl radical does not change the reaction rate significantly.

The structure and stability of the pre-reactive intermediate in the reaction of OH with $HONO_2$ have been predicted theoretically using a variety of methods.[4,9,10] The complex is predicted to form a doubly hydrogen-bonded complex where the H of OH hydrogen-bonds to an oxygen atom of $HONO_2$ and the H of $HONO_2$ hydrogen-bonds to the oxygen atom of OH, forming a planar six-membered ring-like structure as pictured in Figure 1. The stability (D_e) has been predicted to be between 6.9 and 9.8 kcal mol^{-1} while the zero-point corrected binding energy (D_0) is predicted to lie between 5.6 and 8.1 kcal mol^{-1}. A transition state is predicted 3.5 kcal mol^{-1} higher in energy where the O-H bond in $HONO_2$ is extended and the H atom is nearly equidistant between $HONO_2$ and OH.[10] The *ab initio* structure of the transition state supports the proposed mechanism made in kinetic studies that reaction occurs via tunneling of the H atom through the reaction barrier at low temperature.

In our lab, OH-$HONO_2$ is stabilized and probed directly using infrared (IR) action spectroscopy, allowing for spectral characterization of the intermediate as detailed in **Chapter 2**. The complex is formed through the association of photolytically generated OH radicals with $HONO_2$ and subsequent stabilization via three-body collisions in a supersonic jet. IR action spectroscopy is then used to identify both the hydroxyl OH stretch (ν_1) and the OH stretch of nitric acid (ν_2) within the complex. Both observed

Figure 1. (a) Minimum energy geometries of OH-$HONO_2$ and (b) H_2O-HO, and structural parameters used to describe (c) CN-Ne/Ar, and (d) CN-H_2.

a.

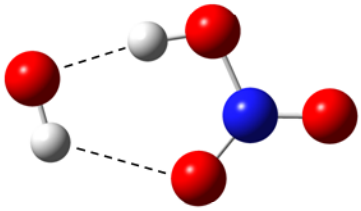

b.

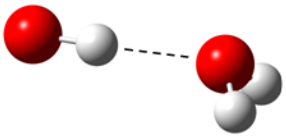

c.

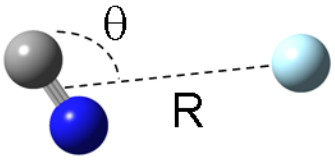

d.

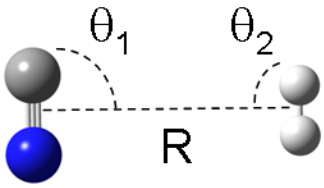

bands display characteristic features of hydrogen bonding,[11] including spectral shifts to lower energy of their respective monomer frequencies and, in the case of ν_2, extensive spectral broadening arising from anharmonic coupling between vibrational states. Vibrational predissociation of the complex upon infrared excitation to form OH and subsequent measurement of the populated rotational states of OH (E_{OH}), allows for determination of an upper limit of the complex's binding energy, D_0, based upon a simple energy balance equation, $h\nu_{IR} - D_0 = E_{HONO_2} + E_{OH} + E_t$. Due to the fact that the internal energy of $HONO_2$ (E_{HONO_2}) and the translational energy of both fragments (E_t) are not characterized, an upper limit alone may be determined of $D_0 \leq 5.3$ kcal mol^{-1}. Complementary *ab initio* calculations provided supporting evidence for the spectral assignments made.

Because of the importance of OH as a "cleanser" of trace species in the atmosphere, it is crucial to find what role complexes with OH, including non-reactive ones, may play in the broader chemistry of the atmosphere.[12] Complexation of OH with water is one such system which has attracted interest. The H_2O-HO complex has been detected directly in infrared spectroscopy in matrices[13-15] and microwave spectroscopy in the gas phase[16-19] in addition to being calculated theoretically via a plethora of different methods.[20-23] Apart from acting as a sink for OH radicals, the OH-H_2O complex is also theoretically predicted to be more reactive than OH, specifically in reaction with saturated hydrocarbons.[12]

The H_2O-HO complex is predicted to have a global minimum structure where the hydrogen atom of OH is hydrogen bonded to the oxygen atom of H_2O. The hydrogen

atoms of the water molecule are situated out-of-plane resulting in a minimum energy C_s symmetry as shown in Figure 1.[20-23] There are two equivalent C_s minima with a planar C_{2v} symmetry structure as a barrier between them, predicted to be ~18 cm^{-1} in magnitude.[22] There is also a second local minimum in which one hydrogen atom of water is hydrogen bonded to the oxygen atom of OH. It is predicted to be less well bound than the global minimum by a factor of ~2. In addition to structural considerations, frequency calculations have been carried out which predicted a red-shift of the OH stretch in the global minimum geometry, consistent with the hydrogen bonding motif.[22,23]

In addition to *ab initio* predictions, the H_2O-HO complex has been observed in argon and neon matrices[13-15] and in the gas phase using microwave spectroscopy.[16-19] Three vibrational modes of the H_2O-HO complex attributed to the various OH stretching states were observed in an argon matrix consistent with the minimum energy geometry predicted by theory. The analogous three bands were also observed in the deuterated counterpart, D_2O-DO, confirming the structural assignment.[13] The OH stretch of the complex (ν_2) was also observed in a Ne matrix.[15] In both matrices, ν_2 was shifted to lower frequency relative to the monomer matrix frequency, verifying the trend predicted theoretically. The H_2O-HO complex and its associated isotopomers, both D and ^{18}O substituted, have also observed in microwave spectroscopy in the gas-phase, where the vibrationally averaged configuration was found to be planar.[16-19]

In our lab, the H_2O-HO complex is stabilized and probed using IR action spectroscopy as described in **Chapter 3**. The OH radical stretch of the complex, ν_2, is identified, shifted to lower wavenumber of the OH monomer stretch, which is a spectral

signature of the hydrogen bond in H_2O-HO. The stability of the H_2O-HO complex is derived in the same manner as described above to be $D_0 \leq 5.14$ kcal mol^{-1}. Complementary *ab initio* calculations verify the observed spectral shift and stability measured experimentally. In addition to the main feature assigned to ν_2, an additional feature is observed, shifted 15 cm^{-1} lower in frequency which is assigned as a hot band originating from an out-of-plane H_2O bending state.

The cyano radical, although not prevalent in Earth's atmosphere, is important in planetary atmospheres, interstellar medium, and is an important product in the combustion of nitrogen containing fuels.[24-28] It is also important in the removal of harmful NO_x products from combustion in a process called reburning. In the combustion of natural gas and other low nitrogen-containing fuels, NO_x is produced in significant quantities such that combustion modification technologies have been developed to decrease their emissions. In the reburning process, a secondary combustion zone is introduced after the main combustion zone where additional fuel is introduced and NO_x undergoes both formation and removal reactions, ultimately leading to a decrease in NO_x concentrations of 50-70%.[25] Although there are several mechanisms for NO_x removal, the basic process begins with carbon-containing radicals which are formed in the reburning stage that reduce the NO concentration by converting it to various species with C-N bonds, including the cyano radical. These species are then reduced in reactions with various radicals to produce NH species that finally react with NO to form N_2. The removal of NO is then twofold; first by reaction with carbon-containing radicals forming CN species, and secondly by reaction with nitrogen-containing radicals.

$$C + NO \rightarrow CN + O$$

$$CN + O_2 \rightarrow NCO + O$$

$$CN + OH \rightarrow NCO + H$$

$$NCO + H \rightarrow NH + CO$$

$$NH + NO \rightarrow N_2 + OH$$

The inclusion of additives to the reburning process can further reduce NO_x emissions by as much as 90%.[25]

In addition to its use as a NO_x "scrubber", the reaction of CN with hydrocarbons in both the gas and solution phase has gained significant interest. [29-37] The reaction of CN with alkanes has been shown to display non-Arrhenius behavior with a negative temperature dependence at low temperature. Specifically, in the case of the reaction of CN with ethane (C_2H_6), the reaction rate exhibited a sharp minimum in the rate constant at ~200 K. Theoretical calculations were carried out to explain the observed behavior, and it was proposed that, at low temperature, the rate determining step for reaction involved the formation of a weakly bound complex. At higher temperature, the barrier to reaction, which is predicted to lie below the reactant asymptote, is surmounted.[38] To accurately model the observed kinetics of CN reactions, it is important to take into account both the formation of stable complexes as well as the presence of a barrier to products and its position above or below the reactant asymptote. While the presence of bound van der Waals complexes have been inferred from the kinetics studies, the complexes have not been probed directly. Preliminary investigation of CN-rare gas and CN-H_2 complexes provides a means for future studies of more complicated systems.

There has been extensive experimental and theoretical work on CN-Ne,[39-42] CN-Ar,[43-46] and CN-H_2/D_2 complexes.[47-51] Thus far, most of the experimental work has

focused on electronic spectroscopy and excited state dynamics in these systems. In all three systems, electronic spectra of the complexes have been recorded in the CN $B\,^2\Sigma^+$-$X\,^2\Sigma^+$ region using laser induced fluorescence (LIF), hereafter referred to as *B*-*X* transitions of the complexes. In CN-Ne, rotationally structured bands have been observed through excitation of the complex to the *B* state and subsequent fluorescence of the complex back to the ground state. The electronic spectrum of CN-Ne displays a progression of vibrational bands with a *B*-*X* electronic origin shifted minimally from free CN.[40,42] The excited state dynamics of both CN-Ar and CN-H_2 are drastically different from that observed in CN-Ne. In CN-Ar, the complex undergoes electronic predissociation after excitation to the *B* state, forming vibrationally excited CN radicals in the *A* state. The resulting long-wavelength and long lifetime CN *A*-*X* fluorescence is then collected. The CN-Ar *B*-*X* spectrum is congested and difficult to analyze, displaying groupings of vibrational bands that are not easily assignable.[44] In CN-H_2, the complex is excited to a continuum above the CN $B\,^2\Sigma^+ + H_2$ asymptote, resulting in CN *B*-*X* fluorescence which is then collected. Due to the bound-free nature of the transition, the CN-H_2 *B*-*X* spectrum is unstructured, however the dissociation threshold has been determined allowing for an estimate of the ground state binding energy, D_0.[50]

In addition to extensive experimental work, *ab initio* calculations on the potential energy surfaces (PES) of CN-Ne,[52,53] Ar,[43] and H_2[51] have been carried out. Two geometric parameters were used to describe the CN-Ne and CN-Ar complexes; *R* is the distance from the center of mass of CN to Ne/Ar and θ is the angle between C, the center of mass of CN, and Ne/Ar as depicted in Figure 1. In CN-H_2, there are four geometric parameters used to describe the complex geometry; *R* is the distance from the center of

mass of CN to the center of mass of H_2, θ_1 is the angle between C, the center of mass of CN, and the center of mass of H_2, θ_2 is the angle between H, the center of mass of H_2, and the center of mass of CN, and ϕ is the dihedral angle defined between H, the center of mass of H_2, the center of mass of CN, and C (Figure 1). In CN-Ne, MRCI+Q surfaces were generated which revealed a long-range interaction between the Ne atom and the CN $X\ ^2\Sigma^+$ radical (R_e=3.75 Å) with a stability, D_e, of only 31.3 cm^{-1}. The potential exhibits a very small anisotropy, with a barrier to free CN rotation within the complex of less than 2 cm^{-1}.[53] In the CN $X\ ^2\Sigma^+$ + Ar potential, RSPT2 calculations predict a more anisotropic potential with a bent minimum configuration (θ_e=133°, R_e=3.83 Å) and larger binding energy, D_e=39 cm^{-1}. The barrier to free rotation of CN within CN-Ar is larger at 27 cm^{-1} compared to CN-Ne. PES calculations for the excited state of CN-Ar were also carried out and reveal a large change in geometry from the ground state which is unsurprising given that the sign of the CN dipole changes in going from the ground $X\ ^2\Sigma^+$ state to the excited $B\ ^2\Sigma^+$ state of CN. The minimum geometry in this case is linear (θ_e=0°) with a shorter bond length, R_e=3.57 Å, and stronger intermolecular interaction, D_e=256 cm^{-1}. In addition, the anisotropy of the excited state is much greater with a barrier to internal rotation of 160 cm^{-1}.[43] Lastly, for CN $X\ ^2\Sigma^+$ + H_2, the global minimum configuration is calculated to be linear (θ_e=0°) with R_e=3.94 Å and D_e=100.89 cm^{-1} using the MRSDCI method. In addition, bound state calculations predict that CN will be bound more strongly to *ortho*-H_2 over *para*-H_2 by 11 cm^{-1}.[51]

Given the shallow nature of the ground states of the CN-Ne and CN-Ar complexes, a progression in the low frequency "bending" mode associated with hindered

internal rotation of CN within the complex is expected in both infrared and vibronic spectra (and is observed and assigned as such in previously recorded CN-Ne *B*-*X* spectra[40]). As such, the ground states are treated in the same manner as laid out by Dubernet et al[54] for open-shell van der Waals complexes which reduces the effective Hamiltonian to the bending mode alone. The reduced Hamiltonian in this case follows a Hund's case (b) approximation and is similar to the closed-shell system because the electron spin is only weakly coupled to the nuclear axis. The diatomic rotational quantum number is denoted as n and its projection onto the intermolecular axis is K which takes on values of n, n-1, n-2,…,0. L is the pseudo-diatomic quantum number which describes end-over-end rotation of the complex and couples with K to form a resultant N, which is the total angular momentum excluding spin and is a good quantum number. As such, quantum states in the ground state and excited state of CN-Ne and in the ground state of CN-Ar are labeled by their hindered rotor state, n^K, CN vibrational state, v_{CN}, and intermolecular stretch, v_s. Because the excited B state of CN-Ar is much more anisotropic, the appropriate quantum labels are those of a linear triatomic where v_b is the intermolecular bending mode and K is its projection onto the intermolecular axis. K in this case takes on values of v_b, v_b-2, v_b-4,…, 0 or 1.

In **Chapter 4**, the ground state of CN-Ne is probed using IR-UV double resonance spectroscopy. The IR laser prepares a hindered rotor level in v_{CN}=2, and the UV subsequently excites the complex to the excited B state. The resulting fluorescence of the complex back to the ground state is then collected. Two rotationally resolved transitions are observed in the infrared and are assigned as transitions from the ground state to $n^K=1^1$ and 1^0 hindered rotor states in v_{CN}=2. The two bands are closely spaced

and display complex rotational structure typical of Coriolis coupling observed in similar HX-rare gas systems.[55-57] A deperturbation analysis similar to that derived previously for HX-rare gas complexes, is carried out to obtain accurate rotational constants for the hindered rotor states and their associated average R values and coupling strength. In addition, the energetic ordering and spacing of the hindered rotor states provides direct experimental information on the angular anisotropy of the CN $X\ ^2\Sigma^+$ + Ne potential and reveals a small barrier to free CN rotation within the complex of ~8 cm^{-1}. Complementary MRCI+Q calculations extrapolated to the one-electron complete basis set limit are carried out and agree remarkably well with the angular potential derived from the experiment. The excited state angular potential is also calculated and indicates a slightly more anisotropic potential with a barrier to internal rotation of ~16 cm^{-1}.

In **Chapter 5**, the *B*-*X* electronic spectrum of CN-Ar is revisited and spectral assignments, previously unidentified,[43] are made using IR-UV fluorescence depletion spectroscopy. Two additional features are observed in the electronic spectrum of CN-Ar in the CN *B*-*X* spectral region to lower frequency. Both bands display rotational structure which is analyzed as a pseudo-diatomic to give rotational constants and associated average separation distances. The lowest energy feature at 25714.1 cm^{-1} is assigned as a transition from the ground state to the (v_{CN}, v_s, v_b^K)=(0,0,0^0) in the excited state while the broader, higher energy feature centered at 25755.5 cm^{-1} is assigned as a combination of two transitions from the ground state to (0,1^1,0) and (0,0^0,1). Fluorescence depletion spectra are then recorded by fixing the IR on a transition from the ground state to v_{CN}=2, n^K=1^1, and scanning the UV laser in the CN *B*-*X* spectral region. All of the observed transitions are depleted by the IR laser, indicating that all of the CN-Ar *B*-*X* features

originate from the same species and share a common ground state. Assignments for the lowest five features in the *B*-*X* electronic spectrum are made based on the observed band types, and previous bound state calculations for the excited state of CN-Ar[43] verify the ordering and energetic spacings observed experimentally. The binding energy of the *B* state of CN-Ar is also derived with the newly observed and assigned feature at 25714.1 cm^{-1} to be D_0=186±2 cm^{-1}. Lastly, the intensity pattern observed in the progression of the bending modes is rationalized by the large angular change predicted in going from the ground state (θ_e=133°) to the excited state(θ_e=0°) in CN-Ar.[43]

In **Chapter 6**, the ground state of CN-Ar and CN-H_2 are probed in a similar fashion to that described above for CN-Ne in IR-UV double resonance. Two transitions are observed attributed to CN-Ar in the infrared originating from the ground state and terminating in v_{CN}=2, n^K=1^1 and 1^0. As in CN-Ne, evidence for Coriolis coupling is observed in the rotational structure of the closely spaced bands and, as such, a deperturbation analysis is carried out to derive deperturbed rotational constants, average values for *R*, and the strength of coupling between the two hindered rotor states. The energetic ordering and spacings of the hindered rotor states are similarly used to derive information on the angular anisotropy of the CN $X\ ^2\Sigma^+$ + Ar potential. The barrier to internal rotation determined of ~12 cm^{-1} is only slightly higher than that determined in CN-Ne of ~8 cm^{-1} indicating that CN is nearly free rotor in the ground state of the CN-Ar complex. The experimental results are compared with previous predictions for CN $X\ ^2\Sigma^+$ + Ar which are found to match the shape of the angular potential well, but predict a larger barrier to internal rotation of 27 cm^{-1}.[43] Two infrared features attributable to linear CN-*ortho*-H_2 are observed and assigned as transitions with ΔK=0 and ΔK=+1 based upon

their observed Σ-Σ and Π-Σ band types. Assignments are verified by comparison of the observed experimental spacing with predicted levels from *ab initio* calculations.[49]

References

1. B. J. Finlayson-Pitts and J. James N. Pitts, *Chemistry of the Upper and Lower Atmosphere*. (Academic Press, San Diego, 2000).
2. J. H. Seinfeld and S. N. Pandis, *Atmospheric Chemistry and Physics*. (John Wiley & Sons, Inc., New York, 1998).
3. S. S. Brown, J. B. Burkholder, R. K. Talukdar, and A. R. Ravishankara, J. Phys. Chem. A **105**, 1605 (2001).
4. J. J. Lamb, M. Mozurkewich, and S. W. Benson, J. Phys. Chem. **88**, 6441 (1984).
5. J. J. Margitan and R. T. Watson, J. Phys. Chem. **86**, 3819 (1982).
6. W. J. Marinelli and H. S. Johnston, J. Chem. Phys. **77**, 1225 (1982).
7. A. R. Ravishankara, F. L. Eisele, and P. H. Wine, J. Phys. Chem. **86**, 1854 (1982).
8. P. H. Wine, A. R. Ravishankara, N. M. Kreutter, R. C. Shah, J. M. Nicovich, R. L. Thompson, and D. J. Wuebbles, Journal of Geophysical Research-Oceans and Atmospheres **86**, 1105 (1981).
9. S. Aloisio and J. S. Francisco, J. Phys. Chem. A **103**, 6049 (1999).
10. W. S. Xia and M. C. Lin, J. Chem. Phys. **114**, 4522 (2001).
11. G. C. Pimentel and A. L. McClellan, *The Hydrogen Bond*. (Reinhold Publishing Corporation, New York, 1960).
12. S. Aloisio and J. S. Francisco, Acc. Chem. Res. **33**, 825 (2000).
13. P. D. Cooper, H. G. Kjaergaard, V. S. Langford, A. J. McKinley, T. I. Quickenden, and D. P. Schofield, J. Am. Chem. Soc. **125**, 6048 (2003).
14. A. Engdahl, G. Karlstrom, and B. Nelander, J. Chem. Phys. **118**, 7797 (2003).

15. K. Tsuji and K. Shibuya, J. Phys. Chem. A **113**, 9945 (2009).

16. C. Brauer, S., G. Sedo, E. Dahlke, S. Wu, E. M. Grumstrup, K. R. Leopold, M. D. Marshall, H. O. Leung, and D. G. Truhlar, J. Chem. Phys. **129**, 104304 (2008).

17. C. S. Brauer, G. Sedo, E. M. Grumstrup, K. R. Leopold, M. D. Marshall, and H. O. Leung, Chem. Phys. Lett. **401**, 420 (2005).

18. Y. Ohshima, K. Sato, Y. Sumiyoshi, and Y. Endo, J. Am. Chem. Soc. **127**, 1108 (2005).

19. Z. Wu, H. A. Gillis, N. V. Klassen, and G. G. Teather, J. Chem. Phys. **78**, 2449 (1983).

20. K. S. Kim, H. S. Kim, J. H. Jang, H. S. Kim, B.-J. Mhin, Y. Xie, and H. F. Schaefer, J. Chem. Phys. **94**, 2057 (1991).

21. B. S. Wang, H. Hou, and Y. S. Gu, Chem. Phys. Lett. **303**, 96 (1999).

22. Y. Xie and H. F. Schaefer, J. Chem. Phys. **98**, 8829 (1993).

23. Z. Zhou, Y. Qu, A. Fu, B. Du, F. He, and H. Gao, Int. J. Quantum Chem. **89**, 550 (2002).

24. D. L. Yang and M. C. Lin, in *The Chemical Dynamics and Kinetics of Small Radicals Part I*, edited by K. Liu and A. Wagner (World Scientific Publishing Co. Pte., Ltd., Singapore, 1995), Vol. 6, pp. 164.

25. V. V. Lissianski, V. M. Zamansky, and W. C. Gardiner, in *Gas-Phase Combustion Chemistry*, edited by W. C. Gardiner (Springer, New York, 2000), pp. 1.

26. F. El-Mahallawy and S. E.-D. Habik, *Fundamentals and Technology of Combustion*. (Elsevier Science Ltd., Oxford, 2002).

27. J. A. Miller and C. T. Bowman, Progress in Energy and Combustion Science **15**, 287 (1989).

28. P. Casavecchia, N. Balucani, L. Cartechini, G. Capozza, A. Bergeat, and G. G. Volpi, Faraday Discussions **119**, 27 (2001).

29. A. C. Crowther, S. L. Carrier, T. J. Preston, and F. F. Crim, J. Phys. Chem. A **113**, 3758 (2009).

30. A. C. Crowther, S. L. Carrier, T. J. Preston, and F. F. Crim, J. Phys. Chem. A **112**, 12081 (2008).

31. A. C. Moskun and S. E. Bradforth, J. Chem. Phys. **119**, 4500 (2003).

32. P. A. Pieniazek, S. E. Bradforth, and A. I. Krylov, J. Phys. Chem. A **110**, 4854 (2006).

33. R. A. Rose, S. J. Greaves, T. A. A. Oliver, I. P. Clark, G. M. Greetham, A. W. Parker, M. Towrie, and A. J. Orr-Ewing, J. Chem. Phys. **134**, 224503 (2011).

34. R. J. Balla, K. H. Casleton, J. S. Adams, and L. Pasternack, J. Phys. Chem. **95**, 8694 (1991).

35. L. R. Copeland, F. Mohammad, M. Zahedi, D. H. Volman, and W. M. Jackson, J. Chem. Phys. **96**, 5817 (1992).

36. I. R. Sims, J. L. Queffelec, D. Travers, B. R. Rowe, L. B. Herbert, J. Karthauser, and I. W. M. Smith, Chem. Phys. Lett. **211**, 461 (1993).

37. D. L. Yang, T. Yu, N. S. Wang, and M. C. Lin, Chem. Phys. **160**, 307 (1992).

38. Y. Georgievskii and S. J. Klippenstein, J. Phys. Chem. A **111**, 3802 (2007).

39. W. G. Lawrence, Y. Chen, and M. C. Heaven, J. Chem. Phys. **107**, 7163 (1997).

40. S. Fei and M. C. Heaven, Proceedings of SPIE - The International Society for Optical Engineering **1858**, 286 (1993).

41. S. Fei and M. C. Heaven, J. Chem. Phys. **98**, 753 (1993).

42. Y. Lin and M. C. Heaven, J. Chem. Phys. **94**, 5765 (1991).

43. J. Han, M. C. Heaven, U. Schnupf, and M. H. Alexander, J. Chem. Phys. **128**, 104308/1 (2008).

44. J. Han, M. C. Heaven, and U. Schnupf, J. Chem. Phys. **128**, 224309/1 (2008).

45. Y. Chen and M. C. Heaven, J. Chem. Phys. **109**, 2808 (1998).

46. H. S. Lin, M. G. Erickson, Y. Lin, W. H. Basinger, W. G. Lawrence, and M. C. Heaven, Chem. Phys. **189**, 235 (1994).

47. A. L. Kaledin and M. C. Heaven, Chem. Phys. Lett. **347**, 199 (2001).

48. Y. Chen and M. C. Heaven, J. Chem. Phys. **112**, 7416 (2000).

49. A. L. Kaledin, M. C. Heaven, and J. M. Bowman, J. Chem. Phys. **110**, 10380 (1999).

50. Y. Chen and M. C. Heaven, J. Chem. Phys. **109**, 5171 (1998).

51. A. L. Kaledin, M. C. Heaven, and J. M. Bowman, J. Chem. Phys. **110**, 10380 (1999).

52. I. Vrábel, V. Lukeš, V. Laurinc, and S. Biskupič, J. Phys. Chem. A **104**, 96 (1999).

53. M. Yang and H. Alexander Millard, J. Chem. Phys. **107**, 7148 (1997).

54. M.-L. Dubernet, D. Flower, and J. M. Hutson, J. Chem. Phys. **94**, 7602 (1991).

55. C. M. Lovejoy, J. M. Hutson, and D. J. Nesbitt, J. Chem. Phys. **97**, 8009 (1992).

56. C. M. Lovejoy and D. J. Nesbitt, J. Chem. Phys. **91**, 2790 (1989).

57. M. D. Schuder, D. D. Nelson, and D. J. Nesbitt, J. Chem. Phys. **94**, 5796 (1991).

Chapter 2:

Spectroscopic Identification and Stability of the Intermediate in the $OH + HONO_2$ Reaction

This research has been published in the *Proceedings of the National Academy of Sciences of the United States of America* (2008), *105*, 12678 and was performed with graduate student Eunice X. J. Li and Marsha I. Lester in the *Department of Chemistry, University of Pennsylvania*. Theoretical calculations were carried out by Joseph S. Francisco in the *Department of Chemistry, Purdue University*.

I. Introduction

Nitric acid is a chemically inactive and photochemically stable reservoir for reactive HO_x and NO_x species in the atmosphere. In the troposphere, $HONO_2$ is usually removed by dry deposition or rainout faster than it is photochemically converted back to NO_x, making it a permanent sink for NO_x (1, 2). In the upper troposphere and stratosphere, where there is no rain, $HONO_2$ can be removed by solar photolysis and reaction with OH (3, 4),

$$OH + HONO_2 \rightarrow H_2O + NO_3 .$$

This reaction results in the conversion of $HONO_2$ into reactive NO_x species, since the unstable nitrate radical rapidly decomposes into NO or NO_2.

Kinetic studies have shown that the OH + $HONO_2$ reaction is unusual in several respects (3, 5-11), particularly under the temperature and pressure conditions found in the lower atmosphere. Under these conditions, this reaction exhibits a negative temperature dependence, a pressure dependence and a strong kinetic isotope effect. The indirect mechanism inferred from these studies consists of initial OH radical addition forming an energized OH-$HONO_2^*$ intermediate, followed by dissociation or reaction to form products. The energized intermediate can also be temporarily stabilized by collisions with bath gas M, and then redissociate to reactants or decompose to products as shown in the following scheme:

$$\begin{array}{rcl} OH + HONO_2 \rightleftarrows OH - HONO_2^* & \rightarrow & H_2O + NO_3 \\ \updownarrow [M] & & \\ OH - HONO_2 & \rightarrow & H_2O + NO_3 \end{array}$$

The unusual kinetic behavior arises because of enhanced formation and collisional stabilization of the reaction intermediate under lower temperature and higher pressure conditions. Yet, the proposed intermediate has not been identified experimentally to date.

Prior theoretical work anticipated that OH + $HONO_2$ can form a doubly hydrogen-bonded complex with a planar six-membered ring-like structure (5, 12, 13). The stability of the OH-$HONO_2$ complex was predicted to be $D_e \sim 6.9\text{-}9.8$ kcal mol^{-1} with an estimated binding energy of $D_0 \sim 5.6\text{-}8.1$ kcal mol^{-1} (12, 13). The transition state to reaction has also been predicted to lie 3.5 kcal mol^{-1} above the reactant asymptote as shown in Fig. 1 (13), with reaction presumably occurring by tunneling through the barrier as evidenced by the large kinetic isotope effect (3).

This paper reports the first experimental identification of the OH-$HONO_2$ intermediate associated with this significant atmospheric reaction. The structure and stability of the reaction intermediate are obtained from direct spectroscopic characterization of the OH-$HONO_2$ complex and its unimolecular dissociation dynamics using an IR pump – UV probe technique (14), in which the UV laser probes the OH products following vibrational predissociation of OH-$HONO_2$ as illustrated in Fig. 1. Two transitions are identified in the fundamental OH stretch region: the OH radical stretch (ν_1) and OH stretch of nitric acid (ν_2) of the OH-$HONO_2$ complex. In addition, these same vibrational transitions are identified for the fully deuterated OD-$DONO_2$ complex. Complementary high-level ab initio calculations are also presented in support of the experimental findings.

Figure 1. Reaction coordinate for the OH + $HONO_2$ → H_2O + NO_3 reaction illustrating the presence of a hydrogen-bonded OH-$HONO_2$ intermediate. The stability of the OH-$HONO_2$ intermediate is taken from current expiermental results and the barrier height separating the intermediate from products is taken from theoretical predictions in this and earlier work (12, 13). The OH-$HONO_2$ intermediate is characterized by infrared action spectroscopy of the OH radical stretch (ν_1) and the OH stretch in nitric acid (ν_2), which involves detection of OH products by UV laser-induced fluorescence

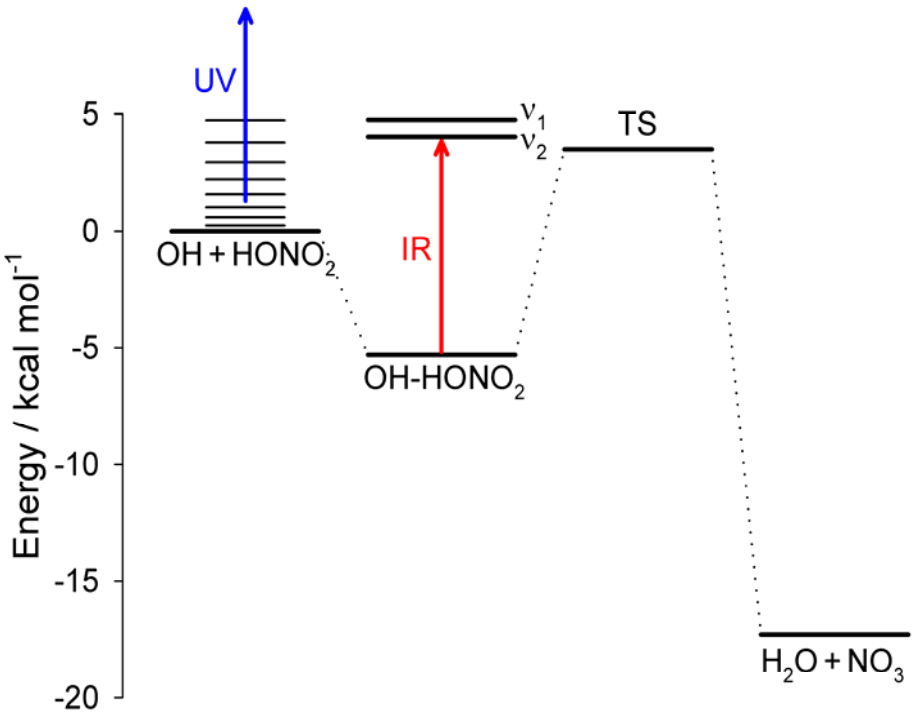
UV
IR
ν_1
ν_2
TS
OH + HONO$_2$
OH-HONO$_2$
H$_2$O + NO$_3$
Energy / kcal mol^{-1}
5
0
-5
-10
-15
-20

II. Results

A. Infrared action spectra

The OH-$HONO_2$ intermediate has been stabilized in a pulsed supersonic jet by combining photolytically generated OH with residual nitric acid precursor as described in detail in the materials and methods section. A spectroscopic search in the fundamental OH stretching region has revealed two features that we attribute to the OH-$HONO_2$ intermediate based on a combination of experimental and theoretical results. Both spectral features were detected with the probe laser fixed on the OH *A*-*X* (1,0) $R_1(3)$ transition. One feature is a rotationally structured band at 3516.8 cm^{-1} (origin) and the second, much broader feature is centered at ~3260 cm^{-1}, as shown in Fig. 2. The significant shift, -290 cm^{-1} from the OH stretch of the $HONO_2$ monomer, and broadening associated with the second feature is characteristic of strong hydrogen bonding, while the modest shift of the structured band, -52 cm^{-1} from free OH, suggests a weaker interaction (15). The vibrational frequencies of these features and their shifts relative to the monomers strongly suggest their assignment as the OH radical stretch (ν_1) and the OH acid stretch (ν_2) modes of OH-$HONO_2$, particularly when compared with theoretical predictions of the spectral shifts (see below and Table 1).

The assignment of the 3516.8 cm^{-1} feature as the OH radical stretch (ν_1) of the OH-$HONO_2$ complex is further supported by analysis of the rotational structure of the band. Preliminary simulations with rotational constants predicted from ab initio theory (see Table A3 in Appendix 1), assumed unchanged upon vibrational excitation, and the

Figure 2. Infrared action spectra of features assigned to the fundamental OH radical stretch (ν_1, blue) and the OH stretch of nitric acid (ν_2, red) of the OH-$HONO_2$ complex. These spectral features are observed with the UV probe laser fixed on the OH *A*-*X* (1,0) $R_1(3)$ line. The fundamental vibrational frequencies of the OH radical and the OH stretch of the nitric acid monomers are indicated with blue and red dash lines, respectively. The integrated intensity of the OH acid stretch relative to the OH radical stretch feature in the infrared action spectrum is 5.5(4):1. The OH acid stretch can be modeled as two broad components (black) at 3248.1(6) and 3270.8(5) cm^{-1} with Lorentzian linewidths of 22 cm^{-1}.

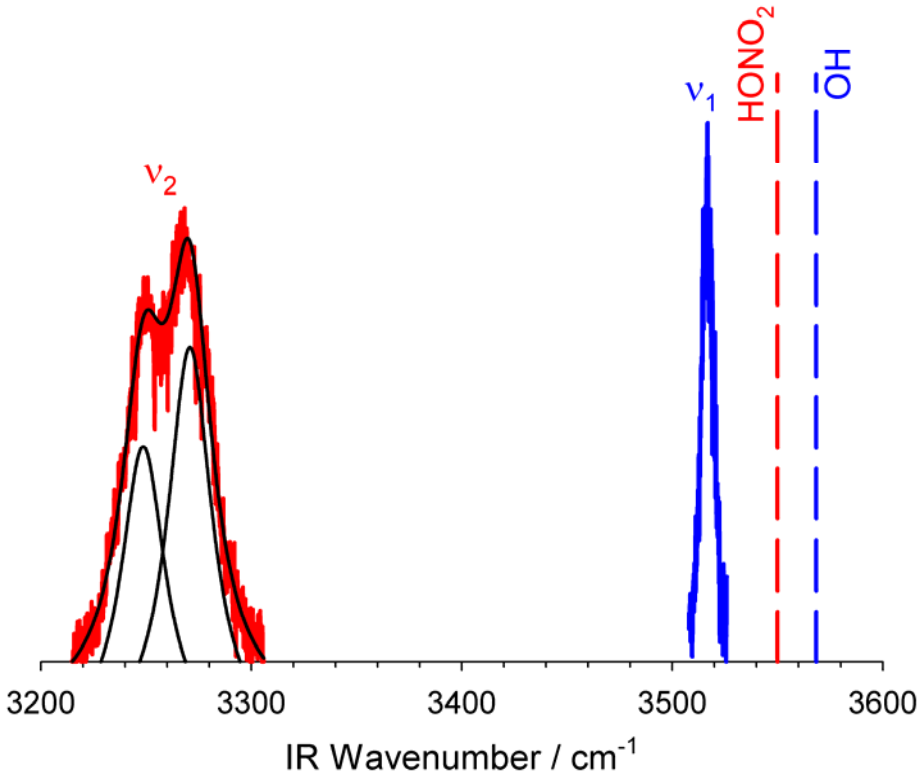
ν2
ν1
HONO2
OH
3200
3300
3400
3500
3600
IR Wavenumber / cm-1

Table 1. Vibrational frequencies (cm^{-1}), spectral shifts (cm^{-1}) relative to the monomer vibrations, and binding energies (kcal mol^{-1}) of the OH-$HONO_2$ complex predicted by various theoretical methods and observed experimentally. The frequencies and shifts of deuterated species are indicated in parentheses.

Vibrational frequencies (cm^{-1})	B3LYP 6-311++G(3df,3pd)[a]	B3LYP 6-311G(*d*,*p*)[b]	QCISD aug-cc-pVDZ[c]	Experiment[c]
OH	3712	3704 (2698)	3683	3568.5 (2631.5)
$HONO_2$	3723	3735 (2719)	3743	3550.0 (2621.5)
OH-$HONO_2$				
ν_1	3639	3621 (2636)	3670	3516.8 (2594)
ν_2	3365	3370 (2463)	3502	3260 (2425)
Δ_1[d]	-73	-83 (-62)	-13	-51.7 (-38)
Δ_2[e]	-358	-365 (-256)	-241	-290 (-197)

Energy (kcal mol^{-1})	CCSD(T) 6-311++G(2d,2p)[a]	G2M(cc3)[b]	CCSD(T) aug-cc-pV∞Z[c]	Experiment[c]
D_e	6.9	9.8	7.4	
D_0	5.6	8.1	5.9	≤ 5.3

[a] Ref. (12)

[b] Ref. (13)

[c] This work.

[d] Spectral shift of OH radical stretch of OH-$HONO_2$ relative to fundamental of free OH.

[e] Spectral shift of OH acid stretch of OH-$HONO_2$ relative to OH stretch of $HONO_2$ monomer.

transition dipole along the OH radical axis capture much of the rotational structure. The observed band structure shown in Fig. 3 was more faithfully reproduced, however, by including a spin-rotation interaction to account for the effects of electronic state mixing in the open-shell species; this effect has been demonstrated previously in high-resolution studies of OH-water and other systems (16-18). The resultant rotational band simulation shown in Fig. 3 extends over ~12 cm^{-1} at 10 K. The rotational band also exhibits some line broadening (homogeneous linewidth of 0.25 cm^{-1} compared to the laser bandwidth of 0.02 cm^{-1}) that likely arises from intramolecular vibrational redistribution (IVR), dissociation, and/or reaction following vibrational excitation.

By contrast, a much broader feature centered around 3260 cm^{-1} and spanning ~80 cm^{-1} in breadth was assigned as the OH acid stretch (ν_2). The resultant spectrum appears to be composed of two broad components, although some rotational substructure is still observable. As shown in Fig. 2, the two broad components can be simulated as bands at 3248.1(6) and 3270.8(5) cm^{-1} with a corresponding intensity ratio of 1:1.4(1) and Lorentzian linewidths of 22 cm^{-1}. The fact that the 3260 cm^{-1} feature (as well as its two subcomponents) is much broader than the OH radical stretch feature is consistent with strong anharmonic coupling between two (or possibly more) vibrational states. We carried out a vibrational deperturbation analysis (19) in an effort to characterize the energies and couplings of zero-order states that might give rise to the two components of the 3260 cm^{-1} feature. A two state deperturbation analysis indicates that the experimentally observed mixed states would arise from coupling between zero-order states at 3257.6(7) and 3261.2(7) cm^{-1}. The analysis also indicates a very strong coupling

Figure 3. High-resolution infrared action spectrum of the OH radical stretch of OH-$HONO_2$ (black) at 3516.8 cm^{-1} (origin). A simulation of the rotational band structure (blue) is generated using rotational constants predicted for the OH-$HONO_2$ complex (Table A3) and assumed spin-rotation parameters, ε_{aa}=-0.25 cm^{-1}, ε_{bb}=-0.55 cm^{-1}, to account for the open-shell character. A simulation of the intensity profile using the *b*-component of the transition dipole moment, rotational temperature of 10 K, and a homogeneous linewidth of 0.25 cm^{-1} provides a good representation of the observed band structure. Atmospheric water absorption lines are indicated with asterisks.

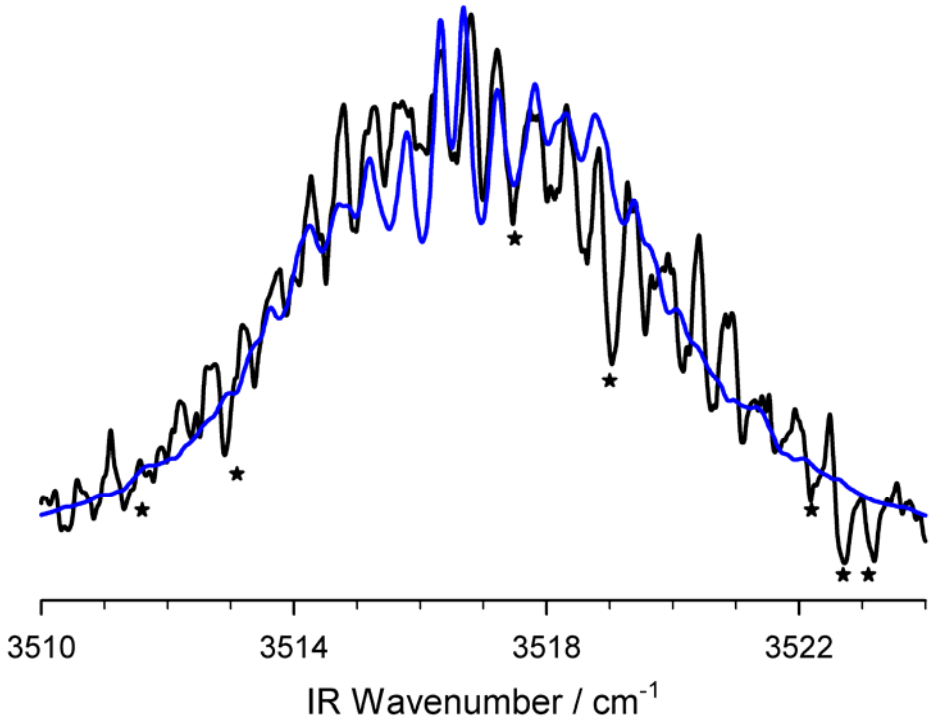
3510
3514
3518
3522
IR Wavenumber / cm-1

of 11.2(2) cm^{-1} between the zero-order states. One of the zero-order states is the optically bright OH acid stretch (ν_2) of OH-$HONO_2$; the identity of the second zero-order state is unknown, but will be the subject of future theoretical studies. The OH stretch in nitric acid is predicted to have a transition intensity ~10 times stronger than that of the OH radical stretch (12). Our experimental measurements yield an integrated intensity ratio of 5.5(4):1 for the acid stretch to the radical stretch in infrared action spectra. The fractional population in the OH product channel being detected is essentially the same (20%) following ν_1 and ν_2 excitation; however, the branching between dissociation and reaction following ν_1 and ν_2 excitation is not known.

In addition, these same vibrational transitions have been identified for the fully deuterated OD-$DONO_2$ complex by infrared action spectroscopy. The spectra were recorded with the probe laser fixed on the $P_1(3)$ line of the OD *A*-*X* (1,0) transition (20). The OD radical stretch (ν_1) of OD-$DONO_2$ is observed at 2594 cm^{-1}, shifted 38 cm^{-1} to lower frequency of that in free OD (21). The OD stretch of $DONO_2$ (ν_2) is observed at 2425 cm^{-1}, corresponding to a -197 cm^{-1} shift compared to the OD stretch of the monomer (21). The OD radical stretch band spans ~15 cm^{-1}, while the OD acid stretch feature is spread over ~40 cm^{-1}. These spectral properties are consistent with a strong hydrogen bond for the acid and a weaker interaction for the radical.

B. OH product state distribution

The IR excitation provides sufficient energy to induce dissociation and/or reaction between the components of the OH-$HONO_2$ intermediate. In this work, we examine the nascent OH $X\ ^2\Pi$ (v=0) product state distribution to provide a direct experimental

determination of the stability of the intermediate. For both ν_1 and ν_2 excitation, the product state distributions peak at the lowest rotational level that can be observed, N=2, F_1,* and fall off with increasing rotational energy, as shown in Fig. 4. There are no noticeable fine structure (Λ-doublet or spin-orbit) preferences. Following ν_1 excitation of OH-$HONO_2$ at 3516.8 cm^{-1}, the highest energetically observed OH level is N=9, F_1, Π(A'') with an internal energy of 1654.6 cm^{-1}; the same OH product state appears to be closed following ν_2 excitation at 3260 cm^{-1} (3268.4 cm^{-1} or 3250.7 cm^{-1}). In the latter case, the highest energetically observed OH channel is N=8, F_1, Π(A'') with an internal energy of 1324.3 cm^{-1}. The ν_1 infrared excitation energy, $h\nu_{IR}$, and the energy of the highest open OH product channel, E_{OH}, indicate that 1862.2 cm^{-1} (5.3 kcal mol^{-1}) is available for dissociation of OH-$HONO_2$, D_0, internal excitation of the $HONO_2$ cofragment, E_{HONO_2}, and translational energy of the recoiling fragments, E_t, according to the following energy balance equation:

$$h\nu_{IR} - D_0 + E_{OH\text{-}HONO_2} = E_{OH} + E_{HONO_2} + E_t$$

The internal energy of OH-$HONO_2$, $E_{OH\text{-}HONO_2}$, is negligible at ~10 K and E_{HONO_2} and E_t are unknown. Therefore, our experiment provides a rigorous upper limit for the OH-$HONO_2$ binding energy of $D_0 \leq 5.3$ kcal mol^{-1}. The same calculation for ν_2 excitation yields $D_0 \leq 5.5$ kcal mol^{-1} (1935.7 cm^{-1}); the large spacing (~330 cm^{-1}) to the next higher OH rotational level, N=9, which appears to be closed, precludes further refinement of this limit.

---

* The population in the lowest rovibrational state, OH $X\ ^2\Pi$ (v=0, N=1), could not be probed because of the large jet-cooled background.

Figure 4. Nascent quantum state distribution of the OH (v=0, N) products observed following excitation the radical stretch (ν_1) at 3516.8 cm^{-1} (upper panel, blue) and the nitric acid stretch (ν_2) at 3268.4 cm^{-1} (lower panel, red) of the OH-$HONO_2$ intermediate. Ticks identify OH rotational levels in the F_1 spin-orbit manifold, while the Π(A′) and Π(A″) Λ-doublet components are distinguished by triangle and circle symbols, respectively. The OH product state distributions peak at low rotational states and fall off with increasing rotational excitation. For ν_1 excitation, the highest observed product state is N=9, F_1 Π(A″) with 1654.6 cm^{-1} of internal energy, while for ν_2 excitation the highest state is N=8, F_1 Π(A″) with 1324.3 cm^{-1} of internal energy. The smooth curves through the data are prior statistical distributions with E_{avail} derived from the IR excitation frequency and the upper limit for the binding energy, $D_0 \leq 5.3$ kcal mol^{-1} (1862.2 cm^{-1}).

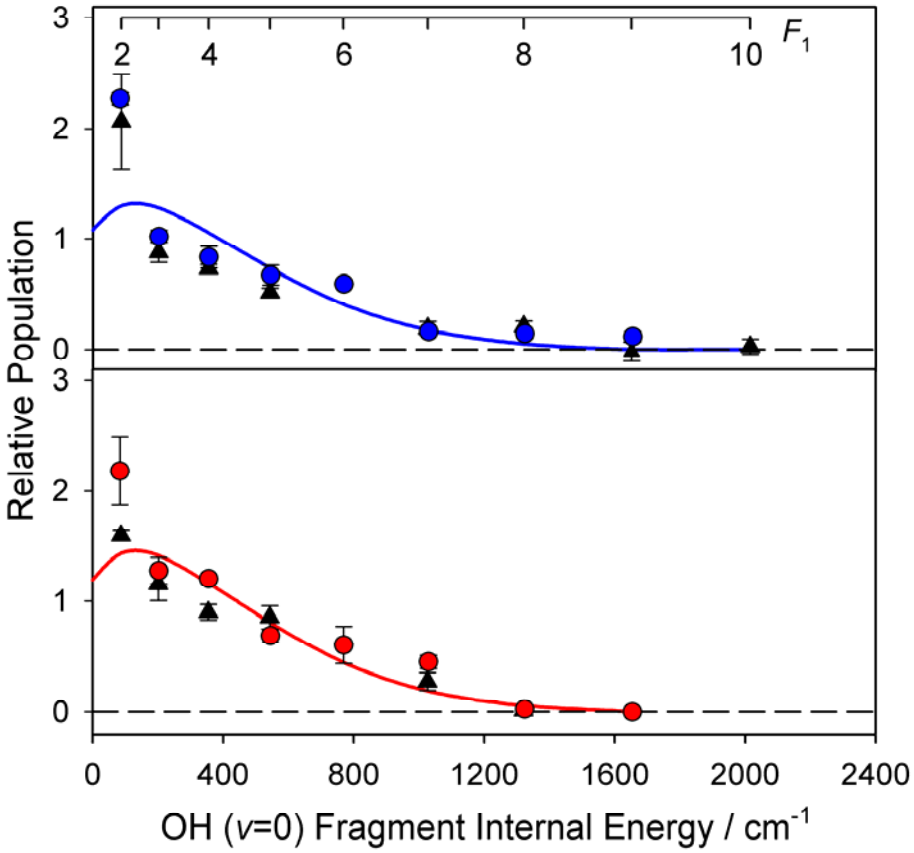
F1
2
4
6
8
10
3
2
1
0
Relative Population
0
400
800
1200
1600
2000
2400
OH (v=0) Fragment Internal Energy / cm-1

The experimental OH $X\,^2\Pi$ (v=0) product rotational distributions were also modeled by a statistical prior distribution (22). The prior distribution assumes that the product states associated with the translational, rotational, and vibrational motions of the OH and $HONO_2$ fragments are populated with equal probability subject only to a constraint on the energy available to products, $E_{avail} = h\nu_{IR} - D_0$ (23). In this experiment, we examine the probability of the OH products being released in a given quantum state and, therefore, we sum the usual formulation (22) over the unobserved $HONO_2$ rotational and vibrational states. The density of $HONO_2$ vibrational states is obtained from a direct count, assuming harmonic vibrations. The density of $HONO_2$ rotational states is treated classically. The prior distributions computed for ν_1 and ν_2 excitation of OH-$HONO_2$ with D_0 = 5.3 kcal mol^{-1} are illustrated as smooth curves through the experimental data in Fig. 4, demonstrating that the distribution is statistical and further validating the binding energy derived from the highest open OH product channel. The statistical distribution clearly indicates some degree of IVR before dissociation and/or reaction.

C. Insights from theory

The optimized geometry of the OH-$HONO_2$ complex is detailed in Appendix 1, Table A1 for the QCISD and CCSD(T) methods with various basis sets and illustrated in Fig. 5a. The hydrogen bond between the acidic proton of nitric acid and the oxygen of OH (O_7-H_5) is predicted to be near linear (172.5°) with a bond length of 1.83 Å at the highest level of theory. A secondary interaction between the hydrogen of the OH radical and a nitric acid oxygen atom (O_3-H_6) is nonlinear (121.2°) with a bond length of 2.28 Å. Natural Bond Orbital (NBO) analysis (shown in Fig. 5, b-e) has been used to investigate

Figure 5. (a) Labeling scheme for the optimized geometry of the OH-$HONO_2$ complex. Natural bond orbital analysis reveals (b) the primary interaction of the sigma antibonding orbital $\sigma^*(O_2\text{-}H_5)$ of nitric acid with the lone pair O_7 of the OH radical and (c) the secondary interaction of the lone pair of O_3 of $HONO_2$ with the sigma antibonding orbital $\sigma^*(O_6\text{-}H_7)$ of the OH radical. The half-filled $p\pi$ orbital of the OH radical in the OH-HNO_3 complex lies perpendicular to the plane of interaction as shown from the (d) top view and (e) side view.

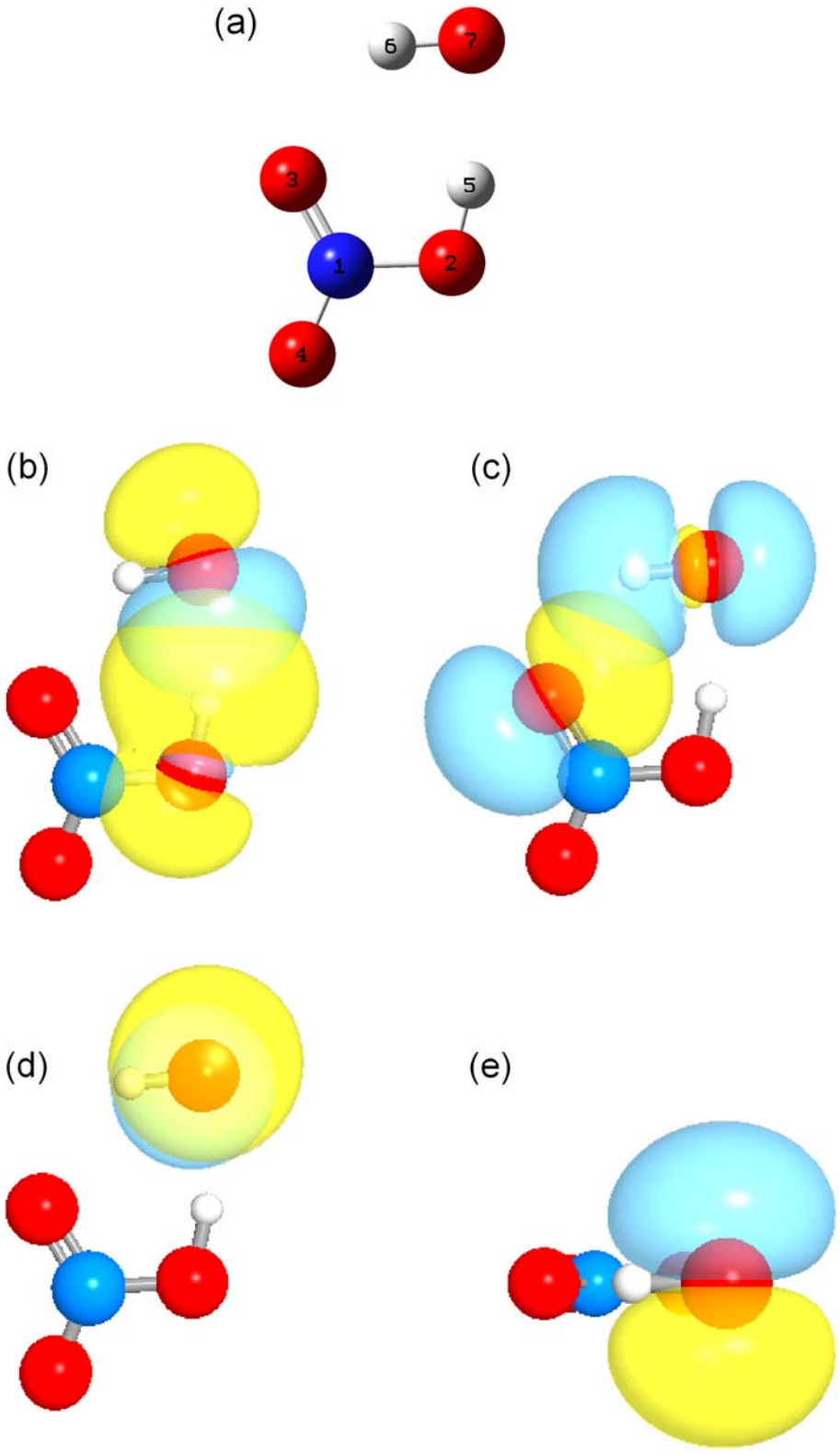
(a)
6
7
3
5
1
2
4
(b)
(c)
(d)
(e)

the nature of hydrogen bonding in the complex (24). A characteristic feature of the radical-molecule complex is the cyclic double hydrogen bonding. The strongest interaction is between the sigma antibonding orbital of the acid, $\sigma^*(O_2\text{-}H_5)$, and the lone pair of the OH radical, O_7. There is also a second interaction involving the lone pair of O_3 of the $HONO_2$ acid and the sigma antibonding orbital of the OH radical, $\sigma^*(O_6\text{-}H_7)$. The unpaired electron of the OH radical does not directly participate in the hydrogen bonding of the OH-$HONO_2$ complex. The unpaired electron is in a $p\pi$-type orbital that lies perpendicular to the plane of interaction.

The spectral shifts for the radical stretch (ν_1) and acid stretch (ν_2) of $HONO_2$ predicted from previous B3LYP (12, 13) and the present QCISD/aug-cc-pVDZ calculations, listed in Table 1, are in good accord with observed shifts, -52 and -290 cm^{-1}, respectively. The computed shifts are derived from harmonic frequency calculations for the complex and monomers. A small spectral shift is predicted for the weakly coupled OH radical stretch (ν_1), while a much larger shift is predicted for the strongly coupled OH acid stretch (ν_2). The integrated intensities of the features are also consistent with the intensity ratio predicted theoretically (12). Both the spectral shifts and intensities indicate that the rotationally structured feature at 3516.8 cm^{-1} and the broad feature at 3260 cm^{-1} correspond to the ν_1 and ν_2 fundamentals of the OH-$HONO_2$ intermediate, respectively. For the fully deuterated complex, the calculated shifts (13) are again in good agreement with the observed spectral shifts. The binding energy of the OH-$HONO_2$ complex has been computed by the CCSD(T) method with various basis sets permitting extrapolation to the complete basis set limit (CBS-∞). The resultant zero-point corrected

binding energy of D_0= 5.9 kcal mol^{-1} is in reasonable ageement with the limiting experimental value of $D_0 \leq$ 5.3 kcal mol^{-1}.

III. Discussion

The properties of the OH-$HONO_2$ complex are expected to be similar to those of the nitric acid-water complex, which has been investigated by ab initio theory (25-28), and observed experimentally by microwave spectroscopy in the gas-phase (29) and infrared spectroscopy in Ar matrices (28, 30). The nitric acid-water complex forms a six-membered ring with the free hydrogen of the water molecule lying out of plane. The microwave study demonstrated that the hydrogen bond between the acidic proton of nitric acid and the oxygen of water is near linear (174.5°) with a bond length of 1.779 Å. The second, weaker interaction between the hydrogen of the OH radical and a nitric acid oxygen atom is nonlinear (119.3°) with a bond length of 2.30 Å (29). The doubly hydrogen-bonded nitric acid-water complex is computed to have a greater stability than OH-$HONO_2$ with $D_0 \sim$ 7.5-8.1 kcal mol^{-1} (25, 26, 28). From the Ar matrix measurement (30), the frequency shift of the OH acid stretch of the nitric acid-water complex from the monomer is -496 cm^{-1}, which is a significantly greater shift than that observed for OH-$HONO_2$ (see Table 1); however, one must be cautious in comparing Ar matrix data to gas-phase data particularly in hydrogen-bonded systems (28). Ab initio calculations also predict a greater spectral shift for the OH acid stretch in the nitric acid-water complex than the OH-$HONO_2$ complex (25, 28, 31), implying both a stronger and shorter hydrogen bond in the nitric acid-water complex.

We can estimate the lifetime of an energized OH-$HONO_2$* intermediate based on rate constants deduced from kinetic modeling of the bimolecular OH + $HONO_2$ reaction (3). Using the rate constants for redissociation of the energized OH-$HONO_2$* adduct back to reactants ($k_{-a} \sim 2.5 \times 10^{10}$ s^{-1}) and unimolecular reaction of OH-$HONO_2$* to form products ($k_b \sim 5.0 \times 10^8$ s^{-1}), we estimate a lifetime ($\tau^{-1} = k_{-a} + k_b$) of ~40 ps for an energized OH-$HONO_2$* intermediate. This compares favorably with the lifetime of 21 ps derived from the homogeneous linebroadening in the experimental spectrum for the OH radical stretch (ν_1) of OH-$HONO_2$.

Fundamental OH radical stretch excitation takes the OH-$HONO_2$ complex in close proximity of the transition state for reaction as shown in Fig. 1. Since the initial OH stretch excitation is rapidly randomized in the intermediate, the branching ratio for inelastic to reactive decay may be analogous to a collision experiment. Kinetic modeling of such experiments (3) suggest that most of the energized OH-$HONO_2$* adducts will redissociate back to reactants rather than forming products ($k_{-a} / k_b \sim 50$), favoring production of OH fragments. This situation is quite favorable for obtaining infrared action spectra of OH-$HONO_2$, as illustrated in the present work. The branching ratio may change for the OH stretch of $HONO_2$, which may enhance reactive decay. Such a change would clearly have an impact on the relative intensities of vibrational bands in infrared action spectra.

The OH radical stretch of OH-$HONO_2$ is expected to be weakly coupled to the reaction coordinate, whereas elongation of the OH bond in $HONO_2$ should drive the transformation from the intermediate to the transition state for reaction. As a result,

excitation of the OH acid stretch of $HONO_2$ in the OH-$HONO_2$ is particularly fascinating because it both induces the necessary geometrical changes to move along the reaction coordinate and provides sufficient energy to reach the barrier to reaction. Future studies will explore the possibility that this excitation enhances production of the NO_3 reaction product.

We have successfully stabilized the OH-$HONO_2$ hydrogen-bonded intermediate in the OH + $HONO_2$ → H_2O + NO_3 reaction in a pulsed supersonic expansion. Vibrational features at 3516.8 cm^{-1} and 3260 cm^{-1} observed via infrared action spectroscopy have been attributed to the OH radical stretch and the OH nitric acid stretch, respectively, of OH-$HONO_2$ complex. These findings have been confirmed by high level ab initio theory and experimental studies of the fully deuterated complex. The identification of this intermediate is important experimental validation of key steps in the mechanism of the OH + $HONO_2$ reaction, which is an important atmospheric reaction that controls the residence time of nitric acid in the atmosphere.

IV. Materials and methods

The OH-$HONO_2$ intermediate is produced by combining photolytically generated OH radicals with residual nitric acid precursor (99.8 % fuming) entrained in pure He or a 20% N_2/He gas mixture (200 to 250 psi), or alternatively Ar carrier gas (60 psi). The production of HO-$HONO_2$ is optimized when $HONO_2$ is photolyzed (ArF excimer laser, ~5 mJ cm^{-2}) within a quartz capillary tube (0.5 mm i.d., 10 mm length) attached to the pulsed valve assembly, indicating that the high pressure conditions in the capillary tube facilitate collisional stabilization of OH-$HONO_2$. The OH-$HONO_2$ intermediate and

residual OH radicals are then cooled in the ensuing supersonic expansion to their lowest quantum states.

Infrared excitation in the OH fundamental stretch region near 2.8-3.1 μm is achieved with a single-mode optical parametric oscillator (OPO, 0.02 cm^{-1} linewidth, ~10 mJ cm^{-2}) pumped by an injection-seeded Nd:YAG laser. The OH $X\ ^2\Pi$ (v=0) fragments resulting from IR excitation are detected by laser-induced fluorescence (LIF) on the $A\ ^2\Sigma^+$ - $X\ ^2\Pi$ (1,0) transition at 282 nm using a frequency-doubled Nd:YAG pumped dye laser. The IR and UV lasers are calibrated using a wavelength meter and/or the well-known positions of OH lines (20, 32). The focused IR and collimated UV laser beams are counterpropagated into the vacuum apparatus, where the two beams are spatially overlapped ~10 nozzle diameters downstream of the exit of the capillary tube. The IR pump laser (10 Hz) is present for every other UV probe laser pulse (20 Hz), which permits data acquisition with active background subtraction of UV only signal arising from residual OH. The time delay between the IR and UV lasers is 50 ns. Similar methods were used for OD-$DONO_2$.

For a given OH $X\ ^2\Pi$ (v=0) product rotational level, N, there are four fine structure sub-states which correspond to Π(A′) or Π(A″) Λ-doublet level levels (in the high J limit) within both the F_1 and F_2 spin-orbit manifolds. Fine-structure resolved detection is relatively straightforward, as P- and R-type main branch transitions originate from Π(A′) levels while Q-type main branch transitions originate from Π(A″) levels. Typically four transitions probing different rotational/fine-structure states were recorded at least three times for the determination of the statistical uncertainty in the signal

intensities. The intensities were determined from the amplitudes of the spectral lines. Conversion of line intensities to ground state populations included a degeneracy correction factor.

All calculations were performed using the GAUSSIAN 03 software (33). The geometries were optimized using the QCISD method with aug-cc-pVDZ basis set as well as the CCSD(T) method with aug-cc-pVDZ and aug-cc-pVTZ basis sets (see Table A1 in Appendix 1). Frequency calculations were performed using the QCISD method with the aug-cc-pVDZ basis set (see Table A2 in Appendix 1). The corresponding rotational constants at the equilibrium position are given in Table A3. We carried out a detailed study of the hydrogen bonded orbitals using a Natural Bond Orbital (NBO) analysis (34). The three dimensional figures of the orbitals derived from this work (Fig. 5) were plotted using NBOVIEW 1.0 (35). The binding energies, both at the equilibrium position D_e and zero point corrected D_0, were extrapolated to the complete basis set limit (CBS aug-cc-pV∞Z) using the CCSD(T) method as shown in Table A4 in Appendix 1.

References

1. Finlayson-Pitts, B. J. & Pitts, J. N. (2000) *Chemistry of the Upper and Lower Atmosphere: Theory, Experiments, and Applications* (Academic Press, San Diego).
2. Wayne, R. P. (2000) *Chemistry of Atmospheres, Third Edition* (Oxford University Press, Inc., New York).
3. Brown, S. S., Burkholder, J. B., Talukdar, R. K. & Ravishankara, A. R. (2001) Reaction of hydroxyl radical with nitric acid: Insights into its mechanism. *J. Phys. Chem. A* **105,** 1605-1614.
4. Wood, E. C., Wooldridge, P. J., Freese, J. H., Albrecht, T. & Cohen, R. C. (2003) A Prototype for In Situ Detection of Atmospheric NO_3 and N_2O_5 via Laser-Induced Fluorescence. *Environ. Sci. Technol.* **37,** 5732-5738.
5. Lamb, J. J., Mozurkewich, M. & Benson, S. W. (1984) Negative activation energies and curved Arrhenius plots. 3. Hydroxyl + nitric acid and hydroxyl + peroxynitric acid. *J. Phys. Chem.* **88,** 6441-8.
6. Margitan, J. J. & Watson, R. T. (1982) Kinetics of the reaction of hydroxyl radicals with nitric acid. *J. Phys. Chem.* **86,** 3819-24.
7. Marinelli, W. J. & Johnston, H. S. (1982) Reaction rates of hydroxyl radical with nitric acid and with hydrogen peroxide. *J. Chem. Phys.* **77,** 1225-34.
8. Ravishankara, A. R., Eisele, F. L. & Wine, P. H. (1982) Study of the reaction of hydroxyl with nitric acid. Kinetics and NO_3 yield. *J. Phys. Chem.* **86,** 1854-8.

9. Brown, S. S., Talukdar, R. K. & Ravishankara, A. R. (1999) Reconsideration of the rate constant for the reaction of hydroxyl radicals with nitric acid. *J. Phys. Chem. A* **103,** 3031-3037.

10. Smith, I. W. M. & Ravishankara, A. R. (2002) Role of hydrogen-bonded intermediates in the bimolecular reactions of the hydroxyl radical. *J. Phys. Chem. A* **106,** 4798-4807.

11. McCabe, D. C., Brown, S. S., Gilles, M. K., Talukdar, R. K., Smith, I. W. M. & Ravishankara, A. R. (2003) Kinetics of the removal of OH(v = 1) and OD(v = 1) by HNO_3 and DNO_3 from 253 to 383 K. *J. Phys. Chem. A* **107,** 7762-7769.

12. Aloisio, S. & Francisco, J. S. (1999) Structure and energetics of hydrogen bonded HO_x-HNO_3 complexes. *J. Phys. Chem. A* **103,** 6049-6053.

13. Xia, W. S. & Lin, M. C. (2001) A multifacet mechanism for the OH + HNO_3 reaction: An ab initio molecular orbital/statistical theory study. *J. Chem. Phys.* **114,** 4522-4532.

14. Derro, E. L., Murray, C., Sechler, T. D. & Lester, M. I. (2007) Infrared action spectroscopy and dissociation dynamics of the HOOO radical. *J. Phys. Chem. A* **111,** 11592 -11601.

15. Florio, G. M., Zwier, T. S., Myshakin, E. M., Jordan, K. D. & Sibert III, E. L. (2003) Theoretical modeling of the OH stretch infrared spectrum of carboxylic acid dimers based on first-principles anharmonic couplings. *J. Chem. Phys.* **118,** 1735-1746.

16. Brauer, C. S., Sedo, G., Grumstrup, E. M., Leopold, K. R., Marshall, M. D. & Leung, H. O. (2005) Effects of partially quenched orbital angular momentum on

the microwave spectrum and magnetic hyperfine splitting in the OH-water complex. *Chem. Phys. Lett.* **401,** 420-425.

17. Ohshima, Y., Sato, K., Sumiyoshi, Y. & Endo, Y. (2005) Rotational spectrum and hydrogen bonding of the H_2O-HO radical complex. *J. Am. Chem. Soc.* **127,** 1108-1109.

18. Marshall, M. D. & Lester, M. I. (2005) Spectroscopic implications of partially quenched orbital angular momentum in the OH-water complex. *J. Phys. Chem. B* **109,** 8400-6.

19. Konen, I. M., Li, E. X. J., Lester, M. I., Vazquez, J. & Stanton, J. F. (2006) Infrared overtone spectroscopy and vibrational analysis of a Fermi resonance in nitric acid: Experiment and theory. *J. Chem. Phys.* **125,** 074310/1-074310/12.

20. Luque, J. & Crosley, D. R. (1999) LIFBASE: Database and spectral simulation program (Version 1.5). SRI International Report MP 99-009.

21. Linstrom, P. J. & Mallard, W. G. (2005) *NIST Chemistry WebBook, NIST Standard Reference Database Number 69* (National Institute of Standards and Technology, Gaithersburg, MD 20899).

22. Baer, T. & Hase, W. L. (1996) *Unimolecular Reaction Dynamics* (Oxford University Press, New York).

23. Konen, I. M., Li, E. X. J., Stephenson, T. A. & Lester, M. I. (2005) Second OH overtone excitation and statistical dissociation dynamics of peroxynitrous acid. *J. Chem. Phys.* **123,** 204318.

24. Hernandez-Soto, H., Weinhold, F. & Francisco, J. S. (2007) Radical hydrogen bonding: Origin of stability of radical-molecule complexes. *J. Chem. Phys.* **127,** 164102.

25. Tao, F.-M., Higgins, K., Klemperer, W. & Nelson, D. D. (1996) Structure, binding energy, and equilibrium constant of the nitric acid-water complex. *Geophys. Res. Lett.* **23,** 1797-1800.

26. Staikova, M. & Donaldson, D. J. (2001) Ab initio investigation of water complexes of some atmospherically important acids: HONO, HNO_3 and HO_2NO_2. *Phys. Chem. Chem. Phys.* **3,** 1999-2006.

27. Kjaergaard, H. G. (2002) Calculated OH-stretching vibrational transitions of the water-nitric acid complex. *J. Phys. Chem. A* **106,** 2979-2987.

28. McCurdy, P. R., Hess, W. P. & Xantheas, S. S. (2002) Nitric acid-water complexes: Theoretical calculations and comparison to experiment. *J. Phys. Chem. A* **106,** 7628-7635.

29. Canagaratna, M., Phillips, J. A., Ott, M. E. & Leopold, K. R. (1998) The nitric acid-water complex: Microwave spectrum, structure, and tunneling. *J. Phys. Chem. A* **102,** 1489-1497.

30. Barnes, A. J., Lasson, E. & Nielsen, C. J. (1994) Molecular complexes of nitric acid with various bases studied by matrix isolation infrared spectroscopy. *J. Mol. Struct.* **322,** 71-4.

31. Miller, Y., Chaban, G. M. & Gerber, R. B. (2005) Theoretical study of anharmonic vibrational spectra of HNO_3, HNO_3-H_2O, HNO_4: Fundamental, overtone and combination excitations. *Chem. Phys.* **313,** 213-224.

32. Dieke, G. H. & Crosswhite, H. M. (1962) The Ultraviolet Bands of OH. *J. Quant. Spectrosc. Radiat. Transf.* **2,** 97.

33. Frisch, M. J., Trucks, G. W., Schlegel, H. B., Scuseria, G. E., Robb, M. A., Cheeseman, J. R., Montgomery, J., J. A., Vreven, T., Kudin, K. N., Burant, J. C., Millam, J. M., Iyengar, S. S., Tomasi, J., Barone, V., Mennucci, B., Cossi, M., Scalmani, G., Rega, N., Petersson, G. A., Nakatsuji, H., Hada, M., Ehara, M., Toyota, K., Fukuda, R., Hasegawa, J., Ishida, M., Nakajima, T., Honda, Y., Kitao, O., Nakai, H., Klene, M., Li, X., Knox, J. E., Hratchian, H. P., Cross, J. B., Bakken, V., Adamo, C., Jaramillo, J., Gomperts, R., Stratmann, R. E., Yazyev, O., Austin, A. J., Cammi, R., Pomelli, C., Ochterski, J. W., Ayala, P. Y., Morokuma, K., Voth, G. A., Salvador, P., Dannenberg, J. J., Zakrzewski, V. G., Dapprich, S., Daniels, A. D., Strain, M. C., Farkas, O., Malick, D. K., Rabuck, A. D., Raghavachari, K., Foresman, J. B., Ortiz, J. V., Cui, Q., Baboul, A. G., Clifford, S., Cioslowski, J., Stefanov, B. B., Liu, G., Liashenko, A., Piskorz, P., Komaromi, I., Martin, R. L., Fox, D. J., Keith, T., Al-Laham, M. A., Peng, C. Y., Nanayakkara, A., Challacombe, M., Gill, P. M. W., Johnson, B., Chen, W., Wong, M. W., Gonzalez, C. & Pople, J. A. (2004) *GAUSSIAN 03, Revision C.02* (Gaussian, Inc., Wallingford, CT).

34. Glendening, E. D., Badenhoop, J. K., Reed, A. E., Carpenter, J. E., Bohmann, J. A., Morales, C. M. & Weinhold, F. (2001) *NBO 5.0* (Theoretical Chemistry Institute, University of Wisconsin, Madison).

35. Wendt, M. & Weinhold, F. (2001) *NBOVIEW 1.0* (Theoretical Chemistry Institute, University of Wisconsin, Madison).

Chapter 3:

Infrared Spectrum and Stability of the H_2O-HO Complex: Experiment and Theory

This research has been published in the *Journal of Physical Chemistry A* (2010), *114*, 1529 and was performed with graduate student Pesia Soloveichik and Marsha I. Lester in the *Department of Chemistry*, *University of Pennsylvania*. Theoretical calculations were carried out by Anne B. McCoy in the *Department of Chemistry, The Ohio State University*.

I. Introduction

Hydroxyl radicals (OH) are expected to form strong hydrogen bonds with water. Such interactions are found in the gaseous environment of the atmosphere,[1] the interface of liquid water and ice,[2,3] and bulk regions of liquid water, snow, and ice.[4] The study of the binary H_2O-HO complex will provide insights on the interactions of OH with a single water molecule and larger water networks found in the aforementioned systems. This paper utilizes experimental gas-phase vibrational spectroscopy in the OH radical stretching region, high-level ab initio calculations, and a two-dimensional vibrational approach to investigate the binary H_2O-HO complex.

Global and local minima of the H_2O-HO complex have been located in previous theoretical calculations.[5-7] At the global minimum geometry, hydrogen bonding occurs between the hydrogen of OH and the oxygen of water. As illustrated in Figure 1, the complex in this geometry has C_s symmetry, with the water molecule at a specific angle ϕ displaced from planarity, where it has C_{2v} symmetry. ϕ is defined as the angle between the O-O axis and the vector bisecting the HOH angle in the water molecule. Minima at this geometry were identified for states of both $^2A'$ and $^2A''$ symmetry, differing in the orientation of the singly occupied pπ-orbital of OH;[6] the $^2A'$ state is the ground state and global minimum. The difference in energy between the two electronic states has been theoretically calculated to be in the range of 105-187 cm^{-1}.[6-9] The stability of H_2O-HO at the global minimum, D_e, relative to the OH + H_2O reactant asymptote has been predicted to be ~4.7-6.4 kcal mol^{-1}.[6-8,10] Another local minimum has been located in which the hydrogen bond occurs between one of the hydrogens in the water and the oxygen of

Figure 1. The H_2O-HO complex in its global minimum geometry. The water monomer is displaced from planarity by an angle ϕ, where ϕ is defined as the angle between the O-O axis (solid line) and the vector bisecting the water molecule (dotted line). The orientation of the a, b, and c inertial axes are also shown.

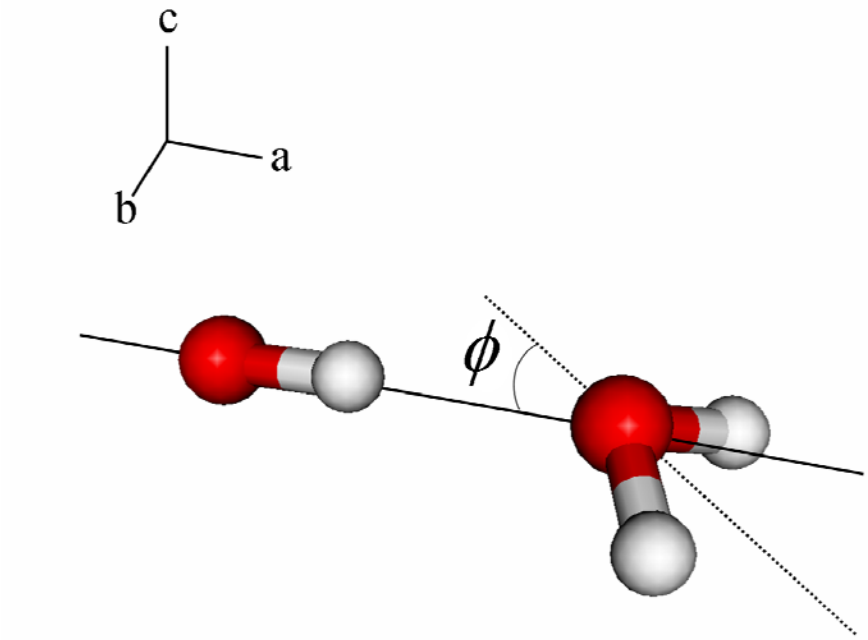
c
a
b
ϕ

OH.[6,7] D_e for the less stable conformer has been predicted to be ~2.5-3.7 kcal mol^{-1}.[5-8,10] Using ab initio calculations, specific regions of the H_2O-HO interaction potential have been mapped out, scanning along one coordinate at a time about various H_2O-HO minima.[11]

The calculated harmonic frequency of the OH radical stretch in H_2O-HO at its global minimum and its shift from that in free OH have also been previously reported.[6,8] A significant shift to lower frequency ranging from -76 to -99 cm^{-1} were calculated at the SCF and RCISD levels of theory,[6] while a larger shift of -156 cm^{-1} was reported in a DFT study.[8]

The H_2O-HO complex has been experimentally observed by infrared spectroscopy in argon and neon matrices.[12-14] Engdahl et al. assigned bands at 3452.3 and 3428.2 cm^{-1} to site-specific fundamental OH radical stretch transitions of the H_2O-HO complex,[12] denoted ν_2 in this paper in accordance with convention. In these ν_2 transitions, the radical acts as the hydrogen bond donor and the water molecule as the acceptor, consistent with the global minimum geometry of H_2O-HO. Cooper et al. determined that a previously unassigned 3442.1 cm^{-1} band is another ν_2 transition of H_2O-HO in the same hydrogen bonded configuration from yet another site in the matrix.[13] The observed H_2O-HO transitions at 3542.2, 3442.1, and 3428.0 cm^{-1} are shifted from the OH monomer in an Ar matrix by –96.0, –106.1, and –120.2 cm^{-1}, respectively. Very recently, the H_2O-HO ν_2 transition in a Ne matrix has been reported at 3472.5 cm^{-1}, shifted –94 cm^{-1} from the OH radical stretch of the monomer.[14] To support this assignment, the analogous three bands were observed upon deuteration; the three

experimental shifts were comparable to the isotopic shift theoretically calculated for the ν_2 transition in D_2O-DO relative to H_2O-HO and at their global minima.[13]

The H_2O-HO binary complex has also been observed in the gas-phase in microwave studies.[15-18] The microwave spectra, recorded using FTMW, were consistent with the global minimum geometry predicted for the complex. Further microwave studies investigated isotopic variants of H_2O-HO, both D and ^{18}O substituted.[15,16,18] These studies analyzed the transition frequencies and derived ρ, the vibrationally averaged $^2A'$-$^2A''$ energy separation, using the formalism of Marshall and Lester.[19] The value of ρ obtained assumes the absence of rotation and spin-orbit coupling. In these microwave studies, the value of ρ varied slightly amongst the many isotopomers, and these differences were attributed to variations in the vibrationally averaged angle between the OH radical bond axis and the a-inertial axis within the isotopomers.[15,16,18]

Several similar closed-shell systems have also been examined previously, namely H_2O-HF and H_2O-HCl in both microwave[20-24] and infrared spectroscopic investigations[25-27] as well as theoretical studies.[21,28,29] The global minimum geometries of H_2O-HF and H_2O-HCl resemble the global minimum geometry of H_2O-HO. The hydrogen bond occurs between the acid hydrogen and the oxygen of the water, and the complexes have C_s symmetry, with the water molecule displaced from planarity at a specific angle ϕ. In H_2O-HF and H_2O-HCl complexes, the lowest frequency vibration is a bending motion of the water molecule out of the plane of the complex (ν_6). This mode is described by a double well potential; the water molecule is displaced from planarity at the global minimum and the barrier corresponds to a planar C_{2v} structure.[20,21] Since the zero-point

level in both H_2O-HCl and H_2O-HF was found to be extremely close to the top of the low-lying barrier, both complexes were determined to be effectively planar.[20,21] In a more detailed investigation of H_2O-HF, however, the average angle ϕ was markedly nonzero.[21] The energy difference between ν_6=0 and ν_6=1 in H_2O-HF was estimated to be 70±3 cm^{-1} and rotational transitions of H_2O-HF within ν_6=1 have also been observed.[20,23]

Similarly, when H_2O-HO forms from hydroxyl radical and water monomers, five additional low-frequency vibrational modes are introduced. This includes the lowest frequency bending mode, ν_6, which, as in H_2O-HF and H_2O-HCl, is described by a double-well potential. At the RCISD(Q)/TZ2P level of theory, the barrier height was previously calculated to be ~18 cm^{-1};[6] a more extensive investigation of the barrier to planarity is carried out in the present study. With such a low-lying barrier, H_2O-HO would be effectively planar. However, H_2O-HO is not truly a planar molecule, since it undergoes large amplitude motion in the out-of-plane bend (ν_6), and the coupling between ν_6 and other modes needs to be considered.

In this study, an experimental gas-phase infrared spectrum of H_2O-HO in the OH radical stretching region is presented for the first time. The infrared action spectrum was recorded while detecting OH $X\ ^2\Pi$ (v=0) products by laser-induced fluorescence. In addition, the OH product state distribution was measured, providing information on the binding energy, D_0, of H_2O-HO. Complementary high-level CCSD(T) calculations in the complete basis set (CBS) limit are carried out to obtain the best estimate of the OH spectral shift and dissociation energy for the binary H_2O-HO complex. Observation of a second feature in the infrared spectrum prompted a theoretical investigation to aid in the

assignment. As a result, a two-dimensional potential incorporating both ν_2, the OH radical stretching mode, and ν_6, the H_2O out-of-plane bending mode, is constructed to shed light on the experimental spectrum and further develop the H_2O-HO interaction potential. This study demonstrates the coupling between these two modes, which leads to changes in the effective potential for the out-of-plane bending motion upon OH vibrational excitation.

II. Experimental Methods

The H_2O-HO complex is formed by combining photolytically generated OH radicals with H_2O vapor in a pulsed supersonic jet. Diluted nitric acid at 60 wt. % (with partial pressures of p_{H_2O} =4.67 torr and p_{HONO_2} =0.79 torr at 20°C)[30] is entrained in 150 psi He and photolyzed at 193 nm using an ArF excimer laser to form OH radicals. Signals attributed to the H_2O-HO complex are absent when water vapor is removed from the carrier gas by using fuming nitric acid at 98 wt % in He. Photolysis occurs in the collisional region of the jet; subsequent collisions stabilize and cool the H_2O-HO complex.

The H_2O-HO complex is identified using infrared action spectroscopy, an IR pump – UV probe technique, which provides high species selectivity and high sensitivity. The IR pump laser is scanned in the fundamental OH stretch region and the UV probe laser detects the resultant OH radical products, i.e. the action, using the sensitive laser-induced fluorescence (LIF) method. This IR-UV technique affords high selectivity for species, such as H_2O-HO, that are both bound by less than the energy of the IR photon

(~10 kcal mol^{-1}) and generate OH radicals upon dissociation in the specific quantum state that is probed. As a result, species such as water clusters will not be detected as the IR laser is scanned.

Infrared excitation in the OH fundamental region (~2.8 μm) is achieved using a optical parametric oscillator (Continuum OPO, 0.02 cm^{-1} linewidth, ~10 mJ cm^{-2}) pumped by an injection-seeded Nd:YAG laser (Continuum Precision 8000, 10 Hz). The OH $X\ ^2\Pi$ (v=0) products resulting from IR excitation of H_2O-HO are detected via LIF on the OH $A\ ^2\Sigma^+$-$X\ ^2\Pi$ (1,0) transition at 280 nm, which is generated by frequency-doubling the output of a Nd:YAG pumped dye laser (Continuum 7020 and ND6000, 20 Hz). The IR and UV lasers are calibrated using a wavelength meter (Coherent Wavemaster) and the well-known positions of OH lines, respectively. The two beams are counter-propagated and spatially overlapped, intersecting the expansion ~20 nozzle diameters downstream from the pulsed valve. This is particularly helpful in cooling residual OH to its lowest quantum state, v=0, N=1, and thereby reducing UV only signals. The IR pump laser (10 Hz) is present for every other UV probe laser pulse (20 Hz), which permits data acquisition with active background subtraction of UV only signal arising from residual OH. The time delay between the IR and UV lasers is set at 50 ns.

The resultant probe laser-induced fluorescence is collimated using a f/1 lens and re-focused on a slit using another f/1 lens. Wavelength discrimination and suppression of scattered probe laser light is achieved using a narrowband interference filter at 313 ± 10 nm that passes OH A-X (1,1) emission before impinging upon a photomultiplier tube (Electron Tubes 9813QB). The signal from the photomultiplier was pre-amplified and

displayed on a digital storage oscilloscope (LeCroy WaveRunner 6050A) interfaced with a PC for further processing.

Infrared action spectra are obtained by scanning the IR laser with the UV laser fixed on the OH *A*-*X* (1,0) $R_1(3)$ transition, which was empirically found to give the best signal-to-background ratio. Multiple scans are recorded to verify reproducibility and then added together to improve the signal-to-noise ratio. The OH $X\ ^2\Pi$ (v=0) product state distribution is also recorded by scanning the UV laser over various well-known OH *A*-*X* (1,0) lines. For each rotational level N, there are four fine-structure sub-states, which in the high N limit correspond to $\Pi(A')$ or $\Pi(A'')$ Λ-doublets within the F_1 or F_2 spin-orbit manifolds. The fine-structure states can be easily resolved by probing different rotational lines, as main-branch P and R lines originate from the $\Pi(A')$ state and Q lines originate from the $\Pi(A'')$ state. Typically four transitions probing different rotational/fine-structure states were recorded at least three times for the determination of the statistical uncertainty in the signal intensities. One OH product state is repeatedly probed before and/or after other measurements and serves as a reference for scaling purposes. The intensities were determined from the amplitudes of the spectral lines. Conversion of line intensities to ground state populations includes a degeneracy correction factor.[31]

III. Theoretical Methods

A. Level of Theory and Basis Set

Density functional theory (DFT) with the B3LYP functional and the Dunning-Huzinaga aug-cc-pVTZ basis set, as implemented in the Gaussian 03 program package,[32]

was used in this study to develop a two-dimensional potential for the H_2O-HO complex. Density functional theory, with the B3LYP functional, has been shown to be an effective descriptor of hydrogen-bonded complexes.[33,34] Diffuse functions need to be included in a hydrogen-bonded complex such as H_2O-HO. Computations of the H_2O-HO energy were carried out at different basis set sizes; the aug-cc-pVTZ basis set was found to be a reasonable compromise between computational expense and accuracy.

We also performed a set of calculations of the equilibrium structure, dissociation energy and harmonic frequencies of H_2O-HO at the CCSD(T) level of theory,[35-38] with various basis sets from which we were able to extrapolate the energy to the complete basis set limit. In particular, the structures were optimized and harmonic frequencies were calculated using aug-cc-pVxZ basis sets with x = D, T and Q.[39,40] A final single point energy calculation is done with the aug-cc-pV5Z basis set using the optimized geometry calculated at the CCSD(T)/aug-cc-pVQZ level of theory. The CBS limits employed by this work is that by Peterson et al.[41] in which the extrapolation was performed using

$$E(n) = E_{CBS} + Ae^{-(n-1)} + Be^{-(n-1)^2} \quad (1)$$

where n is the highest orbital angular momentum quantum number, while A and B are fitting parameters. In this work, n = 2 through 5 for the basis sets from double to quintuple zeta respectively. The vibrational frequencies for both the monomers and complexes were also calculated at the CCSD(T) level with the aug-cc-pVDZ through aug-cc-pVQZ basis sets. The results of these calculations provided high-level benchmarks against which we compare the DFT calculations.

B. Two-Dimensional Potentials and Vibrational Energy Levels

Two-dimensional potential surfaces were constructed as functions of the hydroxyl OH bond length r and the out-plane-angle ϕ for H_2O-HO in the lowest states of $^2A'$ and $^2A''$ symmetry. Here, the out-of-plane-angle is defined to be the angle between the O-O axis and the bisector of the HOH angle in the water molecule.

This potential surface, $V(r,\phi)$, was constructed in two steps. First, a one-dimensional potential surface $V_e(\phi)$ was evaluated for both the $^2A'$ and $^2A''$ states at seventeen values of ϕ ranging from 0° to roughly 85°. At each of these values of ϕ, all other coordinates were optimized to minimize the total energy. The resulting electronic energies and the corresponding geometric parameters are tabulated in Appendix 2 in Tables A1 and A2. To incorporate the OH stretch dependence in the potential, we varied the value of the OH bond length r from 0.75 Å to 1.55 Å in increments of 0.05 Å at each point in the original scan. At this stage all other internal coordinates were constrained to the values that were determined in the first stage. The final two-dimensional $^2A'$and $^2A''$ potentials were completed by symmetry by taking advantage of the fact that $V(r,\phi) = V(r,-\phi)$. (The z-matrix used to vary the OH radical bond length at each optimized angle ϕ is tabulated in Appendix 2 in Table A3.)

In fitting the potential and evaluating vibrational energies, we follow an approach that is similar to ones that have been taken in studies of HOONO.[42-44] Once the potential was constructed, each of the one-dimensional OH stretch slice was fit to a Morse oscillator:

$$V\left(r,\phi\right)=D_e\left(\phi\right)\left[1-\exp(\left(-\alpha\left(\phi\right)\left[r-r_e\left(\phi\right)\right]\right)\right]^2+E(\phi)\,. \tag{2}$$

The frequency, ω_e, and anharmonicity, $\omega_e x_e$, were derived from eq (2). The fit coefficients for the Morse potentials are provided in Appendix 2 (see Tables A4 and A5). With the values of α and r_e constrained to those obtained by fitting our electronic energies to eq. (2), the potential was made more flexible by using an extended Morse potential:

$$V(r,\phi)=\sum_{n=2}^{4}D_n(\phi)[1-\exp(-\alpha(\phi)[r-r_e(\phi)])]^n+E(\phi) \tag{3}$$

Now the coefficients were allowed to vary to optimize the fit of the one-dimensional OH stretch slices to this functional form. (The fit coefficients for the extended Morse potentials are tabulated in Appendix 2 in Tables A6 and A7.) An advantage of this form is that it provided a potential with which we could extrapolate to larger values of r while retaining the appropriate long- and short-range behaviors.

Once we had fit the potentials, a discrete variable representation[45,46] (DVR) was used to calculate the energies and wavefunctions for the ν_2=0 and 1 OH vibrational levels from the extended Morse potential at each angle ϕ. The reduced mass of the OH radical stretch was used. These calculations were performed using an evenly spaced grid of 101 points ranging from an OH bond length of 0.25 Å to 6.25 Å. In this way, adiabatic potentials $V_{\nu_2}\left(\phi\right)$ were generated for the states with zero and one quantum in the OH

stretch. (The points in the double-well potentials $V_{\nu_2}(\phi)$ for ν_2=0 and ν_2=1 for H_2O-HO on the $^2A'$ and $^2A''$ electronic surfaces are tabulated in Appendix 2 in Tables A1 and A2.)

Each $V_{\nu_2}(\phi)$ double-well potential was fit to a function of the form:

$$V_{\nu_2}(\phi) = \sum_{n=0}^{3} c_n^{(\nu_2)} \phi^{2n} \ . \tag{4}$$

(The coefficients for these fits are tabulated in Appendix 2 in Table A8.) A discrete variable representation[45,46] was then used to calculate the energy levels and wavefunctions for the out-of-plane bend from the $V_{\nu_2}(\phi)$ potential for ν_2 = 0 and 1. The reduced mass for the out-of-plane bend vibrational mode (μ_{oop}) was evaluated by treating this motion as a bend for three point masses (m): the oxygen in the OH radical (O_1), the oxygen in the water molecule (O_2), and a point mass placed at the midpoint of the two hydrogens in the water (X) with an associated mass of twice the mass of hydrogen. The reduced mass is given by:[47]

$$\frac{1}{\mu_{\text{oop}}} = \left(\frac{1}{m_{\text{O}_1}} + \frac{1}{m_{\text{O}_2}}\right)\frac{1}{r^2_{\text{O}_1\text{O}_2,e}} + \left(\frac{1}{m_{\text{O}_2}} + \frac{1}{2m_{\text{H}}}\right)\frac{1}{r^2_{\text{O}_2\text{X},e}} + \frac{2\cos\phi}{m_{\text{O}_2} r_{\text{O}_1\text{O}_2,e} r_{\text{O}_2\text{X},e}} \tag{5}$$

In this study, a constant value of μ_{oop} was used and was evaluated for ϕ=0°, and the bond lengths in eq. (5) were obtained from the geometry optimization at this value of ϕ. In the calculations for the out-of-plane bend, we used DVR based on an evenly spaced grid of 202 points in ϕ ranging from −180° to 180°.

C. Dipole Moment Surface and Transition Strengths

In order to calculate the dipole moment surface, the dipole moments were calculated at each of the 17 values of ϕ and at each of the 17 OH distances r. These dipole moment functions were transformed into dipole moments in the principal axis system, $\mu(r,\phi)$.[48]

The transition strengths of various $(\nu_2',\nu_6') \leftarrow (\nu_2'',\nu_6'')$ transitions were evaluated using:

$$\left|M_{\nu_2'',\nu_6'';\nu_2',\nu_6'}\right|^2 = \left\langle \nu_2'',\nu_6''\left|\mu(r,\phi)\right|\nu_2',\nu_6'\right\rangle^2 \tag{6}$$

where μ is the dipole moment in D, and ν_2 and ν_6 are the quantum labels for OH stretch and the angle out-of-plane bend, respectively. This two-dimensional calculation was performed in a series of one-dimensional steps. First, the $\mu(r,\phi)$ curves along both the a- and c-inertial axes were fit to a function of the form:

$$\mu(r,\phi) = \sum_{n=0}^{6} b_n(\phi)\, r^n \,. \tag{7}$$

(The coefficients for these fits are tabulated in Appendix 2 in Tables A9-A12.) Next, the transition moment, $\mu_{10}(\phi) \equiv \left\langle \nu_2''=0\left|\mu(r,\phi)\right|\nu_2'=1\right\rangle$, was calculated along the a- and c-inertial axes at each value of ϕ using the OH stretch DVR grid points and wavefunctions. Further, the resulting $\mu_{10}(\phi)$ curve along the a-inertial axis was fit to a function of the form:

$$\mu_{10}(\phi) = \sum_{n=0}^{4} a_n \cos(n\phi) \tag{8}$$

and the $\mu_{10}(\phi)$ curve along the c-inertial axis was fit to a function of the form:

$$\mu_{10}(\phi) = \sum_{n=1}^{4} c_n \sin(n\phi) . \tag{9}$$

(The coefficients for the fits of $\mu_{10}(\phi)$ along the a- and c-inertial axes for H_2O-HO on the $^2A'$ and $^2A''$ electronic surfaces are tabulated in Appendix 2 in Tables A13 and A14.) Finally, $\langle \nu_6'' | \mu_{10}(\phi) | \nu_6' \rangle$ along the a- and c-inertial axes was subsequently evaluated using the angle out-of-plane DVR grid points and wavefunctions. This two-dimensional calculation yielded the strength of a specific $(\nu_2',\nu_6') \leftarrow (\nu_2'',\nu_6'')$ transition.

IV. Infrared Spectral Results: Experiment and Theory

The H_2O-HO complex was stabilized in a supersonic jet and characterized using infrared action spectroscopy via the approach described in Sec. II. A spectral search in the OH fundamental stretching region revealed the two features shown in Figure 2: a more intense band centered at 3490 cm^{-1} and another band centered at 3475 cm^{-1}, which are detected while monitoring the OH *A*-*X* (1,0) $R_1(3)$ transition. These features are attributed to the H_2O-HO complex based on experimental and theoretical evidence, which is detailed in this and the following sections (Sec. IV and V). The experimental identification is based on the vibrational frequencies and corresponding spectral shifts, associated OH product state distributions, and supporting evidence from the partially resolved rotational structure of the bands. The identification is also supported by high level ab initio calculations of the spectral shift of the hydrogen-bonded OH radical stretch and dissociation energy of the H_2O-HO complex. Finally, in Sec. VI, we offer a likely

Figure 2. Infrared action spectrum attributed to the H_2O-HO complex in the fundamental OH radical stretch region. The UV probe laser was fixed on the OH A-X (1,0) $R_1(3)$ line. The band centered at 3490 cm^{-1} is assigned to the fundamental OH radical stretch (ν_2), while the feature centered at 3475 cm^{-1} is likely a hot band originating from an excited out-of-plane H_2O bend (ν_6) level. The rotational band structure is not analyzed here; however, we note that the spacings of rotational lines in both bands are consistent with the (B+C) rotational constant determined from experimental microwave studies.[17]

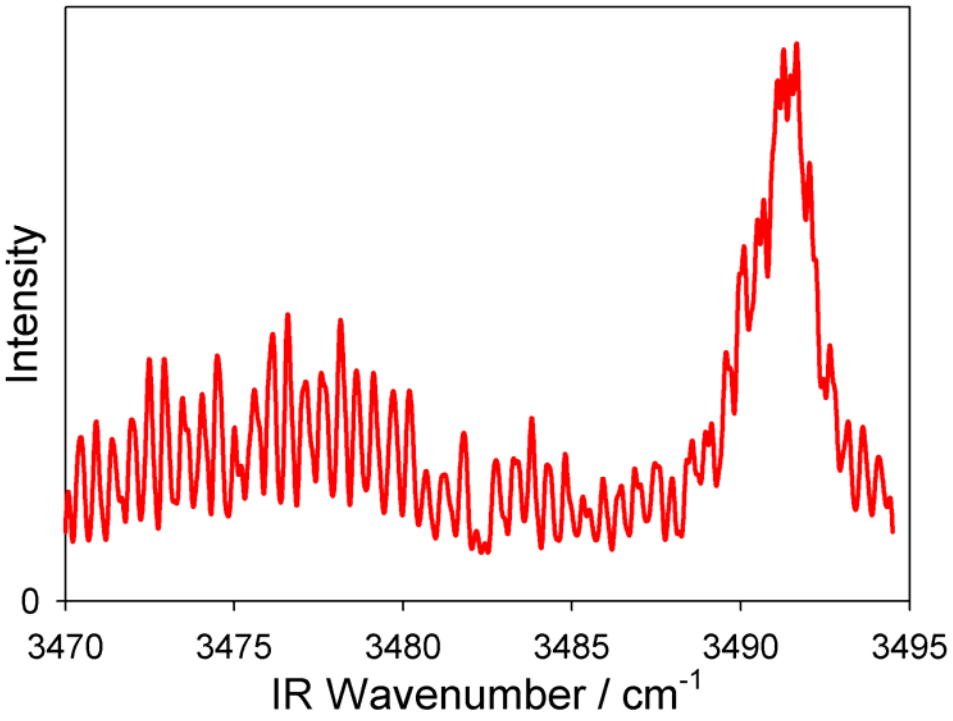
Intensity
0
3470
3475
3480
3485
3490
3495
IR Wavenumber / cm-1

explanation for the observation of two features. Based on theoretical arguments, the stronger feature at 3490 cm^{-1} is assigned to the OH radical stretch (ν_2) of H_2O-HO, while the feature at 3475 cm^{-1} is tentatively attributed to a hot band involving ν_2 and the H_2O out-of-plane bending motion, ν_6.

The infrared features observed at 3490 cm^{-1} and 3475 cm^{-1} are shifted to lower frequency of the OH monomer transition (3568 cm^{-1})[49] by 78 and 93 cm^{-1}, respectively. The OH radical stretch is expected to exhibit a sizable spectral shift and 10-fold enhancement in infrared intensity, making it the strongest infrared transition, upon hydrogen bonding in the H_2O-HO complex.[6] The relative intensities of the bands observed at 3490 and 3475 cm^{-1}, obtained by integrating over a ±4 cm^{-1} range about the central positions of the features, is ~2:1. It should be noted that the intensity ratio is derived from infrared action spectra obtained while monitoring a specific OH product channel.

Both the 3490 and 3475 cm^{-1} bands display partially resolved rotational structure at the 0.15 cm^{-1} resolution shown in Figure 2. The rotational structure of the OH stretching band of H_2O-HO is expected to be quite complicated due to partial quenching of the OH orbital angular momentum in the complex.[19] Marshall and Lester generated simulations of the a-type infrared transition expected for the OH radical stretch (see Fig. 3 of Ref. 19) based on estimated rotational constants and the degree of quenching;[19] the ground state parameters derived in recent FTMW work, (B+C)/2 = 0.2195 cm^{-1} and ρ = −146.5 cm^{-1},[17] confirm that intermediate behavior between the well-established limiting cases (fully quenched or completely unquenched orbital angular momentum) is expected.

While the present resolution is not adequate to permit analysis of the complicated rotational band structure, we comment on the limited rotational structure observed. (Some spectral broadening arises from intramolecular vibrational redistribution and/or vibrational predissociation.) We observe regular spacings of 0.51(6) cm^{-1} in the 3475 and 3490 cm^{-1} bands, although additional substructure is clearly evident in the stronger 3490 cm^{-1} band. These spacings are consistent with the P- and R-branch spacings anticipated for H_2O-HO of twice the effective rotational constant (B+C),[19] offering further support for assignment of the spectrum to the H_2O-HO complex.

The observed spectral shifts of these features are in agreement with previous reports of the OH stretch of H_2O-HO in an Ar matrix of –96 to –120 cm^{-1} and in a Ne matrix of –94 cm^{-1}.[12-14,50] The slight change between the shifts measured in the gas-phase and matrix can be attributed to interactions of the complex with the matrix environment. The observed spectral shifts are also in accord with calculated shifts of the OH radical stretching frequency in the H_2O-HO complex based on SCF and RCISD methods.[6] A larger spectral shift is obtained in the B3LYP calculations performed in this work to generate a two-dimensional potential (see Sec. VI), as had been found in an earlier DFT study.[8] As a result, high level CCSD(T) calculations with very large basis sets are also performed here.

CCSD(T) calculations using aug-cc-pVxZ basis sets with x = D, T and Q were carried out to obtain the harmonic frequencies of the H_2O-HO complex and its constituent monomers. The harmonic frequencies of the stretching modes for H_2O-HO, namely the H_2O symmetric stretch (ν_1), OH radical stretch (ν_2), and H_2O asymmetric

stretch (ν_7), and the corresponding modes in the monomers are listed in Table 1. Only the OH radical stretch is significantly shifted (Δ) from its monomer frequency with harmonic shifts ranging from –94 to –105 cm^{-1} with increasing size of the basis set, and further validating the assignment of one or both of the experimental features to the OH radical stretch (ν_2) of H_2O-HO. (It should be noted that the calculated shifts do not account for changes in anharmonicity of the mode in the complex as compared to the monomer.) Comparison of the CCSD(T) results with the experimental frequencies for the monomers confirms that only the OH radical stretch (ν_2) should appear in the spectral range investigated. The H_2O stretching modes are both higher in frequency and essentially unshifted upon complexation with the OH radical.

A significantly larger spectral shift is anticipated for the OH radical stretch in $(H_2O)_n$-HO clusters with more than one water molecule ($n > 1$) and such clusters are also predicted to have a substantially larger binding energy.[10,51] For example, the spectral shift and binding energy are predicted to nearly double for $(H_2O)_2$-HO compared to the binary complex, and further increases are expected for $(H_2O)_3$-HO. Both properties make larger clusters unlikely to be observed by infrared action spectroscopy in the spectral region of Figure 2. Furthermore, we note that the less stable conformer of H_2O-HO, in which the hydrogen bond occurs between a hydrogen in H_2O and the oxygen of OH, is predicted to have a much smaller shift of the OH radical stretch (less than 10 cm^{-1})[5] and, more generally, no transitions are expected to appear in the spectral range of Figure 2.

Table 1. Vibrational frequencies (cm^{-1}) and spectral shifts (Δ, cm^{-1}) for the high frequency modes of H_2O-HO in the $\tilde{X}\,^2A'$ state

	CCSD(T)			
Vibrational Frequency	aug-cc-pVDZ	aug-cc-pVTZ	aug-cc-pVQZ	Expt.
OH	3683	3720	3740	3568[(a)]
H_2O sym	3787	3811	3831	3657[(b)]
H_2O asym	3905	3920	3941	3756[(b)]
H_2O-HO				
ν_1 (a′)	3788	3811	3831	
ν_2 (a′)	3589	3619	3635	3490
ν_7 (a″)	3903	3918	3939	
Δ_1	1	0	0	
Δ_2	-94	-101	-105	-78
Δ_7	-2	-2	-2	

(a) Ref. 49.

Ref. 63.

V. Dissociation Energy: Experiment and Theory

The IR excitation provides the system with enough energy to dissociate into OH + H_2O, and the nascent OH $X\,^2\Pi$ (v=0) products are detected in various rotational levels and fine-structure states as described in Sec. II. Infrared excitation of the H_2O-HO feature at 3491.3 cm^{-1} results in the OH product state distribution shown in Figure 3. The distribution peaks at the lowest rotational level that can be observed, N=2,[52] falls off to a minimum around N=5-6, and then increases to a small secondary peak at N=9 before dropping to a negligible signal level at N=10. (The inserts show scans across OH A-X (1,0) $Q_2(9)$ and $Q_1(10)$ lines that probe the highest rotational levels.) No significant Λ-doublet or spin-orbit preference is observed.

The OH product state distribution provides direct information on the binding energy, D_0, of the H_2O-HO complex. The highest observed OH product channel is N=9, Π(A″), F_2 with 1694.9 cm^{-1} of internal energy. The infrared excitation, ν_{IR}, at 3491.3 cm^{-1} combined with the internal energy of the OH product, E_{OH}, leaves 1796.4 cm^{-1} (5.14 kcal mol^{-1}) of energy available (E_{avail}) to be distributed between dissociation of H_2O-HO, D_0, internal excitation of H_2O products, E_{H_2O}, and translational recoil of the fragments, E_t, according to the following conservation of energy relationship:

$$h\nu_{IR} - D_0 = E_{avail} = E_{OH} + E_{H_2O} + E_t \qquad (10)$$

The internal energy of H_2O-HO is negligible at the cold rotational temperatures of the supersonic jet (~10 K). The internal energy of H_2O and translational recoil energy are

Figure 3. Nascent quantum state distribution of the OH (v=0, *N*) products observed following excitation of the OH radical stretch, ν_2, of the H_2O-HO complex at 3491.3 cm^{-1}. Ticks as well as filled (black) and open (blue) symbols identify OH rotational levels in the F_1 and F_2 spin-orbit manifolds respectively, whereas the $\Pi(A')$ and $\Pi(A'')$ Λ-doublet components are distinguished by triangles and circles. The OH product state distribution peaks at low *N*, falls off with increasing *N*, and exhibits a secondary peak at *N*=9. The inserts show experimental LIF spectra recorded on the $Q_2(9)$ and $Q_1(10)$ lines of the OH A-X (1,0) band, the former indicating population in the *N*=9, F_2, $\Pi(A'')$ level with 1694.9 cm^{-1} of internal energy. The solid and dotted lines are statistical prior distributions for the F_1 and F_2 manifolds calculated with and without the constraint that the H_2O product is released with one quantum of bend excitation (see text).

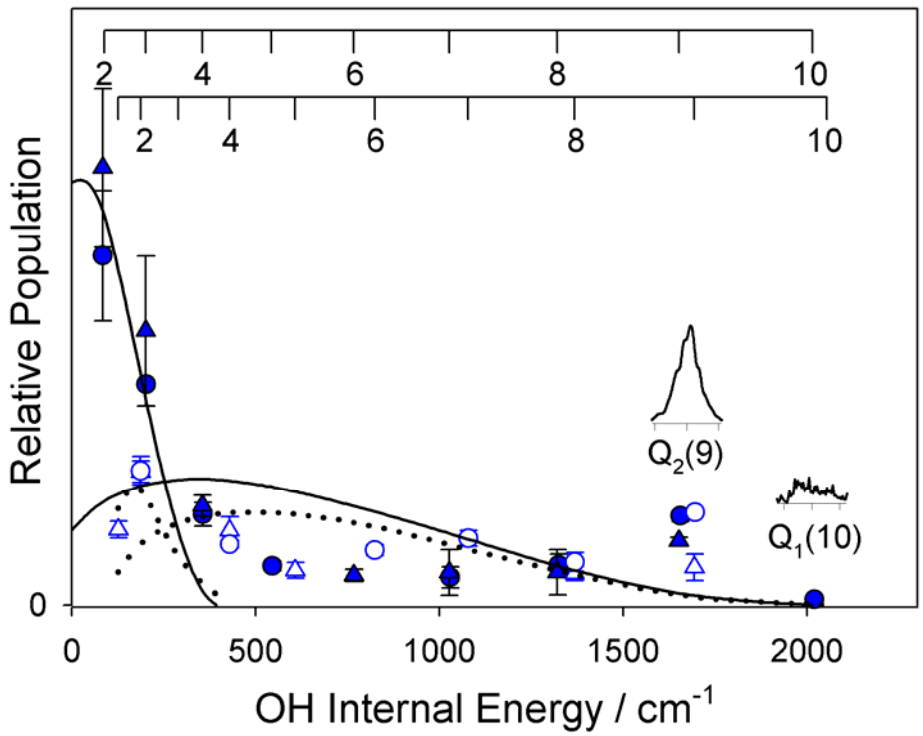
2
4
6
8
10
2
4
6
8
10
Relative Population
0
$Q_2(9)$
$Q_1(10)$
0
500
1000
1500
2000
OH Internal Energy / cm^{-1}

not known from these experiments. As a result, an upper limit for the binding energy of H_2O-HO can be determined and yields $D_0 \leq 5.14$ kcal mol^{-1}.

Complementary calculations of the dissociation energy of the H_2O-HO complex were also performed at the CCSD(T) level of theory with increasing basis set size in order to extrapolate to the complete basis set limit. The resultant energies are given in Table 2, which reveal a limiting value of D_e (CBS-∞) = 5.6 kcal mol^{-1}. Interestingly, the H_2O-HO complex is predicted to have a larger electronic binding energy than those from the best calculations available to date for the water dimer with D_e = 4.9 kcal mol^{-1} at the MP2(FC) basis set limit[53] and D_e = 5.0 kcal mol^{-1} using CCSD(T) with triple ζ basis set and analysis of electron correlation effects.[54] Additionally, Natural Bond Orbital (NBO) analysis has shown that the OH radical is a stronger hydrogen bond donor than H_2O in its interaction with another H_2O molecule.[55] The change in zero point energy (ZPE) between H_2O-HO and its constituent monomers is also needed for comparison with experiment. The best estimate for the change in ZPE based on harmonic frequencies yields a binding energy of D_0 = 3.6 kcal mol^{-1}, which is certainly consistent with the upper limit determined experimentally. It is also anticipated that this number would increase if we were able to account for anharmonicities in all nine vibrational degrees of freedom.

The shape of the OH product state distribution may provide dynamical information on the dissociation. In similar systems, Nizkorodov et al.[56] showed that OH overtone excitation of water dimer and Ar-H_2O results in H_2O products with dominant internal bend excitation. As a result, we consider the possibility of bend excitation of the

Table 2. Dissociation and binding energies (kcal mol^{-1}) for H_2O-HO in the $\tilde{X}\,^2A'$ state

Method	D_e	D_0
CCSD(T)/aug-cc-pVDZ	5.9	3.9
/aug-cc-pVTZ	5.9	3.9
/aug-cc-pVQZ	5.8	3.8
/aug-cc-pV5Z	5.7	3.7
CBS-∞	5.6	3.6

H_2O product in the dissociation of H_2O-HO, which might arise if OH stretch couples with H_2O bend through intramolecular energy transfer across the hydrogen bond. For low OH product N rotational levels ($N < 3$), there is sufficient excess energy available after dissociation to excite one quantum of H_2O bend (1594.6 cm^{-1}), potentially contributing to the peak in the product distribution at low OH rotational energy. For higher OH product N rotational levels ($N \geq 3$), there is not enough energy available to excite the H_2O bend. The excess energy can only go into product rotation and translational recoil.

We simulate the experimental OH $X\ ^2\Pi$ (v=0) product state distribution in Figure 3 with a prior distribution,[57] both with and without explicit assumption of H_2O bend excitation. In general, a prior distribution assumes that the product states associated with the translational, rotational, and vibrational motions of the fragments are populated with equal probability subject only to a energy constraint.[58] We examine the probability of the OH products being released in a given quantum state and, therefore, sum over the unobserved H_2O quantum states. The prior distribution computed with $E_{avail} = h\nu_{IR} - D_0$ provides a reasonably good depiction of the distribution for $N \geq 4$ as illustrated by the smooth curves (for the F_1 and F_2 spin-orbit components) through the experimental data. The $N \leq 3$ portion of the distribution is better simulated when E_{avail} is reduced to ~200 cm^{-1}, the energy available if one quantum of H_2O bend is excited. A near equal weighting of the two simulations is representative of the experimental data, suggesting that approximately half of the H_2O products may be released with bending excitation.

The origin of the small secondary peak at N=9 is not known, but likely arises from a near-resonance in the half-collision scattering dynamics.

The weaker 3475 cm^{-1} band was observed when monitoring one of the most populated OH product states on the A-X (1,0) $R_1(3)$ transition; however, a comprehensive product state distribution was not determined. If this band is indeed a hot band originating from an excited ν_6 level, as proposed in the next section, then the excess energy released to products upon IR excitation would increase by ~65 cm^{-1}. This is unlikely to substantively change the OH product state distribution. However, it should be noted that the intensity ratio derived for the 3490 and 3475 cm^{-1} bands implicitly assumes that the relative population of the OH N=3, $\Pi(A')$, F_1 product state is equivalent in the two product distributions.

VI. Interpretation of IR Action Spectrum

A. $^2A'$ Electronic State

As described in Sec. III, a two-dimensional potential $V(r,\phi)$, incorporating both the OH radical distance (r) and the angle out-of-plane (ϕ), was generated to probe the role of couplings between the corresponding vibrational modes, ν_2 and ν_6, in the infrared spectrum of the H_2O-HO complex. This section discusses the potential constructed for the $^2A'$ surface. Energies of (ν_2,ν_6) quantum states and the resultant frequencies of (ν_2',ν_6') $\leftarrow$ (ν_2'',ν_6'') transitions with their respective transition strengths are computed in order to investigate the origin of the two distinct spectral bands in the experimental spectrum.

The double-well potentials $V_e(\phi)$ for the purely electronic potential and the adiabatic potentials $V_{\nu_2}(\phi)$ for the ν_2=0 and 1 quantum states of H_2O-HO with $^2A'$ symmetry are depicted in Figure 4. For $V_e(\phi)$, the barrier to planarity is 24.3 cm^{-1} and the minima are located at ϕ values of ±37.2°. The barrier height increases with increasing ν_2 to 37.3 and 73.3 cm^{-1} in the ν_2=0 and 1 quantum states, respectively. Additionally, the minimum shifts to larger values of $|\phi|$, specifically 40.5° for ν_2=0 and 45.6° for ν_2=1.

To understand the origins of the width and height of the barrier, we turn to the frequency, ω_e, and anharmonicity, $\omega_e x_e$, obtained from the Morse parameters for the OH radical stretch, developed as a function of ϕ by fitting the electronic energies to eq. (2). These are plotted in Figure 5. The frequency ω_e is a maximum when the complex is planar and decreases to a minimum value at ϕ=±62.7°. The anharmonicity displays the opposite trend, with a local minimum when the complex is planar and a maximum at ϕ=±56.2°. Increasing ω_e increases the transition frequency, while increasing $\omega_e x_e$ decreases the transition frequency. As such, because the maximum in ω_e and minimum in $\omega_e x_e$ occur at larger values of ϕ than the minimum in $V_e(\phi)$, the minimum in the adiabatic potential $V_{\nu_2}(\phi)$ shifts to larger values of $|\phi|$ with increased excitation of the OH stretch.

The behaviors of ω_e and $\omega_e x_e$ are characteristic of hydrogen bonded systems and the overall trends are very similar to those reported for the OH stretch in HOONO.[42,59] In the case of the H_2O-HO complex, these trends can be rationalized as follows. Extension of the OH bond drives the system toward the proton transferred H_3O^+/O^- complex. This

Figure 4. Calculated H_2O-HO potentials as a function of the angle out-of-plane ϕ with all other coordinates optimized to minimize the total energy, using DFT with the B3LYP functional and the aug-cc-pVTZ basis. The purely electronic potentials V_e of $^2A'$ and $^2A''$ symmetry are shown along with the adiabatic potentials $V_{\nu_2}(\phi)$ generated (see text) for H_2O-HO incorporating OH stretch with ν_2=0 and 1. The symbols denote the calculated data points for the $^2A'$ (black, filled symbols) and $^2A''$ (red, open symbols) symmetry potentials, while the curves through the data are the fits. The energies of the ν_6 quantum states associated with the ν_2=0 and 1 quantum levels, denoted as (ν_2,ν_6), on the $^2A'$ (black) and $^2A''$ (red) surfaces are indicated as horizontal lines. The arrows depict the (1,0) ← (0,0) and (1,1) ← (0,1) transitions on the $^2A'$ (black) and $^2A''$ (red) surfaces.

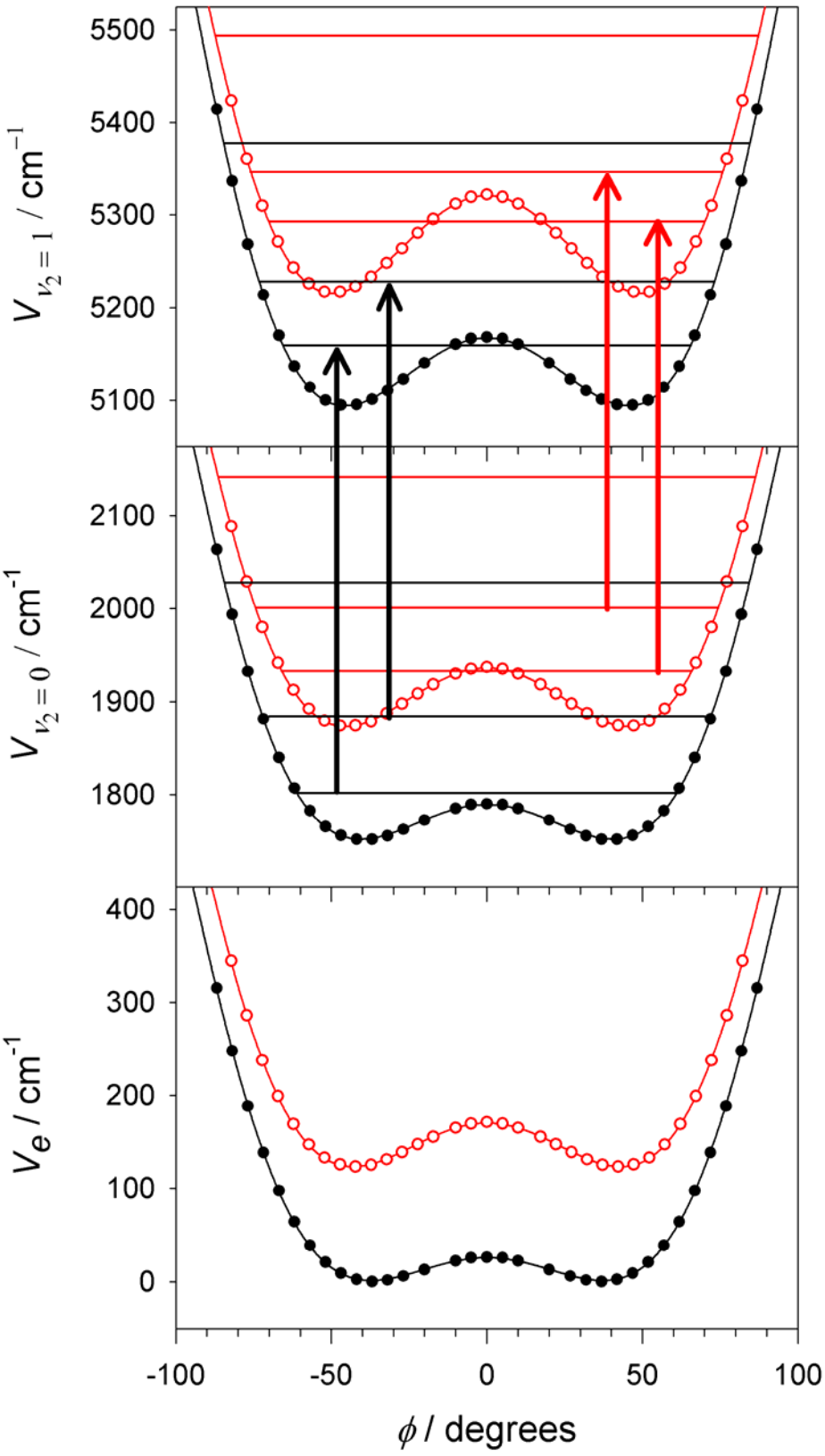
5500
5400
5300
5200
5100
$V_{\nu_2=1}$ / cm^{-1}
2100
2000
1900
1800
$V_{\nu_2=0}$ / cm^{-1}
400
300
200
100
0
V_e / cm^{-1}
-100
-50
0
50
100
ϕ / degrees

Figure 5. Harmonic frequency, ω_e, and anharmonicity, $\omega_e x_e$, of the H_2O-HO potential on the $^2A'$ surface, obtained from the parameters in the Morse fit of the OH radical stretch as a function of the angle out-of-plane ϕ.

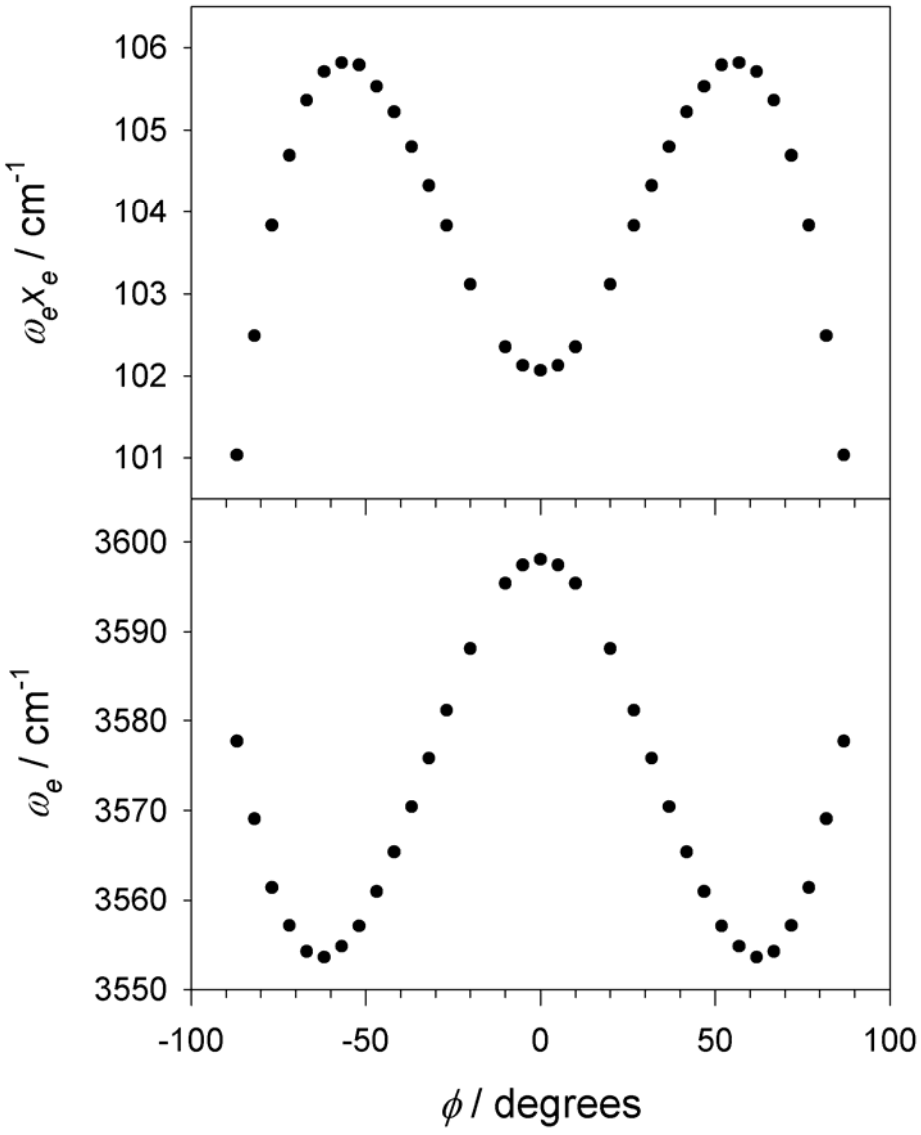
106
105
104
103
102
101
$\omega_e x_e$ / cm^{-1}
3600
3590
3580
3570
3560
3550
ω_e / cm^{-1}
-100
-50
0
50
100
ϕ / degrees

process is more favorable in non-planar geometries, and the possibility of charge transfer lowers the OH frequency and raises its anharmonicity as the H is driven into more favorable H_3O^+ geometries. While the shifts are less dramatic in the present system, similar behavior has been described for $(H_2O)_2^+$, $X^-(H_2O)$, and HCl-$(H_2O)_4$ complexes.[60-62]

Once we evaluated the adiabatic potentials $V_{\nu_2}(\phi)$ for ν_2=0 and 1, they were used to calculate the energies of the (ν_2,ν_6) levels, which are shown with horizontal lines in Figure 4 and compiled in Table 3. An interesting observation emerging from these calculations is that the position of the ν_6=0 energy level changes relative to the barrier to planarity when ν_2=0 and 1, with this level lying 12.7 cm^{-1} above the barrier for ν_2=0 and 7.3 cm^{-1} below the barrier for ν_2=1. The change in barrier height also results in a decrease in the frequency of the out-of-plane bend mode, expressed as the energy difference between the (ν_2,0) and (ν_2,1) states, by 13.7 cm^{-1} for ν_2=1 compared to ν_2 = 0. This observation is the key to our assignment of the lower frequency band in the spectrum, as this decrease in the out-of-plane bend frequency upon OH stretch excitation means that the calculated (1,1) ← (0,1) hot band is shifted by 13.7 cm^{-1} to lower frequency of the (1,0) ← (0,0) fundamental transition. This shift is remarkably similar to the 15 cm^{-1} shift between the two bands observed in the experimental spectrum.

Before pursuing this point and discussing the likelihood of hot-band transitions in the H_2O-HO complex, we must note that the calculated frequencies of these two bands are predicted to be shifted by –176.5 and –190.2 cm^{-1} from free OH, respectively. To

Table 3. Calculated energies for (ν_2,ν_6) levels of H_2O-HO, ν_6 energy spacings (ΔE), frequencies for (ν_2',ν_6') ← (ν_2'',ν_6'') transitions and their corresponding strengths (M^2), and spectral shifts (Δ) relative to free OH for the $^2A'$ and $^2A''$ surfaces. Units in cm^{-1} except as noted. Energies defined relative to the global minimum.

$^2A'$	(ν_2, ν_6=0)	(ν_2, ν_6=1)	ΔE
(ν_2=0, ν_6)	1802.0	1884.2	82.2
(ν_2=1, ν_6)	5159.7	5228.2	68.5
(1,0) ← (0,0)	3357.7		
(1,1) ← (0,1)		3344.0	
Δ	-176.5	-190.2	
M^2 (D^2)	0.0477	0.0483	
$^2A''$	(ν_2, ν_6=0)	(ν_2, ν_6=1)	ΔE
(ν_2=0, ν_6)	1932.9	2000.9	68.0
(ν_2=1, ν_6)	5292.9	5346.5	53.6
(1,0) ← (0,0)	3360.0		
(1,1) ← (0,1)		3345.6	
Δ	-174.2	-188.6	
M^2 (D^2)	0.0448	0.0462	

obtain these numbers, we used the same approach as was used to calculate the adiabatic potential for the complex. Specifically, we calculated the electronic energy as a function of the OH bond length and fitted the results to an extended Morse potential of the form of eq. (2). While these shifts are approximately two times larger than the experimentally observed shifts, they are consistent with the shift of –162.4 cm^{-1} obtained from the harmonic frequencies for the OH radical stretch upon complexation with H_2O using the same method and basis and the –156 cm^{-1} shift in harmonic frequencies reported in a previous DFT study.[8] The significant difference between the experimental and calculated shifts of the OH stretch frequency prompted us to carry out the CCSD(T) calculations with very large basis sets described in previous sections. By going to this high level of theory and an aug-cc-pVQZ basis, the shift in the calculated harmonic frequency of the OH stretch is reduced to –105 cm^{-1}, which is much closer to the observed shift.

The fact that the absolute shift in the calculated OH frequency in H_2O-HO compared to isolated OH at the B3LYP/aug-cc-pVTZ level of theory/basis differs from experiment by ~100 cm^{-1} may lead one to question the accuracy of the calculated 13.7 cm^{-1} shift between the OH fundamental and the hot-band transition with one quantum of excitation in the out-of-plane bend. As indicated above, the frequency of the out-of-plane bend is sensitive to the width and height of the barrier to planarity as well as the changes in these properties upon OH stretch excitation. The latter arises from the variation of the OH stretch frequency ω_e and anharmonicity $\omega_e x_e$ with ϕ. These changes are well-understood. While the B3LYP calculations are not expected to provide an exact treatment, the frequencies and anharmonicites derived from this method (Figure 5)

display the expected trends. A second concern is whether the electronic structure method utilized (B3LYP) provides an accurate description of the width and height of the barrier to planarity. In Table 4, we report equilibrium values of ϕ and barrier heights, calculated using various levels of theory and basis sets. The barrier heights are consistently calculated to be between 16 and 38 cm^{-1}. Most of the calculations and, in particular, the highest level ones give an equilibrium value of $|\phi|$ between 33° and 40°. As a result, we are confident that the B3LYP/aug-cc-pVTZ potential surface provides a good description of the dependence of the electronic energy on the out-of-plane bend coordinate.

Based on the above considerations, the 3490 cm^{-1} experimental band is likely the (1,0) ← (0,0) transition, namely the fundamental OH stretch transition from the ground ν_6 quantum state. The 3475 cm^{-1} experimental band is likely the (1,1) ← (0,1) transition, that is, a hot band originating from an excited out-of-plane bending state (ν_6=1). Additionally, the relative calculated strengths of the (1,0) ← (0,0) and (1,1) ← (0,1) transitions have a ratio of ~1:1, as recorded in Table 3. Again, this result is consistent with the two experimental bands, each with significant intensity.

The proposal that the experimental features at 3490 cm^{-1} and 3475 cm^{-1} are transitions originating from the (0,0) and (0,1) quantum states, respectively, hinges on the possibility that the ν_6=1 state is populated. The (0,1) quantum state is calculated to be only 82.2 cm^{-1} above the ground (0,0) state, and thus can be expected to be populated at vibrational temperatures above 50 K. The fractional population of the (0,1) energy level relative to the (0,0) energy level is calculated to be 0.09 at 50 K, 0.31 at 100 K, and 0.55

Table 4. Calculated heights of the barrier to planarity V_e (ϕ=0) and equilibrium values of the out-of-plane angle (ϕ_e) obtained at different levels of theory/basis sets

Level of theory	V_e (ϕ=0) / cm^{-1}	ϕ_e / degrees
MP2/6-311+G(d,p)	25	28.8
MP2/6-311+G(3df,2p)	17	33.3
MP2/aug-cc-pVDZ	31	34.7
MP2/aug-cc-pVTZ	18	34.2
B3LYP/aug-cc-pVDZ	26	37.2
B3LYP/aug-cc-pVTZ	24	37.2
B3LYP/aug-cc-pVQZ	23	36.0
CCSD/aug-cc-pVDZ	25	36.4
CCSD(T)/aug-cc-pVDZ	38	39.6
CCSD(T)/aug-cc-pVTZ	24	37.0
CCSD(T)/aug-cc-pVQZ	16	33.4

at 200 K, and such vibrational temperatures are certainly plausible under the experimental conditions. It should also be noted that the two spectral features are observed using infrared action spectroscopy. The hot band, with slightly greater excess energy released to products, could be detected with higher efficiency than the fundamental transition, if it has a larger fractional population in the OH N=3, Π(A′), F_1 product state.

Figure 6 shows the $\mu_{10}(\phi)$ transition moment curves projected along the a- and c-inertial axes. The dipole moment along the b-inertial axis in H_2O-HO is zero. The dipole moment along the a-inertial axis is an even function of ϕ, whereas the dipole moment along the c-inertial axis is an odd function of ϕ and nearly invariant about zero. Therefore, since the ν_6=0 wavefunctions are even functions of ϕ and the ν_6=1 wavefunctions are odd functions of ϕ, the only non-zero component of both the (1,0) ← (0,0) and (1,1) ← (0,1) transitions is along the a-inertial axis. The OH radical stretch coordinate lies nearly along the a-inertial axis, consistent with an a-type transition and validating the assumed transition type for the OH radical stretch in Ref. 19.

B. ^{2}A″ Electronic State

The previous section suggests that the two experimental spectral bands are both transitions on the ^{2}A′ electronic surface. We also considered the possibility of the experimental bands resulting from transitions on two different electronic surfaces, one on the ^{2}A′ surface and the other on the ^{2}A″ surface. Therefore, a two-dimensional potential

Figure 6. Calculated transition moment for H_2O-HO, $\mu_{10}(\phi)$ plotted as a function of the angle out-of-plane ϕ. The $\mu_{10}(\phi)$ components along the a-inertial axis (black, filled symbols for data with curve for fit) and c-inertial axis (green, open symbols for data with curve for fit) are shown.

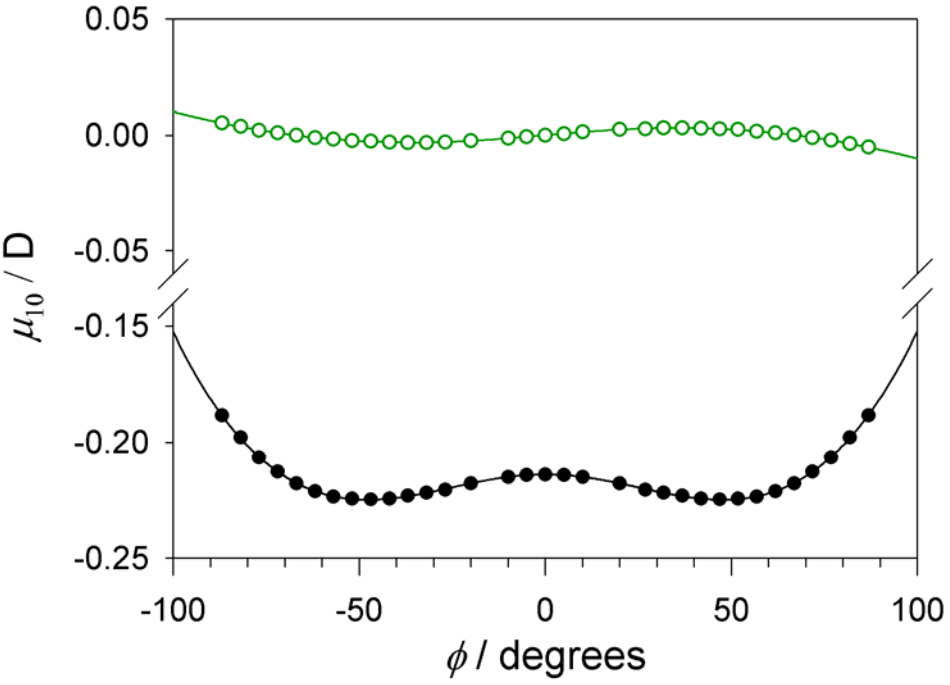
0.05
0.00
-0.05
-0.15
-0.20
-0.25
μ_{10} / D
-100
-50
0
50
100
ϕ / degrees

$V(r,\phi)$ was also constructed for the H_2O-HO complex of $^2A''$ symmetry. Energies of (ν_2,ν_6) quantum states and the frequencies of $(\nu_2',\nu_6') \leftarrow (\nu_2'',\nu_6'')$ transitions with their respective transition strengths were calculated in order to determine the likelihood of this possibility.

The H_2O-HO complex on the $^2A''$ surface follows markedly the same trends as H_2O-HO on the $^2A'$ surface, except for a higher barrier to planarity (46.8 cm^{-1}) and slightly larger $|\phi|$ values (43.0°) at the energetic minima on the purely electronic potential $V_e(\phi)$. As illustrated in Figure 4**,** the barrier height increases for $V_{\nu_2}(\phi)$ on the $^2A''$ surface, rising to 62.7 and 105.1 cm^{-1} for ν_2=0 and 1, respectively. For ν_2=0 the minima are at ϕ=±45.5°, while for ν_2=1 the minima are at ϕ=±49.6°, in much the same way as found for the $^2A'$ surface. As the barrier height increases from ν_2=0 to ν_2=1, the positions of the ν_6=0 energy levels change with respect to the barrier. The (0,0) energy level lies 3.1 cm^{-1} below the barrier, whereas the (1,0) energy level lies 27.7 cm^{-1} below the barrier. The increase in barrier height with OH vibrational excitation decreases the spacing between the ν_6=0 and 1 out-of-plane bending levels in that ν_2 quantum state. On the $^2A''$ electronic surface, as reported in Table 3, the energy spacing of 68.0 cm^{-1} between (0,0) and (0,1) decreases to 53.6 cm^{-1} between (1,0) and (1,1).

Most significantly, as indicated in Table 3, the frequencies of the (1,0) ← (0,0) and (1,1) ← (0,1) transitions on the $^2A''$ surface are remarkably similar to the frequencies of the corresponding transitions on the $^2A'$ surface. The frequency of the (1,0) ← (0,0) transition on the $^2A''$ surface differs by less than 3 cm^{-1} from the predicted frequency for

the corresponding (1,0) ← (0,0) transition on the $^2A'$ surface. The frequency of the (1,1) ← (0,1) transition on the $^2A''$ differs by less than 2 cm^{-1} from the predicted frequency of the corresponding (1,1) ← (0,1) transition on the $^2A'$ surface. As shown in Table 3, the strengths of the two transitions on the $^2A''$ surface are essentially equal and are also comparable to the strengths of the two transitions on the $^2A'$ surface. The similarity in frequency of corresponding transitions on the two electronic surfaces suggests that transitions on the $^2A''$ surface would overlap the corresponding transitions on the $^2A'$ surface. Therefore, the two experimental bands 15 cm^{-1} apart are unlikely to result from the (1,0) ← (0,0) transitions on the two different electronic surfaces.

We have also considered the effect of mixing between the $^2A'$ and $^2A''$ surfaces induced by spin-orbit coupling, using the spin-orbit coupling constant of free OH. This results in the same degree of mixing as described in Ref. 19. This shifts the absolute energies of each of the (ν_2,ν_6) levels on the nominally $^2A'$ and $^2A''$ surfaces by ~30 cm^{-1}. However, the frequencies of the (1,0) ← (0,0) and (1,1) ← (0,1) transitions on the two surfaces are shifted by less than 1 cm^{-1} with the introduction of spin-orbit coupling. Thus, the proposed assignment of the two bands as fundamental and hot band transitions is unchanged.

VII. Conclusions

In this paper, we report the IR action spectrum of H_2O-HO in the OH radical stretching region. The spectrum displays two distinct spectral bands, one at 3490 cm^{-1} and the other at 3475 cm^{-1}, shifted by 78 and 93 cm^{-1} to lower frequency of the OH

stretch frequency in an isolated OH molecule. The higher frequency band in the spectrum has roughly twice the integrated intensity of the lower frequency one. The shift in frequency of the 3490 cm^{-1} band, compared to an isolated OH molecule, is consistent with the harmonic shift calculated at the CCSD(T) level with very large basis sets and the shifts previously reported for the H_2O-HO complex in an Ar matrix. We have assigned this transition to the fundamental in the OH stretch. On the other hand, the lower frequency peak does not correspond to previously observed bands in this system.

In an effort to elucidate the assignment of this band, we undertook a series of calculations. Based on that work, we assign both bands as transitions within the nominally $^2A'$ electronic surface. The 3475 cm^{-1} band is likely a hot band originating from a state with one quantum in the out-of-plane bend. The latter is calculated to be 13.7 cm^{-1} lower in energy than the fundamental in the OH stretch with a comparable transition moment to the ν_2 fundamental transition. We also pursued the possibility that one of the bands involved a transition within the $^2A''$ state. Based on our calculations, the transitions on the $^2A'$ and $^2A''$ electronic states should be overlapping and therefore invoking the second electronic state could not explain the 15 cm^{-1} gap between the two observed bands.

Finally, using action spectroscopy to monitor the absorption of a photon by the H_2O-HO complex enables us to obtain an upper bound on the binding energy of the complex based on the OH product state distribution. Analysis of the distribution arising from exciting the complex at 3491.3 cm^{-1} yields an experimental binding energy of $D_0 \leq$ 5.14 kcal mol^{-1}. The value for D_e, calculated at the CCSD(T) level of theory and the

CBS limit is 5.6 kcal mol^{-1}, while the best estimate for D_0 is 3.6 kcal mol^{-1}. This is very good agreement given the difficulty of such calculations for hydrogen-bonded systems. Future work will be aimed at experimental and theoretical studies of partially and fully deuterated H_2O-HO complexes to ascertain their OH/D radical stretching frequencies, OH/D product state distributions, and binding energies.

References

1. Aloisio, S.; Francisco, J. S. *Acc. Chem. Res.* **2000**, *33*, 825.

2. Hanson, D. R.; Burkholder, J. B.; Howard, C. J.; Ravishankara, A. R. *J. Phys. Chem.* **1992**, *96*, 4979

3. Knipping, E. M.; Lakin, M. J.; Foster, K. L.; Jungwirth, P.; Tobias, D. J.; Gerber, R. B.; Dabdub, D.; Finlayson-Pitts, B. J. *Science* **2000**, *288*, 301.

4. Langford, V. S.; McKinley, A. J.; Quickenden, T. I. *Acc. Chem. Res.* **2000**, *33*, 665

5. Kim, K. S.; Kim, H. S.; Jang, J. H.; Kim, H. S.; Mhin, B.-J.; Xie, Y.; Schaefer, H. F. *J. Chem. Phys.* **1991**, *94*, 2057.

6. Xie, Y.; Schaefer, H. F. *J. Chem. Phys.* **1993**, *98*, 8829.

7. Wang, B. S.; Hou, H.; Gu, Y. S. *Chem. Phys. Lett.* **1999**, *303*, 96.

8. Zhou, Z.; Qu, Y.; Fu, A.; Du, B.; He, F.; Gao, H. *Int. J. Quantum Chem.* **2002**, *89*, 550.

9. Schofield, D. P.; Kjaergaard, H. G. *J. Am. Chem. Soc.* **2004**, *120*, 6930.

10. Cabral do Couto, P.; Guedes, R. C.; Costa Cabral, B. J.; Martinho Simoes, J. A. *J. Chem. Phys.* **2003**, *119*, 7344.

11. Du, S.; Francisco, J. S.; Schenter, G. K.; Iordanov, T. D.; Garrett, B. C.; Dupuis, M.; Li, J. *J. Chem. Phys.* **2006**, *124*, 224318/1.

12. Engdahl, A.; Karlstrom, G.; Nelander, B. *J. Chem. Phys.* **2003**, *118*, 7797.

13. Cooper, P. D.; Kjaergaard, H. G.; Langford, V. S.; McKinley, A. J.; Quickenden, T. I.; Schofield, D. P. *J. Am. Chem. Soc.* **2003**, *125*, 6048.

14. Tsuji, K.; Shibuya, K. *J. Phys. Chem. A* **2009**, *113*, 9945.

15. Brauer, C., S.; Sedo, G.; Dahlke, E.; Wu, S.; Grumstrup, E. M.; Leopold, K. R.; Marshall, M. D.; Leung, H. O.; Truhlar, D. G. *J. Chem. Phys.* **2008**, *129*, 104304.

16. Brauer, C. S.; Sedo, G.; Grumstrup, E. M.; Leopold, K. R.; Marshall, M. D.; Leung, H. O. *Chem. Phys. Lett.* **2005**, *401*, 420.

17. Ohshima, Y.; Sato, K.; Sumiyoshi, Y.; Endo, Y. *J. Am. Chem. Soc.* **2005**, *127*, 1108.

18. Wu, S.; Sedo, G.; Leopold, K. R. *J. Mol. Spectrosc.* **2009**, *253*, 35.

19. Marshall, M. D.; Lester, M. I. *J. Phys. Chem. B* **2005**, *109*, 8400.

20. Kisiel, Z.; Legon, A. C.; Millen, D. J. *Proc. R. Soc. Lond. A* **1982**, *381*, 419.

21. Kisiel, Z.; Pietrewicz, B. A.; Fowler, P. W.; Legon, A. C.; Steiner, E. *J. Phys. Chem. A* **2000**, *104*, 6970.

22. Legon, A. C.; Millen, D. J.; North, H. M. *Chem. Phys. Lett.* **1987**, *135*, 303.

23. Bevan, J. W.; Kisiel, Z.; Legon, A. C.; Millen, D. J.; Rogers, S. C. *Proc. R. Soc. London, Ser. A* **1980**, *372*, 441.

24. Legon, A. C.; Willoughby, L. C. *Chem. Phys. Lett.* **1983**, *95*, 449.

25. Farnik, M.; Weimann, M.; Suhm, M. A. *J. Chem. Phys.* **2003**, *118*, 10120.

26. Huneycutt, A. J.; Stickland, R. J.; Hellberg, F.; Saykally, R. J. *J. Chem. Phys.* **2003**, *118*, 1221.

27. Thomas, R. K. *Proc. R. Soc. London, Ser. A* **1975**, *344*, 579.

28. Re, S.; Osamura, Y.; Suzuki, Y.; Schaefer, H. F., III. *J. Chem. Phys.* **1998**, *109*, 973.

29. Demaison, J.; Lievin, J. *Mol. Phys.* **2008**, *106*, 1249.

30. Clavelin, J. L.; Mirabel, P. *J. Chim. Phys. Phys.-Chim. Biol.* **1979**, *76*, 533.

31. Guyer, D. R.; Huwel, L.; Leone, S. R. *J. Chem. Phys.* **1983**, *79*, 1259.

32. Frisch, M. J.; Trucks, G. W.; Schlegel, H. B.; Scuseria, G. E.; Robb, M. A.; Cheeseman, J. R.; Montgomery, J., J. A.; Vreven, T.; Kudin, K. N.; Burant, J. C.; Millam, J. M.; Iyengar, S. S.; Tomasi, J.; Barone, V.; Mennucci, B.; Cossi, M.; Scalmani, G.; Rega, N.; Petersson, G. A.; Nakatsuji, H.; Hada, M.; Ehara, M.; Toyota, K.; Fukuda, R.; Hasegawa, J.; Ishida, M.; Nakajima, T.; Honda, Y.; Kitao, O.; Nakai, H.; Klene, M.; Li, X.; Knox, J. E.; Hratchian, H. P.; Cross, J. B.; Bakken, V.; Adamo, C.; Jaramillo, J.; Gomperts, R.; Stratmann, R. E.; Yazyev, O.; Austin, A. J.; Cammi, R.; Pomelli, C.; Ochterski, J. W.; Ayala, P. Y.; Morokuma, K.; Voth, G. A.; Salvador, P.; Dannenberg, J. J.; Zakrzewski, V. G.; Dapprich, S.; Daniels, A. D.; Strain, M. C.; Farkas, O.; Malick, D. K.; Rabuck, A. D.; Raghavachari, K.; Foresman, J. B.; Ortiz, J. V.; Cui, Q.; Baboul, A. G.; Clifford, S.; Cioslowski, J.; Stefanov, B. B.; Liu, G.; Liashenko, A.; Piskorz, P.; Komaromi, I.; Martin, R. L.; Fox, D. J.; Keith, T.; Al-Laham, M. A.; Peng, C. Y.; Nanayakkara, A.; Challacombe, M.; Gill, P. M. W.; Johnson, B.; Chen, W.;

Wong, M. W.; Gonzalez, C.; Pople, J. A. *GAUSSIAN 03, revision E.01*; Gaussian, Inc.: Pittsburgh, PA, 2003.

33. Kim, K.; Jordan, K. D. *J. Phys. Chem.* **1994**, *98*, 10089.

34. Novoa, J. J.; Sosa, C. *J. Phys. Chem.* **1995**, *99*, 15837.

35. Hampel, C.; Werner, H.-J. *J. Chem. Phys.* **1996**, *104*, 6286.

36. Knowles, P. J.; Hampel, C.; Werner, H. J. *J. Chem. Phys.* **1993**, *99*, 5219.

37. Raghavachari, K.; Trucks, G. W.; Pople, J. A.; Head-Gordon, M. *Chem. Phys. Lett.* **1989**, *157*, 479.

38. Scuseria, G. E. *Chem. Phys. Lett.* **1991**, *176*, 27.

39. Kendall, R. A.; Dunning, T. H., Jr.; Harrison, R. J. *J. Chem. Phys.* **1992**, *96*, 6796.

40. Woon, D. E.; Dunning, T. H., Jr. *J. Chem. Phys.* **1993**, *98*, 1358.

41. Peterson, K. A.; Woon, D. E.; Dunning, T. H., Jr. *J. Chem. Phys.* **1994**, *100*, 7410.

42. Matthews, J.; Sinha, A. *J. Chem. Phys.* **2005**, *122*, 104313.

43. McCoy, A. B.; Sprague, M. K.; Okumura, M. *J. Phys. Chem. A* **2009**, submitted.

44. Schofield, D. P.; Kjaergaard, H. G.; Matthews, J.; Sinha, A. *J. Chem. Phys.* **2005**, *123*, 134318.

45. Colbert, D. T.; Miller, W. H. *J. Chem. Phys.* **1992**, *96*, 1982.

46. Light, J. C.; Hamilton, I. P.; Lill, J. V. *J. Chem. Phys.* **1985**, *82*, 1400.

47. Wilson Jr., E. B.; Decius, J. C.; Cross, P. C. *Molecular Vibrations: The Theory of Infrared and Raman Vibrational Spectra*; Dover Publications, Inc.: New York, NY, 1980.

48. Johnson, L. M.; McCoy, A. B. *J. Phys. Chem. A* **2006**, *110*, 8213.

49. Coxon, J. A. *Can. J. Phys.* **1980**, *58*, 933.

50. Langford, V. S.; McKinley, A. J.; Quickenden, T. I. *J. Am. Chem. Soc.* **2000**, *122*, 12859.

51. Hamad, S.; Lago, S.; Mejias, J. A. *J. Phys. Chem. A* **2002**, *106*, 9104.

52. The population in the lowest rovibrational state, OH $X\,^2\Pi$ (v=0, N=1), could not be probed because of the large jet-cooled background.

53. Feyereisen, M. W.; Feller, D.; Dixon, D. A. *J. Phys. Chem.* **1996**, *100*, 2993.

54. Tschumper, G. S.; Leininger, M. L.; Hoffman, B. C.; Valeev, E. F.; Schaefer, H. F., III; Quack, M. *J. Chem. Phys.* **2002**, *116*, 690.

55. Lai, C.-H.; Chou, P.-T. *J. Comput. Chem.* **2007**, *28*, 1357.

56. Nizkorodov, S. A.; Ziemkiewicz, M.; Nesbitt, D. J.; Knight, A. E. W. *J. Chem. Phys.* **2005**, *122*, 194316.

57. Baer, T.; Hase, W. L. *Unimolecular Reaction Dynamics*; Oxford University Press: New York, 1996.

58. Konen, I. M.; Li, E. X. J.; Stephenson, T. A.; Lester, M. I. *J. Chem. Phys.* **2005**, *123*, 204318.

59. McCoy, A. B.; Fry, J. L.; Francisco, J. S.; Mollner, A. K.; Okumura, M. *J. Chem. Phys.* **2005**, *122*, 104311.

60. Gardenier, G. H.; Johnson, M. A.; McCoy, A. B. *J. Phys. Chem. A* **2009**, *113*, 4772.

61. Roscioli, J. R.; Diken, E. G.; Johnson, M. A.; Horvath, S.; McCoy, A. B. *J. Phys. Chem. A* **2006**, *110*, 4943.

62. Gutberlet, A.; Schwaab, G.; Birer, O.; Masia, M.; Kaczmarek, A.; Forbert, H.; Havenith, M.; Marx, D. *Science* **2009**, *324*, 1545.

63. Shimanouchi, T. Molecular Vibrational Frequencies. In *NIST Chemistry WebBook, NIST Standard Reference Database Number 69*; Linstrom, P. J., Mallard, W. G., Eds.; National Institute of Standards and Technology: Gaithersburg, MD, 20899, http://webbook.nist.gov, (retrieved August 12, 2009).

Chapter 4:

Experimental Characterization of the Weakly Anisotropic CN $X\ ^2\Sigma^+$ + Ne Potential from IR-UV Double Resonance Studies of the CN-Ne Complex

This research has been published in the *Journal of Chemical Physics* (2011), *134*, 184308 and was performed in conjunction with post-doctorate Joseph M. Beames, second year graduate student Melodie Ting, and Marsha I. Lester in the *Department of Chemistry, University of Pennsylvania* as well as Thomas A. Stephenson in the *Department of Chemistry and Biochemistry, Swarthmore College*.

I. Introduction

Many reactions of CN radicals exhibit unusual kinetic behavior indicative of association of the reactants in a weakly bound radical-molecule complex. This is evident in the reaction kinetics of the CN radical with hydrocarbons,[1,2] which have been studied extensively due to the prevalence of cyanogen in the combustion products of fossil fuels and its resulting role in NO_x chemistry.[3] In such environments, the CN radical acts as a pseudo-halogen, reacting rapidly with the gaseous hydrocarbons through addition or hydrogen abstraction. Large rate coefficients in both of these cases suggest that the reactions are barrierless with negative activation energies indicating that pre-reactive complexes are formed, albeit with short lifetimes.[2] Crossed molecular beam studies of CN radicals with unsaturated hydrocarbons[4] have shown that the first step in the reaction pathway is the production of a collision complex, in which the CN radical adds to the π electron density of the hydrocarbon. Although this type of addition mechanism would not be possible with saturated hydrocarbons, theoretical work by Georgievskii and Klippenstein[5] has predicted a weakly bound van der Waals complex and submerged barrier, separating the pre-reactive complex from product formation, to explain the "strange kinetics" and unusual temperature dependence of the C_2H_6 + CN hydrogen abstraction reaction. Isolating and studying CN radical-rare gas (CN-Rg) complexes provides a starting point to study CN radical-molecule complexes, which have not yet been observed directly.

Thus far, the electronic spectroscopy and excited state predissociation dynamics of CN-Rg and CN-H_2 van der Waals complexes have been examined by Heaven and co-

workers.[6-8] CN-Ne, CN-Ar and CN-H_2 were investigated using laser induced fluorescence (LIF) with initial work on each system focusing on electronic excitation and fluorescence detection in the CN $B\,^2\Sigma^+$-$X\,^2\Sigma^+$ region, hereafter referred to as *B*-*X* transitions of the complexes. The notation used to denote electronic states of these complexes is not rigorous, but has been adopted in this work and all previous studies to denote states which correlate closely with those of free-CN. Rotationally structured CN-Ne *B* (v_{CN}=0)–*X* (v_{CN}=0) excitation spectra were observed by collection of *B*-state fluorescence from the complex itself, with the electronic origin lying close in energy to that of free-CN. This is in stark contrast to the dynamics of CN-Ar and CN-H_2 complexes upon *B*-*X* excitation: CN-Ar rapidly predissociates into CN $A\,^2\Pi$ + Ar, such that rovibronic spectra could be observed only by collecting CN *A*-*X* emission. The CN-H_2 *B*-*X* excitation spectrum displays no resolvable structure and was attributed to bound-free excitation with subsequent emission from CN $B\,^2\Sigma^+$ products. These studies provide a significant amount of information on the excited *B* (and *A*) electronic states of these CN complexes; however, little spectroscopic information was obtained on these CN complexes in their ground electronic state. The present study provides the first infrared spectroscopic study of a CN radical complex, specifically CN-Ne, which is utilized to characterize the anisotropy of the CN $X\,^2\Sigma^+$ + Ne intermolecular potential. Similar studies of CN-Ar and CN-H_2 will be reported elsewhere.

Alexander and co-workers have generated high level *ab initio* potential energy surfaces (PES) for CN-Ne, CN-Ar and CN-H_2, and these were subsequently used in analysis of spectroscopic data, giving insight on the structure and dynamics of the

complexes.[9-12] The CN $X\,^2\Sigma^+$ + Ne MRCI+Q surface indicates a long-range van der Waals type interaction with Ne bound to the CN $X\,^2\Sigma^+$ radical by just 31.3 cm^{-1} (D_e) at an intermolecular separation (R_e) of 3.75 Å. The intermolecular potential exhibits minimal anisotropy, with a barrier to CN internal rotation of less than 2 cm^{-1}. Another *ab initio* study of the CN $X\,^2\Sigma^+$ + Ne potential by Vrábel *et al*. yielded a similar angular dependence for the interaction energy using restricted (and unrestricted) MP2 theory,[13] with D_e=32.0 cm^{-1}, R_e=3.75 Å, and a barrier to internal rotation of less than 5 cm^{-1}. The anisotropy of the ground state PES changes for different partners; for example, the CN $X\,^2\Sigma^+$ + Ne and H_2 potentials are relatively flat,[11,12] with CN likely to undergo almost free internal rotation, while the CN $X\,^2\Sigma^+$ + Ar potential is predicted to be more anisotropic with a bent minimum energy structure.[9] The minimum energy configuration also changes upon electronic excitation of CN to the $B\,^2\Sigma^+$ state, which reverses the direction of the CN dipole moment,[14] with CN-Ar favoring a linear minimum energy configuration.

Given the shallow nature of the ground and excited state potentials for CN-Rg complexes, both infrared and vibronic spectra will likely be dominated by progressions in the low frequency 'bending' vibration associated with hindered internal rotor motion. For this reason, this work follows the guide to open shell van der Waals complexes by Dubernet *et al.* which reduces the effective Hamiltonian for the system to that of the bending (or internal hindered rotor) mode alone.[15,16] For complexes of CN in $^2\Sigma^+$ states, which includes its $X\,^2\Sigma^+$ and $B\,^2\Sigma^+$ electronic states, this reduced Hamiltonian follows Hund's case (b) approximations and is similar to that of a closed shell system because the

unpaired electron spin is only weakly coupled to the nuclear axes. It should be noted that the quantum labels used in such approximations in previous literature are not consistent, and therefore it is useful to define the notation that will be used throughout this work. In such atom-diatom complexes, the diatomic monomer rotational quantum number (denoted as n) is quantized along the intermolecular axis.[15,17] This projection quantum number is labeled K. L is the pseudo diatomic quantum number for the end-over-end rotation of the complex, and this can couple with K to form the resultant N, which is the total angular momentum (excluding electron spin) and is a good quantum number. Electron spin can only weakly couple with N, and therefore is neglected. As a result, CN-Ne states will be labeled by their hindered rotor state (n^K), CN vibrational state (ν_{CN}), and CN electronic state (X or B), as needed; the intermolecular stretch (ν_s) is not observed and therefore is generally not included in state labels.

This paper focuses on the CN-Ne complex, which has previously been investigated through electronic spectroscopy in the B-X region by Heaven and co-workers.[7,8] In the present work, an IR-UV double resonance technique is employed to probe the ground electronic state of the CN-Ne complex, principally with two quanta of CN stretch, leading to the observation of several rotationally resolved bands. The rotational structure of these bands and spacings between associated angular states are used to obtain new information on the anisotropy of the CN $X\,^2\Sigma^+$ + Ne potential, which is complemented by high level *ab initio* calculations and compared with previous experimental work on this system.

Figure 1. IR-UV double resonance scheme is shown on schematic radial potentials for CN ($B\,^2\Sigma^+$, $X\,^2\Sigma^+$) + Ne. The IR laser prepares CN-Ne complexes with two quanta of CN stretch and possible intermolecular excitation. The UV laser subsequently promotes vibrationally excited CN-Ne to the excited electronic state correlating with CN $B\,^2\Sigma^+$ (v=0) + Ne, giving rise to a laser-induced fluorescence signal. Upon photolysis at 193 nm, CN-Ne X (v_{CN}=2) can also be observed directly in the jet expansion (without IR excitation) and is probed on B (v_{CN}=0)-X (v_{CN}=2) transitions, denoted as UV′.

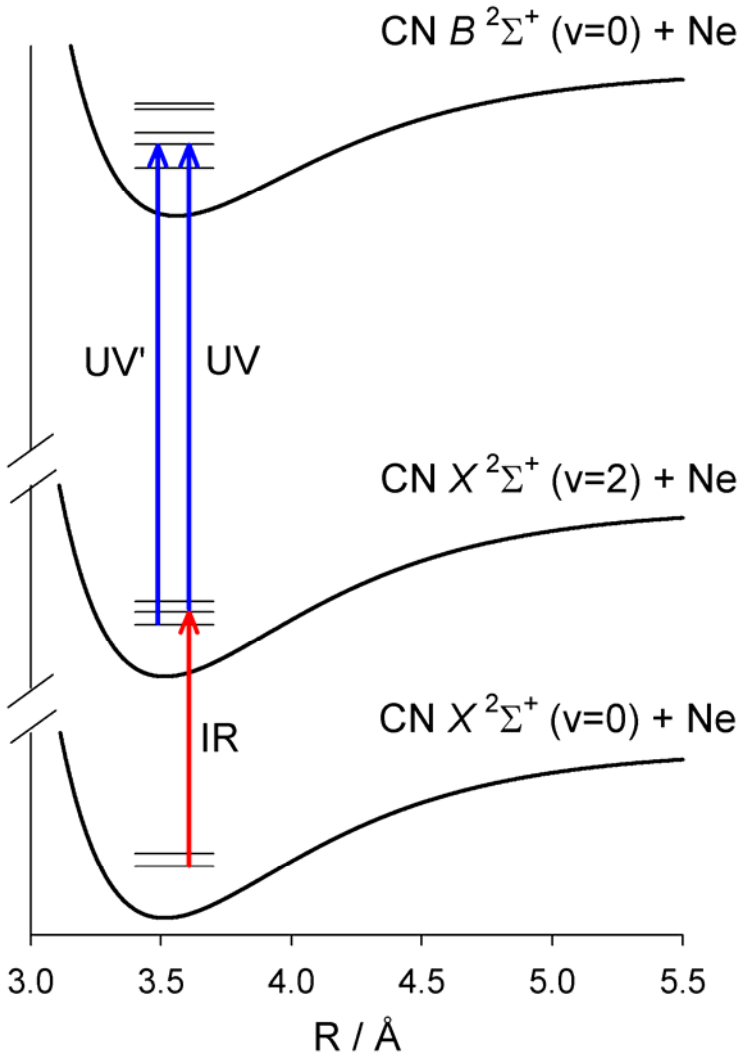
CN $B\,^2\Sigma^+$ (v=0) + Ne
UV'
UV
CN $X\,^2\Sigma^+$ (v=2) + Ne
IR
CN $X\,^2\Sigma^+$ (v=0) + Ne
3.0
3.5
4.0
4.5
5.0
5.5
R / Å

II. Experimental and Theoretical Methods

An IR-UV double resonance technique is utilized to obtain IR spectra of CN-Ne in the CN stretch overtone region as well as UV spectra in the CN $B\,^2\Sigma^+(v=0)$-$X\,^2\Sigma^+(v=2)$ spectral region. As depicted schematically in Figure 1 the IR laser prepares the CN-Ne complexes with two quanta of CN vibrational excitation. The UV laser then promotes the vibrationally excited CN-Ne complexes to the electronically excited *B* state, from which *B*-*X* fluorescence is collected. IR spectra are recorded by fixing the UV laser on a CN-Ne electronic transition and scanning the IR laser, while UV enhancement spectra are obtained by fixing the IR laser on a CN-Ne vibrational transition and scanning the UV laser.

Cyanogen iodide (ICN), which served as the CN radical precursor, is synthesized following methods described previously.[18] ICN vapor (1 torr at 25°C)[19] is entrained in a 75% Ne/He carrier gas (30 psi) by flowing the carrier gas over solid ICN contained in a PTFE sample holder.[7,8] CN radicals are generated by 193 nm[20] or 248 nm[21] photolysis (Coherent, LPX 105i excimer laser) of the ICN vapor in the throat of a pulsed supersonic expansion (General Valve, Parker Hannifin Series 9). The photolytically generated CN radicals associate with Ne in the collisional region of the expansion to form CN-Ne complexes. At a distance approximately 10 nozzle diameters downstream from the orifice, the gas mixture is interrogated with the spatially overlapped, counter-propagating IR and UV laser beams.

Tunable IR radiation with a 0.1 cm^{-1} bandwidth is generated with an optical parametric oscillator (OPO, LaserVision), pumped by an injection-seeded Nd:YAG laser

(Continuum Precision II 8000), and operates in the CN overtone region at ~2.5 μm at typical pulse powers of 10 mJ. The probe laser is the output of a Nd:YAG (Innolas, SL600) pumped dye laser (Radiant Dyes, Narrowscan) using Coumarin 460 dye, which operates in the vicinity of the CN $B\,^2\Sigma^+$-$X\,^2\Sigma^+$ (0,2) transition at ~460 nm at considerably less than 1 mJ/pulse; the fundamental dye output has a bandwidth of 0.1 cm^{-1}. The IR laser is focused into the center of the molecular beam using a 50 cm focal length lens, and is overlapped spatially with the collimated but unfocused UV laser. Both IR and UV lasers are calibrated using a wavelength meter (Coherent Wavemaster). The IR laser (10 Hz) is run at half the repetition rate of the UV laser (20 Hz) so that active background subtraction, [(IR + UV) – UV], can be employed on alternating laser shots to remove any background UV-only signal from IR-UV double resonance spectra. The delay between the IR and UV lasers is typically set at 50 ns. The resulting fluorescence in the CN *B* (v=0)–*X* (v=0) region (with a lifetime of τ= 65 ns) is collimated using f/1 optics and passed through a 390 (FWHM = 10 nm) bandpass filter before impinging on a photomultiplier tube (ET Enterprises 9816B). The laser-induced fluorescence signal is then preamplified and displayed on a digital storage oscilloscope (LeCroy WaveRunner 44xi) attached to a PC for further analysis.

Rovibronic spectra of uncomplexed CN radicals were recorded to assess its rotational and vibrational distributions in the supersonic jet. The resulting experimental spectra were simulated using a rotational temperature of ~4 K, but with significant vibrational population observed in higher vibrational levels including v=2 at both photolysis wavelengths. In addition, CN-Ne complexes were readily detected with two

quanta of CN vibrational excitation without IR excitation when 193 nm photolysis was utilized. In some cases, this resulted in a UV-only signal from the probe laser alone, which was subtracted in IR-UV double resonance spectra. This CN-Ne UV-only signal was eliminated with photolysis at 248 nm, resulting in nearly zero background when recording IR-UV spectra.

Ab initio potential energy surfaces were generated for CN $X\,^2\Sigma^+$ + Ne and CN $B\,^2\Sigma^+$ + Ne as a function of the CN center-of-mass to Ne distance (R) and intermolecular angle (θ) at a fixed, experimentally determined, CN bond length (r = 1.1718 Å).[22] The angle θ between R and r is defined as 0° for the linear CN-Ne configuration, adopting the convention of previous workers. The surfaces were generated using multireference configuration interaction (MRCI) energies with a Davidson correction (MRCI+Q), following the approach of Yang and Alexander[12] and extending their prior work with extrapolation to the one electron complete basis set (CBS) limit. The procedures used for the MRCI calculations and extrapolation to the CBS limit are given in Appendix 3. The potential energy landscape was generated by calculating energies every 0.25 Å for 3 Å < R < 4.5 Å and R = 6 Å for 10 values of θ between 0° (CN-Ne) and 180° (Ne-CN). All calculations were carried out in the MolPro suite of programs.[24]

III. Experimental Results

Following 193 nm photolysis of ICN in Ne carrier gas, two new CN-Ne features are observed upon UV-only excitation in the CN B (v=0)–X (v=2) spectral region, neither of which can be attributed to CN alone. Analogous CN-Ne spectral features have been observed previously in the CN B (v=0)–X (v=0) region by Heaven and coworkers.[7,8] The

CN-Ne features in the B (v=0)–X (v=2) region are assigned as transitions from X (ν_{CN}=2, n^K=0^0) to B (0, 0^0 and 1^1), with no intermolecular stretch (ν_s) excitation, by comparison with the prior assignments in the B (v=0)–X (v=0) region. The energy difference between analogous CN-Ne features in the two regions is 4058.6(1) cm^{-1} and corresponds to two quanta of CN stretch with no intermolecular excitation (n^K=0^0) in the ground electronic state of the CN-Ne complex. This value is within experimental uncertainty of the overtone transition of the CN monomer at 4058.55 cm^{-1}.[25] The negligible change in the CN stretching frequency upon complexation is indicative of very little change in binding energy for CN-Ne upon CN stretch excitation.

IR-UV double resonance spectra of CN-Ne are also recorded with the IR laser preparing various hindered rotor states (ν_{CN}=2, n^K) in the ground X electronic state and subsequent UV laser excitation to (ν_{CN}=0, n^K) levels in the excited B electronic state as shown in Figure 1. IR-UV double resonance excitation was initially achieved with the IR laser positioned at 4061.7 cm^{-1}. The UV laser was then scanned revealing five features in the UV enhancement spectra as shown in Figure 2. Upper state assignments are made by comparing the energy and rotational band structures of the features observed in the B (v=0)–X (v=2) region with those previously reported in the B (v=0)–X (v=0) region (see Table 2). The sum of the IR and UV transition frequencies correspond precisely to the UV transition frequencies of CN-Ne features in the B (v=0)–X (v=0) region.[7]

IR spectra of CN-Ne, such as the band seen at 4061.7(1) cm^{-1} in Figure 3, are then recorded by scanning the IR laser with the UV laser fixed on the Q-branch of an

Figure 2. UV transitions observed for CN-Ne complexes in the B (v_{CN}=0)-X (v_{CN}=2) region following IR excitation at 4061.7 cm^{-1}, which prepares the X (v_{CN}, n^K)=(2,1^1) state. The UV transitions terminate on various n^K hindered rotor states (with ΔE spacings) in the excited B (v_{CN}=0) electronic state as indicated by the energy level diagram and spectral band labels.

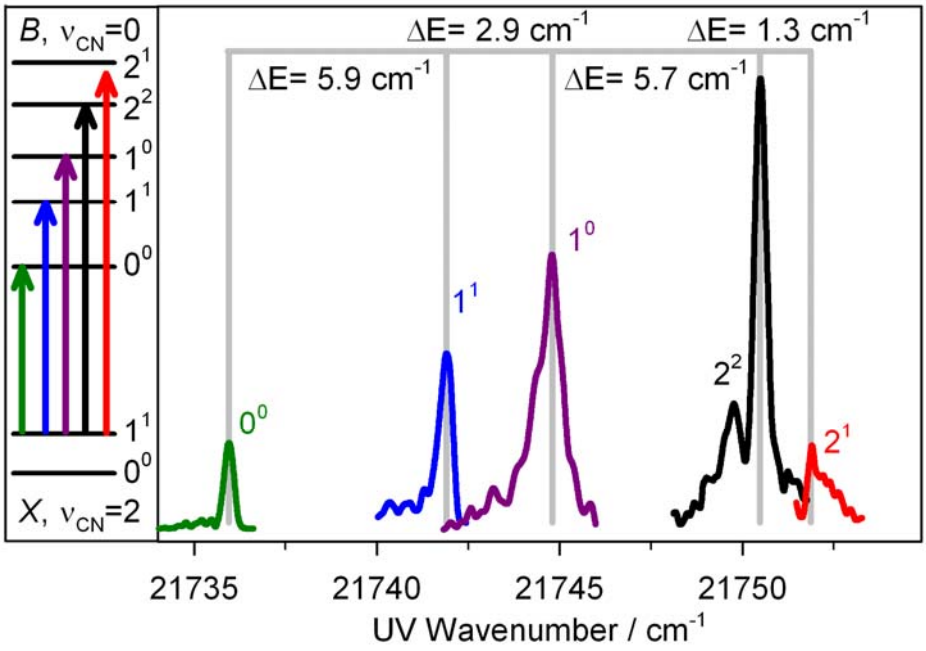
B, ν_CN=0
2^1
2^2
1^0
1^1
0^0
1^1
0^0
X, ν_CN=2
ΔE= 2.9 cm^-1
ΔE= 1.3 cm^-1
ΔE= 5.9 cm^-1
ΔE= 5.7 cm^-1
0^0
1^1
1^0
2^2
2^1
21735
21740
21745
21750
UV Wavenumber / cm^-1

Figure 3. Rotationally structured CN-Ne bands in the CN overtone region observed by IR-UV double resonance spectroscopy. The n^K hindered rotor states (and ΔE spacings) associated with the IR transitions are indicated in the energy level diagram and spectroscopic labels. The 0^0-0^0 transition (grey) is not observed in IR spectra because of Δn=±1 selection rules, but is deduced from electronic transitions (see text and Table 1).

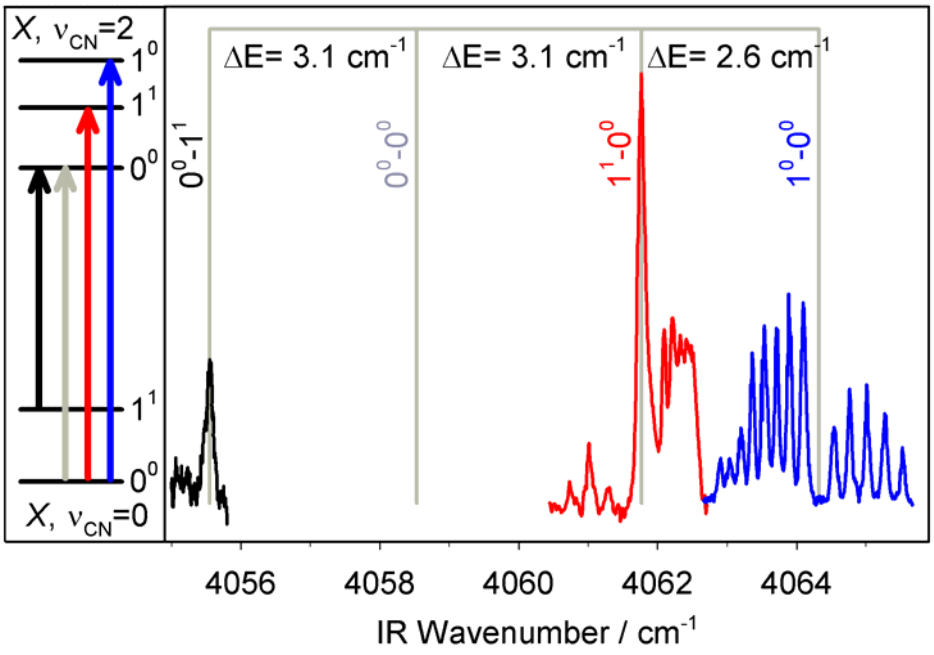
X, ν_CN=2
1^0
1^1
0^0
1^1
0^0
X, ν_CN=0
ΔE= 3.1 cm^-1
ΔE= 3.1 cm^-1
ΔE= 2.6 cm^-1
0^0-1^1
0^0-0^0
1^1-0^0
1^0-0^0
4056
4058
4060
4062
4064
IR Wavenumber / cm^-1

Table 1. Experimental CN-Ne band origins (cm^{-1}) with corresponding CN stretch and hindered rotor assignments (ν_{CN}, n^K) for IR and UV transitions in IR-UV double resonance spectra and one-photon *B*-*X* electronic transitions. Uncertainties in the band positions are consistent with the IR and UV laser bandwidths of 0.10 cm^{-1}.

IR transition	UV transition	*B*-*X* transition[a]
2045.6 ($1,1^1$-$0,0^0$)	23766.7 ($0,2^2$-$1,1^1$)	25812.3 ($0,2^2$-$0,0^0$)
4055.55 ($2,0^0$-$0,1^1$)	21745.0 ($0,1^1$-$2,0^0$)	25800.6 ($0,1^1$-$0,1^1$)
[4058.6 ($0,0^0$-$0,0^0$)][b]	21739.2 ($0,0^0$-$2,0^0$)	25797.8 ($0,0^0$-$0,0^0$)
4061.74 ($2,1^1$-$0,0^0$)	21736.0 ($0,0^0$-$2,1^1$)	25797.8 ($0,0^0$-$0,0^0$)
↓	21741.9 ($0,1^1$-$2,1^1$)	25803.7 ($0,1^1$-$0,0^0$)
↓	21744.8 ($0,1^0$-$2,1^1$)	25806.5 ($0,1^0$-$0,0^0$)
↓	21750.5 ($0,2^2$-$2,1^1$)	25812.3 ($0,2^2$-$0,0^0$)
↓	21751.9 ($0,2^1$-$2,1^1$)	25813.6 ($0,2^1$-$0,0^0$)
4064.32 ($2,1^0$-$0,0^0$)	21749.3 ($0,2^1$-$2,1^0$)	25813.6 ($0,2^1$-$0,0^0$)
6051.6 ($3,1^1$-$0,0^0$)	21884.3 ($1,2^2$-$3,1^1$)	27936.0 ($1,2^2$-$0,0^0$)

[a] Refs. 7,8.

[b] This IR transition is not allowed and not observed in the present work. See text.

Table 2. Spectroscopic constants (cm^{-1}) for CN-Ne derived from infrared overtone spectra.

	Ground state	Hindered internal rotor states	
	$(0,0^0)$	$(2,1^1)$	$(2,1^0)$
ν_0 (origin)		4061.74(10)	4064.32(10)
B_e (expt.)[a]	0.106(2)	0.093(2)	0.111(2)
B (deperturbed)		0.108(2)	0.097(2)
$\langle R^2 \rangle^{1/2}$ (Å)	3.70(4)	3.71(4)	3.92(4)
β $[(2,1^1) - (2,1^0)]$[b]			0.195(4)

[a] Rotational constants from experimental data for *e* symmetry levels.

[b] Coriolis coupling term between $(\nu_{CN}, n^K) = (2,1^1)$ and $(2,1^0)$ hindered rotor states.

electronic transition, in this case at 21750.5(1) cm^{-1}. Positioning the UV laser on the *Q*-branch is advantageous for observing rotationally structured IR spectra without scanning the UV laser. Simulation of the UV transition indicates that the *Q*-branch encompasses $N \leq 7$ rotational levels as a result of power broadening, which adds a Lorentzian component to the linewidth of 0.5 cm^{-1}. Spectra of other IR bands of CN-Ne are recorded in a similar fashion, however, in each case using different UV transitions since the IR transitions terminate on different hindered rotor states. The band origins of the IR and UV transitions used to obtain IR-UV double-resonance spectra are listed in Table 1. Varying the IR-UV time delay shows that the vibrationally activated CN-Ne complexes are long-lived, with lifetimes longer than several microseconds. The long lifetime of CN-Ne upon CN overtone excitation is consistent with slow vibrational relaxation of CN (v=2) with nonreactive partners studied previously.[26]

Figure 3 is a composite of the rotationally-structured spectra for the three CN-Ne bands observed in the CN overtone region. The position of the pure CN overtone stretch for CN-Ne, (v_{CN}=2, $n^K=0^0$)–($0,0^0$) at 4058.6 cm^{-1}, is also shown but is derived from electronic spectra (above). The IR band at 4061.7 cm^{-1} is a perpendicular transition with characteristic *P*, *Q*, *R* branch band structure, consistent with assignment as a $\Delta K = 1$ transition. The transition at 4064.3 cm^{-1} is a parallel transition displaying *P* and *R* branches, but no *Q*-branch, indicative of a $\Delta K = 0$ transition. Since the strongest infrared transitions are expected to originate from the ground state of CN-Ne *X* ($0,0^0$) and follow a $\Delta n = \pm 1$ selection rule, as inferred from allowed *P*- and *R*-lines in IR spectra of free CN, the bands at 4061.7 and 4064.3 cm^{-1} are readily assigned to upper states with ($2,1^1$) ($\Delta K =$

1) and $(2,1^0)$ (ΔK= 0), respectively. The third feature observed at 4055.6(1) cm^{-1} is attributed to a hot band since it lies to lower energy of the unobserved pure CN stretch of the complex. The *Q*-branch of the IR band is indicative of a ΔK= 1 transition, most likely due to the $(2,0^0)$-$(0,1^1)$ transition. This is validated by the sum of the IR and UV transition frequencies, 25800.6 cm^{-1}, which has previously been attributed to a *B* (ν_{CN}=0)–*X* (ν_{CN}=0) transition originating from the $(0,1^1)$ state.[7]

For a few experiments, the OPO is operated in the CN fundamental region at 4.9 μm (0.5 mJ/pulse) and the second overtone region at 1.6 μm (15 mJ/pulse). Strong IR transitions are observed for CN-Ne at 2045.6(1) and 6051.6(1) cm^{-1}, shifted 3.2(1) and 3.3(1) cm^{-1} to higher energy of the corresponding band origins for free CN, respectively. For these experiments, the UV laser is positioned on CN-Ne *B* (ν_{CN}=0)–*X* (ν_{CN}=1) and *B* (ν_{CN}=1)–*X* (ν_{CN}=3) transitions at 23766.7(1) and 21884.2(1) cm^{-1}, respectively. The sums of the IR and UV frequencies in these instances correspond to known CN-Ne *B* (ν_{CN}=0)–*X* (ν_{CN}=0) and *B* (ν_{CN}=1)–*X* (ν_{CN}=0) transitions, respectively. The similar shifts of the CN-Ne fundamental, overtone (see Figure 3), and second overtone transitions from those in free CN leads to their assignment as (ν_{CN}=1, 2, or $3,1^1$)-$(0,0^0)$ transitions. The similar shift in three spectral regions suggests that there is little change in the hindered rotor states with various degrees of CN vibrational excitation.

The rotational band structures of the IR features at 4061.7 cm^{-1} and 4064.3 cm^{-1} are not straightforward to analyze. The close proximity of the n^K=1^1 and 1^0 upper states (< 3 cm^{-1}) will likely result in sizable Coriolis coupling or other perturbations that would lead to complicated rotational structures and intensity patterns. Initial rotational analyses

Figure 4. Experimental and simulated rotational band contours for the (ν_{CN}, n^K) = ($2,1^1$) ← ($0,0^0$) (upper panel) and ($2,1^0$) ← ($0,0^0$) (lower panel) transitions. The red/blue traces are experimental spectra from IR-UV double resonance measurements, while the black traces are simulations with rotational temperature of 10 K and laser linewidth of 0.1 cm^{-1}. The simulations are based on fits to *P*- and *R*-branch lines only. Rotational assignments are shown as ticks. The dashed gray line illustrates the contour for the *Q*-branch anticipated using the same (perturbed) rotational constant for the ($2,1^1$) upper state. The experimental *Q*-branch structure is well represented (red) using the deperturbed rotational constant derived for the ($2,1^1$) upper state. The simulated line intensities are based on Hönl-London factors.

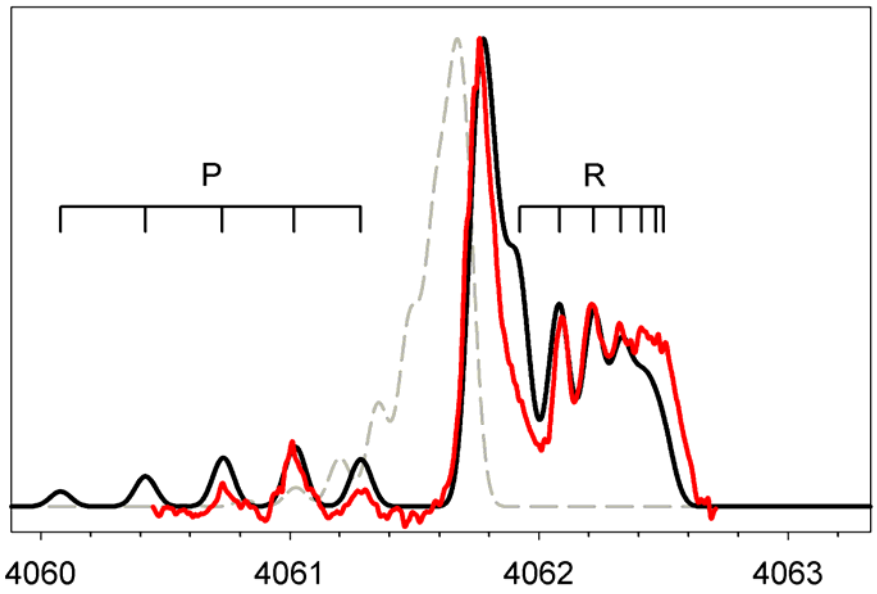
P
R
4060
4061
4062
4063

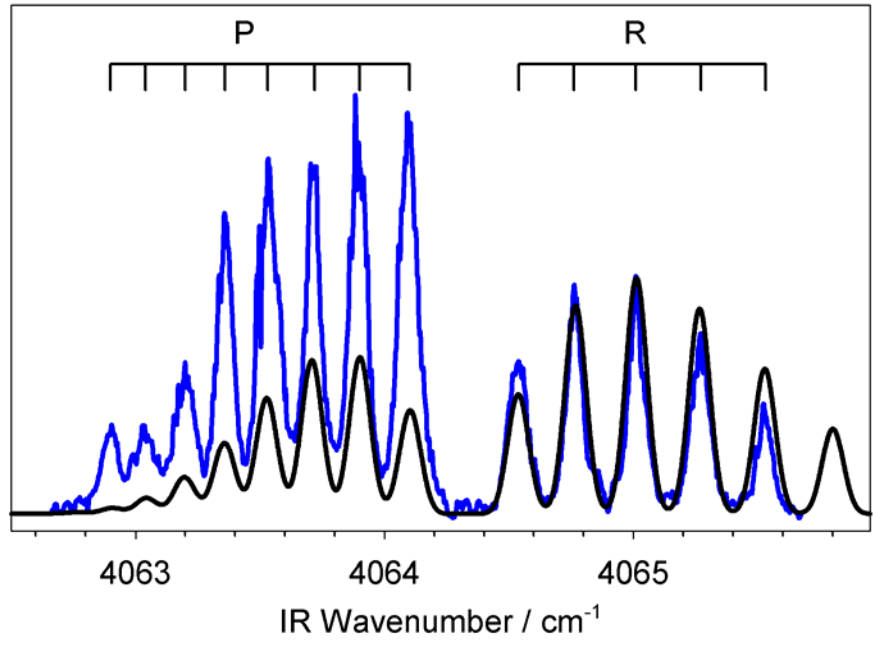
P
R
4063
4064
4065
IR Wavenumber / cm-1

of the 4061.7 cm^{-1} and 4064.3 cm^{-1} bands are carried out using the PGOPHER program for simulating rotational structure.[27] The line positions of the *P* and *R* branches in both bands are fit by floating a common ground state ($0,0^0$) rotational constant, B_{00}, the rotational constants for the two upper states ($2,1^1$ and $2,1^0$), B_{11} and B_{10}, and band origins, ν_{11} and ν_{10}, for both transitions. The unresolved *Q*-branch of the former transition is not included in the fit. The resultant spectral simulations with rotational temperature of 10 K and laser linewidth of 0.1 cm^{-1} are shown in Figure 4 and the derived constants are listed in Table 2.

Several aspects of the experimental and simulated rotational band structures shown in Figure 4 are worthy of note. The *R*-branch of the ($2,1^1$)-($0,0^0$) band at 4061.7 cm^{-1} appears congested, indicative of an *R*-branch bandhead (B_{11} □ B_{00}), suggesting that a perturbing state is pushing the rotational levels of the ($2,1^1$) state downward. In addition, the position and shading of the *Q*-branch of the ($2,1^1$)-($0,0^0$) band is dramatically different from that predicted (dashed curve in upper panel) by spectroscopic constants (Table 2) generated from analysis of the P and R branches. Furthermore, the relative intensities of *P* and *R* branch lines of the ($2,1^0$)-($0,0^0$) band at 4064.3 cm^{-1} do not match those anticipated from Hönl-London factors in the simulation (lower panel).

The preliminary rotational analysis of *P*- and *R*-branch lines yields a ground state rotational constant, B_{00}, of 0.106(2) cm^{-1}, in good accord with that reported previously based on electronic spectroscopy studies.[7,8] On the other hand, the derived upper state rotational constants, B_{11}=0.093(2) cm^{-1} and B_{10}=0.111(2) cm^{-1}, differ significantly from

the ground state value. The difference could arise from coupling between the two upper states and/or changes in the geometry of the complex as discussed below.

IV. Analysis

A. Coriolis coupling effects and deperturbation analysis

As presented in Sec. III, several aspects of the rotationally structured CN-Ne bands suggest a perturbation between the (v_{CN}, n^K) = ($2,1^1$) and ($2,1^0$) upper states. A significant body of work has been published by Nesbitt and co-workers on infrared spectra of closed-shell HX and DX (X=F, Cl)-Rg complexes in which Coriolis coupling between closely-spaced states has been used to explain very similar experimental findings.[28,29] These HX-Rg systems exhibit *J*-dependent shifts in energy levels and deviations in rotational transition strengths, which were analyzed as an *l*-doubling perturbation between intermolecular bending and/or stretching levels. A similar analysis is performed here for CN-Ne to elucidate 'deperturbed' rotational constants for the bands in question, and to account for the line positions and band shapes observed, although no effort is made here to explicitly treat the line intensities, which are a influenced both by the Coriolis coupling, and by the double resonance nature of the experiments.

The HX-Rg systems studied by Nesbitt and co-workers were treated as linear complexes, in which the lowest Σ-Σ bending transition terminates on *e* symmetry upper rotational levels (with equivalent notation of $n^K=1^0$ for the upper state); this is also the case for *P*- and *R*-branch lines of the Π-Σ band (with $n^K=1^1$ upper state). The *Q*-branch lines of the Π-Σ bending transition, however, terminate on *f* symmetry upper levels. The close proximity of the two upper states can give rise to noticeable Coriolis coupling

between *e* symmetry rotational levels, which is treated by modeling the upper state energy levels through a modified rotational Hamiltonian. The *Q*-branch of the Π-Σ transition is not perturbed.

Analogous Coriolis coupling is immediately evident in CN-Ne overtone spectra. Preliminary analysis of the transition to the $(2,1^1)$ state indicates that the upper state rotational constant for *e* symmetry levels, B_{11}, derived from *P* and *R* branch lines, is reduced relative to the unperturbed ground state value. The *Q* branch of this transition, which terminates solely on *f* symmetry levels, is not resolved and therefore cannot be used to obtain an unperturbed rotational constant for the $(2,1^1)$ state; thus, we utilize B_{00} for comparisons. Assuming the reduction in rotational constant for the 1^1 state is a result of Coriolis coupling, we deduce that the perturbing state lies higher in energy and is presumably the nearby $(2,1^0)$ state.

A complete deperturbation analysis was then undertaken using a modified rotational Hamiltonian

$$\hat{H} = \begin{pmatrix} H_{11} & H_{12} \\ H_{21} & H_{22} \end{pmatrix} \tag{1}$$

with matrix elements

$$H_{11} = \nu_{10} + B_{10}[N(N+1) - K^2] \tag{2}$$

$$H_{22} = \nu_{11} + B_{11}[N(N+1) - K^2] \tag{3}$$

$$H_{12} = H_{21} = \beta[N(N+1)]^{1/2} \tag{4}$$

where B_{10} and B_{11} are the deperturbed rotational constants for the $(2,1^0)$ and $(2,1^1)$ states, ν_{10} and ν_{11} are their respective band origins listed in Table 2. The constant β is related to

the magnitude of the Coriolis coupling. The eigenvalues for this *N*-dependent Hamiltonian are fit using a least-squares method to rotational energy levels for the $(2,1^0)$ and $(2,1^1)$ states, which were obtained from simulation of *P* and *R* branch lines described in Sec. III. All parameters except the band origins are allowed to float in the fitting procedure. Fitting the rotational energy levels in this fashion reveals a strong Coriolis coupling between the $(2,1^0)$ and $(2,1^1)$ hindered internal rotor states of CN-Ne, which are separated by only 2.6(1) cm^{-1}, with β of 0.195 cm^{-1} and deperturbed rotational constants also listed in Table 2. The deperturbation analysis shows that Coriolis coupling increases / decreases the magnitude of the experimentally observed rotational constant for the $(2,1^0)$ / $(2,1^1)$ (*f* symmetry) state by nearly 20% compared to its unperturbed value.

The rotational constants for the ground state and hindered internal rotor states, the latter following deperturbation, are then used to evaluate the average intermolecular distance, $\langle R^2 \rangle^{1/2}$, between the center-of-mass of CN and Ne using a pseudo-diatomic model. This yields an average separation distance in the ground $(0,0^0)$ state of 3.70(4) Å. The average separation in the vibrationally excited $(2,1^1)$ state is essentially unchanged at 3.71(4) Å, whereas the $(2,1^0)$ state shows a substantial increase in the average distance of 3.92(4) Å. This indicates a significant change in the properties of hindered rotor states with $n^K=1^1$ and 1^0 as discussed below.

B. Hindered rotor analysis

The IR-UV double resonance experiments reveal several hindered rotor states supported by the CN $X\,^2\Sigma^+$ (v=2) + Ne intermolecular potential, namely states with n^K = 0^0, 1^1, and 1^0. No intermolecular stretching states have been observed and thus we focus

our theoretical analysis exclusively on the angular states. In this section, we use the assignments and energy spacings of these hindered internal rotor states to deduce information about the anisotropy of the CN $X\,^2\Sigma^+$ (v=2) + Ne potential based solely on the experimental results, which is then extended to CN $X\,^2\Sigma^+$ (v=0) + Ne and compared with prior results on CN $B\,^2\Sigma^+$ (v=0) + Ne.[7] The resultant angular potentials for CN ($X\,^2\Sigma^+$, $B\,^2\Sigma^+$) + Ne are then compared with those obtained from high level *ab initio* theory in Sec. V.

The hindered rotor analysis is based on the theoretical treatment for open-shell diatom-rare gas complexes developed by Dubernet *et al.*[15] (and briefly summarized in Appendix 3), utilizing two parameters, V_{10} and V_{20}, to describe the anisotropy of the system. The parameters can be determined directly from the hindered rotor state spacings observed experimentally, and can then be inserted into the truncated Legendre polynomial

$$V(\theta) = V_{10}\cos\theta + V_{20}\left(3\cos^2\theta - 1\right)/2 \tag{5}$$

in order to model the angular intermolecular potential while neglecting any isotropic contribution.

Dubernet *et al.*[15] provide a discussion of the limits imposed on these parameters; however, certain restrictions can be derived from the experimental data alone. For example, a simple inspection of the CN-Ne X (v_{CN}=2) hindered rotor energy level spacings shows that V_{10} is closer to the limit of V_{10}=0 than V_{10}=2b (illustrated by Fig. 2 of Ref 15). Furthermore, the energy ordering of the $(2,1^1)$ and $(2,1^0)$ states indicates that V_{20}

is positive, while the larger spacing between the $(2,0^0)$ and $(2,1^1)$ states as compared to the $(2,1^1)$ and $(2,1^0)$ states limits the magnitude of V_{20} to less than 5.1 cm^{-1}. A unique solution for V_{10} and V_{20} is found within these constraints yielding values of -1.6 cm^{-1} and 4.3 cm^{-1}, respectively, which reproduce the experimentally observed energy spacings precisely. To account for the experimental uncertainty associated with measurement of the IR band origins (±0.1 cm^{-1}), we also derive a corresponding range of V_{10} and V_{20} values, specifically -2.1 to -0.8 cm^{-1} for V_{10} and 4.3 ± 0.1 cm^{-1} for V_{20}. It should be noted that sign of V_{10}, indicating a preference for Ne binding to a specific end of the CN radical, cannot be determined from the experimental methods or associated theoretical analysis used in this work and as such the sign of V_{10} is arbitrary; we assume V_{10} is negative following prior work.

The corresponding energy spacings for CN-Ne X (v_{CN}=0) were then calculated using the same values for the potential anisotropy parameters (V_{10} = -1.6 cm^{-1}, V_{20} = 4.3 cm^{-1}) and the appropriate monomer rotational constant for CN $X\,^2\Sigma^+$ (v=0). This yields an energy spacing between CN-Ne X $(0,0^0)$ and $(0,1^1)$ states, which is in excellent agreement with the only experimentally observed spacing of 3.1(1) cm^{-1}. These anisotropy parameters for the X (v_{CN}=0) state of CN-Ne differ somewhat from those reported previously, particularly for V_{20}.[7]

Repeating this analysis for CN-Ne B (v_{CN}=0), based on the n^K=0^0, 1^1, 1^0, 2^2, and 2^1 hindered rotor states observed in the B (v=0)–X (v=2) and B (v=0)–X (v=0) spectral regions, we obtain values of 8.2 cm^{-1} and 0.6 cm^{-1} for the potential anisotropy parameters

Figure 5. Potential anisotropy for CN $X\,^2\Sigma^+$ (ν_{CN}=2) + Ne as a function of intermolecular angle θ. Upper panel: The solid line indicates the effective angular potential, represented by equation (7), while the dotted and dashed lines give the individual contributions from the smaller V_{10} and dominant V_{20} terms derived from the experimental hindered rotor spacings. The grey shaded regions indicate the experimental uncertainties associated with V_{10} and V_{20}. Lower panel: The *ab initio* data points are illustrated by red crosses. The black trace is a fit to the *ab initio* data using the Legendre expansion in equation (8) with an additional isotropic component.

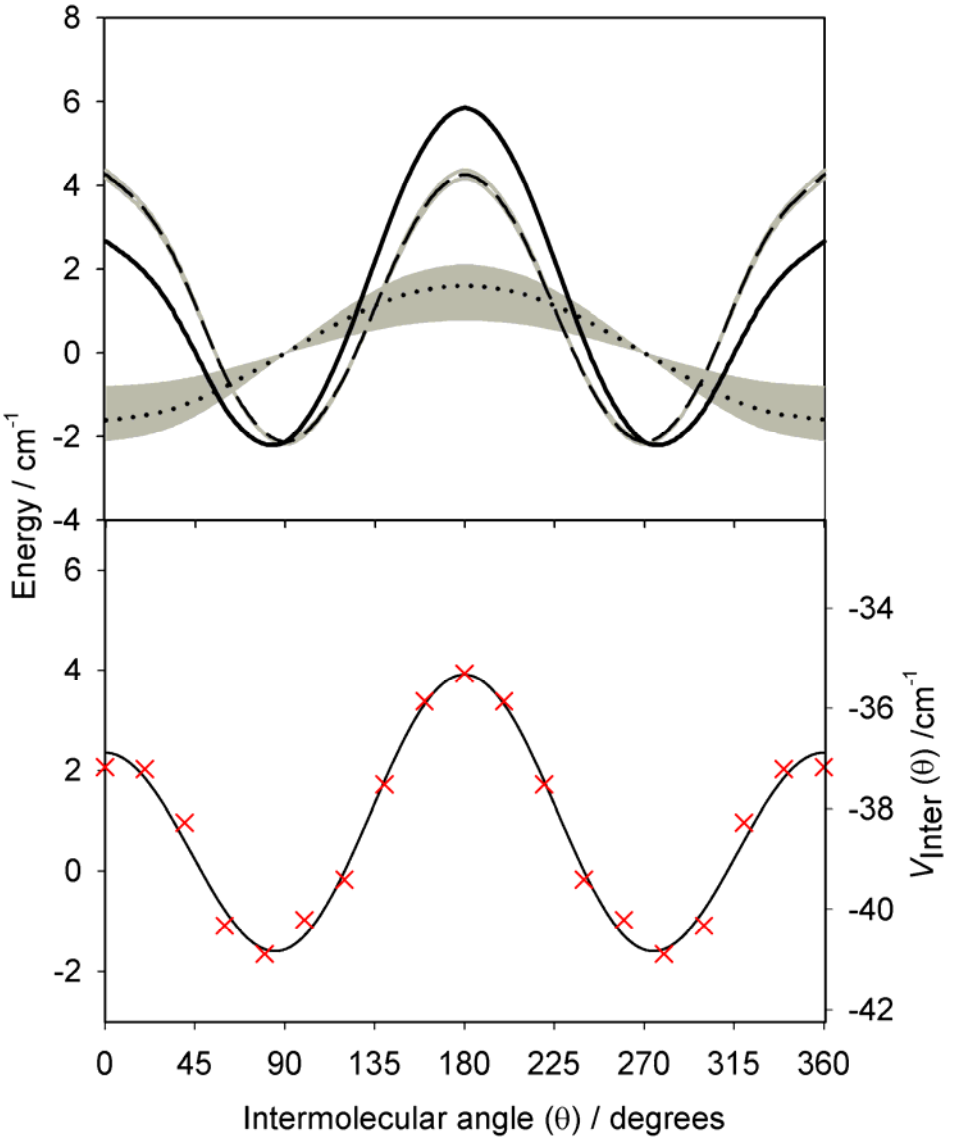
8
6
4
2
0
-2
-4
Energy / cm-1
6
4
2
0
-2
-34
-36
-38
-40
-42
VInter (θ) /cm-1
0
45
90
135
180
225
270
315
360
Intermolecular angle (θ) / degrees

Figure 6. Potential anisotropy for CN $B\ ^2\Sigma^+$ (v_{CN}=0) + Ne as a function of θ. Upper panel: The solid line indicates the effective angular potential, represented by equation (7), while the dotted and dashed lines represent the dominant V_{10} and much smaller V_{20} terms deduced from the experimental hindered rotor spacings in the excited electronic state. Lower panel: The *ab initio* data points are indicated by red crosses. The black trace is a fit to the *ab initio* data using the Legendre expansion in equation (8) with an additional isotropic component.

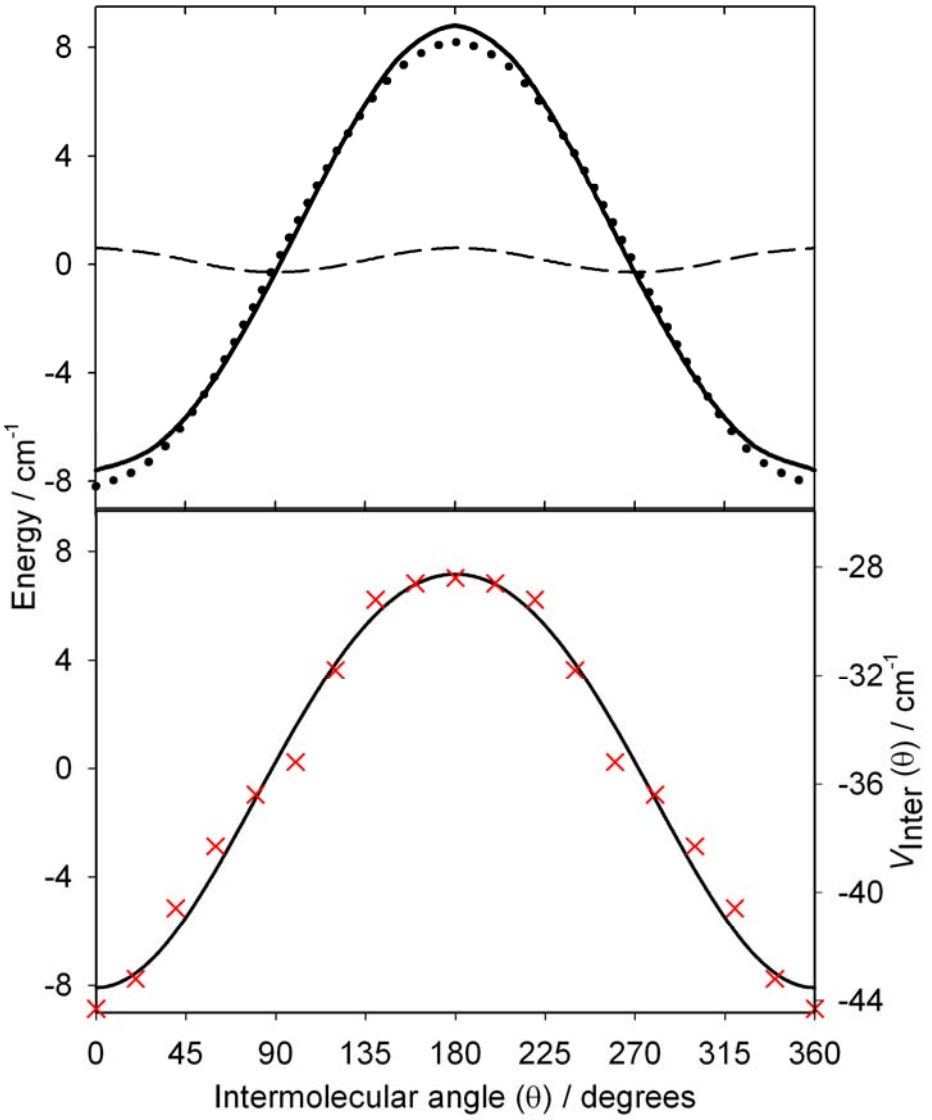
8
4
0
-4
-8
Energy / cm-1
8
4
0
-4
-8
-28
-32
-36
-40
-44
VInter (θ) / cm-1
0
45
90
135
180
225
270
315
360
Intermolecular angle (θ) / degrees

V_{10} and V_{20}, respectively. These parameters are in good accord with results from a prior analysis by Fei and Heaven.[7]

The effective angular dependence of the CN $X\,^2\Sigma^+$ (v) + Ne potential is then plotted using the truncated Legendre polynomial expansion shown in equation (5). The V_{10} and V_{20} anisotropy parameters are radially-averaged over the intermolecular distances sampled experimentally for CN X (v=2) and are consistent with the data available for CN X (v=0), where rotational analysis indicates an average CN-Ne separation of $\langle R^2 \rangle^{1/2}$ =3.70(4) Å for the ground state. $V(\theta)$ as well as the individual terms in Eqn. (5) with associated uncertainties (shown as shaded regions) are plotted in the upper panel of Figure 5. A similar graph shown in the upper panel of Figure 6 depicts the effective angular dependence of the CN $B\,^2\Sigma^+$ (v=0) + Ne potential for comparison, again neglecting isotropic contributions. The angular dependence of the potentials derived from this analysis of hindered internal rotor states of the CN-Ne complex are discussed in the following section.

V. Discussion

A. Experimental determination of potential anisotropy

The angular potential $V(\theta)$ for CN $X\,^2\Sigma^+$ + Ne, derived from the analysis of observed hindered rotor states (Sec. IV and Appendix 3) and shown in the upper panel of Figure 5, indicates that the minimum energy geometry of CN $X\,^2\Sigma^+$ + Ne is non-linear with a shallow minimum at $\theta \sim 80°$. The ground state angular potential is dominated by the V_{20} anisotropy term, although the smaller V_{10} term tips the minimum away from 90°. The barrier ($\theta \sim 0, 180°$) to internal CN rotation is only ~8 cm^{-1}, indicating a weakly

anisotropic potential close to the free rotor limit. As a result, the ground state of the CN-Ne complex will have a bent configuration on average, while undergoing wide amplitude motion in the internal bending coordinate. By contrast, the CN $B\ ^2\Sigma^+$ + Ne potential, plotted in the upper panel of Figure 6, shows that the minimum energy configuration in the excited B electronic state is linear with a somewhat higher barrier ($\theta \sim 180°$) to internal rotation of ~16 cm^{-1}. In this case, the potential anisotropy is dominated by the V_{10} term.

The anisotropy parameters and correlation diagram shown in Appendix 3, Figure A1 were generated using the CN X (v=2) monomer rotational constant. Regeneration of the correlation diagram for CN $X\ ^2\Sigma^+$ (v=0, 1, and 3) + Ne, using the appropriate CN monomer rotational constants with identical V_{10} and V_{20} anisotropy parameters, predicts 0^0 to 1^1 hindered rotor spacings in each CN spectral region. The values produced in this fashion are consistent with the spacing in each region between the experimentally observed CN-Ne 1^1 feature and the anticipated position of the 0^0 band, which is assumed to be unchanged from the CN monomer stretch. Thus, the potential anisotropy for CN $X\ ^2\Sigma^+$ + Ne shown in Figure 5 appears to be essentially unchanged for CN (v=0-4).

B. *Ab initio* MRCI potentials for CN ($X\ ^2\Sigma^+$, $B\ ^2\Sigma^+$) + Ne

Figure 7 shows 2D *ab initio* potential energy surfaces (PES) for the ground CN $X\ ^2\Sigma^+$ + Ne and excited CN $B\ ^2\Sigma^+$ + Ne electronic states, generated in the fashion described in Sec. II and Appendix 3. The ground state surface obtained using the MRCI+Q/CBS method builds on that previously reported by Yang and Alexander[12] based on MRCI+Q/aVTZ calculations with both counterpoise and size-consistency corrections.

Figure 7. CASSCF(9,8)//MRCI+Q/CBS *ab initio* potentials for the CN $X\,^2\Sigma^+$ + Ne and CN $B\,^2\Sigma^+$ + Ne electronic states. Points were generated every 0.25 Å in the radial coordinate between 3 and 4.5 Å and then at 6 Å. Radial data were produced every 20° between θ =0° and 180°. The potential energy surfaces show distinctly different minimum energy geometries. Lower panel: CN $X\,^2\Sigma^+$ + Ne displays a potential minimum at θ =80° with an R_e of ~3.5 Å and a D_e of 41 cm^{-1}. Upper panel: CN $B\,^2\Sigma^+$ + Ne exhibits a deeper potential minimum for linear CN-Ne (θ =0°) with a significantly longer R_e of ~3.75 Å and a D_e of 44 cm^{-1}.

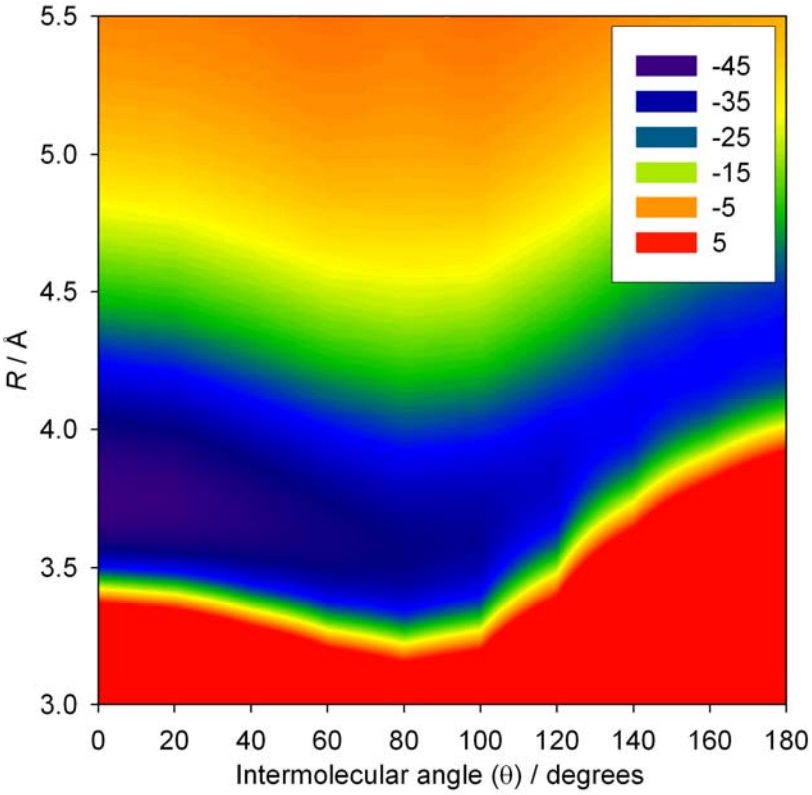
-45
-35
-25
-15
-5
5
5.5
5.0
4.5
4.0
3.5
3.0
R / Å
0
20
40
60
80
100
120
140
160
180
Intermolecular angle (θ) / degrees

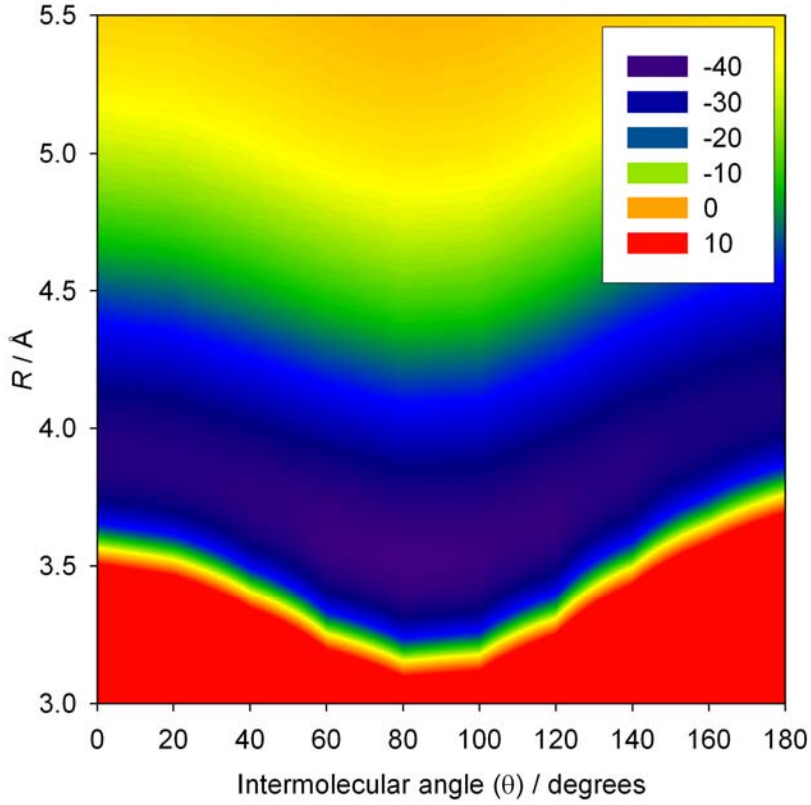
-40
-30
-20
-10
0
10
5.5
5.0
4.5
4.0
3.5
3.0
R / Å
0
20
40
60
80
100
120
140
160
180
Intermolecular angle (θ) / degrees

The *ab initio* PES generated in this work exhibits a shallow global minimum at $\theta = 80°$, consistent with the experimentally determined anisotropy for the CN $X\,^2\Sigma^+$ + Ne potential, but differs from the nearly isotropic potential with very shallow minima at linear $\theta = 0°$ and 180° configurations predicted using aVTZ basis set. Fitting a radial slice of the potential landscape to a Morse potential at the minimum energy geometry ($\theta = 80°$) yields an intermolecular distance of $R_e = 3.51$ Å and a dissociation energy of $D_e \sim 41$ cm^{-1}.

The lower panel of Figure 5 shows the angular dependence of the *ab initio* potential for CN $X\,^2\Sigma^+$ + Ne. The theoretical curve was generated by fitting the radial coordinate at fixed values of θ to a Morse potential, and thereby obtaining the minimum energy at each θ. Combining the results at each angle produces a 1D minimum energy path through the 2D intermolecular potential. This angular potential was fit to the Legendre expansion shown in equation (7) in order to evaluate theoretical anisotropy parameters, yielding V_{10} and V_{20} values of -0.8 ± 0.1 cm^{-1} and 3.2 ± 0.2 cm^{-1}, respectively, for CN $X\,^2\Sigma^+$ + Ne, where the uncertainty represents 1σ in the Legendre fitting procedure.

The *ab initio* CN $B\,^2\Sigma^+$ + Ne PES (upper panel of Figure 7) exhibits a much higher degree of anisotropy than the ground state, favoring a linear geometry (θ=0°) with $R_e = 3.76$ Å and $D_e \sim 44$ cm^{-1} evaluated in the same manner as above. Once again, a minimum energy angular path through the potential energy landscape was generated and fit to a truncated Legendre polynomial, shown in the lower panel of Figure 6. The CN $B\,^2\Sigma^+$ + Ne potential anisotropy is dominated by a V_{10} term of −7.6 ± 0.3 cm^{-1}, with

Figure 8. Hindered rotor probability distributions for the CN-Ne $(0,0^0)$, CN-Ne $(0,1^0)$ and CN-Ne $(0,1^1)$ states (red) correlating with CN $X\,^2\Sigma^+$ + Ne compared with the free rotor probability distributions (blue). The hindered rotor wavefunctions are generated from the body-fixed diagonalization of the experimental angular potential (Figure 5).

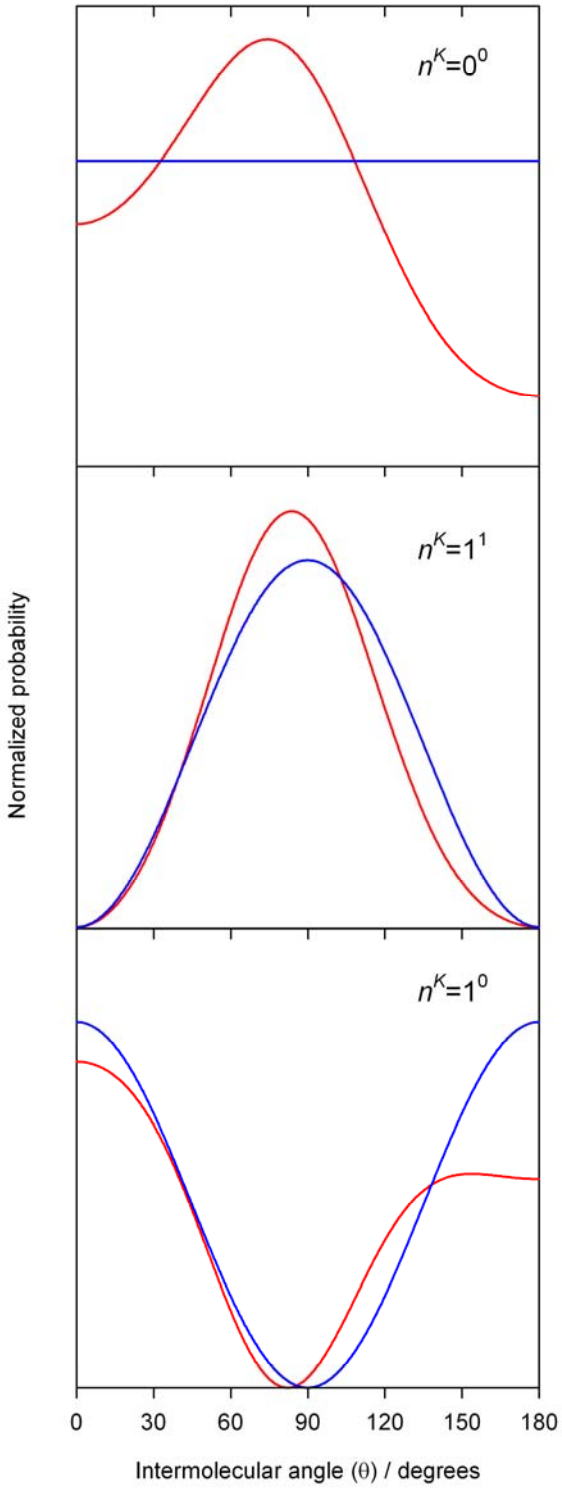
$n^K=0^0$
$n^K=1^1$
$n^K=1^0$
Normalized probability
0
30
60
90
120
150
180
Intermolecular angle (θ) / degrees

significantly less dependence on V_{20} (-0.5 ± 0.4 cm^{-1}). Figures 5 and 6 allow comparisons between the theoretical anisotropy parameters and those determined experimentally. The *ab initio* calculations reproduce the angular dependence of the CN $X\ ^2\Sigma^+$ + Ne and CN $B\ ^2\Sigma^+$ + Ne potentials remarkably well. The relative signs of the V_{10} anisotropy parameters can also be determined from these *ab initio* potentialsThe excellent agreement between experiment and theory validates these new *ab initio* potentials and the need for complete basis set extrapolation, rather than utilizing counterpoise correction and basis set superposition error approximations with small basis sets.

C. Generation of body fixed wavefunctions and implications

Wavefunctions for the hindered rotor state are produced through the diagonalization of the experimental angular potential for CN $X\ ^2\Sigma^+$ + Ne (Figure 5). Like other studies of rare-gas van der Waals complexes,[29,30] the potential is diagonalized in a body-fixed free rotor basis to give the angular eigenfunctions as a function of θ. The probability distributions for the $n^K = 0^0$, 1^1 and 1^0 levels are shown in Figure 8. In each case, the broad distributions are indicative of wide amplitude hindered internal rotor motion. The probability distribution for the 0^0 level is peaked in bent configurations slightly favoring the N-side of CN, whereas free rotor behavior samples all configurations with equal probability. The 1^0 level has maximum probability at linear Ne-CN and CN-Ne orientations, but with somewhat greater likelihood for Ne to be located on the C-side of CN compared to free rotor behavior. The 1^1 level is nearly free rotor-like with a most probable bent configuration.

The probability distributions can also be used to explain the different rotational constants (deperturbed) obtained for the CN-Ne ($2,1^0$) hindered rotor state as compared to the ($2,1^1$) and ($0,0^0$) levels (see Table 3). The rotational constant for the CN-Ne ($2,1^0$) level is some 10% smaller than those for the other two levels, indicating a corresponding increase in the Ne to CN (center-of-mass) distance for the CN-Ne ($2,1^0$) level. The longer effective bond length for the 1^0 level appears to stem from its most probable linear configuration, which differs from the 0^0 and 1^1 levels where non-linear configurations are most probable. This can be understood by examining the CN $X\,^2\Sigma^+$ + Ne *ab initio* potential (Figure 7), which shows that the optimized intermolecular bond length changes from 3.5 Å at the global minimum with $\theta = 80°$ to 3.9 Å for linear Ne-CN ($\theta = 0°$). The van der Waals interaction allows the Ne atom to get closer to C≡N center-of-mass on a sideways approach as compared to a head-on approach to either end of the CN radical. The experimentally derived average bond lengths follow this trend with 3.71(4) Å for the ($2,1^1$) level and 3.70(4) Å for the ($0,0^0$) level, which have bent configurations, and 3.92(4) Å for the ($2,1^0$) level with a linear most probable configuration.

D. Comparison with previous work

Rotational analysis of the IR-UV double resonance spectra reported in this work has afforded the re-evaluation of the CN-Ne ground state rotational constant as 0.106(1) cm^{-1}, which is in excellent agreement with the value previously reported by Fei and Heaven.[7] The weak coupling of the CN stretch to intermolecular degrees of freedom is evident in the very small shift in CN stretching frequency upon complexation, which was also noted in the previous electronic spectroscopy. The IR spectra obtained in the

fundamental, overtone, and second overtone regions (for analogous hindered rotor states) show that the CN-Ne hindered rotor band positions change very little with increasing quanta of vibration in the C-N stretching coordinate as compared with free CN stretch. The experimental spectra have also allowed the assignment of accurate anisotropy parameters for CN $X\,^2\Sigma^+$ +Ne, where V_{10} and V_{20} are -1.6 cm^{-1} and 4.3 cm^{-1}, respectively, and for CN $B\,^2\Sigma^+$ +Ne where V_{10} and V_{20} are -8.2 cm^{-1} and 0.6 cm^{-1}. These values have been determined directly from the energy spacings of hindered internal rotor states, with V_{20} for CN $X\,^2\Sigma^+$ +Ne close to the value estimated (5.1 cm^{-1}),[7] and with the excited state values in excellent agreement with those reported by Lin and Heaven.[8]

The new *ab initio* potential energy surface for CN $X\,^2\Sigma^+$ + Ne shows the weakly anisotropic ground state potential energy surface to have a non-linear minimum energy configuration, consistent with the bent minimum energy configuration predicted with MP2 methods,[13] yet contrary to the linear minimum energy geometry for the nearly isotropic potential reported by Yang and Alexander.[12] The new CN $B\,^2\Sigma^+$ + Ne potential indicates that the electronically excited state favors a linear configuration. These potentials have been used to produce minimum energy paths as a function of intermolecular angle for both ground and electronically excited states, and these are in very good agreement with those generated from the experimental hindered rotor analysis. These surfaces have also been used to determine the signs of the anisotropy parameters.

VI. Conclusions

The infrared spectrum of a weakly bound complex of the CN radical is observed for the first time, specifically for the CN-Ne complex. Infrared spectra of jet-cooled CN-

Ne are obtained principally in the CN overtone region at ~2.5 μm via an IR-UV double resonance scheme; analogous spectra are recorded in the fundamental CN stretch and second overtone regions. The IR spectra access various hindered internal rotor states of the complex with $n^K = 0^0$, 1^1, and 1^0. UV excitation in the $B\ ^2\Sigma^+$(v=0)–$X\ ^2\Sigma^+$(v=2) spectral region promotes CN-Ne to the excited B (v_{CN}=0) state. The energy difference between analogous transitions observed in the B (v=0)–X (v=2) and B (v=0)–X (v=0) regions yields the pure CN overtone stretch of CN-Ne ($n^K = 0^0$) at 4058.6(1) cm^{-1}, which is unchanged from that of free CN.

Rotationally structured bands of the CN-Ne complex are identified at 4055.55(1), 4061.74(1), and 4064.32(1) cm^{-1} upon CN overtone excitation and are assigned as follows: (v_{CN}, n^K) = $(2,0^0)$-$(0,1^1)$ (hot band), $(2,1^1)$-$(0,0^0)$, and $(2,1^0)$-$(0,0^0)$. Rotational levels of the closely spaced $(2,1^1)$ and $(2,1^0)$ states of CN-Ne X (v_{CN}=2) accessed through P-and R-branch lines in the IR spectra exhibit noticeable perturbations due to Coriolis coupling. A deperturbation analysis is carried out to extract accurate spectroscopic constants for the hindered internal rotor state and the magnitude of the N-dependent coupling.

In addition, the energetic ordering of the $n^K = 0^0$, 1^1, and 1^0 states and the spacings between them, specifically ΔE = 3.1(1) and 2.6(1) cm^{-1} for v_{CN}=2 and more limited data for other v_{CN}, provide detailed information on the angular anisotropy of the CN $X\ ^2\Sigma^+$ + Ne potential. The theoretical framework of Dubernet *et al.*[15] for open-shell diatom-rare gas complexes is utilized to construct a bending Hamiltonian and solve for its eigenvalues, which are compared with experimental spacings. The procedure is iterated

to deduce radially-averaged anisotropy parameters,

$V(\theta) = V_{00} + V_{10}\cos\theta + V_{20}\left(3\cos^2\theta - 1\right)/2$, characterizing the anisotropic portion of the intermolecular potential. The weakly anisotropic potential favors a bent CN-Ne configuration on average with only an 8 cm^{-1} barrier to internal rotation of CN, giving rise to wide amplitude motion. High-level *ab initio* calculations of the CN $X\,^2\Sigma^+$ + Ne potential were carried out for comparison with the experimentally derived potential. The angular *ab initio* potential for CN-Ne, obtained by optimizing the radial potential at each angle, is in remarkably good agreement with experiment.

References

1. R. J. Balla, K. H. Casleton, J. S. Adams, and L. Pasternack, J. Phys. Chem. **95** (22), 8694 (1991); I. R. Sims, J. L. Queffelec, D. Travers, B. R. Rowe, L. B. Herbert, J. Karthauser, and I. W. M. Smith, Chem. Phys. Lett. **211** (4-5), 461 (1993); D. L. Yang, T. Yu, N. S. Wang, and M. C. Lin, Chem. Phys. **160** (2), 307 (1992).
2. L. R. Copeland, F. Mohammad, M. Zahedi, D. H. Volman, and W. M. Jackson, J. Chem. Phys. **96** (8), 5817 (1992).
3. B. Atakan and J. Wolfrum, Chem. Phys. Lett. **186** (6), 547 (1991).
4. N. Balucani, O. Asvany, A. H. H. Chang, S. H. Lin, Y. T. Lee, R. I. Kaiser, and Y. Osamura, The Journal of Chemical Physics **113** (19), 8643 (2000).
5. Y. Georgievskii and S. J. Klippenstein, Journal of Physical Chemistry A **111** (19), 3802 (2007).
6. Y. Chen and M. C. Heaven, J. Chem. Phys. **109** (13), 5171 (1998); J. Han, M. C. Heaven, U. Schnupf, and M. H. Alexander, J. Chem. Phys. **128** (10), 104308/1 (2008).
7. S. Fei and M. C. Heaven, Proc. SPIE-Int. Soc. Opt. Eng. **1858** (Laser Techniques for State-Selected and State-to-State Chemistry), 286 (1993).
8. Y. Lin and M. C. Heaven, J. Chem. Phys. **94** (8), 5765 (1991).
9. J. Han, M. C. Heaven, and U. Schnupf, J. Chem. Phys. **128** (22), 224309/1 (2008).
10. A. L. Kaledin and M. C. Heaven, Chem. Phys. Lett. **347** (1,2,3), 199 (2001).

11. A. L. Kaledin, M. C. Heaven, and J. M. Bowman, J. Chem. Phys. **110** (21), 10380 (1999).

12. M. Yang and H. Alexander Millard, J. Chem. Phys. **107** (18), 7148 (1997).

13. I. Vrabel, V. Lukes, V. Laurinc, and S. Biskupič, J. Phys. Chem. A **104** (1), 96 (2000).

14. R. Thomson and F. W. Dalby, Can. J. Phys. **46** (24), 2815 (1968).

15. M.-L. Dubernet, D. Flower, and J. M. Hutson, J. Chem. Phys. **94** (12), 7602 (1991).

16. M.-L. Dubernet and J. M. Hutson, J. Chem. Phys. **101** (3), 1939 (1994).

17. J. M. Hutson, Advances in Molecular Vibrations and Collision Dynamics **1**, 1 (1991).

18. J. Larsen, D. Madsen, J.-A. Poulsen, T. D. Poulsen, S. R. Keiding, and J. Thogersen, The Journal of Chemical Physics **116** (18), 7997 (2002); A. C. Moskun and S. E. Bradforth, J. Chem. Phys. **119** (8), 4500 (2003).

19. R. J. Lewis, Sr., (John Wiley & Sons).

20. M. Lambert, B. Callen, H. Dugan, S. V. Filseth, F. J. Morgan, and C. M. Sadowski, Chem. Phys. Lett. **139** (1), 45 (1987).

21. M. A. O'Halloran, H. Joswig, and R. N. Zare, J. Chem. Phys. **87** (1), 303 (1987).

22. G. Herzberg, *Molecular Spectra and Molecular Structure*, Second ed. (Van Nostrand Reinhold Company, New York, 1950); F. A. Jenkins, Physical Review **31** (4), 539 (1928).

24. MOLPRO.

25. D. Cerny, R. Bacis, G. Guelachvili, and F. Roux, J. Mol. Spectrosc. **73** (1), 154 (1978).

26. R. Fei, D. E. Adelman, T. Carrington, C. H. Dugan, and S. V. Filseth, Chem. Phys. Lett. **232** (5-6), 547 (1995); K. M. Hickson, C. M. Sadowski, and I. W. M. Smith, Chem. Phys. Lett. **372** (3-4), 443 (2003).

27. PGOPHER, a Program for Simulating Rotational Structure, C. M. Western, University of Bristol, http://pgopher.chm.bris.ac.uk.

28. C. M. Lovejoy, J. M. Hutson, and D. J. Nesbitt, J. Chem. Phys. **97** (11), 8009 (1992); C. M. Lovejoy and D. J. Nesbitt, J. Chem. Phys. **91** (5), 2790 (1989).

29. M. D. Schuder, D. D. Nelson, and D. J. Nesbitt, J. Chem. Phys. **94** (9), 5796 (1991).

30. D. J. Nesbitt, C. M. Lovejoy, T. G. Lindeman, S. V. Oneil, and D. C. Clary, J. Chem. Phys. **91** (2), 722 (1989).

Chapter 5:

Insights on the CN $B\ ^2\Sigma^+$ + Ar potential from UV fluorescence excitation and IR depletion studies of the CN-Ar complex

This research has been submitted to the *Journal of Chemical Physics* and was performed in conjunction with post-doctorate Joseph M. Beames and Marsha I. Lester in the *Department of Chemistry, University of Pennsylvania*.

I. Introduction

Reactions of the cyano radical (CN) with hydrocarbons have been extensively studied due to their relevance in planetary atmospheres, interstellar media, and combustion processes.[1-4] Many of these reactions display unusual kinetic behavior including negative temperature dependencies and reaction rates approaching the gas-kinetic limit.[5] Theoretical studies have shown that the rates of such reactions depend on the presence of a barrier, its position above or below the reactant asymptote, as well as the presence of pre-reactive wells that can facilitate reaction.[6,7] Stabilizing pre-reactive complexes in these wells and interrogating them directly will help elucidate the reaction pathways. Isolating and studying CN complexes with rare gases (Ne, Ar) and simple molecular partners (H_2/D_2) provides a starting point for investigating pre-reactive complexes of CN with reactive molecular partners, including solvent molecules.[8-14]

Thus far, most experimental studies of CN-Ar have focused on electronic excitation of the complexes in the CN $A\ ^2\Pi$ - $X\ ^2\Sigma^+$ and CN $B\ ^2\Sigma^+$ - $X\ ^2\Sigma^+$ spectral regions, hereafter referred to as *A*-*X* or *B*-*X* transitions of the complex, and the ensuing dynamics on these excited electronic surfaces.[15,16] In this work, we focus on *B*-*X* laser induced fluorescence (LIF) experiments and IR-UV fluorescence depletion (FD) measurements, using the schemes illustrated in Fig. 1, which together provide new information on the CN-Ar *B*-*X* spectrum and enable assignments. To record CN-Ar *B*-*X* spectra, the complex was excited from its ground state to intermolecular levels of the CN-Ar *B* (v_{CN}=0) excited state, which undergo electronic predissociation to form predominantly

Figure 1. Laser-induced fluorescence (LIF), fluorescence depletion (FD), and IR-UV double resonance (DR) schemes for probing CN-Ar complexes are illustrated on schematic radial potentials for CN ($B\,^2\Sigma^+$, $X\,^2\Sigma^+$) + Ar. The UV laser promotes CN-Ar from its ground state to intermolecular levels in the *B* state, which undergo electronic predissociation to form vibrationally excited CN $A\,^2\Pi$ products. The long lifetime (>6 μs) and long wavelength (>600 nm) *A*-*X* fluorescence is then collected. For FD and DR measurements, the IR laser excites CN-Ar from its ground state to a hindered internal rotor level with two quanta of CN stretch. In FD, the ground state depletion of CN-Ar induced by the IR laser results in depletion of the UV LIF signal. In DR, the vibrationally excited CN-Ar complex prepared by IR excitation is further promoted to the *B* state and detected via UV LIF.

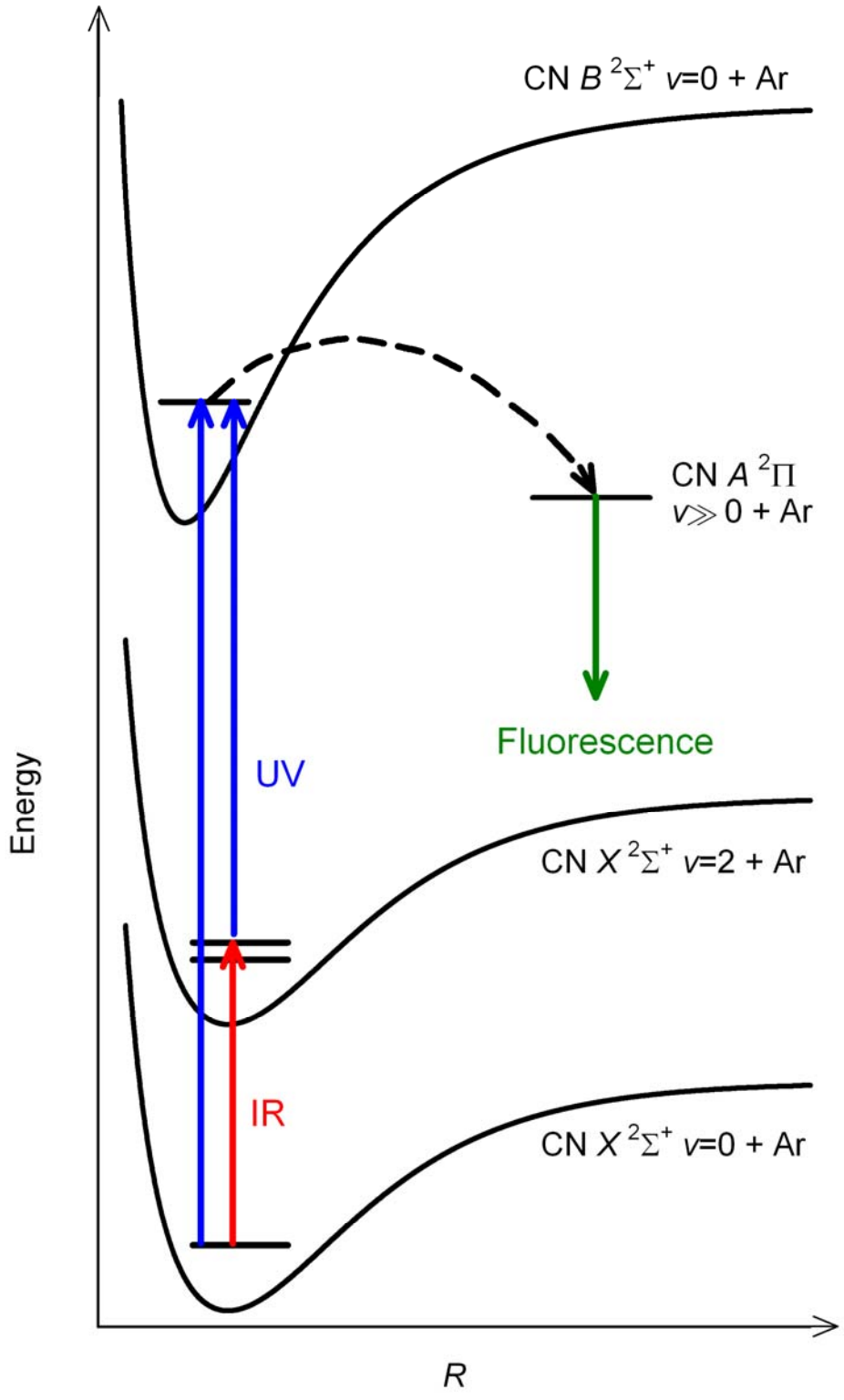
CN $B\ ^2\Sigma^+$ v=0 + Ar
CN $A\ ^2\Pi$
$v \gg$ 0 + Ar
Fluorescence
UV
IR
CN $X\ ^2\Sigma^+$ v=2 + Ar
CN $X\ ^2\Sigma^+$ v=0 + Ar
Energy
R

CN $A\ ^2\Pi$ (v=8,9) + Ar. The subsequent long lifetime (τ>6μs) and long wavelength (450-750 nm) CN *A*-*X* fluorescence was then collected as a function of excitation energy. The previously reported electronic excitation spectrum of CN-Ar exhibited a complicated pattern of bands, only a few of which were rotationally analyzed, and quantum labels were not assigned.[15] This earlier work also determined the ground state binding energy of the CN-Ar complex at $D_0'' = 102(2)$ cm^{-1}.

There have also been high level *ab initio* [RSPT2/aug-cc-pVTZ] calculations of the relevant potential energy surfaces to aid in the interpretation of the *B*-*X* electronic spectra of CN-Ar.[15,17] The CN $X\ ^2\Sigma^+$ + Ar potential is predicted to be relatively shallow with a well depth (D_e'') of ~140 cm^{-1} and an equilibrium bond length (R_e'') of ~3.8 Å, where *R* is the distance from the CN center-of-mass to Ar. The minimum energy path along the angular coordinate, θ, where θ is the angle between Ar, the center-of-mass of CN, and nitrogen, reveals that the potential is weakly anisotropic about the N≡C–Ar configuration with a barrier to CN internal rotation of ~27 cm^{-1} and $\theta_e'' \sim 130°$.[15] The potential for electronically excited CN $B\ ^2\Sigma^+$ + Ar exhibits a deeper minimum than that for CN $X\ ^2\Sigma^+$ + Ar with $D_e' \sim 260$ cm^{-1} and $R_e' \sim 3.6$ Å. The minimum energy configuration in the excited electronic state is linear C≡N–Ar ($\theta_e' \sim 0°$). The excited state surface has significant anisotropy with a barrier to CN internal rotation of ~160 cm^{-1}. The minimum energy configuration for the excited state potential differs considerably from the ground state, presumably due to the change in sign of CN dipole moment upon electronic excitation,[18] suggesting that more favorable Franck-Condon overlap will be

achieved with electronic excitation in combination with intermolecular bend and/or stretch excitation.

The CN ($X\,^2\Sigma^+$, $B\,^2\Sigma^+$) + Ar potentials are significantly different from one another and, therefore, the appropriate quantum labels for the bound states of the CN-Ar complex differ for the two surfaces.[15] In the ground electronic state, CN undergoes nearly free rotation within the complex and the appropriate quantum labels are those for hindered internal rotor states, namely n, the rotational angular momentum of CN (excluding spin), and K, the projection of n onto the intermolecular axis R, which takes on integer values of n. When including CN stretch (v_{CN}) and intermolecular stretch (v_s), the appropriate quantum labels for the ground electronic state are (v_{CN}, v_s, n^K). For the more strongly anisotropic linear CN-Ar complex in the excited B state, the correlation diagram by Dubernet *et al*. (Fig. 2 of Ref. 19) indicates that the appropriate quantum labels are those of a linear triatomic (v_{CN}, v_s, v_b^K) molecule. The angular states are denoted with a bending quantum number v_b, and its projection K on the intermolecular axis R takes on values of v_b, v_b-2, …, 0 or 1. The rotational levels of the complex in both electronic states are described by the quantum number N, the total angular momentum excluding spin, which is a good quantum number because electron spin is decoupled.[20]

This group recently demonstrated that extensive new information on the hindered internal rotor levels of the CN-Ne complex in its ground electronic state could be obtained using infrared spectroscopy, specifically IR-UV double resonance (DR), which enabled experimental characterization of the weakly anisotropic CN $X\,^2\Sigma^+$ + Ne potential.[21] The present study utilizes a related approach, IR-UV fluorescence depletion,

but for a different purpose, namely, to verify that CN-Ar features in the *B*-*X* electronic spectrum originate from a common ground state level. In this technique, IR absorption by CN-Ar depletes the ground state population, which in turn depletes the *B*-*X* laser induced fluorescence signal associated with the complex. LIF and FD methods are used to identify and/or assign new spectral features to lower energy than reported previously as well as other features attributed to the CN-Ar complex in the CN *B*-*X* (0,0) spectral region. The intermolecular levels of CN-Ar in the *B* state, accessed through the *B*-*X* transitions, are then compared with the bound states computed for the CN $B\ ^2\Sigma^+$ + Ar potential. The binding energy of CN-Ar in the excited *B* electronic state is also determined.

II. Experimental methods

Electronic and infrared spectra of the CN-Ar complex are obtained using LIF, DR, and FD methods. For these experiments, ICN vapor is entrained in a 10% Ar gas mixture with He balance at 80 psi, patterned after a previous report.[15] CN radicals are generated by the 248 nm photolysis[22] (Coherent, LPX 105i excimer laser) of ICN vapor at the throat of a pulsed supersonic expansion. The photolytically generated CN radicals associate with Ar in the collisional region of the expansion to form CN-Ar complexes, which are cooled in the ensuing expansion. The backing pressure is varied to obtain conditions that give the best binary CN-Ar complex signals. The CN-Ar complex is probed spectroscopically in the collision free region approximately 15 nozzle diameters downstream from the pulse valve orifice.

Electronic excitation in the CN $B\,^2\Sigma^+$ - $X\,^2\Sigma^+$ region is achieved using the output of a Nd:YAG (Innolas, SL600, 20 Hz, 7 ns) pumped dye laser (Radiant Dyes, Narrowscan, 0.1 cm^{-1} bandwidth) with LDS 765 dye, which is frequency doubled (Inrad Autotracker III) to produce tunable radiation from 386 to 388 nm with typical pulse energies of 2 mJ. For several experiments, a narrower linewidth is utilized from a dual grating dye laser (Continuum, ND6000, 0.08 cm^{-1}). Tunable IR radiation in the CN overtone region at ~2.5 μm is generated by an optical parametric oscillator (OPO, LaserVision) pumped by an injection-seeded Nd:YAG laser (Continuum Precision II 8000, 10 Hz, 8 ns) with typical pulse powers of 10 mJ. The frequencies of the IR and UV lasers were calibrated using a wavemeter (Coherent Wavemaster).

For FD and DR measurements, the IR laser is gently focused using a 50 cm focal length lens, where it is spatially overlapped with the unfocused UV laser. Both lasers are orthogonal to the molecular beam axis. The UV laser is typically delayed by 20 ns with respect to IR excitation for FD and DR experiments. In all types of experiments, the UV LIF is collected with f/1 optics and detected using a photomultiplier tube (PMT, ET Enterprises 9816B). Electronic excitation of CN-Ar to the *B* state results in CN $A\,^2\Pi$ - $X\,^2\Sigma^+$ fluorescence, which passes through 600 nm longpass and 650 nm shortpass filters. The signal detected at the PMT is then preamplified and displayed on a digital storage oscilloscope (LeCroy WaveRunner 44xi) attached to a PC for further analysis.

For FD and DR experiments, the IR laser pulse (10 Hz) is present for every other UV laser pulse (20 Hz) such that the signal (or background) generated by the UV laser alone can be subtracted from that resulting from both the IR and UV lasers [(IR+UV)-

UV]. For FD measurements, the percent depletion is evaluated using [(IR+UV) – UV]/UV · 100%.

III. Results

A. Electronic spectroscopy via laser-induced fluorescence studies

The LIF spectrum of CN-Ar in the *B*-*X* (0,0) region is reexamined in the present work, including scans to lower wavenumber than covered in the previous study by Heaven and coworkers.[15] The present study does not focus on the high energy extreme of the spectrum, where spectral congestion precludes assignment of features. The previous investigation ascribed a weak feature at 25901.1 cm^{-1} to the 'last bound state'.[15] The resultant UV LIF spectrum, displayed in Fig. 2, consists of series of features, many of which were observed previously. We use the empirical labels [a_i, b_i, … for i=0-3] adopted in the earlier work to identify specific features. We will reassign several of these features with rigorous quantum labels in the present work. A few of the previously identified CN-Ar features, specifically a_1, b_1, and c_1 at 25781.5, 25814.9, and 25846.2 cm^{-1}, are not observed by LIF or FD methods under the present experimental conditions. The absence of these features is discussed in Sec. C. In addition, we observe two new features at 25714.1 cm^{-1} and 25755.2 cm^{-1}, which lie to lower wavenumber than covered in the previous study, as indicated with asterisks in Fig. 2. There is also a broad underlying background in the LIF spectrum, indicated with a dashed grey line, which has been attributed to higher order CN-$(Ar)_n$ clusters by Han *et al*.[15]

The two newly observed spectral features were recorded at higher resolution (0.08 cm^{-1} dye laser fundamental) and display rotational structure as shown in Fig. 3. The

Figure 2. Laser-induced fluorescence (LIF) spectrum of CN-Ar in the *B*-*X* (0,0) spectral region. A series of CN-Ar features are observed, many of which were reported previously,[15] and are marked with ticks and empirical labels, a_i (i=2, 3), b_i (i=0, 2, 3), c_i (i=0, 2, 3), and d_i (i=0, 1); other features (a_1, b_1, and c_1) previously ascribed to CN-Ar are not observed by LIF or FD in the present work. Additional CN-Ar features marked with asterisks are observed to lower wavenumber than investigated previously. The dashed grey line is a fit to the broad underlying baseline attributed to larger CN-$(Ar)_n$ complexes.

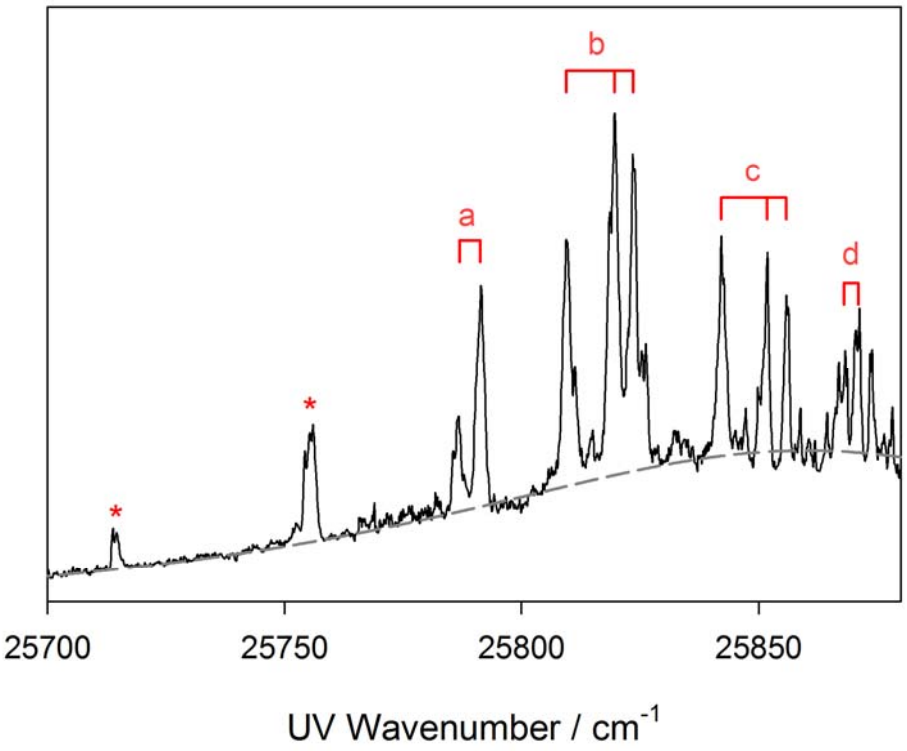
a
b
c
d
*
*
25700
25750
25800
25850
UV Wavenumber / cm-1

Figure 3. Rotational band structures and simulated contours for the newly observed CN-Ar features in the *B*-*X* (0,0) LIF spectrum. The upper panel shows the parallel band structure of the lowest energy CN-Ar feature at 25714.1 cm^{-1} assigned as a transition to the lowest (v_{CN}, v_s, v_b^K) = ($0,0,0^0$) level of the *B* state. The lower panel shows the CN-Ar feature that lies approximately 40 cm^{-1} higher, which appears to be two bands. The *R*-branch structure of the higher energy component is attributed to a parallel transition to an excited intermolecular stretch ($0,1,0^0$) of the *B* state. The lower energy component is likely to be a perpendicular transition to an excited bend ($0,0,1^1$) of the *B* state. Simulations are based on the spectroscopic constants given in Table 1 with T=1.4 K and Γ=0.18 cm^{-1}.

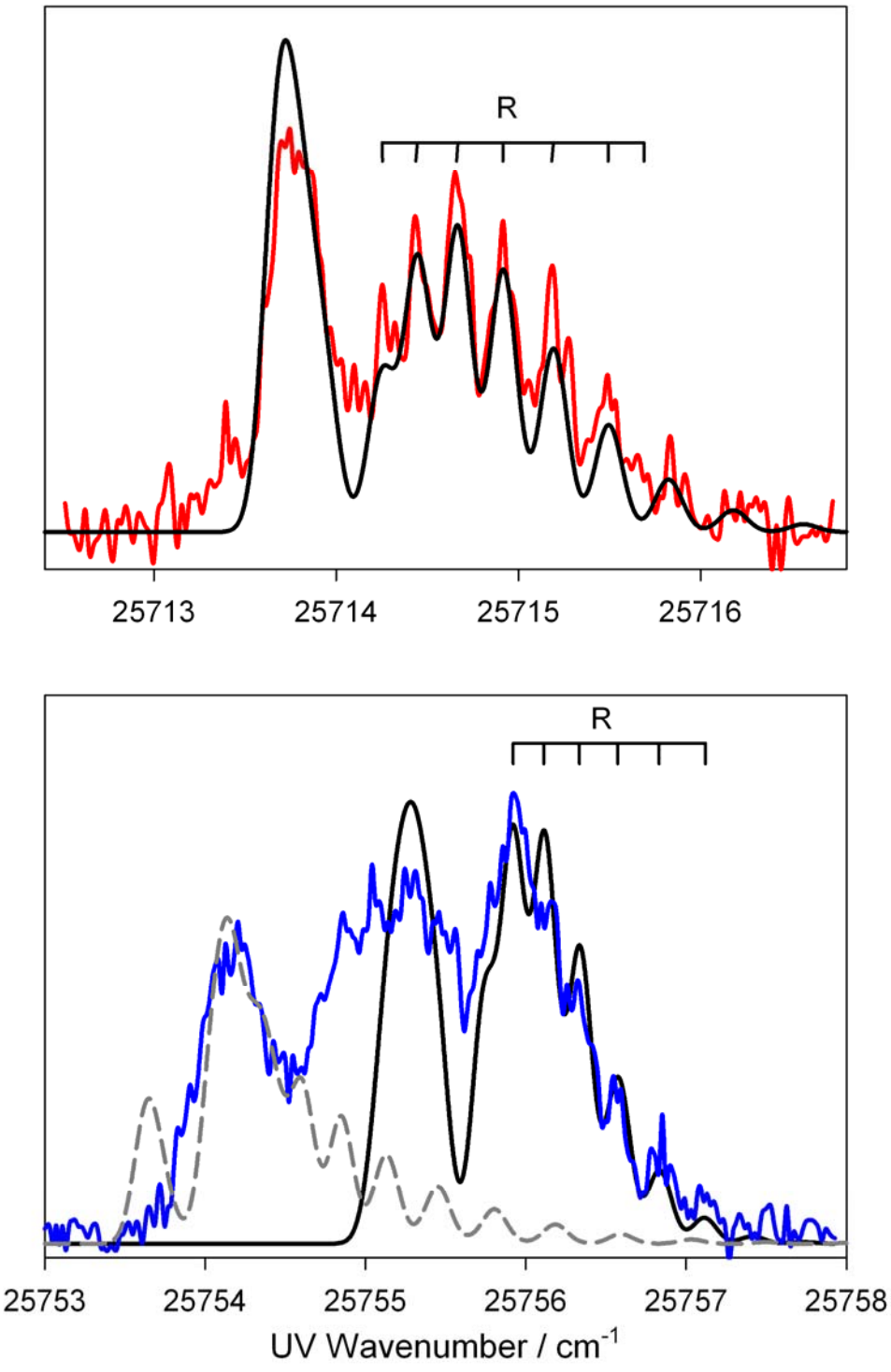
R
25713
25714
25715
25716
R
25753
25754
25755
25756
25757
25758
UV Wavenumber / cm-1

lowest energy CN-Ar feature at 25714.1 cm^{-1} is shifted 83.8 cm^{-1} to lower wavenumber of the CN *B*-*X* (0,0) monomer origin at 25797.9 cm^{-1}.[23] This feature exhibits a parallel band contour (ΔK=0) with widely spaced *R*-branch lines and a compressed *P*-branch, indicative of a significant increase in rotational constant ($B' > B''$) upon electronic excitation. The rotational band structure is analyzed and simulated using the PGOPHER program.[24] The rotational band contour is initially fit by floating the ground state rotational constant, B'', upper state rotational constant, B', band origin, ν_0, and experimental parameters (rotational temperature, *T*, and linewidth, Γ). The B'' value determined in this manner is effectively the same as that obtained from higher resolution infrared spectra of the CN-Ar complex, B_0''=0.069(2) cm^{-1}, presented in Sec. B. The excited state rotational constant is much larger at B'=0.083(2) cm^{-1}, giving rise to the asymmetric band contour with a *P*-branch band head. The results of the fit are summarized in Table 1 and shown as a simulation in Fig. 3. The corresponding average bond length for what is tentatively assigned as the lowest CN-Ar level (ν_{CN}, ν_s, ν_b^K) = ($0,0,0^0$) in the excited *B* state, $\langle R^2 \rangle^{1/2}$ = 3.59(4) Å, is deduced from B'.

The second newly observed feature centered at 25755.2 cm^{-1} exhibits three subcomponents and encompasses a larger wavenumber range (~4 cm^{-1}) than would be expected for a single band of CN-Ar (~2.5 cm^{-1}) under our experimental conditions. This suggests that more than one transition is contributing to this feature. Nevertheless, the high energy edge of the feature displays rotational structure which can be analyzed. After fixing B_0'' at 0.069(2) cm^{-1}, this rotational structure can be fit as an *R*-branch with B'=0.079(2) cm^{-1} and band origin of 25755.6(1) cm^{-1}. The fit is simulated in Fig. 3 as a

parallel band type (ΔK=0), consistent with the dip near the origin, indicating excitation to a *B* state level without bend excitation ($v_b^K=0^0$). This intermolecular level lies 41.5 cm^{-1} to higher energy of the lowest level with a corresponding average bond length of 3.68(4) Å. The nearly 0.1 Å increase in bond length suggests that this may be an excited intermolecular stretch (v_s=1) of the complex; however, one must be cautious because of possible perturbations from the neighboring level in the excited *B* state that gives rise to the lower energy portion of this feature. The latter does not exhibit resolved rotational structure; it is likely to be a perpendicular (ΔK=1) transition to an excited bend ($v_b^K= 1^1$) lying 40.0 cm^{-1} to higher energy of the lowest level. A plausible simulation is generated with B_0'' and $\Delta B \sim +0.015$ cm^{-1}. As seen in Fig. 3, the simulation (dashed grey line) overlaid with the experimental spectrum reproduces the general shape of the lower energy portion of the feature reasonably well. The closely spaced (v_{CN}, v_s, v_b^K) = ($0,0,1^1$) and ($0,1,0^0$) levels in the *B* state may be coupled, but we lack the spectral resolution in this region required to decipher any such perturbations. These tentative assignments are supported by bound state calculations for CN-Ar,[15] discussed in depth later, where an excited bend ($v_b^K=1^1$) and excited intermolecular stretch (v_s=1) are predicted to lie in close proximity to one another approximately 40 cm^{-1} above the zero-point level in the excited *B* electronic state.

B. Infrared spectroscopy via fluorescence depletion and IR-UV double resonance methods

In this section, we show that infrared excitation of the CN-Ar complex in the CN overtone region can be used to induce ground state depletion for FD studies. However,

Figure 4. IR overtone spectra of CN-Ar excited from the ground state to a hindered internal rotor level ($n^K=1^1$) with $v_{CN}=2$ obtained by fluorescence depletion (FD) and double resonance (DR) methods. The band is simulated as a perpendicular transition; note that the *P*- and *R*-lines are perturbed due to Coriolis coupling of the upper state with another nearby state.[25] A significant ground state depletion is observed on the *Q*-branch (vertical grey line), which is used for subsequent UV fluorescence depletion measurements.

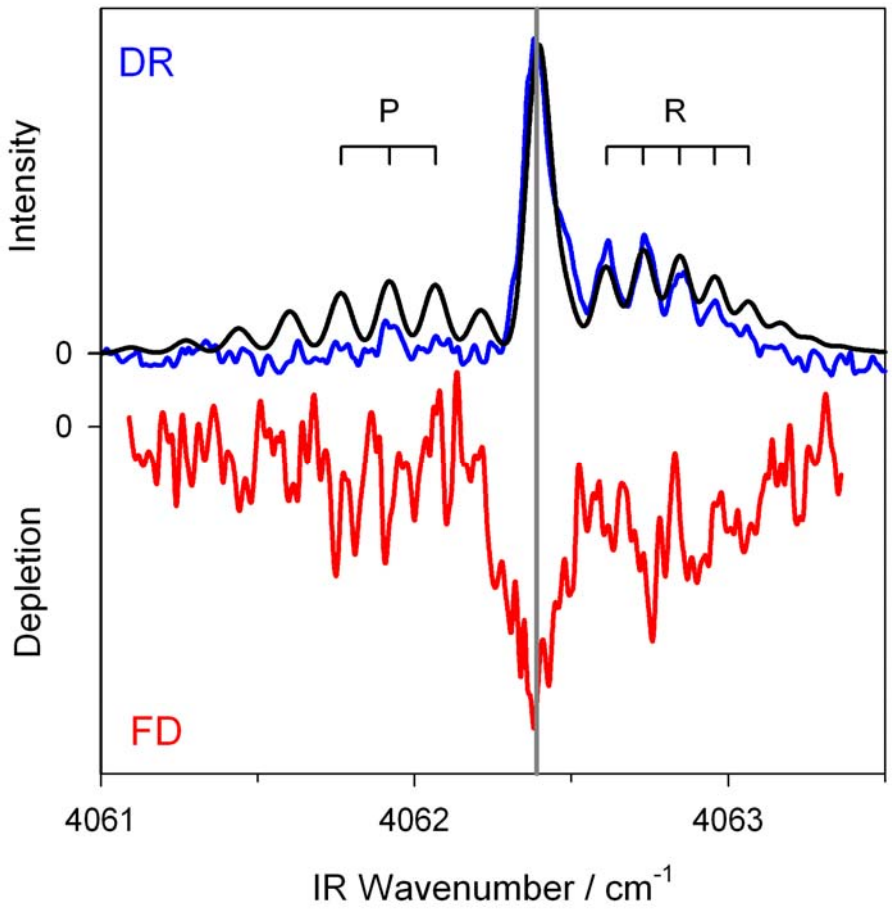
DR
P
R
Intensity
0
0
Depletion
FD
4061
4062
4063
IR Wavenumber / cm-1

the infrared transition(s) of the CN-Ar complex must first be identified. The FD method was initially tested for the CN-Ne complex, where CN overtone transitions have previously been reported by this group using IR-UV double resonance spectroscopy.[21] For CN-Ne, we pumped the *Q*-branch of the IR overtone transition at 4061.7 cm^{-1} and observed a ~10% depletion on the *R*-branch of the *B*-*X* (0,0) transition at 25797.7 cm^{-1}. For CN-Ar, we scanned the IR laser in the CN overtone region with the UV laser fixed on feature b_2 in the *B*-*X* (0,0) spectrum at 25819.6 cm^{-1}. An IR induced depletion of ~9% is observed at 4062.4 cm^{-1}, which is shifted +3.8 cm^{-1} from the origin of the overtone transition of free CN.[26] Scanning over the IR band reveals the *PQR* rotational structure of a perpendicular transition. The maximum depletion is seen for the *Q*-branch and rotational substructure is apparent in the *R*-branch as shown in Fig. 4. However, FD is not a zero background method: small percentage depletions are observed on a large LIF signal background. Nevertheless, in the next section (Sec. C), FD is used to show that the CN-Ar features observed in the *B*-*X* (0,0) region by LIF (Sec. A) originate from a common lower level, namely the lowest intermolecular level of the ground electronic state.

As shown previously for CN-Ne and demonstrated here for CN-Ar, we can achieve much higher quality IR spectra using an IR-UV double resonance technique,[21] which is essentially a zero-background method. The DR technique involves the sequential IR excitation of CN-Ar in the CN overtone region, followed by UV excitation of CN-Ar in the *B*-*X* (2,2) region. The experimental procedures, results, and analysis of IR spectra obtained using the DR method are presented in a companion paper.[27] Here,

Table 1. Spectroscopic constants for rotationally structured bands assigned in IR and UV *B*-*X* spectra of CN-Ar.

CN-Ar	ν_0 (cm^{-1})	B (cm^{-1})	$\langle R^2 \rangle^{1/2}$ (Å)
X (ν_{CN}, ν_s, n^K)			
$(0,0,0^0)$		0.069(2)	3.94(4)
		0.0690[a]	3.94[a]
B (ν_{CN}, ν_s, ν_b^K)			
$(0,0,0^0)$	25714.1(1)	0.083(2)	3.59(4)
		0.0763[a]	3.74[a]
$(0,0,1^1)$	[25754.1][b]		
$(0,1,0^0)$	25755.6(1)	0.079(2)	3.68(4)
$(0,0,2^0)$-a_2[c]	25786.9(2)	0.075(3)[c]	3.8(1)
$(0,1,1^1)$-a_3[c]	25791.3(2)	B_e 0.080(3)[c]	3.7(1)
		B_f 0.078(3)[c]	

[a] Theoretical predictions from Ref. 15.

[b] See Sec. III. A for modeling of the $(0,0,1^1)$ state.

[c] Features labeled as a_2 and a_3 in Ref. 15 were fit with B''=0.066(3) cm^{-1} and 0.069(3) cm^{-1}, respectively.

we emphasize that the 4062.4 cm^{-1} feature is attributable to CN-Ar, and is more clearly revealed using DR with the UV laser fixed at 25964.5 cm^{-1}. The IR scans of the CN-Ar feature at 4062.4 cm^{-1}, obtained using the FD and DR methods, are shown in Fig. 4. Rotational analysis of the 4062.4 cm^{-1} feature for CN-Ar yields spectroscopic constants for the ground and vibrationally excited states. The rotational constant for the ground state of CN-Ar with (v_{CN}, v_s, n^K) = (0,0,0^0) is B_0''=0.069(2) cm^{-1} (Table 1), corresponding to an average CN center-of-mass to Ar bond length, $R_0'' = \langle R^2 \rangle^{1/2}$, of 3.94(4) Å. As detailed in the companion paper,[27] the upper vibrational state of CN-Ar can be assigned as a hindered internal rotor level with (v_{CN}, v_s, n^K) = (2,0,1^1). The *P*- and *R*-lines of the upper state are perturbed by Coriolis coupling, and thus they are fit with a different rotational constant than the *Q*-branch lines.[25] The simulation shown includes the effects of Coriolis coupling.

C. Electronic spectroscopy via fluorescence depletion methods

UV FD measurements are then carried out to determine if the features attributed to CN-Ar in the *B*-*X* LIF spectrum share a common ground state level. For these FD measurements, the IR laser is fixed on the peak of the *Q*-branch of the CN-Ar transition at 4062.4 cm^{-1} (grey vertical line in Fig. 4) and the UV laser is scanned over the LIF spectrum from 25700 to 25850 cm^{-1}. As can be seen in Fig. 5, there is a one-to-one correspondence between the sharp CN-Ar features observed in LIF and FD spectra. This confirms that all of these transitions originate from the same CN-Ar ground state level, specifically, (v_{CN}, v_s, n^K) = (0,0,0^0) in the *X* state. In particular, we emphasize that the two newly observed features at 25714.1 and 25755.6 cm^{-1} at the low energy extreme of

Figure 5. Electronic spectra of CN-Ar in the *B*-*X* (0,0) region recorded by laser-induced fluorescence (LIF) and fluorescence depletion (FD) methods. The underlying broad background (dashed curve) due to higher order CN-$(Ar)_n$ complexes is subtracted from the LIF spectrum (Fig. 2). There is a one-to-one correspondence between the sharp features seen in the LIF and FD spectra, indicating that they originate from a common ground state level of CN-Ar. The lowest energy features are assigned as transitions to (v_{CN}=0, v_s, v_b^K) levels in the excited *B* state. The top axis indicates the stability of these CN-Ar levels relative to the CN $B\ ^2\Sigma^+$ + Ar asymptote.

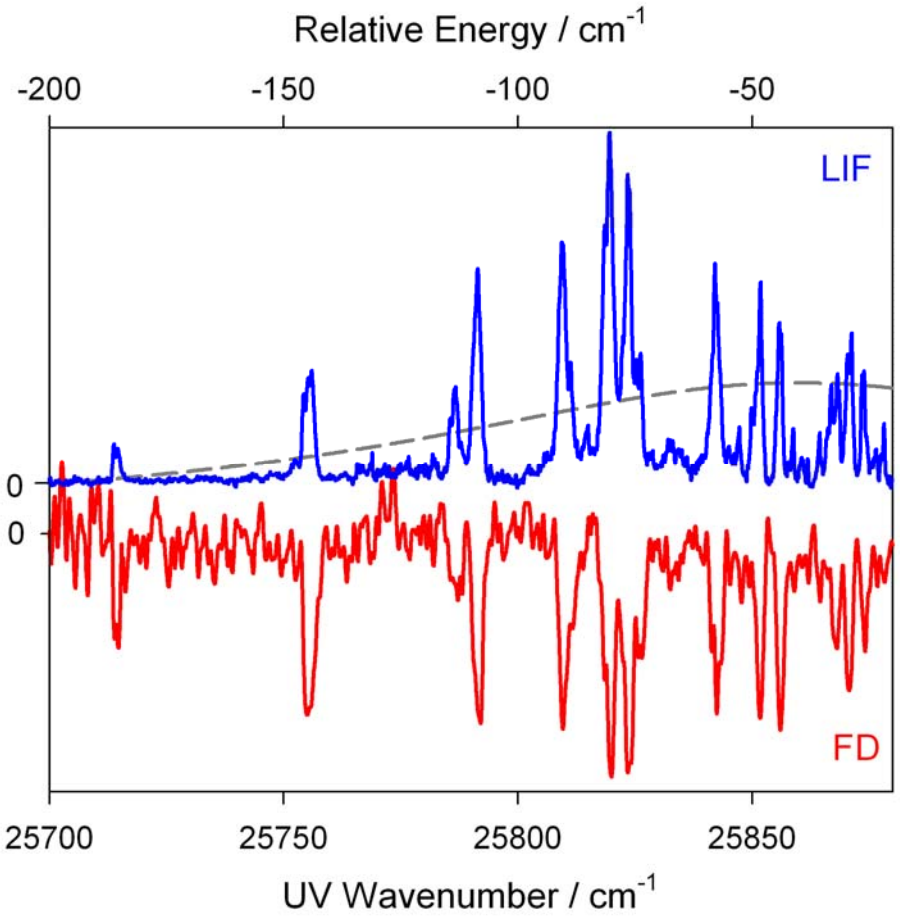
Relative Energy / cm-1
-200
-150
-100
-50
LIF
0
0
FD
25700
25750
25800
25850
UV Wavenumber / cm-1

the UV spectra are CN-Ar transitions originating from the zero-point level of the ground electronic state. Scans extending 50 cm^{-1} lower in energy revealed no additional features. Furthermore, we note that three UV transitions previously ascribed to CN-Ar, a_1, b_1, and c_1 at 25781.5, 25814.9, and 25846.2 cm^{-1}, are not observed by LIF or FD methods in this work. Thus, these three features (a_1, b_1, c_1) cannot originate from the zero-point level of the ground electronic state of CN-Ar; nor were we able to assign them as hotbands of CN-Ar. In addition, the broad background seen in LIF spectra (Fig. 2), which has been subtracted from the LIF spectrum in the upper panel of Fig. 4, is clearly not observed in the corresponding FD trace shown in the lower panel of Fig. 4, confirming that it does not originate from the binary CN-Ar complex. As stated earlier, the broad background likely stems from higher order CN-$(Ar)_n$ clusters.[15]

IV. Discussion

Laser-induced fluorescence in combination with IR-UV fluorescence depletion measurements have revealed two new *B*-*X* features that are attributed to transitions from the ground state of the CN-Ar complex. The lowest energy feature at 25714.1 cm^{-1} is ascribed as a transition to the lowest (zero-point) level (v_{CN}, v_s, v_b^K)=(0,0,0^0) in the excited *B* electronic state. With this assignment, the binding energy for CN-Ar in the excited *B* electronic state is immediately obtained, $D_0' = 186(2)$ cm^{-1}, based on its spectral shift (-83.8 cm^{-1}) from free CN and the previously determined ground state binding energy for CN-Ar, $D_0'' = 102(2)$ cm^{-1}. This experimental binding energy agrees remarkably well with that predicted theoretically ($D_0' = 183.1$ cm^{-1}),[15] providing further support for the assignment.

Figure 6. Experimentally observed CN-Ar *B*-*X* features plotted as a function of UV wavenumber (left) and energy relative to the CN $B\ ^2\Sigma^+$ + Ar dissociation limit (right). The widths of the grey bars depict the breadths of the observed UV transitions. The calculated bound states[15] based on the *ab initio* potential for CN $B\ ^2\Sigma^+$ + Ar are shown for comparison using separate columns for intermolecular levels with v_s=0 (blue) and v_s=1-3 (red).

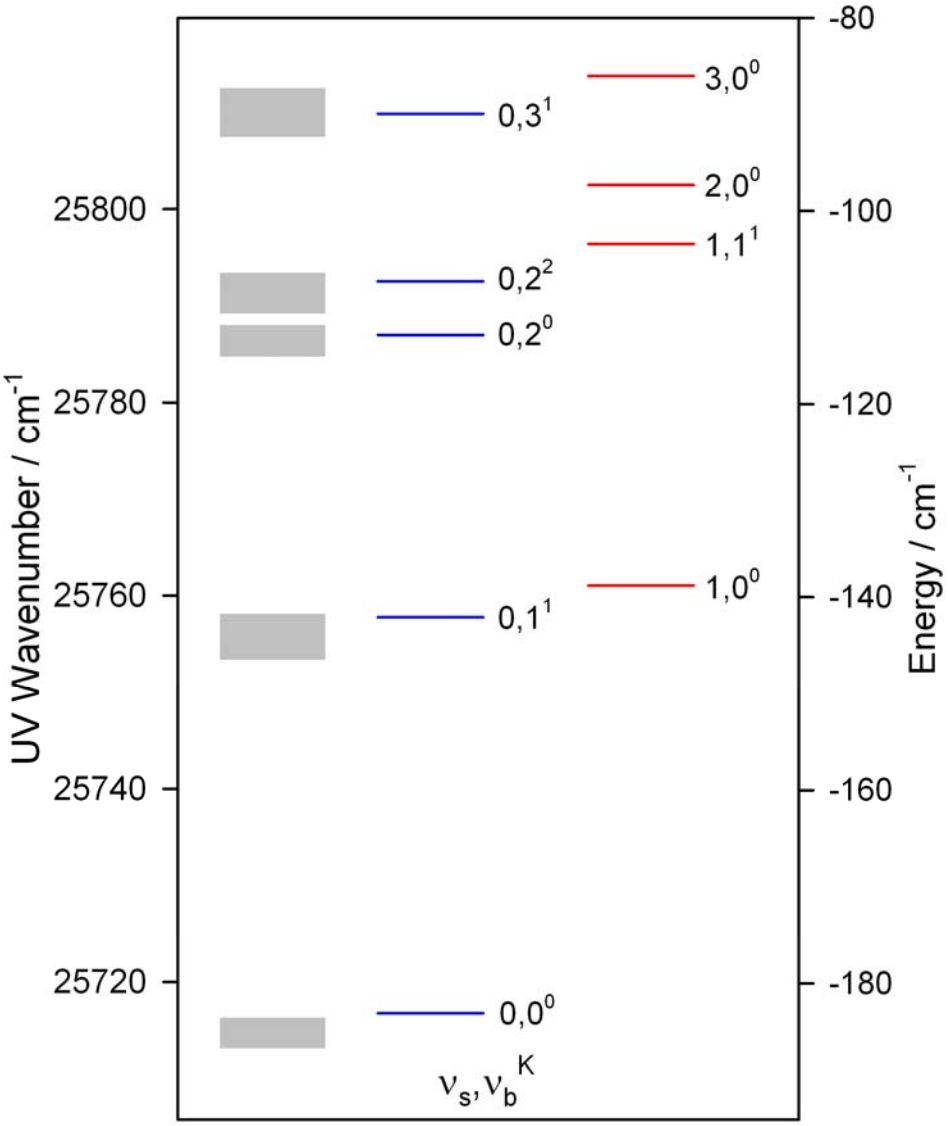
UV Wavenumber / cm-1
Energy / cm-1
25800
25780
25760
25740
25720
-80
-100
-120
-140
-160
-180
0,3^1
0,2^2
0,2^0
0,1^1
0,0^0
3,0^0
2,0^0
1,1^1
1,0^0
νs,νb K

The CN-Ar ground state binding energy combined with the CN *B*-*X* (0,0) origin indicate that the excitation energy required to reach the CN $B\ ^2\Sigma^+$ + Ar dissociation limit is 25,900(2) cm^{-1}, in accord with the 'last bound level' reported previously.[15] The UV wavenumbers for the CN-Ar *B*-*X* features observed in both LIF and FD scans (Fig. 5), originating from the common ground state, can then be converted directly into a stabilization energy of each CN-Ar level relative to the CN $B\ ^2\Sigma^+$ + Ar asymptote. These two equivalent scales are used in Fig. 6 to discuss the CN-Ar intermolecular energy level pattern in the excited *B* electronic state.

The UV wavenumbers of the CN-Ar *B*-*X* features (and corresponding stabilization energies) are displayed in Fig. 6 with the width of each bar representing the breadth of the experimentally observed feature. This is noteworthy for the feature centered at 25755.2 cm^{-1}, which we have analyzed as two overlapping bands. The bound states[15] previously computed based on the *ab initio* potential for CN $B\ ^2\Sigma^+$ + Ar are also shown in Fig. 6 for comparison, stacking intermolecular levels with v_s=0 and v_s=1-3 in two separate columns. The excellent agreement between experiment and theory for the energies of the lowest CN-Ar levels (stability greater than 100 cm^{-1}) is striking. This indicates that the lowest CN-Ar levels accessed by *B*-*X* electronic excitation are intermolecular bending levels with increasing v_b^K and/or intermolecular stretch excitation in the *B* state.

We next discuss the assignment of the lowest energy features in the CN-Ar *B*-*X* spectrum based on their UV wavenumber (or stabilization energy), rotational band structure, and transition type. The UV wavenumber of the lowest energy feature at

25714.1 cm^{-1} (-186 cm^{-1}) is assigned as a transition to the zero-point level (v_{CN}, v_s, v_b^K) = ($0,0,0^0$) of the excited *B* state with the parallel band contour leading to *K*=0 assignment. The next higher feature centered around 25755.2 cm^{-1} (-145 cm^{-1}) is attributed to partially overlapped bands arising from excitation to closely-spaced ($\Delta E \sim 1.5$ cm^{-1}) (and possibly coupled) intermolecular bend ($0,0,1^1$) and stretch ($0,1,0^0$) levels of the *B* state. The higher energy feature exhibits partial rotational structure consistent with a *K*=0 assignment. The quantum assignments are supported by the similarity of the observed energy level pattern to that predicted theoretically. Furthermore, if the true zero-point level should lie at still lower energy than reported here, which could be unobserved because of poor Franck-Condon overlap, then the resultant v_b^K level pattern would no longer be consistent with that for a linear triatomic molecule.

Experiment and theory are not in complete agreement, specifically with regard to the rotational constant B_0' and, therefore, the average intermolecular bond length $\left\langle R^2 \right\rangle^{1/2}$ = 3.59(4) Å for CN-Ar *B* ($0,0,0^0$) derived from experiment vs. a value of 3.74 Å predicted theoretically from close-coupled methods.[15] The latter differs quite significantly from R_e = 3.57 Å and R_0 = 3.60 Å evaluated for an extended Morse potential at θ=0° based on the *ab initio* data; the origin of this discrepancy is not known. In addition, we find that the intermolecular stretch observed experimentally (41.5 cm^{-1}) is approximately 7% lower in frequency than that computed theoretically (44.3 cm^{-1}). These discrepancies suggest limitations in the representation of the radial portion of the potential for CN $B\ ^2\Sigma^+$ + Ar.

The next two higher CN-Ar features at 25786.9 cm^{-1} (a_2) and 25791.3 cm^{-1} (a_3) were previously rotationally analyzed and shown to have parallel and perpendicular transition types to upper states with K=0 and 1, respectively.[15] Their corresponding stabilization energies, -113 cm^{-1} and -109 cm^{-1}, with respect to the CN $B\ ^2\Sigma^+$ + Ar limit can be compared with the predicted bound states in this energy range (see Fig. 6): (v_{CN}, v_s, n^K) = (0,0,2^0), (0,0,2^2) and (0,1,1^1) at -113, -107, and -103 cm^{-1}. As noted above, the intermolecular stretch appears to be slightly overestimated by theory, which would suggest increased stabilization for (0,1,1^1). The projection quantum number K indicates that B-X excitation is accessing the (0,0,2^0) and (0,1,1^1) upper states from the ground state zero-point level. The previous analysis of the rotational structure for a_3 was complicated due to Coriolis coupling of the upper state, now ascribed as (0,1,1^1), to another close-lying state, and distinct rotational constants were extracted for *e* symmetry levels accessed through *P*- and *R*-lines vs. *f* symmetry levels from *Q*-lines, as summarized in Table 1. Possible candidates for the perturbing state(s) to lower energy of (0,1,1^1) are (0,0,2^2) or perhaps the even lower (0,0,2^0) state. However, we lack sufficient information about the perturbing state to carry out a deperturbation analysis.

The intensity of the lowest energy features in the B-X LIF and FD spectra increases with increasing intermolecular excitation in the excited B electronic state. This provides experimental evidence of the large change in the CN-Ar potential – primarily in the angular coordinate – between the ground X and excited B electronic states. The Franck-Condon overlap from the ground state to the more strongly bound levels of CN-Ar in the excited B electronic state is poor, but increases with intermolecular bend

Figure 7. Minimum energy angular potentials for CN $X\,^2\Sigma^+$ + Ar (lower) and CN $B\,^2\Sigma^+$ + Ar (upper) derived from *ab initio* data[15] are plotted as a function of intermolecular angle θ. Superimposed on the angular potentials are the positions of the zero-point level in the ground state and intermolecular bending levels in the excited *B* state from experiment (solid) and theory (dashed). The angular states are labeled with quantum numbers n^K in the ground state and $v_b{}^K$ in the excited *B* state (see text).

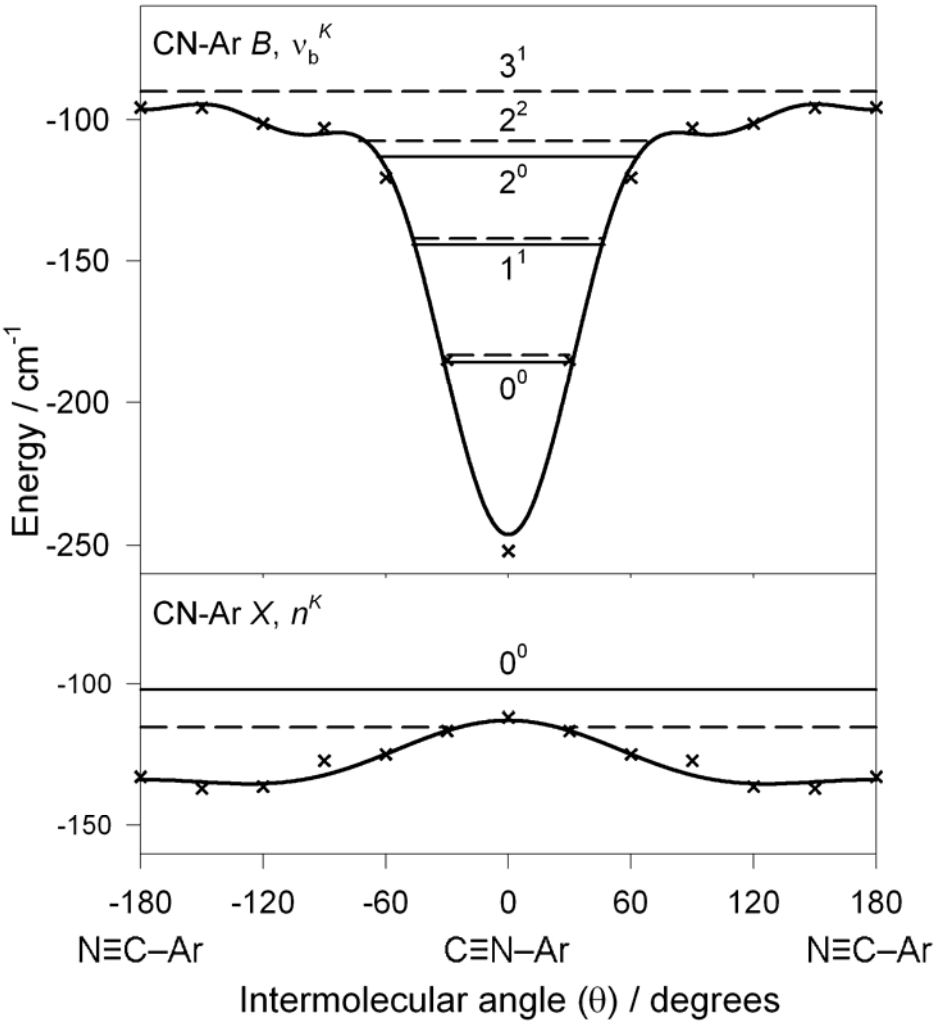
CN-Ar B, ν_b^K
3^1
2^2
2^0
1^1
0^0
-100
-150
-200
-250
Energy / cm^{-1}
CN-Ar X, n^K
0^0
-100
-150
-180
-120
-60
0
60
120
180
N≡C–Ar
C≡N–Ar
N≡C–Ar
Intermolecular angle (θ) / degrees

excitation. The large change in angular coordinate of the CN-Ar potential results from the change in sign of the CN dipole moment from the $X\,^2\Sigma^+$ to $B\,^2\Sigma^+$ state.[18]

The angular dependence of the *ab initio* potentials for CN ($B\,^2\Sigma^+$, $X\,^2\Sigma^+$) + Ar can be examined by fitting the *R*-dependent grid points at each θ (see Table III of Ref. 15) to an extended Morse form to obtain minimum energy values. These values are then used to map out minimum energy pathways as a function of θ for the *X* and *B* electronic states, which are plotted in Fig. 7. The angular potential changes from a shallow, relatively flat potential about linear N≡C–Ar ($\theta = 180°$) in the *X* state to a deeper and more strongly anisotropic potential about linear C≡N–Ar ($\theta = 0°$) in the *B* state. Superimposed on the angular potentials in Fig. 7 are the positions of the zero-point level in the ground state and intermolecular bending levels in the excited state derived from experiment (solid) and theory (dashed). Again, this illustrates the poor Franck-Condon overlap and corresponding weak intensity of transitions from the zero-point level of the ground state to the lowest intermolecular levels of the *B* state.

V. Conclusion

The CN $B\,^2\Sigma^+$ + Ar potential is experimentally characterized using UV laser-induced fluorescence and IR-UV fluorescence depletion studies of the CN-Ar complex. IR overtone excitation from the ground state to an excited (v_{CN}, v_s, n^K) = ($2,0,1^1$) hindered rotor state is used for IR-UV fluorescence depletion measurements, which provide unequivocal evidence that features assigned to CN-Ar *B*-*X* transitions originate from a common ground state level. Two new CN-Ar *B*-*X* features are seen to lower wavenumber than previously reported[15] and display rotational structure that is analyzed.

The lowest energy feature at 25714.1 cm^{-1} is assigned as a transition from the ground state to the zero-point level ($0,0,0^0$) of the excited *B* state based on the observed parallel band type (ΔK=0). A broader feature at 25755.2 cm^{-1} is attributed to two partially overlapped transitions from the ground state to the ($0,0,1^1$) and ($0,1,0^0$) intermolecular levels in the excited *B* state. With these new observations, the features previously labeled a_2 and a_3 in Ref. 15 can also be assigned to transitions from the ground state to the ($0,0,2^0$) and ($0,1,1^1$) intermolecular levels in the *B* state. The prior analysis of the rotational band structures for features a_2 and a_3 showed that these features are transitions to *K*=0 and 1 levels. The energy level pattern of these lowest CN-Ar *B*-*X* features is in good accord with the bound intermolecular levels computed for the *B* state. With observation of the zero-point level, the CN-Ar binding energy in the *B* state is also determined to be 186(2) cm^{-1}. The intensity pattern of the lowest energy features in the *B*-*X* LIF and FD spectra is explained using a Franck-Condon argument wherein the overlap of the ground state with the excited *B* state becomes more favorable with increasing amounts of bend excitation. This arises from the large predicted change in the CN ($B\,^2\Sigma^+$, $X\,^2\Sigma^+$) + Ar potentials upon electronic excitation from a weakly anisotropic potential about the linear N≡C–Ar configuration in the ground state to a more strongly bound linear C≡N–Ar structure in the excited *B* electronic state.

References

1. B. Atakan and J. Wolfrum, Chem. Phys. Lett. **186**, 547 (1991).
2. R. J. Balla, K. H. Casleton, J. S. Adams, and L. Pasternack, J. Phys. Chem. **95**, 8694 (1991).
3. L. R. Copeland, F. Mohammad, M. Zahedi, D. H. Volman, and W. M. Jackson, J. Chem. Phys. **96**, 5817 (1992).
4. I. R. Sims, J. L. Queffelec, D. Travers, B. R. Rowe, L. B. Herbert, J. Karthauser, and I. W. M. Smith, Chem. Phys. Lett. **211**, 461 (1993).
5. I. W. M. Smith, Angewandte Chemie International Edition **45**, 2842 (2006).
6. Y. Georgievskii and S. J. Klippenstein, Journal of Physical Chemistry A **111**, 3802 (2007).
7. D. Talbi and I. W. M. Smith, Phys. Chem. Chem. Phys. **11**, 8477 (2009).
8. A. C. Crowther, S. L. Carrier, T. J. Preston, and F. F. Crim, J. Phys. Chem. A **112**, 12081 (2008).
9. S. J. Greaves, R. A. Rose, T. A. A. Oliver, D. R. Glowacki, M. N. R. Ashfold, J. N. Harvey, I. P. Clark, G. M. Greetham, A. W. Parker, M. Towrie, and A. J. Orr-Ewing, Science **331**, 1423 (2011).
10. A. C. Crowther, S. L. Carrier, T. J. Preston, and F. F. Crim, J. Phys. Chem. A **113**, 3758 (2009).
11. A. C. Moskun and S. E. Bradforth, J. Chem. Phys. **119**, 4500 (2003).
12. P. A. Pieniazek, S. E. Bradforth, and A. I. Krylov, J. Phys. Chem. A **110**, 4854 (2006).

13. D. Raftery, M. Iannone, C. M. Phillips, and R. M. Hochstrasser, Chem. Phys. Lett. **201**, 513 (1993).

14. R. A. Rose, S. J. Greaves, T. A. A. Oliver, I. P. Clark, G. M. Greetham, A. W. Parker, M. Towrie, and A. J. Orr-Ewing, J. Chem. Phys. **134**, 224503 (2011).

15. J. Han, M. C. Heaven, U. Schnupf, and M. H. Alexander, J. Chem. Phys. **128**, 104308 (2008).

16. J. Han, M. C. Heaven, and U. Schnupf, J. Chem. Phys. **128**, 224309 (2008).

17. M. H. Alexander, X. Yang, P. J. Dagdigian, A. Berning, and H. J. Werner, J. Chem. Phys. **112**, 781 (2000).

18. R. Thomson and F. W. Dalby, Can. J. Phys. **46**, 2815 (1968).

19. M.-L. Dubernet, D. Flower, and J. M. Hutson, J. Chem. Phys. **94**, 7602 (1991).

20. G. Herzberg, *Molecular Spectra and Molecular Structure I. Spectra of Diatomic Molecules*, Second ed. (Van Nostrand Reinhold Company, New York, 1950).

21. J. M. Beames, B. A. O'Donnell, M. Ting, M. I. Lester, and T. A. Stephenson, J. Chem. Phys. **134**, 184308 (2011).

22. M. A. O'Halloran, H. Joswig, and R. N. Zare, J. Chem. Phys. **87**, 303 (1987).

23. H. Ito, Y. Ozaki, K. Suzuki, T. Kondow, and K. Kuchitsu, J. Mol. Spectrosc. **127**, 283 (1988).

24. *PGopher, a program for simulating rotational structure*, C. M. Western, University of Bristol, http://pgopher.chm.bris.ac.uk.

25. In a companion paper, rotational constants for *e* (B_e =0.072 cm^{-1}) and *f* (B_f =0.067 cm^{-1}) parity levels associated with the (v_{CN}, v_s, n^K) = (2,0,1^1) hindered rotor state

are derived and used here to simulate the 4062.4 cm^{-1} feature. Within this band, the *Q*-branch transitions terminate on *f* parity levels, while the *P* and *R* branch transitions terminate on *e* parity levels.

26. D. Cerny, R. Bacis, G. Guelachvili, and F. Roux, J. Mol. Spectrosc. **73**, 154 (1978).

27. B. A. O'Donnell, J. M. Beames, and M. I. Lester, J. Chem. Phys., submitted (2012).

Chapter 6:

Experimental characterization of the CN $X\ ^2\Sigma^+$ + Ar and H_2 potentials via IR-UV double resonance spectroscopy

This research has been submitted to the *Journal of Chemical Physics* and was performed in conjunction with post-doctorate Joseph M. Beames and Marsha I. Lester in the *Department of Chemistry, University of Pennsylvania*.

I. Introduction

CN radical-molecule reactions are important in many environments, including planetary atmospheres, interstellar media, and combustion, and also serve as models for fundamental reaction dynamics in polyatomic systems.[1-4] For example, CN radical reactions play an important role in the formation of CN-containing organic molecules in planetary atmospheres such as Titan, as well as the formation and destruction of NO_x in the combustion of nitrogen-containing fuels.[4] Kinetic studies[5] and, more recently, theoretical investigations[6,7] of gas-phase hydrogen abstraction reactions of CN radicals with molecular partners indicate that the rate-determining step in many cases is the formation of a weakly bound radical-molecule complex. The unusual temperature dependencies of these CN radical-molecule reactions are further explained with a low barrier separating the pre-reaction complex from products, the barrier lying slightly above or below the reactant asymptote, the latter termed a 'submerged' barrier.[6,7] In addition, complexes and/or solvent caging may play an important role in condensed phase reactions, as shown recently in CN radical interactions with solvents.[8-14] In particular, association of the CN radical with halogenated solvents in pre-reactive complexes has been postulated to explain the observed ultrafast reaction dynamics in the condensed phase.[10,11] As a result, CN radical-solvent complexes provide an important reference point for comparing reactions in gases and liquids.

The pre-reactive complexes inferred in gaseous and condensed phase studies of CN radical-molecule reactions have not yet been detected directly. To date, only weakly-bound CN radical-rare gas (Rg) and H_2-CN complexes have been observed, primarily by electronic spectroscopy in the CN $B\,^2\Sigma^+$ - $X\,^2\Sigma^+$ and CN $A\,^2\Pi$ - $X\,^2\Sigma^+$ spectral regions,[15-19]

hereafter referred to as the *B*-*X* and *A*-*X* transitions of the complex. The presence of a heavier partner is expected to quench the fluorescence from the complex, as found previously in studies of OH with molecular partners,[20] and also evident in CN-Ar by rapid $B\,^2\Sigma^+ \rightarrow A\,^2\Pi$ electronic energy transfer.[17] As a result, this group is pursuing infrared spectroscopic methods to characterize CN radical complexes with UV detection of the CN complex or photofragment, following analogous studies of OH radical complexes with molecular partners.[21-23] We have demonstrated the viability of this approach in an initial IR-UV double resonance study of the CN-Ne complex,[24] which is extended in the present work to CN-Ar and H_2-CN complexes.

Previous electronic spectroscopic studies of CN-Ar and H_2-CN revealed information on the structure and/or stability of the complexes. Electronic excitation of CN-Ar to the *B* state initiates electronic predissociation of the complex to form CN in high vibrational levels of the $A\,^2\Pi$ state. The resultant long-lived, long wavelength CN $A\,^2\Pi$ - $X\,^2\Sigma^+$ fluorescence was then collected as a function of excitation energy. Although many CN-Ar features were originally identified in the *B*-*X* electronic excitation spectrum,[17] additional features to lower wavenumber have recently been observed, rotationally analyzed, and assigned as described in a companion paper.[25] In addition, the ground state binding energy was determined previously to be D_0''=102(2) cm^{-1} utilizing optical-optical double resonance measurements. By contrast, *B*-*X* excitation of the H_2-CN complex reveals only a bound-free transition above the CN $B\,^2\Sigma^+ + H_2$ asymptote,[18] leading to CN *B*-*X* emission. The ground state binding energy D_0''=38(1) cm^{-1} was determined from the onset of the continuum by subtracting the CN *B*-*X* (0,0) origin.

High-level *ab initio* calculations have also been carried out for the CN $X\ ^2\Sigma^+$ + Rg and H_2 systems.[17,24,26] The CN + Rg potentials are evaluated as a function of two geometric parameters: the distance R between the center-of-mass of CN and the Rg atom, and the angle θ between the CN bond axis and the Rg atom, where θ =0° and 180° corresponds to CN-Rg and NC-Rg, respectively. For CN + H_2, the equivalent parameters (R,θ_1) refer to the distance and angle with respect to the center-of-mass of H_2. The CN $X\ ^2\Sigma^+$ + Ne *ab initio* calculations [MRCI+Q/CBS] indicate that the minimum energy configuration for CN-Ne is bent (θ~80°) with R_e~3.5 Å and a well depth of D_e~40 cm^{-1}. The CN-Ne potential is only weakly anisotropic with a predicted barrier to internal rotation of 6 cm^{-1}.[24] By contrast, the minimum energy configuration computed [RSPT2/aug-cc-pVTZ] for CN-Ar is slightly bent (θ~130°) with R_e~3.8 Å and a larger well depth of D_e~140 cm^{-1}.[17] In addition, the CN-Ar potential is predicted to be more anisotropic with a barrier to internal rotation of ~27 cm^{-1}. Finally, the CN $X\ ^2\Sigma^+$ + H_2 potential is computed [SDCI(D,CP)/avtz-f] to have its global minimum in a linear configuration (θ_{1e}~0°) with R_e~3.9 Å and D_e~100 cm^{-1}.[26] Calculations indicate that *ortho*-H_2 will be more strongly bound to CN than *para*-H_2 by ~11 cm^{-1} (ΔD_0). Given that the nuclear spin statistics also favor *ortho*-H_2 (*ortho*:*para* = 3:1) in normal H_2, one can anticipate that *ortho*-H_2-CN will be more readily formed than *para*-H_2-CN at low temperatures.

The infrared spectrum of the CN-Ar complex is expected to be similar to that reported recently for the CN-Ne complex,[24] since both CN $X\ ^2\Sigma^+$ + Rg potentials have shallow wells with weak anisotropies. For CN-Ne (v_{CN}=2), hindered internal rotor levels

(n^K= 1^1 and 1^0) of the complex were observed in the CN overtone region and the lowest n^K= 0^0 level was detected by UV spectroscopy. The energetic ordering and spacings of the hindered rotor levels were used for direct experimental determination of the angular anisotropy of the CN $X\ ^2\Sigma^+$ + Ne potential, revealing a small barrier of only ~8 cm^{-1} to free rotation of CN within the complex. In addition, the minimum energy configuration was found to be bent (θ~80°), agreeing well with *ab initio* calculations [MRCI+Q/CBS].

Building on the previous study of CN-Ne, we adopt the same quantum labels for CN-Ar using ($v_{CN,}$ v_s, n^K) to denote the CN stretch (v_{CN}), intermolecular stretch (v_s), and hindered internal rotor (n^K) level. Here, *n* refers to the rotational quantum number of CN and *K* is its projection onto the intermolecular axis. The rotational levels of CN-Ar are denoted with *N*, referring to the total angular momentum excluding spin, which is a good quantum number as electron spin is decoupled.[27] For H_2-CN, the appropriate quantum labels are $\left(v_{CN}, j_{H_2}, K, v_s\right)$,[26] where j_{H_2} refers to *para*- or *ortho*-H_2 and *K* is the projection of the total angular momentum excluding spin onto the intermolecular axis. (Note that *n* is not a rigorous quantum number for *ortho*-H_2-CN or its IR transitions.)

This work focuses on infrared spectroscopy of CN-Ar and, to a lesser extent, H_2-CN complexes using an IR-UV double resonance scheme. Various intermolecular states of the complexes are identified with two quanta of CN stretch (v_{CN}=2) in transitions originating from their ground states (v_{CN}=0). The ordering, spacings, and rotational structure of hindered internal rotor states of CN-Ar provide new information on the CN $X\ ^2\Sigma^+$ + Ar potential. The experimental results are compared with ground state parameters deduced from prior electronic spectroscopy studies[17] as well as properties of the *ab initio*

potential for CN $X\ ^2\Sigma^+$ + Ar.[17] For H_2-CN, experimental observations are compared with the results of previous bound state calculations carried out on *ab initio* potentials.[26]

II. Experimental Methods

In this study, an IR-UV double resonance technique is used to record IR spectra of the CN-Ar complex in the CN overtone region. As shown in Fig. 1, an IR laser is used to excite CN-Ar from its ground vibrational state to a hindered internal rotor level of the complex with CN (v_{CN}=2). A UV laser subsequently promotes CN-Ar from this hindered rotor state to the excited B (v_{CN}=2) vibronic state. The CN-Ar complex then undergoes electronic predissociation to form highly vibrationally excited CN $A\ ^2\Pi$ products, from which A-X fluorescence is collected.

To form CN-Ar complexes, ICN precursor is synthesized as described previously[14,28] and entrained in carrier gas (80 psi, 10% Ar/He). The ICN vapor is introduced into a vacuum chamber via a pulsed valve nozzle where it is photolyzed at the throat of a supersonic expansion with a KrF (248 nm) excimer laser (Coherent, LPX 105i) to form I/I* + CN.[29] The CN radicals then associate with Ar in the carrier gas to form the CN-Ar complex, which is subsequently cooled via collisions in the ensuing expansion. The expansion conditions are optimized for producing binary CN-Ar complexes, while minimizing formation of larger CN-$(Ar)_n$ clusters. At a distance of ~15 nozzle diameters downstream, the CN-Ar complex is interrogated with counterpropogating IR and UV beams. For a few experiments, ArF (193 nm) excimer photolysis is utilized with the UV probe laser only.

Tunable IR light with a bandwidth of 0.10 cm^{-1} is generated using an optical parametric oscillator (OPO, LaserVision) pumped by an injection-seeded Nd:YAG laser

Figure 1. IR-UV double resonance method is illustrated on schematic radial potentials for CN ($X\ ^2\Sigma^+$, $B\ ^2\Sigma^+$) + Ar. The IR laser excites the CN-Ar complex from its ground state to hindered internal rotor levels with two quanta of CN stretch (v_{CN}=2). The UV laser subsequently promotes vibrationally excited CN-Ar to the excited B (v_{CN}=2) electronic state of the complex. CN-Ar then undergoes electronic predissociation to form vibrationally excited CN $A\ ^2\Pi$, which give rise to A-X fluorescence. Upon photolysis at 193 nm, CN-Ar X (v_{CN}=2) can also be observed directly in the expansion (without IR excitation) and is probed on B-X (2,2) transitions, denoted as UV′.

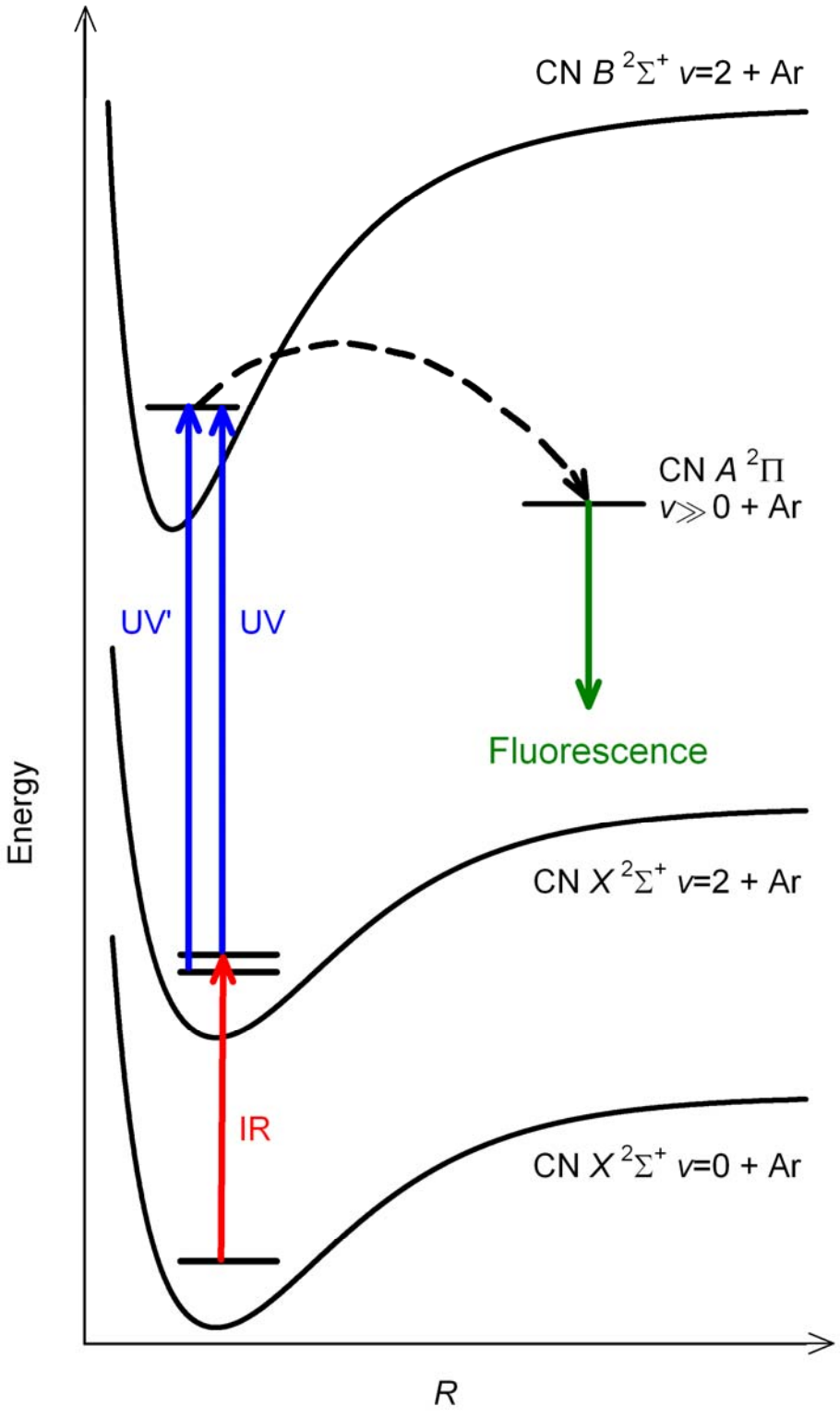
CN $B\ ^2\Sigma^+$ v=2 + Ar
CN $A\ ^2\Pi$
$v \gg 0$ + Ar
UV'
UV
Fluorescence
CN $X\ ^2\Sigma^+$ v=2 + Ar
IR
CN $X\ ^2\Sigma^+$ v=0 + Ar
Energy
R

(Continuum Precision II 8000, 10 Hz, 8 ns). It is operated in the CN overtone region at ~2.5 μm with typical pulse powers of 10 mJ. The UV radiation is generated by frequency doubling (Inrad Autotracker III) the output of a Nd:YAG (Innolas, SL600, 20 Hz, 7 ns) pumped dye laser (Radiant Dyes, Narrowscan), which operates in the vicinity of the *B-X* (0,0), (2,2), and (2,0) regions at approximately 388, 385, and 333 nm, respectively. Both IR and UV lasers were frequency calibrated using a wavemeter (Coherent Wavemaster). The IR laser is gently focused into the center of the molecular beam using a lens with a focal length of 50 cm. The unfocused but collimated UV laser is spatially overlapped with the IR laser and delayed 20 ns after the IR pulse. The resulting laser induced fluorescence is collimated using f/1 optics and passes through a series of filters optimized for collection of CN *A-X* fluorescence (600 nm longpass filter and 650 nm shortpass filter). The light then impinges on a photomultiplier tube (ET Enterprises 9816B) after which the signal is preamplified and displayed on a digital storage oscilloscope (LeCroy WaveRunner 44xi) attached to a PC for further analysis.

The IR laser pulse (10 Hz) is present for every other UV laser pulse (20 Hz) such that the signal generated by the UV laser alone (background) can be subtracted from that resulting from both the IR and UV lasers [(IR+UV)-UV]. This active background subtraction procedure is used in acquiring all spectral data presented herein. Two different scanning procedures are employed to record IR spectra. In constant energy sum scanning (CESS), the IR and UV lasers are scanned simultaneously in opposite directions such that the frequency sum of the IR and UV lasers remains constant. This technique is used in initial scans to find IR spectral features of the CN-Ar complex. After IR features

are identified, the UV laser is fixed, while the IR laser is scanned to record rotationally resolved spectra.

In a few experiments, a 30% H_2 in He carrier gas (100 psi) is used to record the first infrared spectra of the H_2-CN complex. The experimental procedures are the same for H_2-CN except that the complex is detected by UV excitation to the CN $B\,^2\Sigma^+$ (v=2) + H_2 dissociation limit, resulting in CN *B*-*X* (2,1) fluorescence at ~420 nm. The fluorescence is collected using a 420 nm bandpass filter in combination with a 400 nm longpass filter to block scatter from the UV probe laser.

III. Results

A. IR overtone excitation of CN-Ar

Using 193 nm photolysis, CN-Ar complexes with two quanta of CN vibrational excitation (v_{CN}=2) are readily detected without IR excitation, as seen previously for CN-Ne complexes.[24] Electronic spectra recorded in the *B*-*X* (2,2) region display several features readily attributable to CN-Ar, which correlate with similar features previously reported in the *B*-*X* (0,0) region and denoted as b_0, b_2, b_3, c_0, and c_2 in Ref. 17. We show in a companion paper that these CN-Ar features in the *B*-*X* (0,0) region originate from a common ground state level with n^K=0.[25] Spectra recorded in the *B*-*X* (2,0) region reveal only the two largest features, denoted as b_0 and b_2 in the *B*-*X* (0,0) region, centered at 30017.7 cm^{-1} and 30026.9 cm^{-1}. Many more CN-Ar features and stronger overall signal levels are observed in the *B*-*X* (2,2) region, which is likely a result of the more favorable Franck-Condon overlap for diagonal transitions in the CN stretching coordinate. Comparison of features b_0 and b_2 in the *B*-*X* (2,2) region, centered at 25959.2 cm^{-1} and 25968.4 cm^{-1}, respectively, with those in the *B*-*X* (2,0) region, yields the pure CN

overtone stretch of CN-Ar at 4058.5(2) cm^{-1}. This corresponds to two quanta of CN stretch with no intermolecular excitation (v_{CN}, v_s, n^K) = (2,0,0^0) in the ground electronic state. This value is essentially the same as the monomer CN overtone transition[30] at 4058.55 cm^{-1} and indicates that the binding energy of CN-Ar is unchanged with CN stretch excitation. Additional detail on determination of the pure overtone transition of CN-Ar is given in Appendix 4, including spectra shown in Fig. A1 of CN-Ar in the *B*-*X* (0,0), (2,2), and (2,0) regions.

IR-UV double resonance spectra of CN-Ar are recorded using 248 nm photolysis, eliminating the UV-only signal originating from vibrationally excited CN-Ar (v_{CN}=2). Survey scans are obtained using the CESS method with the sum of the IR and UV laser wavenumbers set at 30026.9 cm^{-1}, corresponding to the largest CN-Ar feature (b_2) in the *B*-*X* (2,0) electronic spectrum. The two lasers are simultaneously scanned, covering a 20 cm^{-1} region in the infrared between 4058 and 4078 cm^{-1}. The pure CN overtone transition is not observed, as expected, due to the $\Delta n = \pm 1$ selection rule for IR transitions between hindered internal rotor states of the complex. An IR feature centered at 4062.4 cm^{-1} is observed, which displays a strong *Q*-branch, along with *P*- and *R*-branch structure, indicative of a perpendicular transition. A smaller IR feature is also found centered about 4065.0 cm^{-1} with *P* and *R* rotational structure, but no *Q*-branch, of a parallel band type. The vibrationally excited CN-Ar (and H_2/D_2-CN) complexes with (v_{CN}=2) are long-lived with lifetimes greater than several microseconds.

The IR laser promotes CN-Ar to different hindered internal rotor states, as evident from their transition frequencies and band types. The best signal-to-noise ratios for the two IR bands were found using different UV transitions in the *B*-*X* (2,2) region. For the

lower feature at 4062.4 cm^{-1}, the UV laser was fixed at 25964.5 cm^{-1} [IR+UV = 30026.9 cm^{-1} (b_2)], while for the higher energy feature at 4065.0 cm^{-1}, the UV laser was fixed at 25941.1 cm^{-1} [IR+UV = 30006.1 cm^{-1} (a_3)]. The rotationally resolved IR spectra of hindered rotor states of the CN-Ar complex, obtained using this IR-UV double resonance method, provide an abundance of new spectral information on the complex in its ground electronic state.

Figure 2 shows a compilation of the two CN-Ar features observed in the CN overtone region as well as the position of the unobserved pure CN overtone stretch of the complex at 4058.5 cm^{-1} derived from electronic spectra (described above). The CN-Ar feature at 4062.4 cm^{-1} lies 3.9 cm^{-1} to higher energy and is assigned as a transition originating from the ground state (v_{CN}, v_s, n^K) = ($0,0,0^0$) and terminating on the ($2,0,1^1$) hindered rotor state based on the $\Delta n = +1$ selection rule and its perpendicular band type (ΔK=1 transition).[25] The CN-Ar feature at 4065.0 cm^{-1} lies an additional 2.6 cm^{-1} to higher energy and is assigned as a transition from the ground state ($0,0,0^0$) to the ($2,0,1^0$) hindered rotor state based on its parallel band type (ΔK=0 transition).

Although the IR features are relatively straightforward to assign based on their band contours, the rotational structures (shown in Fig. 3) of these closely spaced bands are much more difficult to analyze. The close proximity of the $n^K = 1^0$ and 1^1 upper states (< 3 cm^{-1}) is expected to result in Coriolis coupling, as seen previously for CN-Ne, which would lead to complicated rotational structures and intensity patterns. Initial rotational analyses are carried out using the PGOPHER program.[31] The line positions of the *P*- and *R*-branches in both bands are fit simultaneously by floating a common ground state rotational constant, B_{00}, the rotational constants for the upper states, B_{11} and B_{10}, and band

Figure 2. Rotationally structured CN-Ar bands in the CN overtone region observed using IR-UV double resonance spectroscopy. The n^K hindered rotor states associated with the IR transitions, along with their ΔE energy spacings, are labeled on the spectra and energy level diagram. The pure overtone (0^0-0^0) transition, indicated with a grey line, is not observed due to IR selection rules, but can be deduced from CN-Ar electronic transitions (see text).

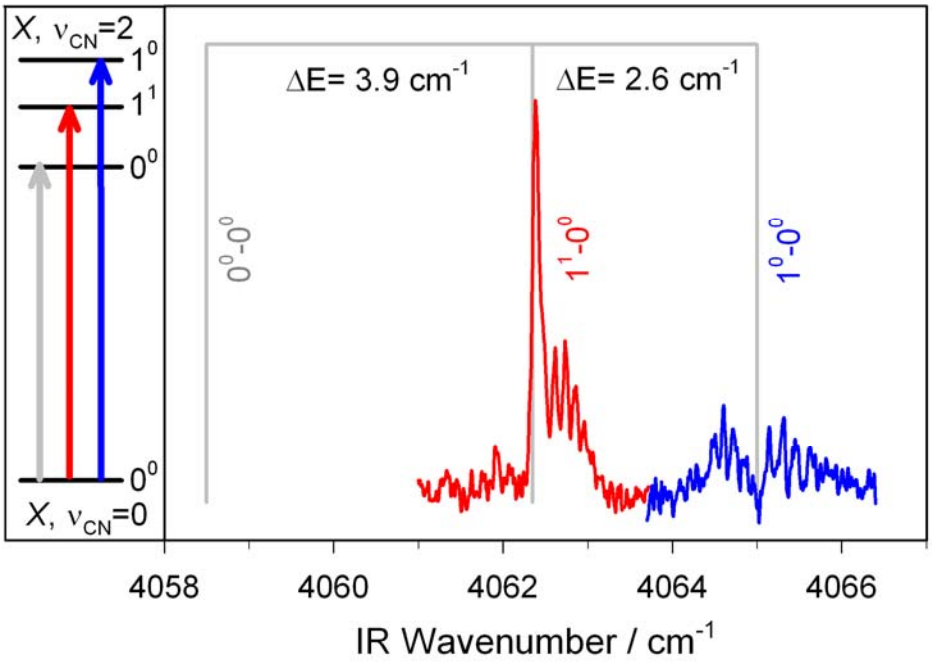
X, ν_CN=2
1^0
1^1
0^0
0^0
X, ν_CN=0
ΔE= 3.9 cm^-1
ΔE= 2.6 cm^-1
0^0-0^0
1^1-0^0
1^0-0^0
4058
4060
4062
4064
4066
IR Wavenumber / cm^-1

Figure 3. Experimental and simulated band contours for transitions to the (v_{CN}, v_s, n^K) = ($2,0,1^1$) (upper panel) and ($2,0,1^0$) (lower panel) hindered internal rotor states of CN-Ar originating from its ground ($0,0,0^0$) state. The red and blue traces are the experimental spectra, while the black traces are simulations with rotational temperature of 1.4 K and laser bandwidth of 0.1 cm^{-1}. The simulations are based on fits to *P*- and *R*-lines only. Rotational assignments are denoted as ticks. The dashed grey line corresponds to the *Q*-branch contour anticipated using the same (perturbed) rotational constant for the ($2,0,1^1$) state. The ($2,0,1^1$) upper state rotational constant derived from the deperturbation analysis provides a much better representation of the experimental *Q*-branch structure (included in solid black line fit). The simulated line intensities are based on standard Hönl-London factors.

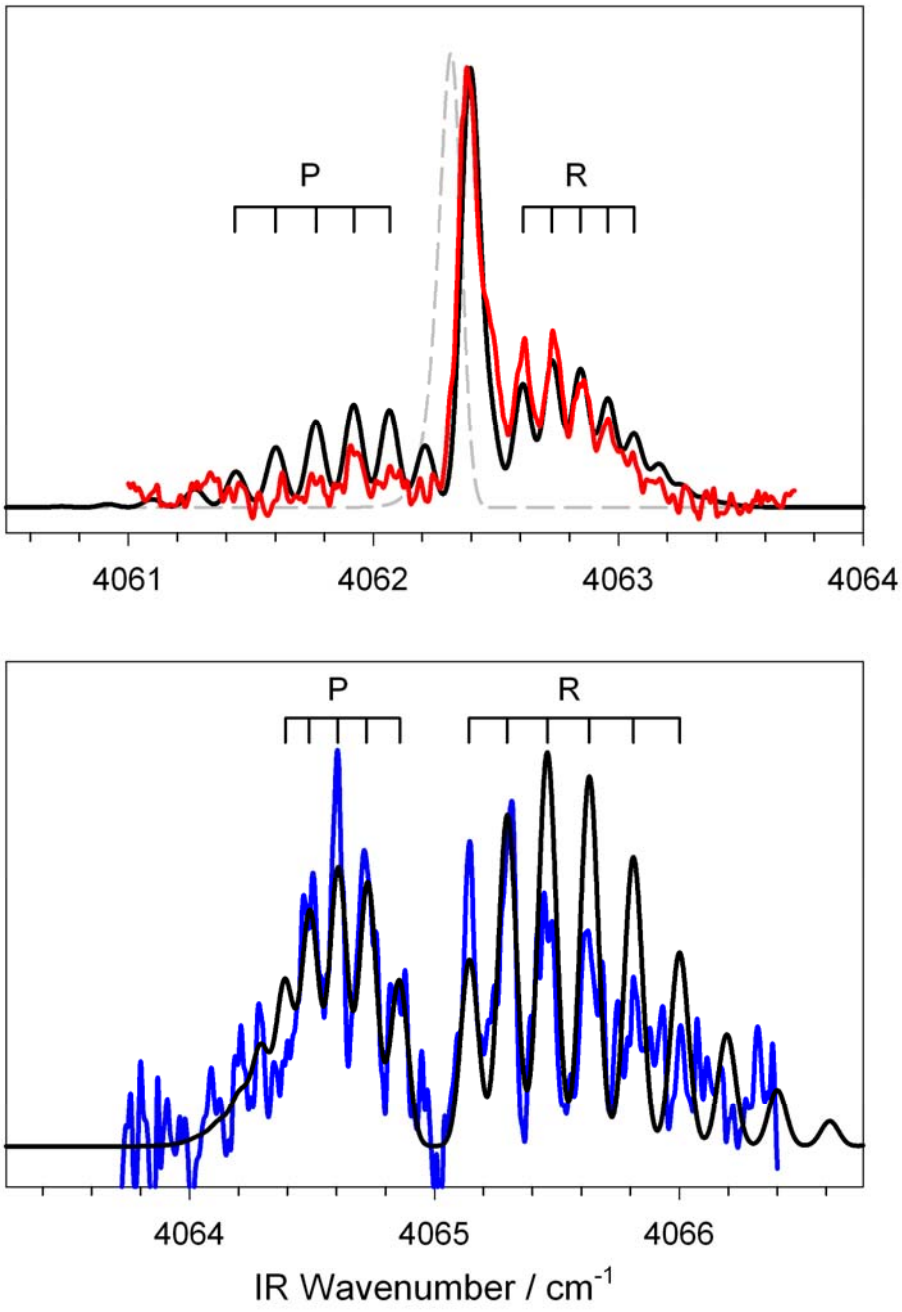
P
R
4061
4062
4063
4064
P
R
4064
4065
4066
IR Wavenumber / cm-1

origins, v_{11} and v_{10}. The *Q*-branch in the perpendicular transition is not included in the fit for reasons which will be discussed below. The resulting spectral simulations are shown in Fig. 3 with a rotational temperature of 1.4 K and a Gaussian linewidth of 0.1 cm^{-1} (IR laser bandwidth). The derived spectroscopic constants are listed in Table 1.

This preliminary rotational analysis yields a ground state rotational constant, B_{00}, of 0.069(1) cm^{-1}, which is in excellent agreement with the rotational constant derived previously from CN-Ar *B*-*X* (0,0) spectra (see Table 1).[17] On the other hand, the upper state rotational constants, B_{10} and B_{11}, differ significantly from B_{00}. These changes may arise from perturbations in the rotational structure of the closely spaced features. The most striking evidence of Coriolis coupling is the observed position and shading of the *Q*-branch for the 4062.4 cm^{-1} band when compared to a simulation based on rotational constants derived from the *P*- and *R*-branches (grey dashed line) in Fig. 3 (top panel). A deperturbation analysis of the 4062.4 and 4065.0 cm^{-1} bands is carried out in Sec. IV. A.

B. Infrared overtone excitation of H_2-CN

Infrared spectra of the H_2-CN complex are also obtained using a similar IR-UV double resonance method. In this case, the IR OPO is scanned in the CN overtone region with the UV laser positioned near the peak of the bound-free transition in the *B*-*X* (2,2) region at 26010 cm^{-1}, which lies ~30 cm^{-1} above the CN $B\,^2\Sigma^+$ (v=2) + H_2 dissociation threshold. Two IR features are observed as shown in Fig. 4: a parallel band (ΔK=0) with resolved *P*- and *R*-branch lines centered at 4061.3 cm^{-1} and a perpendicular band (ΔK=1) with an apparent *Q*-branch and no noticeable *P* or *R* structure at 4066.0 cm^{-1}. Although the two IR features are closely spaced (ΔE = 4.7 cm^{-1}), there is no spectroscopic evidence that points to significant Coriolis coupling, as has been suggested by Kaledin and

Table 1. Spectroscopic constants (cm^{-1}) for CN-Ar (v_{CN}, v_s, n^K) states derived from infrared overtone spectra and deperturbation analysis.

	Ground state	Hindered internal rotor states	
(v_{CN}, v_s, n^K)	($0,0,0^0$)	($2,0,1^1$)	($2,0,1^0$)
v_0 (origin)		4062.4(1)	4065.0(1)
B_e (expt.)[a]	0.069(2) 0.066(3), 0.069(3)[b]	0.066(2)	0.073(2)
B (deperturbed)		0.072(2)	0.068(2)
$\langle R^2 \rangle^{1/2}$ (Å)	3.94(4)	3.85(4)	3.97(4)
β [($2,0,1^1$)-($2,0,1^0$)][c]			0.110(4)

[a] Rotational constants from experimental data for *e* symmetry levels. The rotational constants are labeled in the text as B_{00}, B_{11}, and B_{10} for the ($0,0,0^0$), ($2,0,1^1$), and ($2,0,1^0$) states, respectively.

[b] Ground state rotational constants derived from the a_2 and a_3 bands of CN-Ar in the *B*-*X* (0,0) electronic spectrum (Ref. 17).

[c] Coriolis coupling term between (v_{CN}, v_s, n^K) = ($2,0,1^1$) and ($2,0,1^0$) hindered rotor states.

Figure 4. Infrared overtone spectrum of H_2-CN complex obtained using a similar IR-UV double resonance technique with UV fixed at 26010 cm^{-1}. The rotationally resolved feature at 4061.3 cm^{-1} is simulated as a $\Sigma \leftarrow \Sigma$ (parallel) band originating from the nominally linear ground state of *ortho*-H_2-CN $\left(v_{CN}, j_{H_2}, K, v_s\right)$ = (0,1,0,0) to a vibrationally excited (2,1,0,0) state. Rotational lines utilized to derive rotational constants are labeled. The higher energy feature at 4066.0 cm^{-1} is tentatively ascribed as the *Q*-branch of a $\Pi \leftarrow \Sigma$ (perpendicular) band to the (2,1,1,0) state of *ortho*-H_2-CN.

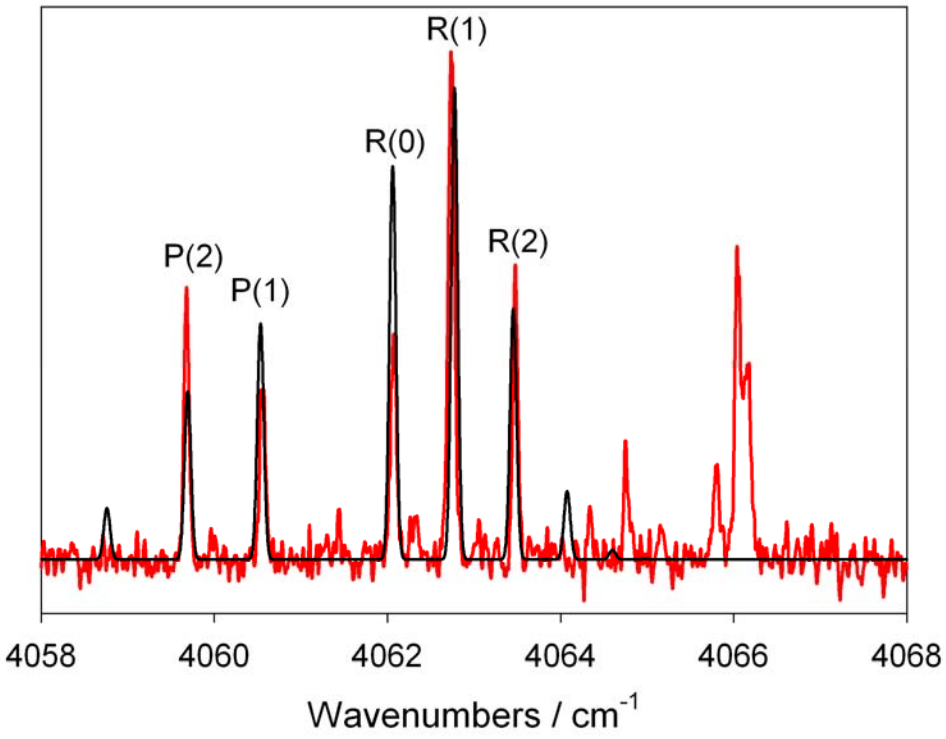
R(1)
R(0)
P(2)
P(1)
R(2)
4058
4060
4062
4064
4066
4068
Wavenumbers / cm-1

Heaven;[19] this issue is revisited in Sec. IV. Similar IR features are observed for D_2-CN at 4061.6 and 4066.6 cm^{-1}, but lack sufficient signal-to-noise ratio for analysis at this time.

The rotational structure of the parallel band of H_2-CN at 4061.3(1) cm^{-1} (origin) has been analyzed to determine rotational constants for the ground (v_{CN}=0) and vibrationally excited (v_{CN}=2) states of B'' = 0.39(1) cm^{-1} and B' = 0.38(1) cm^{-1}. This ground state B'' value differs considerably from that previously reported [0.31(1) cm^{-1}], which was based on rotational analysis of the H_2-CN electronic spectrum in the *A*-*X* (2,0) region;[19] see Appendix 4 for a plausible reanalysis (Fig. A2) of the earlier data. The rotational constants derived from the IR spectral analysis are then used to determine the average intermolecular bond length, $\langle R^2 \rangle^{1/2}$, between the centers-of-mass of CN and H_2 assuming a linear C≡N–H-H configuration based on the minimum energy structure predicted theoretically.[26,32] The average intermolecular bond length is 4.26(8) Å in the ground state and increases slightly upon vibrational overtone excitation to 4.32(8) Å. Assuming that the lowest energy feature promotes *ortho*-H_2-CN from its ground state to the corresponding lowest intermolecular level with v_{CN}=2, the spectral shift from free CN, +2.7 cm^{-1}, indicates a small decrease in the stability of H_2-CN (v_{CN}=2) relative to H_2-CN (v_{CN}=0). Combining the spectral shift with the previously determined binding energy for H_2-CN (v_{CN}=0), D_0''=38(1) cm^{-1}, yields a binding energy for H_2-CN (v_{CN}=2) of 35(1) cm^{-1}. These spectroscopic observables are compared with the results from prior bound state calculations in Sec. V.

IV. Analysis

A. Coriolis coupling effects and deperturbation analysis

1. CN-Ar

As described in Sec. III. A, the infrared spectrum of CN-Ar exhibits complicated rotational structures and intensity patterns indicative of Coriolis coupling between the $n^K=1^1$ and 1^0 hindered rotor states in $v_{CN}=2$. Similar behavior has been observed in IR transitions to closely spaced $K=0$ and 1 states of CN-Ne and HX-Rg complexes.[24,33-35] The N-dependent shifts of rotational energy levels in these previous studies were analyzed as an l-doubling perturbation between intermolecular bending and/or stretching levels. The same analysis is carried out here for CN-Ar to evaluate deperturbed rotational constants and the strength of the Coriolis coupling. Note that the line intensities are not modeled in the present analysis because of the double resonance nature of the experiments.

Coriolis coupling occurs only between rotational levels of the same symmetry. For the IR overtone transition to the CN-Ar (v_{CN}, v_s, n^K) = ($2,0,1^1$) hindered rotor state at 4062.4 cm^{-1}, the P- and R-lines terminate on levels with e symmetry, while the Q-lines terminate on levels of f symmetry. For the IR transition to the CN-Ar ($2,0,1^0$) hindered rotor state at 4065.0 cm^{-1}, the P- and R-lines again terminate on levels of e symmetry. Coriolis coupling occurs between the e symmetry levels of these two hindered rotor states, $n^K=1^1$ and 1^0, causing readily apparent perturbations in the P- and R-branches. The f symmetry levels of the $n^K=1^1$ hindered rotor state, and therefore the Q-branch, are left unperturbed.

Preliminary rotational analyses of the P- and R-branches of the 4062.4 and 4065.0 cm^{-1} bands give values for B_{11} and B_{10} (e symmetry levels) that differ considerably from one another and B_{00} (see B_e (expt.) in Table 1.) A simulation based on these constants for

the 4062.4 cm^{-1} band results in a *Q*-branch (position and shading), which does not match that measured experimentally (Fig. 3, upper panel, dashed grey line), indicating a significant change from the unperturbed rotational constant for the *f* symmetry levels of the upper $n^K=1^1$ state. Indeed, B_{11} for the *f* symmetry levels must be greater than B_{00} to give rise to the *Q*-branch shading observed. The smaller B_{11} value relative to B_{00} derived from experiment for the *e*-levels suggests that the 1^1 state is perturbed by a state higher in energy. The nearby 1^0 state, which has a larger B_{10} relative to B_{00}, is the perturbing state to higher energy and it is similarly perturbed by the lower energy 1^1 state.

A complete deperturbation analysis was then undertaken using a modified rotational Hamiltonian to model the experimentally observed rotational energy levels

$$\hat{H} = \begin{pmatrix} H_{11} & H_{12} \\ H_{21} & H_{22} \end{pmatrix}$$

with matrix elements

$$H_{11} = \nu_{10} + B_{10}[N(N+1) - K^2]$$

$$H_{22} = \nu_{11} + B_{11}[N(N+1) - K^2]$$

$$H_{12} = H_{21} = \beta[N(N+1)]^{1/2}$$

The band origins, ν_{10} and ν_{11}, are kept constant while the deperturbed rotational constants, B_{10} and B_{11}, and the Coriolis coupling parameter, β, are allowed to float in a least-squares fit of the eigenvalues of the *N*-dependent Hamiltonian to the rotational energy levels of the 1^1 and 1^0 states obtained from simulation of *P*- and *R*-branch lines (described in Sec. III. A). The fit reveals strong Coriolis coupling between the closely spaced (ν_{CN}, ν_s, n^K) = (2,0,1^1) and (2,0,1^0) hindered internal rotor states of CN-Ar with $\beta \sim 2B$ and deperturbed

rotational constants listed in Table 1. This analysis shows that Coriolis coupling perturbs the rotational constants by ~7% compared to their unperturbed values.

The *Q*-branch of the 4062.4 cm^{-1} band can be simulated with the deperturbed rotational constant for the upper state (v_{CN}, v_s, n^K) = (2,0,1^1). The position and shading of the *Q*-branch now reproduces the experimental spectrum (Fig. 3, black trace), where *P*- and *R*-branches are simulated with the perturbed constant. The deperturbed rotational constants for the (2,0,1^1) and (2,0,1^0) hindered rotor states and the unperturbed ground state (0,0,0^0) of CN-Ar are then used to determine average intermolecular distances, $\left\langle R^2 \right\rangle^{1/2}$, between the center-of-mass of the CN monomer and Ar. This yields an average separation distance in the ground (v_{CN}, v_s, n^K) = (0,0,0^0) state of 3.94(4) Å. The CN-Ar separation in the (2,0,1^0) state is similar to the ground state with an average distance of 3.97(4) Å, while the (2,0,1^1) distance is slightly shorter at 3.85(4) Å. This suggests a small, but noticeable change in the most probable configuration of hindered rotor states with different n^K, which can be explained with a relatively simple picture.

Examination of the *ab initio* CN $X\ ^2\Sigma^+$ + Ar potential shows that the minimum value of *R* changes significantly as a function of the C≡N–Ar angle, ranging from ~3.7 Å at T-shaped configurations to ~4.2 Å at linear geometries.[17] This means that the Ar atom can approach the center-of-mass of CN more closely in bent configurations (sideways approach) than in linear geometries (head on approach to either end of CN). If one assumes that CN acts as a nearly free rotor in the n^K= 1^0 and 1^1 states of CN-Ar, the probability distributions for a free-rotor may be used to develop a deeper understanding of apparent changes in bond length between hindered rotor states in CN-Ar. As seen in Fig. 8 of Ref. 24, the n^K= 1^0 state of a free rotor has its highest probability at linear

configurations, while the 1^1 state of a free rotor has its highest probability in bent configurations. The resulting experimental bond lengths in CN-Ar follow this trend: the excited ($2,0,1^0$) hindered rotor state has a longer bond length, 3.94(4) Å, and samples linear (or nearly linear) most probable configurations, while the excited ($2,0,1^1$) hindered rotor state has a shorter bond length of 3.85(4) Å and samples bent configurations. The ground ($0,0,0^0$) state also has a longer bond length of 3.97(4) Å, and this suggests that its most probable configuration is also linear or near-linear (N≡C–Ar).

2. H_2-CN

Previously, it has been suggested that the ground state of H_2-CN (v_{CN}=0) is perturbed as a result of significant Coriolis coupling with a nearby intermolecular state.[19] In principle, one would like to carry out a deperturbation analysis for the corresponding lowest intermolecular level of H_2-CN and the nearby intermolecular state with v_{CN}=2, which are accessed via IR transitions at 4061.3 and 4066.0 cm^{-1}. However, the lack of observable *P*, *R* rotational structure for the higher energy feature precludes such an analysis. On the other hand, the original reason for invoking Coriolis coupling appears to be refuted by the new IR data. The average intermolecular bond length $\left\langle R^2 \right\rangle^{1/2} = 4.26(8)$ derived from the ground state rotational constant is in accord with the expectation value $\left\langle R \right\rangle = 4.26$ Å evaluated from the probability amplitude for the lowest bound state of *ortho*-H_2-CN.[26]

B. Hindered rotor analysis

In this section, we use the assignments and energy spacings of the observed hindered rotor levels to obtain information on the anisotropy of the CN $X\,^2\Sigma^+$ (v=2) + Ar

potential based solely on the experimental results. The resultant angular potential is then compared with that of the *ab initio* potential for CN $X\ ^2\Sigma^+$ + Ar reported previously.[17] The hindered rotor analysis is based on the theoretical treatment for open shell complexes developed by Dubernet *et al*.[36] The intermolecular potential V_{inter} is modeled as a truncated Legendre expansion with radially averaged anisotropy parameters V_{10} and V_{20} as coefficients (see Sec. V. A). The bending Hamiltonian, assumed to be decoupled from the intermolecular stretch, is evaluated for specific values of V_{10} and V_{20} to determine energies for the hindered internal rotor n^K states. The eigenvalues are obtained by diagonalizing the Hamiltonian with matrix elements composed of potential coupling coefficients (see Eq. 11 of Ref. 36). The values for V_{10} and V_{20} are varied iteratively until the energy spacings and ordering of the n^K states calculated match those observed experimentally (with associated uncertainties) for v_{CN}=2, n^K=0^0, 1^1, and 1^0.

Dubernet *et al*. present general trends in the energy level pattern for angular states of complexes containing open-shell diatoms in Σ states based on limiting values of V_{10} and V_{20}.[36] Inspection of their correlation diagrams constructed as a function of V_{20} with fixed V_{10}=0 and 2*b* in Figs. 2c and 2d of Ref. 36, respectively, shows that V_{10} lies closer to the 2*b* limit for CN-Ar. Indeed, V_{10} must be closer to 3*b* in order to capture the ordering of the CN-Ar hindered internal rotor states and the larger spacing between the n^K=0^0 and 1^1 states of 3.9(2) cm^{-1} compared to the smaller spacing between the n^K=1^1 and 1^0 states of 2.6(1) cm^{-1}. A correlation diagram specific to CN-Ar (v_{CN}=2) (see Appendix 4, Fig. A3) was then constructed for a fixed value of V_{10} ~ 3*b* [*b*=1.856 cm^{-1} for CN $X\ ^2\Sigma^+$ (v=2)] as a function of V_{20}. This shows that the ordering and spacings of the hindered rotor states also requires V_{20} to be positive. A unique solution for V_{10} and V_{20} of 5.2 cm^{-1}

and 3.2 cm^{-1}, respectively, yields the experimental spacings precisely. To account for the experimental uncertainty in the spacings, a corresponding range of V_{10} and V_{20} values is also derived, specifically V_{10} from 4.8 to 5.5 cm^{-1} and V_{20} from 2.6 to 3.8 cm^{-1}. The sign of V_{10}, indicating a preference for Ar binding to the C or N side of CN, cannot be determined from the experimental data alone. The positive sign for V_{10}, favoring the C-side of CN, is adopted from the previously calculated *ab initio* potential energy surface.[17]

V. Discussion

A. Angular potential for CN + Ar

The effective angular dependence of the CN $X\,^2\Sigma^+$ + Ar potential is then plotted as a function of θ in the top panel of Fig. 5 using the experimentally determined V_{10} and V_{20} coefficients in a truncated Legendre polynomial expression

$$V(\theta) = V_{10}\cos\theta + \frac{V_{20}\left(3\cos^2(\theta) - 1\right)}{2}$$

The angular potential is relatively flat from 90 to 270°. The V_{10} term dominates the overall shape of the potential, resulting in a minimum closer to linear N≡C–Ar than linear C≡N–Ar. The V_{20} coefficient has a somewhat smaller effect, extending the nearly flat region of the potential. The barrier to CN internal rotation in the complex is only 12 cm^{-1}, indicating a weakly anisotropic potential close to the free-rotor limit. As a result, the ground state of CN-Ar will undergo large amplitude motion in the angular coordinate within the relatively flat potential about the linear N≡C–Ar configuration.

The lower panel of Fig. 5 shows the angular dependence of the *ab initio* potential for CN $X\,^2\Sigma^+$ + Ar previously reported.[17] The theoretical curve was generated by fitting the radial data at fixed values of θ to an extended Morse potential, thereby obtaining the

Figure 5. Potential anisotropy for CN $X\ ^2\Sigma^+$ + Ar as a function of intermolecular angle θ. The upper panel shows the radially averaged angular potential (solid line) derived from the experimental hindered rotor spacings with v_{CN}=2. The dotted and dashed lines give the individual contributions from the larger V_{10}= 5.2 cm^{-1} term and smaller V_{20}= 3.2 cm^{-1} term with gray lines or shading indicating the associated experimental uncertainty. The lower panel displays the radially minimized energy at each θ from previous *ab initio* calculations (Ref. 17) as red crosses with a fit (black curve) to the *ab initio* data based on the Legendre expansion.

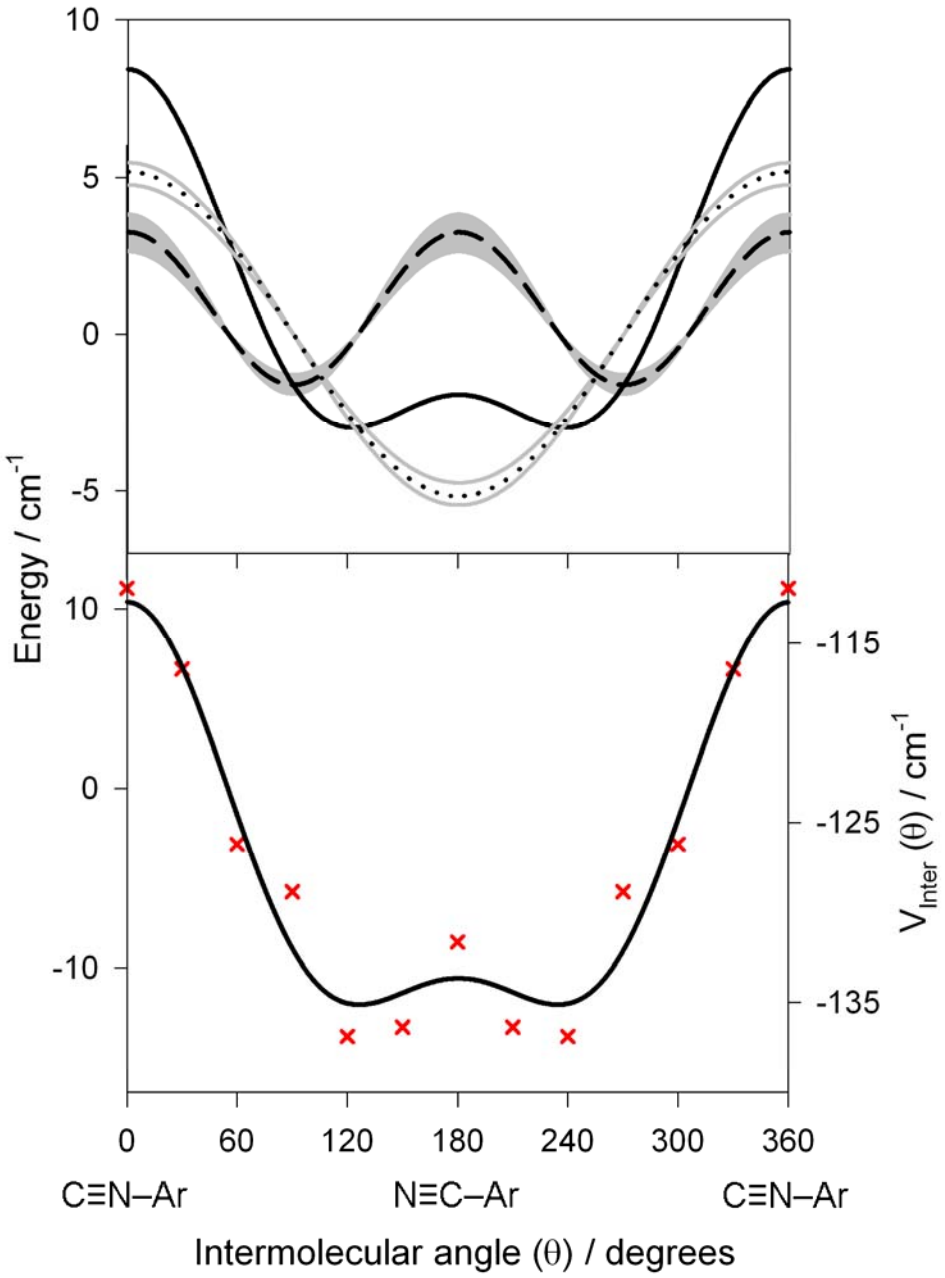
10
5
0
-5
Energy / cm-1
10
0
-10
-115
-125
-135
Vinter (θ) / cm-1
0
60
120
180
240
300
360
C≡N–Ar
N≡C–Ar
C≡N–Ar
Intermolecular angle (θ) / degrees

minimum energy at each angle. Plotting the minimum energy for each θ produces a one-dimensional angular minimum energy path through the two-dimensional potential. This angular potential is fit to the same truncated Legendre expansion employed above in the experimental analysis, yielding values of V_{10} and V_{20} of 10.9 cm^{-1} and 4.3 cm^{-1}, respectively. The *ab initio* calculation reproduces the shape of the CN $X\ ^2\Sigma^+$ + Ar experimental potential very well and affords determination of the sign of V_{10}. However, the *ab initio* calculation predicts a much larger barrier to CN internal rotation of 27 cm^{-1} compared to the experimental value of 12 cm^{-1}.

B. H_2-CN potential

The IR spectral data is obtained using normal H_2, which means that the observed IR features could be due to complexes of CN with *ortho*-H_2 (j_{H_2} =1), *para*-H_2 (j_{H_2} =0), or both. As noted in the Introduction, one might expect *ortho*-H_2-CN to be formed more readily than *para*-H_2-CN in the supersonic expansion because of its greater binding energy (D_0) (26.3 cm^{-1} for *ortho*-H_2 vs. 15.4 cm^{-1} for *para*-H_2 with CN from bound state calculations)[26] and more favorable spin statistics (*ortho*:*para* = 3:1). Indeed, previous infrared spectroscopic studies of analogous complexes of HF and OH with H_2 have revealed only the *ortho*-H_2-HX complexes.[21,37]

The intermolecular potential for H_2 + CN differs from H_2 + HX in that the minimum energy configuration is predicted to be linear C≡N–H-H rather than T-shaped H_2-HX. In these systems, the attractive dipole-quadrupole interaction favors linear and T-shaped configurations, although the linear configuration is more favorable. The smaller quadrupole-quadrupole interaction is repulsive for linear configurations and attractive for T-shaped configurations. The change in minimum energy geometry

between H_2-HX and H_2-CN has been attributed to the much smaller quadrupole moment of CN,[26] which leads to less repulsion from the quadrupole-quadrupole interaction in linear configurations as compared to HF or OH with H_2. For the T-shaped complexes of HX with H_2, the angular momentum vector for *ortho*-H_2 (j_{H_2}=1) lies along the intermolecular axis, giving rise to a ground state for *ortho*-H_2-HX with K=1 and a $\Pi \leftarrow \Pi$ infrared transition for the HX stretch, while the unobserved *para*-H_2-HX complex would have a ground state with K=0 and a $\Sigma \leftarrow \Sigma$ infrared transition.

By contrast, since the average configuration for *ortho*-H_2-CN is linear, the angular momentum vector for *ortho*-H_2 (j_{H_2}=1) would lie perpendicular to the intermolecular axis. As a result, one would anticipate the ground state of *ortho*-H_2-CN to have zero projection (K=0) of the total angular momentum (excluding spin) on the intermolecular axis. Infrared overtone transitions (v_{CN}=2) of *ortho*-H_2-CN would then be expected to exhibit either $\Sigma \leftarrow \Sigma$ (parallel) or $\Pi \leftarrow \Sigma$ (perpendicular) band types originating from its ground state $\left(v_{CN}, j_{H_2}, K, v_s\right) = \left(0,1,0,0\right)$ to $\left(2,1,0,0\right)$ and $\left(2,1,1,0\right)$ upper states, and both appear to be observed experimentally. The spacing of these features (4.7 cm^{-1}) is in good accord with bound state calculations,[19] which predict a K=1 state lying 5.1 cm^{-1} above the K=0 ground state for *ortho*-H_2-CN. In addition, the intermolecular bond length $\left\langle R^2 \right\rangle^{1/2} = 4.26(8)$ Å for the ground state agrees with the expectation value $\left\langle R \right\rangle = 4.26$ Å for the lowest bound state of *ortho*-H_2-CN. Finally, the previously determined experimental binding energy, D_0''=38(1) cm^{-1}, is in reasonable accord with that predicted for *ortho*-H_2-CN (26.3 cm^{-1}).[26] The experimental observables, namely IR transition type, bond length, intermolecular spacing, and binding energy, all point to *ortho*-H_2-CN in a

near linear configuration as the spectral carrier in the infrared spectrum presented in this work and the *B*-*X* bound-free transition reported earlier. It should be noted that *para*-H_2-CN, which is expected to be far less abundant, is predicted to have the same infrared transition type, a somewhat longer $\langle R \rangle$ at 4.40 Å, a similar spacing between K=0 and 1 levels (4.6 cm^{-1}), and a smaller binding energy of 15.4 cm^{-1}.[26]

VI. Conclusions

The infrared spectrum of the weakly bound CN-Ar van der Waals complex is recorded in the first overtone region of CN using an IR-UV double resonance scheme. The infrared spectra probe hindered rotor states in v_{CN}=2 of CN-Ar with $n^K = 1^1$ and 1^0, while subsequent UV excitation in the *B*-*X* (2,2) spectral region promotes CN-Ar to the excited *B* (v_{CN}=2) state. UV spectra recorded in the *B*-*X* (2,2) and (2,0) regions without IR excitation, using 193 nm photolysis to produce CN (v=2), yield the pure CN overtone stretch of CN-Ar ($n^K=0^0$) at 4058.5 cm^{-1}, which is unchanged from that of free CN (4058.55 cm^{-1}).

Rotationally structured infrared spectra recorded in the first overtone region of CN in CN-Ar are identified at 4062.4 cm^{-1} and 4065.0 cm^{-1} and assigned as transitions from the ground state to (v_{CN}, v_s, n^K) = (2,0,1^1) and (2,0,1^0), respectively. The rotational levels of *e* parity in the closely spaced $n^K=1^1$ and 1^0 hindered rotor states, accessed through *P*- and *R*-branch lines, display clear perturbations due to Coriolis coupling. A deperturbation analysis is carried out to derive accurate rotational constants for the hindered rotor states and determine the magnitude of the coupling, β.

Furthermore, the energy spacings between the hindered rotor states of CN-Ar and their respective ordering provide detailed information on the angular anisotropy of the

CN $X\ ^2\Sigma^+$ + Ar potential energy surface. The theoretical framework of Dubernet *et al.* for open-shell diatom-rare gas complexes is used to obtain eigenvalues for a bending Hamiltonian, which are compared with experimental spacings. This procedure yields radially averaged anisotropy parameters, V_{10} = 5.2 cm^{-1} and V_{20} = 3.2 cm^{-1} and associated uncertainties, of a truncated Legendre expansion, which are used to model the angular dependence of the ground state potential. The weakly anisotropic potential is found to be relatively flat about a linear N≡C–Ar configuration with a barrier to internal rotation of only 12 cm^{-1}, indicating nearly free rotation of CN within the CN-Ar complex. The experimental anisotropy is compared to that predicted theoretically[17] by optimizing the radial potential at each angle. The *ab initio* angular potential closely matches that determined experimentally; however, the barrier to free internal rotation is larger at ~27 cm^{-1}.

The infrared spectrum of H_2-CN in the CN overtone region reveals a parallel $\Sigma \leftarrow \Sigma$ band at 4061.3 cm^{-1} with an intermolecular bond length of $\left\langle R^2 \right\rangle^{1/2}$ = 4.26(8) Å and the *Q*-branch of a second feature at 4066.0 cm^{-1}. In contrast to a previous report based on electronic spectroscopy,[19] the bond length derived from the IR spectrum is in agreement with the average value predicted theoretically for *ortho*-H_2-CN in a linear C≡N–H-H configuration. The transition types demonstrate that CN $X\ ^2\Sigma^+$ forms a weakly-bound linear complex with the more abundant *ortho*-H_2 (j_{H_2} =1), resulting in a ground state with zero projection (*K*=0) of the total angular momentum (excluding spin) along the intermolecular axis.

References

1. R. J. Balla, K. H. Casleton, J. S. Adams, and L. Pasternack, J. Phys. Chem. **95**, 8694 (1991).
2. L. R. Copeland, F. Mohammad, M. Zahedi, D. H. Volman, and W. M. Jackson, J. Chem. Phys. **96**, 5817 (1992).
3. I. R. Sims, J. L. Queffelec, D. Travers, B. R. Rowe, L. B. Herbert, J. Karthauser, and I. W. M. Smith, Chem. Phys. Lett. **211**, 461 (1993).
4. D. L. Yang and M. C. Lin, in *The Chemical Dynamics and Kinetics of Small Molecules Part I*, edited by K. Liu and A. Wagner (World Scientific Publishing Co. Pte. Ltd., Singapore, 1995), Vol. 6, pp. 164.
5. I. W. M. Smith, Angew. Chem. Int. Edit. **45**, 2842 (2006).
6. Y. Georgievskii and S. J. Klippenstein, J. Phys. Chem. A **111**, 3802 (2007).
7. D. Talbi and I. W. M. Smith, Phys. Chem. Chem. Phys. **11**, 8477 (2009).
8. S. J. Greaves, R. A. Rose, T. A. A. Oliver, D. R. Glowacki, M. N. R. Ashfold, J. N. Harvey, I. P. Clark, G. M. Greetham, A. W. Parker, M. Towrie, and A. J. Orr-Ewing, Science **331**, 1423 (2011).
9. R. A. Rose, S. J. Greaves, T. A. A. Oliver, I. P. Clark, G. M. Greetham, A. W. Parker, M. Towrie, and A. J. Orr-Ewing, J. Chem. Phys. **134**, 244503 (2011).
10. A. C. Crowther, S. L. Carrier, T. J. Preston, and F. F. Crim, J. Phys. Chem. A **112**, 12081 (2008).
11. A. C. Crowther, S. L. Carrier, T. J. Preston, and F. F. Crim, J. Phys. Chem. A **113**, 3758 (2009).

12. P. A. Pieniazek, S. E. Bradforth, and A. I. Krylov, J. Phys. Chem. A **110**, 4854 (2006).

13. D. Raftery, M. Iannone, C. M. Phillips, and R. M. Hochstrasser, Chem. Phys. Lett. **201**, 513 (1993).

14. A. C. Moskun and S. E. Bradforth, J. Chem. Phys. **119**, 4500 (2003).

15. Y. Lin and M. C. Heaven, J. Chem. Phys. **94**, 5765 (1991).

16. S. Fei and M. C. Heaven, Proc. SPIE-Int. Soc. Opt. Eng. **1858**, 286 (1993).

17. J. Han, M. C. Heaven, U. Schnupf, and M. H. Alexander, J. Chem. Phys. **128**, 104308 (2008).

18. Y. Chen and M. C. Heaven, J. Chem. Phys. **109**, 5171 (1998).

19. A. L. Kaledin and M. C. Heaven, Chem. Phys. Lett. **347**, 199 (2001).

20. M. I. Lester, R. A. Loomis, R. L. Schwartz, and S. P. Walch, J. Phys. Chem. A **101**, 9195 (1997).

21. D. T. Anderson, R. L. Schwartz, M. W. Todd, and M. I. Lester, J. Chem. Phys. **109**, 3461 (1998).

22. P. Soloveichik, B. A. O'Donnell, M. I. Lester, J. S. Francisco, and A. B. McCoy, J. Phys. Chem. A **114**, 1529 (2010).

23. M. W. Todd, D. T. Anderson, and M. I. Lester, J. Phys. Chem. A **104**, 6532 (2000).

24. J. M. Beames, B. A. O'Donnell, M. Ting, M. I. Lester, and T. A. Stephenson, J. Chem. Phys. **134**, 184308 (2011).

25. B. A. O'Donnell, J. M. Beames, and M. I. Lester, J. Chem. Phys., submitted (2012).

26. A. L. Kaledin, M. C. Heaven, and J. M. Bowman, J. Chem. Phys. **110**, 10380 (1999).

27. G. Herzberg, *Molecular Spectra and Molecular Structure I. Spectra of Diatomic Molecules*, Second ed. (Van Nostrand Reinhold Company, New York, 1950).

28. J. Larsen, D. Madsen, J.-A. Poulsen, T. D. Poulsen, S. R. Keiding, and J. Thogersen, J. Chem. Phys. **116**, 7997 (2002).

29. M. A. O'Halloran, H. Joswig, and R. N. Zare, J. Chem. Phys. **87**, 303 (1987).

30. R. Engleman, J. Mol. Spectrosc. **49**, 106 (1974).

31. *PGopher, a program for simulating rotational structure*, C. M. Western, University of Bristol, available at http://pgopher.chm.bris.ac.uk.

32. The pseudo-diatomic assumption used previously in Ref. 19 for converting *B* to *R* is not appropriate for linear C≡N–H-H.

33. C. M. Lovejoy, J. M. Hutson, and D. J. Nesbitt, J. Chem. Phys. **97**, 8009 (1992).

34. C. M. Lovejoy and D. J. Nesbitt, J. Chem. Phys. **91**, 2790 (1989).

35. M. D. Schuder, D. D. Nelson, and D. J. Nesbitt, J. Chem. Phys. **94**, 5796 (1991).

36. M. L. Dubernet, D. Flower, and J. M. Hutson, J. Chem. Phys. **94**, 7602 (1991).

37. C. M. Lovejoy, D. D. Nelson, and D. J. Nesbitt, J. Chem. Phys. **87**, 5621 (1987).

Chapter 7

Future Directions

These studies mark the first experiments investigating weakly bound CN complexes using infrared excitation. The IR-UV methods described here to probe CN-Ne, CN-Ar, and CN-H_2 van der Waals complexes may be adapted to the study of more complicated systems. Bimolecular reactions and differences in their rates and dynamics between the condensed and gas phases have attracted much interest. Solvent interactions in particular have been shown to have a pronounced effect on the dynamics of chemical reactions. Reactions of CN with alkanes and chloroalkanes in solution[1-7] have been one specific group of reactions that have been investigated because of the facile formation of CN and detection of both CN reactant and HCN product. ICN is known to photodissociate in solution to produce CN and both CN and HCN are easily detected in solution using UV and IR absorption spectroscopy, respectively. The presence of stable CN-solvent complexes have been proposed to play a crucial role in reaction in the condensed phase. Specifically, formation and reaction of structurally different CN-solvent complexes dictate the rates of CN removal and HCN formation.

One such system involves complexation of CN with dichloromethane and subsequent reaction.[2] In kinetic studies, HCN product formation was found to occur more rapidly than CN reactant was consumed. A kinetic scheme was proposed to account for the apparent anomaly between the two measurements. Two structurally different CN-CH_2Cl_2 complexes which react at different rates and do not interconvert on the time scale of the reaction are deemed responsible. A weakly bound, less abundant linear complex reacts rapidly with CH_2Cl_2 to form HCN products, while a more strongly bound bridged complex reacts slowly to form ClCN. Thus, the slowly decaying CN reactant signal arises from formation of the bridged complex, while the rapid formation

of HCN proceeds through reaction of the linear complex as shown in Figure 1. Because CN is highly reactive and acts as a pseudo-halogen, it is also useful to compare the analogous reaction of Cl with alkanes in CH_2Cl_2.[8] In these reactions, the disappearance of CN and production of HCN occur with the same rates, consistent with a simple kinetic picture and in sharp contrast to the equivalent reaction with CN.

As such, it would be interesting to produce the implied complexes in the gas phase and probe them directly in an IR action scheme as was employed in detection and characterization of the OH-$HONO_2$ and H_2O-HO complexes. The CN-CH_2Cl_2 complexes could be produced in the same manner by combining ICN vapor and dichloromethane (~0.5 torr at 20°C), photolyzing the ICN to produce CN radicals, and forming the CN-CH_2Cl_2 complexes through collisions in the supersonic jet. IR excitation of the CN stretch and possibly other modes, including the CH stretching modes around ~3000 cm^{-1} will likely cause dissociation through intramolecular vibrational redistribution (IVR) provided the infrared photon provides enough energy to break apart CN and CH_2Cl_2. Electronic structure calculations suggest binding energies of 430 cm^{-1} for the linear complex and 1540 cm^{-1} for the bridging complex, and if this is the case, IR excitation should provide ample energy. The resulting CN fragments produced from predissociation may then be probed using the CN $B\ ^2\Sigma^+$ - $X\ ^2\Sigma^+$ electronic transition and collecting the subsequent fluorescence. In this manner, information on the structure and stability of one or possibly both CN-CH_2Cl_2 complexes can be attained, providing direct confirmation of the proposed kinetic mechanism.

This is just one example of future experiments that could be carried out. Complexes of CN with alkanes,[1-7] H_2O,[9] and NH_3[10] have all been proposed to be

important in reaction, and would be attractive systems to study. The development of IR-UV techniques for the study of CN-Ne, CN-Ar, and CN-H_2 has provided a gateway to the study of more complex systems.

Figure 1. Scheme for the reaction of CN with CH_2Cl_2. HCN is produced through formation of a linear complex (top pathway) while CN is consumed through formation of a stable bridged complex (bottom pathway) which reacts slowly to form ClCN.

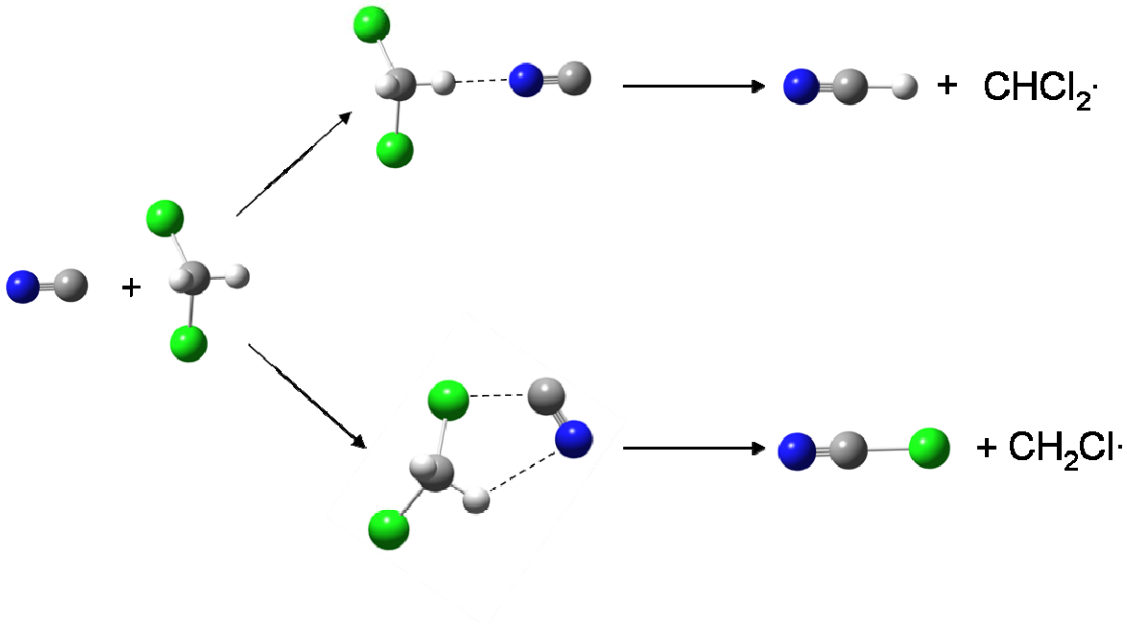
+
+ CHCl2·
+ CH2Cl·

References

1. A. C. Crowther, S. L. Carrier, T. J. Preston, and F. F. Crim, J. Phys. Chem. A **113**, 3758 (2009).
2. A. C. Crowther, S. L. Carrier, T. J. Preston, and F. F. Crim, J. Phys. Chem. A **112**, 12081 (2008).
3. C. Huang, W. Li, A. D. Estillore, and A. G. Suits, J. Chem. Phys. **129**, (2008).
4. I. R. Sims, J. L. Queffelec, D. Travers, B. R. Rowe, L. B. Herbert, J. Karthauser, and I. W. M. Smith, Chem. Phys. Lett. **211**, 461 (1993).
5. B. Atakan and J. Wolfrum, Chem. Phys. Lett. **186**, 547 (1991).
6. D. L. Yang, T. Yu, N. S. Wang, and M. C. Lin, Chem. Phys. **160**, 307 (1992).
7. S. J. Greaves, R. A. Rose, T. A. A. Oliver, D. R. Glowacki, M. N. R. Ashfold, J. N. Harvey, I. P. Clark, G. M. Greetham, A. W. Parker, M. Towrie, and A. J. Orr-Ewing, Science **331**, 1423 (2011).
8. L. Sheps, A. C. Crowther, S. L. Carrier, and F. F. Crim, J. Phys. Chem. A **110**, 3087 (2006).
9. P. A. Pieniazek, S. E. Bradforth, and A. I. Krylov, J. Phys. Chem. A **110**, 4854 (2006).
10. D. Talbi and I. W. M. Smith, Phys. Chem. Chem. Phys. **11**, 8477 (2009).

Appendix 1:

Spectroscopic Identification and Stability of the Intermediate in the $OH + HONO_2$ Reaction Supporting Information

This research has been published in the *Proceedings of the National Academy of Sciences of the United States of America* (2008), *105*, 12678 Supporting Information and was performed with graduate student Eunice X. J. Li and Marsha I. Lester in the *Department of Chemistry, University of Pennsylvania*. Theoretical calculations were carried out by Joseph S. Francisco in the *Department of Chemistry, Purdue University*.

Table A1. Optimized geometry for OH-$HONO_2$ in Å for distances and degrees for angles

	QCISD	CCSD(T)	
Coordinate	aug-cc-pVDZ	aug-cc-pVDZ	aug-cc-pVTZ
O_7H_6	0.982	0.984	0.978
O_7H_5	**1.855**	**1.895**	**1.827**
H_6O_3	**2.386**	**2.315**	**2.281**
H_5O_2	0.986	0.990	0.986
N_1O_2	1.384	1.398	1.386
N_1O_3	1.226	1.232	1.223
N_1O_4	1.202	1.209	1.199
$H_6O_3N_1$	116.8	116.8	116.7
$N_1O_2H_5$	104.2	103.8	104.0
$O_7H_5O_2$	**174.0**	**173.2**	**172.4**
$O_7H_6O_3$	**117.7**	**120.7**	**121.2**
$O_2N_1O_4$	114.6	114.5	114.7
$O_3N_1O_4$	128.6	128.7	128.6
$H_5O_2N_1O_4$	180.0	180.0	180.0

Table A2. Vibrational frequencies (cm^{-1}) for OH-$HONO_2$

Species	Mode number	Mode description	QCISD aug-cc-pVDZ	CCSD(T) aug-cc-pVDZ	Expt.
OH	1	OH stretch	3683	3683	3568[a]
$HONO_2$	1 (a')	OH stretch	3743	3702	3550[b]
	2	ND asym. stretch	1761	1743	1708.2
	3	HON bend	1379	1344	1330.7
	4	NO sym. stretch	1351	1323	1324.9
	5	NO_2 deform	920	878	878.6
	6	NO' stretch	669	639	646.6
	7	ONO' bend	588	569	579.0
	8 (a")	NO_2 out of plane	786	758	762.2
	9	HO torsion	482	470	455.8
OH·$HONO_2$	1	O_7H_6 stretch	3670		3516.8[c]
	2	O_2H_5 stretch	3502		3260
	3	NO_4 stretch	1758		
	4	NO_2H_5 bend	1456		
	5	NO_3 stretch	1361		
	6	O_3NO_4 bend	949		
	7	$NO_2O_3O_4$ umbrel.	795		
	8	O_2NO_3 bend	687		
	9	NO_2H_5 wag	673		
	10	O_2NO_4 bend	627		
	11	$H_6O_7H_5$ asym. stretch	428		
	12	$O_2H_5O_2$ bend	194		
	13	$O_7H_5O_2$ sym. stretch	185		
	14	$O_7H_6O_3$ bend	113		
	15	$H_6O_7H_5O_2$ torsion	69		

[a] Jacox, M. E. (1985) Comparison of the ground state vibrational fundamentals of diatomic molecules in the gas phase and in inert solid matrices. *J. Mol. Spectrosc.* **113,** 286-301.

[b] McGraw, G. E., Bernitt, D. L. & Hisatsune, I. C. (1965) Vibrational spectra of isotopic nitric acids. *J. Chem. Phys.* **42,** 237-244.

[c] This work.

Table A3. Rotational constants for OH-$HONO_2$

Method	Rotational Constants (MHz)		
	A	B	C
QCISD/aug-cc-ppVDZ	12300	2746	2245
CCSD(T)/aug-cc-pVDZ	12110	2773	2256
CCSD(T)/aug-cc-pVTZ	12322	2817	2283

Table A4. Binding energetics for the OH-$HONO_2$ complex

	Total Energy (Hartree)			Relative Energy (kcal mol^{-1})	
Method	OH	$HONO_2$	$OH \cdot HONO_2$	D_e	D_0
QCISD/aug-cc-pVDZ	-75.58111	-280.28162	-355.87444	7.3	5.8
CCSD(T)/aug-cc-pVDZ	-75.58408	-280.31257	-355.90892	7.7	6.2
CCSD(T)/aug-cc-pVTZ	-75.64550	-280.54503	-356.20274	7.6	6.1
CCSD(T)/aug-cc-pVQZ	-75.66449	-280.61849	-356.29490	7.6	6.0
CBS-∞ (aug-cc-pV∞Z)				7.4	5.9

Appendix 2:

Infrared Spectrum and Stability of the H_2O-HO Complex: Experiment and Theory Supporting Information

This research has been published in the *Journal of Physical Chemistry A* (2010), *114*, 1529 and was performed with graduate student Pesia Soloveichik and Marsha I. Lester in the *Department of Chemistry, University of Pennsylvania* and Anne B. McCoy in the *Department of Chemistry, The Ohio State University*.

Table A1. Energies of purely electronic potential V_e and adiabatic potentials V_{ν_2} with ν_2 = 0 and 1 for H_2O-HO on the $^2A'$ surface as a function of out-of-plane angle ϕ. Energies in cm^{-1} relative to the energy of H_2O-HO at its global minimum geometry.

ϕ (°)	V_e	$V_{\nu_2=0}$	$V_{\nu_2=1}$
-86.84	315.13	2063.46	5414.04
-81.84	247.58	1993.45	5336.17
-76.84	188.49	1932.31	5268.17
-71.84	138.57	1881.44	5213.61
-66.84	97.59	1840.05	5169.98
-61.84	64.55	1807.67	5138.39
-56.84	38.85	1782.62	5114.07
-51.84	20.60	1765.83	5100.12
-46.84	8.96	1756.17	5094.81
-41.84	2.38	1751.74	5095.20
-36.84	0.00	1751.79	5100.80
-31.84	1.62	1755.87	5110.62
-26.84	5.94	1762.59	5123.00
-20.00	12.85	1772.55	5140.34
-10.00	22.19	1785.04	5160.50
-5.00	25.49	1789.21	5166.82
0.00	26.03	1790.01	5168.26
5.00	25.49	1789.21	5166.82
10.00	22.19	1785.04	5160.50
20.00	12.85	1772.55	5140.34
26.84	5.94	1762.59	5123.00
31.84	1.62	1755.87	5110.62
36.84	0.00	1751.79	5100.80
41.84	2.38	1751.74	5095.20
46.84	8.96	1756.17	5094.81
51.84	20.60	1765.83	5100.12
56.84	38.85	1782.62	5114.07
61.84	64.55	1807.67	5138.39
66.84	97.59	1840.05	5169.98
71.84	138.57	1881.44	5213.61
76.84	188.49	1932.31	5268.17
81.84	247.58	1993.45	5336.17
86.84	315.13	2063.46	5414.04

Table A2. Energies of purely electronic potential V_e and adiabatic potentials V_{ν_2} with ν_2 = 0 and 1 for H_2O-HO on the $^2A''$ surface as a function of out-of-plane angle ϕ. Energies in cm^{-1} relative to the energy of H_2O-HO at its global minimum geometry.

ϕ (°)	V_e	$V_{\nu_2=0}$	$V_{\nu_2=1}$
-82.20	344.74	2088.43	5423.24
-77.20	286.03	2028.81	5360.58
-72.20	237.74	1980.00	5309.49
-67.20	199.10	1941.55	5270.89
-62.20	169.23	1912.43	5242.98
-57.20	147.24	1892.00	5225.94
-52.20	133.01	1879.44	5216.95
-47.20	125.64	1874.29	5216.93
-42.20	123.41	1874.47	5222.76
-37.20	125.33	1878.90	5233.13
-32.20	131.01	1887.22	5247.82
-27.20	139.14	1897.62	5263.63
-22.20	147.66	1908.46	5280.23
-17.20	155.55	1918.36	5295.19
-10.00	165.13	1929.95	5311.79
-5.00	169.60	1935.24	5319.13
0.00	171.22	1937.13	5321.70
5.00	169.60	1935.24	5319.13
10.00	165.13	1929.95	5311.79
17.20	155.55	1918.36	5295.19
22.20	147.66	1908.46	5280.23
27.20	139.14	1897.62	5263.63
32.20	131.01	1887.22	5247.82
37.20	125.33	1878.90	5233.13
42.20	123.41	1874.47	5222.76
47.20	125.64	1874.29	5216.93
52.20	133.01	1879.44	5216.95
57.20	147.24	1892.00	5225.94
62.20	169.23	1912.43	5242.98
67.20	199.10	1941.55	5270.89
72.20	237.74	1980.00	5309.49
77.20	286.03	2028.81	5360.58
82.20	344.74	2088.43	5423.24

Table A3. Z-matrix used to vary the OH bond length in H_2O-HO at a specific value of ϕ. O1 is the oxygen of water, O2 is the oxygen of the OH radical, X1 is a dummy atom, H1 is the hydrogen of the OH radical, and H2 and H3 are the hydrogens of the water. R_{OH} is the OH radical bond distance that is varied. All other coordinates are fixed.

O1						
O2	O1	Distance1				
X1	O1	Distance2	O2	ϕ		
H1	O2	R_{OH}	O1	Angle1	X1	0
H2	O1	Distance4	X1	Angle2	H1	90
H3	O1	Distance5	X1	Angle2	H1	-90

Table A4. Fit coefficients for the Morse potential as a function of ϕ for H_2O-HO on the $^2A'$ surface. At each value of ϕ the one-dimensional energy vs. OH bond distance slices were fit to the Morse potential:

$$V(r,\phi) = D_e(\phi)\left[1-\exp\left(\left(-\alpha(\phi)\left[r-r_e(\phi)\right]\right)\right)\right]^2 + E(\phi)$$

Energies are in J.

ϕ (°)	α (*10^{10} m^{-1})	r_e (*10^{-11} m)	D_e (*10^{-19})	E (*10^{-16})
0.00	2.39593778	9.82437182	6.29869884	-6.63743787
5.00	2.39662401	9.82458946	6.29294450	-6.63743809
10.00	2.39925014	9.82519741	6.27197709	-6.63743863
20.00	2.40818307	9.82748526	6.20034033	-6.63744014
26.84	2.41649433	9.82962779	6.13399375	-6.63744119
31.84	2.42227091	9.83151849	6.08653258	-6.63744184
36.84	2.42769704	9.83345961	6.04117197	-6.63744197
41.84	2.43259606	9.83530606	5.99983823	-6.63744135
46.84	2.43619715	9.83706384	5.96741440	-6.63743994
51.84	2.43920366	9.83873188	5.93954303	-6.63743757
56.84	2.43950816	9.83991654	5.93041475	-6.63743401
61.84	2.43826239	9.84086619	5.93260654	-6.63742906
66.84	2.43424798	9.84136541	5.95425671	-6.63742276
71.84	2.42649485	9.84133293	6.00201182	-6.63741507
76.84	2.41653236	9.84086990	6.06639267	-6.63740568
81.84	2.40087000	9.83975794	6.17230625	-6.63739475
86.84	2.38371340	9.83832933	6.29174039	-6.63738216

Table A5. Fit coefficients for the Morse potential as a function of ϕ for H_2O-HO on the $^2A''$ surface. At each value of ϕ the one-dimensional energy vs. OH bond distance slices were fit to the Morse potential:

$$V(r,\phi) = D_e(\phi)\left[1-\exp\left(\left(-\alpha(\phi)\left[r-r_e(\phi)\right]\right)\right)\right]^2 + E(\phi)$$

Energies are in J.

ϕ (°)	α (*10^{10} m^{-1})	r_e (*10^{-11} m)	D_e (*10^{-19})	E (*10^{-16})
0.00	2.38052996	9.82466965	6.40275998	-6.63740992
5.00	2.38133079	9.82488720	6.39600592	-6.63741020
10.00	2.38410475	9.82541315	6.37419275	-6.63741098
17.20	2.39045346	9.82682565	6.32332123	-6.63741261
22.20	2.39706990	9.82814862	6.27169081	-6.63741392
27.20	2.40444836	9.82963533	6.21420656	-6.63741531
32.20	2.41018630	9.83139842	6.16698048	-6.63741671
37.20	2.41737443	9.83329445	6.10981079	-6.63741756
42.20	2.42343883	9.83516215	6.06041034	-6.63741772
47.20	2.42894659	9.83695069	6.01540907	-6.63741709
52.20	2.43367543	9.83861033	5.97622973	-6.63741547
57.20	2.43573321	9.83996088	5.95558943	-6.63741261
62.20	2.43801289	9.84110296	5.93462033	-6.63740822
67.20	2.43679295	9.84180994	5.93781477	-6.63740240
72.20	2.43395380	9.84207492	5.95349548	-6.63739493
77.20	2.42738046	9.84183696	5.99502512	-6.63738571
82.20	2.42050664	9.84118183	6.04087957	-6.63737441

Table A6. Fit coefficients for the extended Morse potential as a function of ϕ for H_2O-HO on the $^2A'$ surface. At each value of ϕ, the values of r_e and α obtained from the Morse fit were fixed in the extended Morse potential:

$$V(r,\phi) = \sum_{n=2}^{4} D_n(\phi)[1-\exp(-\alpha(\phi)[r-r_e(\phi)])]^n + E(\phi)$$

Energies are in J.

ϕ (°)	D_2 (*10^{-19})	D_3 (*10^{-22})	D_4 (*10^{-20})	E (*10^{-16})
0.00	6.22016841	1.74843557	1.43353944	-6.63743255
5.00	6.21491651	1.75994946	1.42316608	-6.63743280
10.00	6.19593336	1.84219671	1.38446541	-6.63743347
20.00	6.13050605	2.08554150	1.26078456	-6.63743538
26.84	6.06950221	2.25257318	1.15545790	-6.63743676
31.84	6.02572973	2.34947684	1.08320571	-6.63743765
36.84	5.98341125	2.42351663	1.02381555	-6.63743797
41.84	5.94402796	2.56216486	0.98485523	-6.63743747
46.84	5.91271130	2.64313095	0.96188914	-6.63743613
51.84	5.88551579	2.74175835	0.94705902	-6.63743380
56.84	5.87400400	2.89742489	0.98820853	-6.63743007
61.84	5.87288203	3.06400074	1.04674316	-6.63742489
66.84	5.88852091	3.27062542	1.15571893	-6.63741818
71.84	5.92634553	3.47187457	1.33809222	-6.63740982
76.84	5.97849803	3.60445333	1.56714504	-6.63739963
81.84	6.06597003	3.59679520	1.92024234	-6.63738750
86.84	6.16540971	3.19915272	2.31341210	-6.63737364

Table A7. Fit coefficients for the extended Morse potential as a function of ϕ for H_2O-HO on the $^2A''$ surface. At each value of ϕ, the values of r_e and α obtained from the Morse fit were fixed in the extended Morse potential:

$$V(r,\phi) = \sum_{n=2}^{4} D_n(\phi)[1-\exp(-\alpha(\phi)[r-r_e(\phi)])]^n + E(\phi)$$

Energies are in J.

ϕ (°)	D_2 (*10^{-19})	D_3 (*10^{-22})	D_4 (*10^{-20})	$E(\phi)$ (*10^{-16})
0.00	6.31023960	1.45739080	1.70876004	-6.63740371
5.00	6.30428692	1.45786412	1.69278627	-6.63740404
10.00	6.28458431	1.58707469	1.64987997	-6.63740495
17.20	6.23881971	1.78509079	1.54743039	-6.63740691
22.20	6.19205426	2.02197060	1.44960705	-6.63740852
27.20	6.13995227	2.19698510	1.34292148	-6.63741025
32.20	6.09655263	2.33985596	1.26717455	-6.63741189
37.20	6.04411660	2.47976292	1.17414462	-6.63741304
42.20	5.99827371	2.57421263	1.10439982	-6.63741343
47.20	5.95600588	2.69564105	1.05042639	-6.63741297
52.20	5.91897130	2.78315914	1.00814899	-6.63741149
57.20	5.89808262	2.88266347	1.01058883	-6.63740861
62.20	5.87700007	2.98709318	1.00994164	-6.63740420
67.20	5.87725163	3.10592734	1.06248825	-6.63739818
72.20	5.88859782	3.25274045	1.14071790	-6.63739041
77.20	5.92194691	3.42050361	1.29137248	-6.63738064
82.20	5.95956601	3.51954814	1.44512330	-6.63736880

Table A8. Fit coefficients for the adiabatic potentials $V_{\nu_2}(\phi)$ with ν_2=0 and ν_2=1 for H_2O-HO on the $^2A'$ and $^2A''$ surfaces. Each $V_{\nu_2}(\phi)$ double-well potential was fit to the functional form:

$$V_{\nu_2}(\phi) = \sum_{n=0}^{3} c_n^{(\nu_2)} \phi^{2n}$$

Energies are in J.

	$^2A'$, ν_2=0 (*10^{-20})	$^2A'$, ν_2=1 (*10^{-20})	$^2A''$, ν_2=0 (*10^{-20})	$^2A''$, ν_2=1 (*10^{-20})
$c_0^{(\nu_2)}$	3.5543	10.2640	3.8458	10.569
$c_1^{(\nu_2)}$	-0.3085	-0.4827	-0.41587	-0.59172
$c_2^{(\nu_2)}$	0.3434	0.4361	0.37882	0.4652
$c_3^{(\nu_2)}$	-0.0463	-0.0581	-0.05137	-0.06312

Table A9. Fit coefficients for $\mu(r,\phi)$ along the a-inertial axis as a function of ϕ for H_2O-HO on the $^2A'$ surface. The $\mu(r,\phi)$ curves were fit to the functional form:

$$\mu(r,\phi) = \sum_{n=0}^{6} b_n(\phi) r^n$$

Coefficients are in Debye/m^n.

ϕ (°)	b_0	b_1 (*10^{10})	b_2	b_3 (*10^{30})	b_4	b_5	b_6
0.00	5.6670	-14.11606	33.32639	-37.26668	21.55043	-5.14376	0.27280
5.00	6.0662	-16.44456	38.81067	-44.05625	26.21045	-6.82453	0.52172
10.0	5.8644	-15.45308	36.60569	-41.49021	24.55445	-6.25501	0.43952
20.0	6.0360	-16.98435	40.48620	-46.68110	28.38650	-7.71301	0.66196
26.8	6.0992	-17.92915	43.02210	-50.25979	31.15194	-8.79964	0.83095
31.8	6.2889	-19.56630	47.18763	-55.84498	35.29132	-	1.08046
36.8	6.1881	-19.56776	47.41453	-56.45528	35.95180	-	1.13681
41.8	6.1338	-20.02661	49.00911	-59.11688	38.26267	-	1.30599
46.8	6.6772	-23.77218	57.91879	-70.35700	46.16766	-	1.75070
51.8	6.4715	-23.37589	57.25299	-69.94191	46.19718	-	1.78793
56.8	6.6213	-25.09740	61.64268	-75.88159	50.66153	-	2.07007
61.8	6.5873	-25.83874	63.76985	-79.06898	53.26276	-	2.25853
66.8	6.5999	-26.80206	66.20139	-82.37139	55.77075	-	2.42707
71.8	6.8664	-29.19138	71.82420	-89.44207	60.75716	-	2.72145
76.8	6.8338	-29.95259	73.72988	-92.05162	62.76887	-	2.86580
81.8	6.4777	-28.89377	71.32040	-89.26095	61.01955	-	2.80647
86.8	6.2983	-28.77164	70.87851	-88.61253	60.53559	-	2.79288

Table A10. Fit coefficients for $\mu(r,\phi)$ along the c-inertial axis as a function of ϕ for H_2O-HO on the $^2A'$ surface. The $\mu(r,\phi)$ curves were fit to a function of the form:

$$\mu(r,\phi) = \sum_{n=0}^{6} b_n(\phi) r^n$$

Coefficients are in Debye/m^n.

ϕ (°)	b_0	b_1	b_2	b_3	b_4	b_5	b_6
0.00	0	0	0	0	0	0	0
5.00	-0.05128	-0.56010	1.28687	-1.55435	1.04706	-0.37836	0.05733
10.0	0.03781	-1.90873	4.40365	-5.35451	3.63052	-1.31196	0.19744
20.0	-0.59353	0.01359	-0.04174	0.06574	-0.02640	-0.02821	0.01457
26.8	-0.67146	-0.57290	1.33475	-1.60676	1.10620	-0.44182	0.07850
31.8	-0.84337	-0.32131	0.73843	-0.85162	0.58055	-0.25556	0.05246
36.8	-0.85995	-0.88959	2.08396	-2.49403	1.69393	-0.65913	0.11393
41.8	-1.07775	-0.27779	0.76603	-0.95666	0.69519	-0.32273	0.06863
46.8	-1.42056	1.10209	-2.39655	2.89900	-1.91532	0.60291	-0.06532
51.8	-1.20264	-0.59383	1.47641	-1.70144	1.10853	-0.44534	0.08495
56.8	-1.52484	0.82566	-1.70828	2.12859	-1.45523	0.45388	-0.04358
61.8	-1.75823	1.87715	-4.27423	5.46571	-3.85062	1.34913	-0.17949
66.8	-1.35622	-0.62953	1.55484	-1.59417	0.88884	-0.32877	0.06579
71.8	-1.54540	0.32942	-0.69010	1.24386	-1.09815	0.39628	-0.04158
76.8	-1.81780	1.80752	-4.10088	5.47715	-4.02434	1.45918	-0.19973
81.8	-1.86941	2.13571	-4.81685	6.38856	-4.67540	1.70221	-0.23657
86.8	-1.78188	1.85125	-4.33528	6.10280	-4.68827	1.77737	-0.25732

Table A11. Fit coefficients for $\mu(r,\phi)$ along the a-inertial axis as a function of ϕ for H_2O-HO on the $^2A''$ surface. The $\mu(r,\phi)$ curves were fit to a function of the form:

$$\mu(r,\phi) = \sum_{n=0}^{6} b_n(\phi) r^n$$

Coefficients are in Debye/m^n.

ϕ (°)	b_0	b_1	b_2 (*10^{20})	b_3	b_4 (*10^{40})	b_5	b_6 (*10^{60})
0.00	-5.76226	14.7383	-34.68508	38.8095	-22.59285	5.61864	-0.37630
5.00	-5.86128	15.3557	-36.16955	40.6878	-23.90910	6.10106	-0.44847
10.0	-6.01418	16.3641	-38.60185	43.7766	-26.07818	6.89233	-0.56529
17.2	-6.31633	18.3721	-43.34114	49.7052	-30.20114	8.38664	-0.78486
22.2	-6.17717	17.9703	-42.65860	49.2069	-30.08777	8.40637	-0.79246
27.2	-6.31889	19.2773	-46.08733	53.9084	-33.61893	9.76386	-1.00077
32.2	-6.62094	21.4280	-51.15676	60.2428	-38.02200	11.36550	-1.23801
37.2	-6.46186	21.1874	-51.01168	60.6234	-38.66727	11.71775	-1.30368
42.2	-6.77460	23.6381	-57.03878	68.4620	-44.32265	13.84703	-1.62937
47.2	-6.63457	23.5870	-57.22974	69.1386	-45.10327	14.23363	-1.69933
52.2	-6.38651	23.0362	-56.39217	68.7229	-45.25323	14.43551	-1.74820
57.2	-6.87131	26.5867	-64.84776	79.3934	-52.75503	17.21524	-2.17054
62.2	-6.75141	26.8553	-65.87403	81.2131	-54.39998	17.95258	-2.29955
67.2	-6.83601	28.2262	-69.21329	85.5618	-57.56699	19.17854	-2.49448
72.2	-6.97697	29.9620	-73.40498	90.9466	-61.42359	20.64791	-2.72521
77.2	-6.68999	29.4066	-72.43900	90.2256	-61.27247	20.73938	-2.76113
82.2	-6.78297	30.8519	-75.74648	94.2976	-64.09760	21.80295	-2.92793

Table A12. Fit coefficients for $\mu(r,\phi)$ along the c-inertial axis as a function of ϕ for H_2O-HO on the $^2A''$ surface. The $\mu(r,\phi)$ curves were fit to a function of the form:

$$\mu(r,\phi) = \sum_{n=0}^{6} b_n(\phi) r^n$$

Coefficients are in Debye/m^n.

ϕ (°)	b_0	b_1	b_2	b_3	b_4	b_5	b_6
0.00	0	0	0	0	0	0	0
5.00	-0.14756	0.00334	-0.08909	0.19802	-0.18251	0.07350	-0.01074
10.0	-0.36192	0.26446	-0.49365	0.46055	-0.20860	0.02600	0.00498
17.2	-0.44933	-0.41019	0.97513	-1.24017	0.90729	-0.37448	0.06636
22.2	-0.40622	-1.35275	2.91732	-3.30728	2.10912	-0.73994	0.11205
27.2	-0.69414	-0.57781	1.32031	-1.57918	1.08572	-0.43175	0.07604
32.2	-0.85311	-0.41021	0.95715	-1.15910	0.82463	-0.35376	0.06797
37.2	-0.82569	-1.26078	2.96486	-3.63037	2.51287	-0.96503	0.15989
42.2	-1.11929	-0.21079	0.50711	-0.56617	0.39227	-0.19788	0.04693
47.2	-0.97416	-1.58674	3.71469	-4.47144	3.03530	-1.14530	0.18786
52.2	-1.38333	0.15928	-0.21410	0.22883	-0.09638	-0.04742	0.03002
57.2	-1.51732	0.48622	-0.91953	1.08738	-0.68336	0.16083	0.00061
62.2	-1.81613	1.81719	-4.01338	4.90723	-3.29634	1.09624	-0.13598
67.2	-1.65198	0.64761	-1.36396	1.80882	-1.29025	0.40964	-0.03838
72.2	-1.66307	0.48770	-0.95607	1.31786	-0.96420	0.29292	-0.02045
77.2	-1.71990	0.72412	-1.47830	2.00499	-1.46903	0.48357	-0.04900
82.2	-2.05010	2.54285	-5.66432	7.13567	-4.96136	1.73215	-0.23197

Table A13. Fit coefficients for transition dipole $\mu_{10}(\phi)$ for H_2O-HO on the $^2A'$ surface.

The $\mu_{10}(\phi)$ curve along the a-inertial axis was fit to the functional form

$$\mu_{10}(\phi) = \sum_{n=0}^{4} a_n \cos(n\phi) .$$

The $\mu_{10}(\phi)$ curve along the c-inertial axis was fit to the functional form

$$\mu_{10}(\phi) = \sum_{n=1}^{4} c_n \sin(n\phi) .$$

Coefficients are in Debye.

n	a_n	c_n
0	-0.103849	
1	-0.180134	-0.00946219
2	0.0802444	0.0117991
3	-0.0134553	-0.00318896
4	0.00315529	0.000851898

Table A14. Fit coefficients for transition dipole $\mu_{10}(\phi)$ for H_2O-HO on the $^2A''$ surface.

The $\mu_{10}(\phi)$ curve along the a-inertial axis was fit to the functional form

$$\mu_{10}(\phi) = \sum_{n=0}^{4} a_n \cos(n\phi) .$$

The $\mu_{10}(\phi)$ curve along the c-inertial axis was fit to the functional form

$$\mu_{10}(\phi) = \sum_{n=1}^{4} c_n \sin(n\phi) .$$

Coefficients are in Debye.

n	a_n	c_n
0	0.132593	
1	0.127822	-0.00661315
2	-0.0623971	0.00858682
3	0.00983493	-0.00188011
4	-0.00285507	0.000572737

Appendix 3:

Experimental Characterization of the Weakly Anisotropic CN $X\ ^2\Sigma^+$ + Ne Potential from IR-UV Double Resonance Studies of the CN-Ne Complex Supplementary Material

This research has been published as Supplementary material in the *Journal of Chemical Physics* (2011), *134*, 184308 and was performed in conjunction with post-doctorate Joseph M. Beames, second year graduate student Melodie Ting, and Marsha I. Lester in the *Department of Chemistry, University of Pennsylvania* as well as Thomas A. Stephenson in the *Department of Chemistry and Biochemistry, Swarthmore College*.

I. Theoretical Methods

The orbitals used in the MRCI calculations were generated using state-averaged complete active space self-consistent field theory (CASSCF). A CASSCF(9,8) active space was used in the calculations with the lowest 3 states of A' symmetry included in the state averaging. The MRCI calculations excluded only the lowest three 1s orbitals from the MRCI, allowing all single and double excitations from the remaining occupied orbitals into all virtual orbitals. C_s symmetry was used for all non-linear configurations, and C_{2v} for $\theta = 0°$ and 180° with care taken to ensure that the active space and state averaging were consistent between different symmetries.

Energies were calculated at each geometry using augmented correlation consistent basis sets (aug-cc-pVXZ) of varying cardinal number (X = 3,4,5). CASSCF energies and electron correlation energies from these calculations were used to extrapolate to the complete one-electron basis set limit (CBS). The Karton-Martin protocol was used as a two-point extrapolation method for the CASSCF energies, while the uniform singlet- and triplet-pair extrapolation scheme of Varandas was used to extrapolate the MRCI+Q electron correlation energy, utilizing energies from all three basis sets.[1-3] Extrapolation to the CBS limit in this fashion is used as an alternative to the counterpoise correction techniques employed in previous studies as a way of minimizing basis set superposition error.

II. Hindered Rotor Analysis

This work follows the theoretical treatment for open-shell diatom-rare gas complexes developed by Dubernet *et al.*,[4] in which the intermolecular potential $V_{\text{inter}}(R,\theta)$

is expressed as a Legendre polynomial expansion truncated after the first few terms. R is implicitly fixed at an effective intermolecular distance sampled experimentally. C_1 and C_2 are Legendre polynomials terms in θ, and V_{10} and V_{20} are radially-averaged anisotropy parameters characterizing the intermolecular potential. The model Hamiltonian for the bending (hindered rotational) motion of CN-Ne with CN in a Σ state following Hund's case (b) is then

$$H_{bend}^{(0)} = E^0 + bn(n+1) + V_{10}C_1 + V_{20}C_2 \tag{A1}$$

It is assumed that the intermolecular stretch can be decoupled from the hindered internal rotor motion and that the overall rotation of the complex can be neglected. Here, b is rotational constant for the CN monomer in a specific vibronic state.

Next, we adopt the formulation presented by Dubernet *et al.*[4] for evaluating the bending Hamiltonian with specific values of V_{10} and V_{20} to derive energies for the hindered rotor n^K states. The eigenvalues are obtained by diagonalizing an $n \times n'$ matrix form of the Hamiltonian with matrix elements composed of potential coupling coefficients

$$\langle nK | C_l | n'K \rangle = (-1)^K \left[(2n+1)(2n'+1) \right]^{1/2} \times \begin{pmatrix} n & l & n' \\ 0 & 0 & 0 \end{pmatrix} \begin{pmatrix} n & l & n' \\ -K & 0 & K \end{pmatrix} \tag{2}$$

Plotting the resultant energies of the n^K states as a function of V_{20} (for fixed V_{10}) generates a correlation diagram, specific to CN-Ne in a designated CN vibrational and electronic state. The correlation diagram generated for CN-Ne X (v_{CN}=2) is shown in Figure A1, obtained using the rotational constant of CN $X\,^2\Sigma^+$(v=2) (b=1.856 cm^{-1}).[5] The potential anisotropy terms, V_{10} and V_{20}, were varied until the n^K energy spacings were brought into agreement with those of the 0^0,1^1 and 1^0 hindered rotor states observed

experimentally (with associated uncertainties) for CN-Ne X (v_{CN}=2) as indicated by the vertical line in Figure A1. With two energy spacings for CN-Ne X (v_{CN}=2) we are able to determine both V_{10} and V_{20}, without the need for further assumptions or analysis. This process was then repeated to determine if these potential anisotropy parameters are consistent with the n^K states observed experimentally for CN-Ne X (v_{CN}=0) and confirm the parameters previously obtained for CN-Ne B (v_{CN}=0).[6]

Figure A1. Correlation diagram depicting the energies of n^K states for CN-Ne X (ν_{CN}=2). The different line styles indicate increasing quanta in K, with the solid line indicating K=0 followed by long dashed and short dashed lines. The different colors indicate increasing quanta in n with black indicating n = 0 followed by red then green. The width of the blue vertical line indicates the range of values of V_{20}, at a fixed value of V_{10} (-1.6 cm^{-1}), where the n^K spacings are within experimental uncertainty (0.1 cm^{-1}).

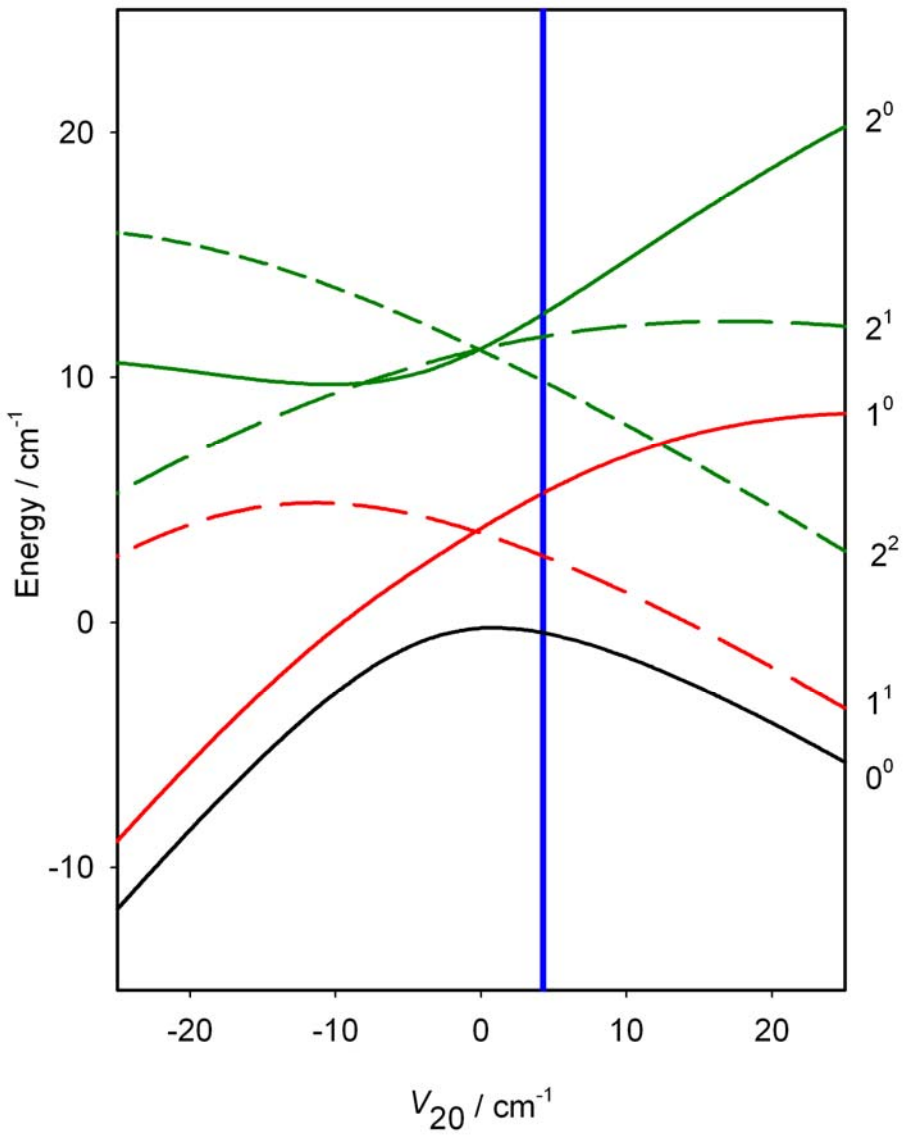
20
10
0
-10
Energy / cm-1
-20
-10
0
10
20
V20 / cm-1
2^0
2^1
1^0
2^2
1^1
0^0

References

1. A. J. C. Varandas, *J. Chem. Phys.* **113**, 8880 (2000).
2. A. J. C. Varandas, *J. Chem. Phys.* **126**, 244105 (2007).
3. A. J. C. Varandas, *J. Chem. Phys.* **129**, 234103 (2008).
4. M.-L. Dubernet, D. Flower, and J. M. Hutson, *J. Chem. Phys.* **94**, 7602 (1991).
5. D. Cerny, R. Bacis, G. Guelachvili, and F. Roux, *J. Mol. Spectrosc.* **73**, 154 (1978).
6. S. Fei and M. C. Heaven, *Proc. SPIE-Int. Soc. Opt. Eng.* **1858**, 286 (1993).

Appendix 4:

Characterization of Complexes of CN $X\ ^2\Sigma^+$ with Ar and H_2 via IR-UV Double Resonance Spectroscopy Supplementary Material

This research will be published as Supplementary material in the *Journal of Chemical Physics* and was performed in conjunction with post-doctorate Joseph M. Beames and Marsha I. Lester in the *Department of Chemistry, University of Pennsylvania*.

I. Determination of pure overtone transition of CN-Ar

To determine the pure overtone transition of CN-Ar, (v_{CN}, v_s, n^K) = (2,0,0^0) ← (0,0,0^0), electronic excitation spectra are recorded in the CN *B*-*X* (2,2) and CN *B*-*X* (2,0) regions. Multiple features are observed in the *B*-*X* (2,2) spectral region which may be correlated with transitions observed in the *B*-*X* (0,0) region[1] (Figure A1, blue and red traces). Two strong features are observed in the *B*-*X* (2,0) region at 30017.7 cm^{-1} and 30026.9 cm^{-1} which, when compared to the same features observed in the *B*-*X* (2,2) region (at 25959.2 cm^{-1} and 25968.4 cm^{-1}), allow for determination of the pure overtone transition in the method described below.

To accurately obtain the value for the pure overtone transition, a frequency offset is applied to the CN-Ar *B*-*X* (2,2) spectrum in steps of 0.10 cm^{-1} from 4058 cm^{-1} to 4060 cm^{-1}. The CN-Ar *B*-*X* (2,0) and *B*-*X* (2,2) spectra are then subtracted and a resulting residual trace is recorded for each value of the offset. The process is iterated for each offset value and a set of residuals are recorded for each. The standard deviations of the residual traces are then calculated and compared at each offset value. The minimum was found to be at 4058.5 cm^{-1} with an uncertainty of ±0.2 cm^{-1}, corresponding to the approximate bandwidth of the UV laser used to record the spectra.

Figure A1. CN-Ar *B*-*X* LIF spectra recorded in the CN *B*-*X* (0,0) region (blue), CN *B*-*X* (2,2) region (red), and CN *B*-*X* (2,0) region (black). A schematic representation of the electronic transitions is shown on the left-hand side of the figure. Spectral labels from Ref. 1 are also shown above observed transitions observed in the CN *B*-*X* (0,0) region.

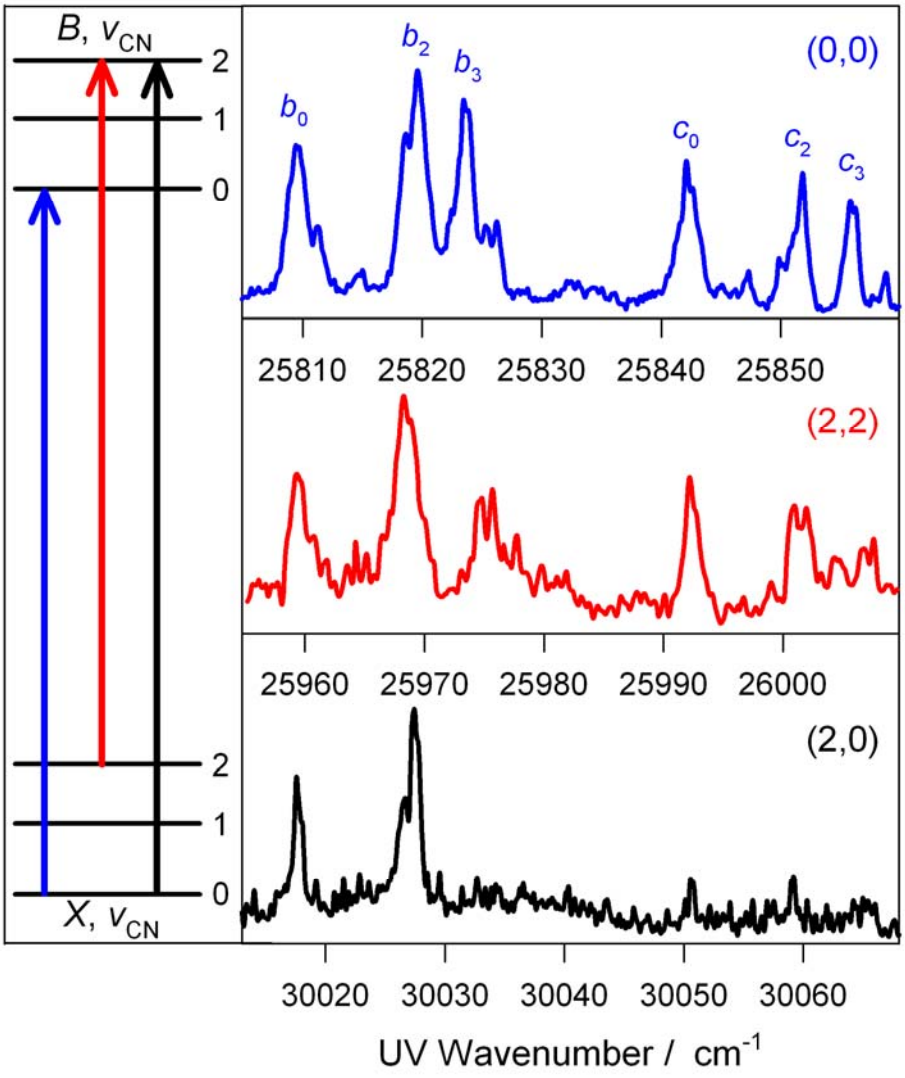
B, v_CN
2
1
0
X, v_CN
2
1
0
b0
b2
b3
c0
c2
c3
(0,0)
25810
25820
25830
25840
25850
(2,2)
25960
25970
25980
25990
26000
(2,0)
30020
30030
30040
30050
30060
UV Wavenumber / cm-1

II. Reassignment of H_2-CN *A*-*X* spectrum

An alternative spectral assignment is proposed for the H_2-CN *A*-*X* spectrum recorded by Kaledin *et al*.[2] The transition was originally simulated as a ΔK=1 type transition with a band origin of 12656.9 cm^{-1}, corresponding to the position of the *Q*-branch of the perpendicular transition, and rotational constants, B''=0.31 cm^{-1} and B'=0.28 cm^{-1}. The transition is simulated here with the ground state rotational constant, B''=0.39 cm^{-1}, derived from the IR spectrum, B'=0.36 cm^{-1}, and band origin of 12656.1 cm^{-1}. The *Q*-branch now corresponds to what was previously assigned as a congested *P*-branch. The transition that was assigned as *Q*(1) is resimulated as *R*(0) and the corresponding higher energy peaks make up the *R*-branch. The *P*-branch is predicted to be small relative to the *Q*- and *R*-branches and could be unobserved in the experimental spectrum.

Figure A2. Alternative simulation of band contour for the *A*-*X* electronic transition of H_2-CN with rotational temperature of 4 K and Lorentzian linewidth of 0.25 cm^{-1}. Rotational assignments are denoted as ticks.

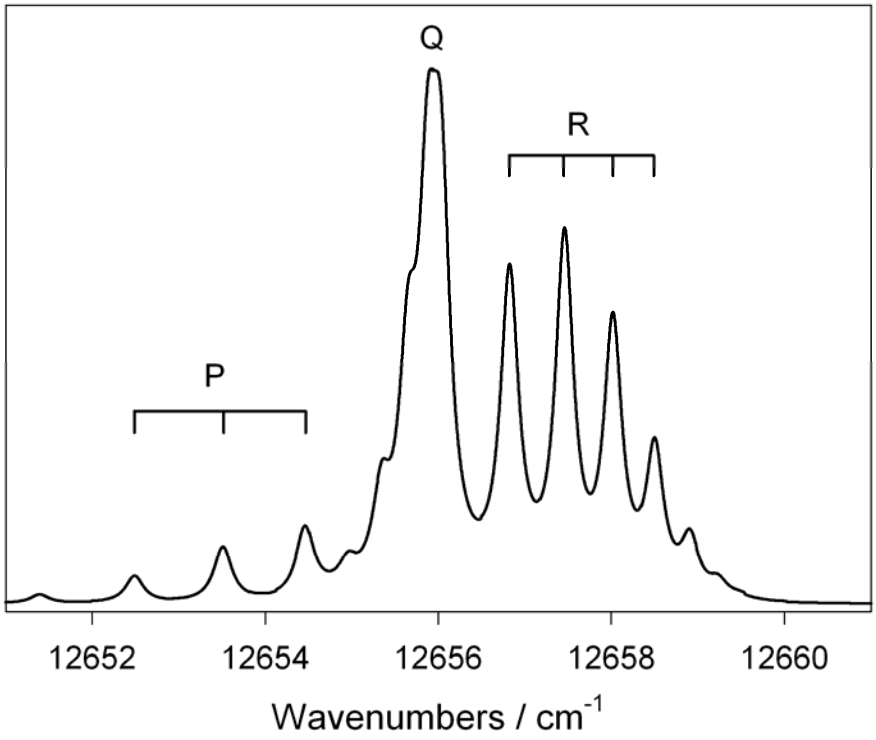
Q
R
P
12652
12654
12656
12658
12660
Wavenumbers / cm-1

Figure A3. Correlation diagram depicting the energies of n^K states for CN-Ar X (v_{CN}=2) at constant V_{10} (5.2 cm^{-1}) as a function of V_{20}. States of increasing n are indicated by line color where black corresponds to n=0, red to n=1, and green to n=2. Different K states are indicated by line type where the solid lines designate K=0, the long dashed lines, K=1, and the short dashed lines, K=2. The blue reference line reflects the range of values of V_{20} that reproduce the observed spacings based on experimental uncertainty, from 2.6 to 3.8 cm^{-1}.

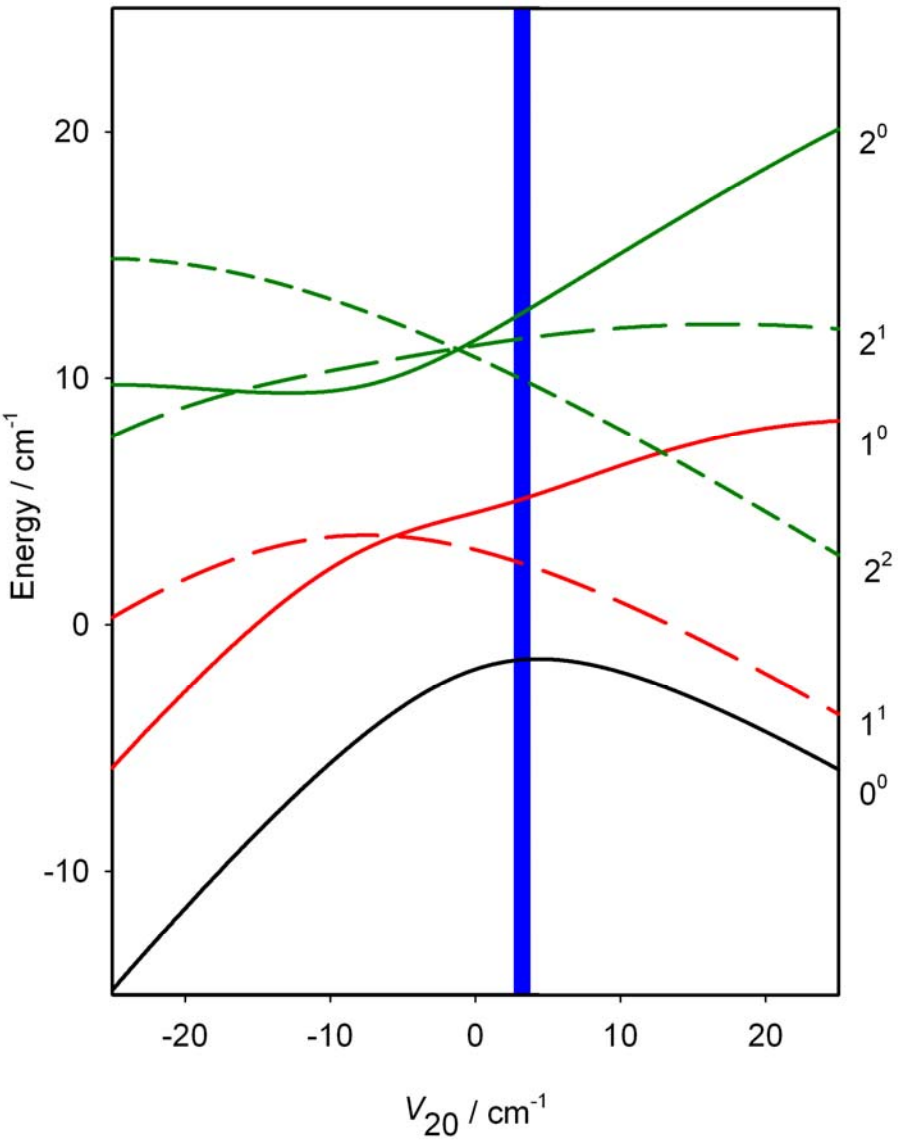
20
10
0
-10
Energy / cm-1
-20
-10
0
10
20
V20 / cm-1
2^0
2^1
1^0
2^2
1^1
0^0

References

1. J. Han, M. C. Heaven, U. Schnupf, and M. H. Alexander, J. Chem. Phys. **128**, 104308 (2008).

2. A. L. Kaledin and M. C. Heaven, Chem. Phys. Lett. **347**, 199 (2001).